Gamma radiation from type Ia Supernovae

Gamma Strahlung von Typ Ia Supernovae

Alkifron Spyridon Sonnberger

Abschlussarbeit im Masterstudiengang Physik
Physik-Department
Technische Universität München

Supervisor: Prof. Dr. Roland Diehl
Submitted on: 2. July 2019

Max Planck Institute for extraterrestrial Physics
Department of High Energy Astrophysics

2019

Abstract

Motivation The purpose of this thesis is to study the γ-ray emission of SN2014J and SN2011fe, two nearby type Ia supernovae that exploded in galaxies M82 and M101, respectively. γ-rays have the power to give insights into the distribution and kinematics of radioactive nickel, an element presumably produced during the explosion. Comparing the calculated fluxes to explosion models, conclusions about the progenitor system and the explosion mode can be drawn. The distances to SN2014J and SN2011fe should allow the detection of the most prominent γ-ray lines from the ^{56}Ni decay chain and give estimates on the mass of radioactive ^{56}Ni synthesized in the explosion.

Aims The three main objectives of this work are to analyze the early spectra of both explosions and look for an early γ-ray emission from ^{56}Ni, to use the whole observation dataset to explore the variability and spectral properties of the brightest ^{56}Co lines and finally to investigate the energy band, where the emission from the annihilation of positrons, produced through the β^+-decay channel of ^{56}Co is expected.

Methods The datasets used in this study are obtained from spectrometer SPI on INTEGRAL. The celestial fluxes are derived using an empirical background modeling approach for SPI that takes advantage of the longevity of the mission to precisely model the instrumental background. The adequacy of the background modeling was tested with various methods, optimized to achieve maximum sensitivity. Both supernovae have excellent exposure times, 4.2Ms over 37 orbits for SN2014J and 2.8Ms over 20 orbits for SN2011fe. To calculate line fluxes, free Gaussian line models were fitted to the data using the χ^2-minimization technique.

Results The early spectra of both supernovae showed early ^{56}Ni emission. The corresponding fluxes were converted into $M_{^{56}\mathrm{Ni}}^{\mathrm{SN2014J}}=0.13\pm0.07 M_\odot$ and $M_{^{56}\mathrm{Ni}}^{\mathrm{SN2011fe}}=0.19\pm0.12 M_\odot$ near the surface of SN2014J and SN2011fe, respectively. γ-ray emission from the prominent lines of ^{56}Co, the 847keV and the 1238keV lines, was detected in the all-mission spectrum of SN2014J, as well as in shorter epochs, with detection significances exceeding 3σ. Combining the results of all approaches, I determined a synthesized ^{56}Ni mass of $M_{^{56}\mathrm{Ni}}=0.59\pm0.11 M_\odot$ for SN2014J. For SN2011fe, 2σ upper limits at $\sim 2.5\times10^{-4}$ph/cm^2/s and 1.5×10^{-4}ph/cm^2/s for the 847keV and 1238keV lines respectively, were derived, which were too high to exclude possible explosion models. Finally, my analysis of the energy band relevant for positron annihilation shows traces of an excess number of positrons, compared to the positron production rate derived from the fluxes of the 847keV line. The data indicate a positronium fraction of zero, while the positron escape during the first five months of supernova evolution is negligible. However, the large errors in the fitted line parameters do not allow firm conclusions about the fate of the positrons inside type Ia supernova envelopes.

Acknowledgements

I would very much like to thank Prof. Dr. Roland Diehl for offering me this thesis and for every piece of advice and knowledge I got from him. I am really grateful to him for the encouragement and support throughout the project and for all the fruitful and inspiring conversations we had during the time of my thesis.

I am very grateful to the Max Planck Institute of extraterrestrial physics for granting me the opportunity to write my thesis in a supportive and friendly research environment and to the Max Planck Computing & Data Facility for their readiness to help, whenever I faced computing issues.

I would also like to thank Thomas Siegert and Christoph Weinberger for introducing me to the fundamental aspects of data analysis and for making their data analysis programs available to me. Special thanks to my office mate Simon Steinmassl for his ideas and comments.

Last but not least, I want to deeply thank my family for providing all the means to go through this thesis and for the continuous trust, support and love I felt throughout my study years in Munich.

Munich, 2 July 2019

Alkifron Spyridon Sonnberger

Contents

List of Figures

List of Tables

List of Acronyms

ACS -Anticoincidence shield

APD -Avalanche photodiode

BGO -Bismuth germanate ($Bi_4Ge_3O_{12}$)

BH -Black hole

CE -Compton scattering effect

CGRO -Compton Gamma Ray Observatory

CMB -Cosmic Microwave Background

CO -Carbon oxygen

COMPTEL -Compton telescope

DD -Double degenerate

EC -Electron capture

ESA -European Space Agency

ESO -European Southern Observatory

eV -electron volt

FCFV -Fully coded field of view

FWHM -Full width at half maximum

GeNonSatTot -Germanium non-saturated total events

GeSatTot -Germanium saturated total events

GRB -Gamma-ray burst

HRD -Hertzsprung-Russel diagram

HST -Hubble Space Telescope

IBIS -Imager on-Board the INTEGRAL Satellite

IC -Inverse Compton effect

IGE -Iron-group element

IME -Intermediate-mass element

INTEGRAL -International Gamma-Ray Astrophysics Laboratory

ISM -Interstellar medium

JEM-X -Joint European X-Ray Monitor

MIR -Middle infrared

NIR -Near infrared

NS -Neutron star

OMC -Optical Monitoring Camera

OSSE -Oriented Scintillation Spectrometer Experiment

PCFV -Partially coded field of view

PE -Photoelectric absorption effect

PMT -Photomultiplier tube

PNS -Proto-neutron star

PP -Pair-production effect

Ps -Positronium

PSAC -Plastic scintillator anticoincidence subassembly

PSD -Pulsed shape discriminator

QED -Quantum electrodynamics

SD -Single degenerate

SFR -Star formation rate

SN -Supernova

SNR -Signal-to-noise ratio

SPI -Spectrometer aboard INTEGRAL

UT -Universal time

UVOIR -Ultraviolet-optical-infrared

WD -White Dwarf

1. Introduction

Ever since the ancient times, humans turned their eyes toward the sky to observe the countless little point sources of light that they named stars, and other periodic and transient phenomena, like the phases of the moon, solar and lunar eclipses, the movements of the planets in the night sky, the flybys of comets as well as sudden, temporary appearances of 'new' stars, that shone brightly for several week before fading back into darkness. These 'new-stars', known as 'supernovae' in our time, as well as many other astronomical events, have been recorded since antiquity and were often linked with omens of good and bad fortune, like prosperity, famish, wars, peace, etc.

The lust of observing and understanding the Universe has not dwindled until modern times. After the realization, in the 19^{th} century, that the visible light is only a minuscule fraction of a vast electromagnetic spectrum, ranging from low-energy radio waves up to highly energetic gamma-rays (from now on γ-rays), astronomers started building continuously more and more sophisticated instruments, each of them sensitive to a different type of electromagnetic radiation. The fact that every particular astrophysical process emits electromagnetic radiation in a very specific energy domain, turns a multi-wavelength study of an astrophysical object into a necessity. The goal of modern astronomy, thus, is to collect and study the complete emission spectrum of an astrophysical phenomenon, in order to obtain a complete picture of the physical processes that took place in a faraway corner of spacetime.

Thermonuclear supernovae are perfect examples of the progress that can be made when observational evidence from all wavelength bands, as well as theoretical work, are combined. First of all, they are of vital importance in modern astrophysics and cosmology, involving most areas of current astrophysical research, like binary evolution, particle acceleration, stellar hydrodynamics and radiation transport (Hillebrandt et al. 2013). Besides, thermonuclear supernovae play a fundamental role in the chemical and dynamical evolution of their host galaxy, by recycling matter and triggering star formation. However, their greatest contribution to astrophysics is their use as distance indicators in extragalactic cosmology, based on the homogeneity of their light curves (Leibundgut 2001). There is common consensus that they are powered from the energy input of radioactive materials synthesized during the explosion, the most abundant of them being ^{56}Ni (Arnett 1982). Its decay γ-rays are reprocessed inside the ejecta and emitted in other bands of the electromagnetic spectrum. The exact amount of synthesized ^{56}Ni is found to vary between explosions, questioning thus the validity of thermonuclear supernovae as standard candles. This class of explosions can only be used as a powerful extragalactic distance tool if its underlying physics is understood to the greatest extent. Today, it is widely accepted that thermonuclear supernovae originate from the thermonuclear explosion of White Dwarfs in binary systems (Hoyle and Fowler 1960). However, the exact nature of the companion star, as well as the hydrodynamical evolution of the explosion remain elusive and disallow a complete physical picture of the event and restrict their use for cosmological conclusions. Despite the considerable progress of observations, the absence of a nearby galactic event in the era of modern astronomy conceals the answers to fundamental questions on the exact physical nature of thermonuclear explosions.

In this regard, two thermonuclear supernovae that exploded in the years 2011 and 2014 have the potential to change that. In particular, SN2011fe in galaxy M101 and SN2014J in galaxy M82, at distances of 6.4Mpc and 3.5Mpc respectively, are the long-sought 'nearby' explosions, whose

proximity offers a unique opportunity to study extensively the nature of these events across the electromagnetic spectrum, from radio to γ-rays. In fact, a large ensemble of astronomic observation tools on Earth and in orbit turned their fields of view toward these rare celestial events, trying to gather as much astrophysical information as possible. These triggered further work by theoreticians, who tuned their models to match and adequately explain observations. The hand-in-hand collaboration between simulations and observations can provide the missing pieces to the long undetermined riddle of these cataclysmic explosions.

In this context, the aim of this master thesis is to analyze the γ-ray spectrum of the two nearby thermonuclear supernovae and search for the γ-emission produced through the decay chain of ^{56}Ni to ^{56}Co to ^{56}Fe. Radioactive ^{56}Ni is presumably synthesized in large quantities during the explosion and its decay γ-rays are believed to power-up the light curve for months after the explosion (Arnett 1969). A complete ^{56}Ni analysis is done by investigating all its prominent γ-ray lines, as well as those from ^{56}Co, its radioactive daughter nucleus. One of the decay modes of ^{56}Co results in the emission of positrons, that are born at relativistic speeds and interact with their environment in various ways.

The main goals of this work are to take advantage of the direct link of γ-radiation to the radioactive decay of nuclei to derive ^{56}Ni masses and constrain or at least indicate the most appropriate progenitor system and explosion mode theorized for the aforementioned stellar explosions. Furthermore, by analyzing the energy range where positron annihilation with electrons should be measurable, the propagation and annihilation conditions of positrons in an expanding supernova envelope are inspected and subsequently, the positron escape fraction of thermonuclear supernovae is determined. Even if a small fraction of positrons succeeds in evading annihilation in the explosion debris and escapes into the interstellar medium, γ-ray data could confirm thermonuclear supernovae as major contributors of the strong positron annihilation signal measured across the Milky Way (Weidenspointner et al. 2006; Siegert 2017).

The data used in this study are obtained from spectrometer SPI on the INTErnational Gamma-Ray Astronomy Laboratory (INTEGRAL), a γ-ray telescope in space, observing the high-energy Universe between 20-8000keV since the year 2002 (Winkler et al. 2003). Despite the fact that thermonuclear supernovae are strong sources of γ-radiation during the first months of their evolution, extragalactic distances make the signal very faint in this energy domain of the electromagnetic spectrum for the current generation of γ-ray telescopes. Thus, a very careful data analysis is an essential prerequisite, in order to extract the faint celestial emission γ-ray fluxes from a large instrumental background, resulting from the continuous bombardment of the spacecraft by highly energetic cosmic particles. This is achieved by using an empirical background approach for SPI that takes advantage of the longevity of the mission to model precisely the instrumental background.

The thesis is structured as follows: Chapter 2 presents the basic astrophysical background concerning the evolution and subsequent explosion of stars. The main focus of this chapter lies, however, in the properties, candidate progenitor systems and diversity of thermonuclear supernovae, which are triggered by low to intermediate-mass stars. Thermonuclear supernovae are major sources of positrons and γ-photons, whose properties are presented in chapter 3. In particular, the physics concerning positrons, starting from the production and continuing with their deceleration and subsequent annihilation, with direct references to thermonuclear supernovae, is discussed in the first part of chapter 3. Subsequently, the production and interaction of γ-rays as well as the physical concept of radioactivity, are presented. In chapter 4, an overview of ESA's satellite, INTEGRAL and its observing spectrometer SPI is given. Following that, the background model used and the methods for analyzing the highly background dominated γ-ray data are discussed and presented.

Chapter 5 comprises a complete γ-ray picture of SN2014J in M82, while chapter 6 contains the same for SN2011fe in M101. Finally, chapter 8 summarises the results, points out similarities and differences between the two targeted objects and discusses further improvements for future supernovae studies in the γ-band.

2. Stars and Supernova explosions

2.1. Stars and their evolution

Stars are shining gas spheroids that are born when massive molecular clouds collapse under their own gravity, become hotter and ultimately reach core temperatures and densities where hydrogen can fuse. Through most of their lifetimes, stars are stable, owing to the fact that the inward gravitational force is in hydrostatic equilibrium with the outward gas pressure force from the energy released during nuclear burning. Due to their effective surface temperatures of several thousand Kelvin, stars shine brightly in the night sky, as most of the emission at this temperature regime reaches a maximum in the optical band. In their cores, however, they reach temperatures of $T_c \sim 10^7$ K and higher.

Like most astrophysical objects, stars show diverse stellar properties. Their masses range between $\sim 0.08 M_\odot$ and several $100 M_\odot$, while their radii span a range between $\sim 0.001 R_\odot$ and $\sim 2000 R_\odot$. Red dwarf stars shine 1000 times fainter than the Sun; on the other end, the most luminous blue stars exceed the solar luminosity by more than six orders of magnitude. Their effective surface temperatures can vary from 2500K to $\sim$ 30000K or more (Janka 2017). At the beginning of the 20$^{\text{th}}$ century, astronomers Ejnar Hertzsprung and Henry Norris Russel attempted to classify stars according to their luminosities and effective surface temperatures, thus developing the so-called Hertzsprung-Russel diagram (HRD).

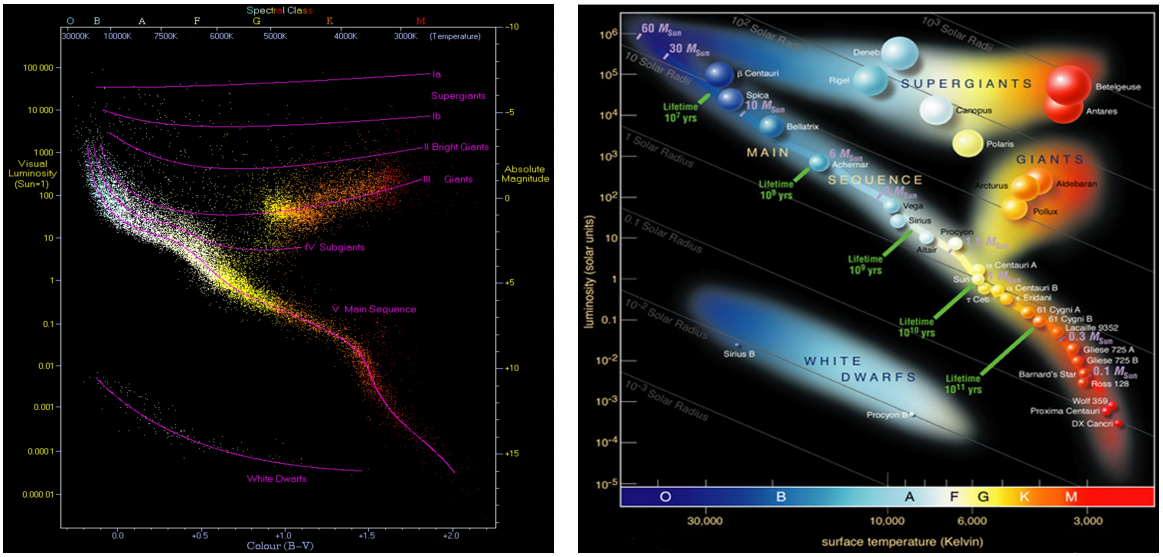

(a) A HRD involving stars from the Hipparcos the Gliese catalog. (R.Powell, www.atlasoftheuniverse.com)

(b) A HRD showing many well known stars of the Milky Way (from www.ESO.org)

Figure 2.1.: Two common representations of HRD diagrams

Every star has its own distinctive position on the HRD, where the coolest and dimmest stars are

located on the bottom right of the diagram and the hottest and brightest stars are found on the top left corner. The most striking feature of the HRD is a continuous, diagonal band called the main sequence, where $\sim 90\%$ of all stars are arranged. Stars spend the longest part of their existence on the main sequence, burning hydrogen to helium; the reaction that provides the required energy to maintain hydrostatic equilibrium.

For low-mass stars, like the Sun, this stage can last several billion years. Massive stars with high luminosities burn their fuel much faster than low-mass stars, depleting their hydrogen reserves within a few million years. As the star approaches the end of the hydrogen burning stage, a progressively higher amount of helium is accumulated in its core. Since no nuclear fusion takes place to counteract the gravitational force, the helium core contracts, releasing thereby gravitational binding energy. The virial theorem for stars dictates that half of the released gravitational binding energy is used to increase the internal energy of the star, i.e. the helium core gets hotter. If the temperature exceeds $T_c \sim 10^8$K, the so-called triple-α reaction commences (Woosley et al. 2002). This process fuses helium into more massive α-based nuclei, like carbon and oxygen, while the residual hydrogen continues to burn in a shell enclosing the core. At this moment, the star leaves the main sequence, expands its radius and moves towards higher luminosities, hence becoming a giant or a super-giant.

The fusing sequence from lighter to heavier and more tightly bound elements can have multiple stages, depending on the initial mass of the star and consequently on the temperature of its core. Stars more massive than ~ 8 times the Sun end up with a core formed of iron-group elements (IGEs), which have the highest binding energies per nucleon (Fowler and Hoyle 1964). Further fusing of iron is an endothermic reaction. Thus, the long stage of nuclear burning ends and the star reaches the final stages of its life.

2.2. Core-Collapse supernovae

Massive stars with initial masses $M_* \geq 8M_\odot$ go through all burning stages and start accumulating iron in their cores. Iron is the element with the highest binding energy per nucleon and thus further fusing into heavier elements is energetically disfavored. Having lost its energy supply by nuclear burning, the iron core slowly contracts up to the point, where electrons become degenerate and their Fermi energy becomes high enough to halt the contraction induced by the gravity of the star. However, as further iron is produced through Si burning in a shell around the core, the temperature in the core continues to rise until relativistic electrons start interacting with ambient ions via electron capture (Janka 2017). This interaction not only reduces the electron density and consequently the Fermi pressure in the core, but also removes energy from the system, through the escape of energetic neutrinos. The pressure does not rise fast enough to counteract the inward gravitational force and the core collapses. For stars with initial masses $M_* \sim 10M_\odot$, electron captures and the subsequent neutrino escape are the primary causes of gravitational instability.

Stars with initial masses $M_* \geq 10M_\odot$ reach higher core temperatures in the final stages of their lives ($T_c \geq 10^{10}$K) that lead to an increased fraction of energetic γ-photons. These break up iron-group nuclei down to α-nuclei, protons and neutrons, which is an endothermic process called photodisintegration and removes energy from the core. The former iron core transforms into a so-called proto-neutron star (Woosley et al. 2002). In addition, relativistic electrons are captured by protons, producing neutrons and neutrinos, where the latter escape the system and further decrease the outward pressure of the core leading to its gravitational collapse.

The implosion stops abruptly when the core density rises beyond nuclear matter densities $\rho_c \geq 10^{14}$

g/cm^3. At this stage, the neutron degeneracy pressure[1] takes over and prevents further contraction. However, the equilibrium point is crossed and pressure waves begin propagating outward; the core bounces. At the edge between the abruptly halted core and the still-collapsing layers, a shock front that moves radially outward and photodisintegrates the in-falling overlying stellar material is generated. However, this reaction consumes $\sim$ 9MeV per nucleon, reducing thereby dramatically the strength of the shock front ($E_{loss} \sim 10^{51}$erg per $0.1M_\odot$). Electron capture reactions and the subsequent neutrino escape further decrease the energy of the shock front that after a few hundred kilometers should stall.

How the core-collapse and the subsequent bounce lead to a successful explosion cannot be reliably explained, despite years of extensive studies and sophisticated computer simulations. It is believed that neutrino energy deposition could provide the necessary energy to revive the shock front and keep it propagating outwards (Colgate and White 1966; Bethe 1990; Sukhbold et al. 2016) but firm conclusions about the explodability of core-collapses in supernova simulations cannot be made. It is general consensus that a fraction of the ejecta fall back to the center as a result of gravitational attraction, albeit the mass cut, defined as the borderline between matter that is ejected and matter that falls back, is one of the most uncertain quantities. Simulations indicate that a fraction of massive stars fail to generate strong enough outward moving shocks and implode forming black holes (Heger et al. 2003).

There is observational evidence, that core-collapse supernovae produce compact remnants. Depending on several characteristics of the progenitor star, like rotation, initial and iron core masses, the final mass cut and others, either a neutron star (NS) or a black hole (BH) remain as a collapsed remnant. Their masses depend strongly on the final mass cut during the explosion and are hence quite uncertain. Observations constrain the mass of neutron stars between $1.0M_\odot$ and $1.8M_\odot$ and for black holes between $5M_\odot$ and $20M_\odot$ (Ozel and Freire 2016; Wiktorowicz et al. 2014). In fact, several objects in the center of supernova nebulae have been identified, among them the Crab pulsar, a highly magnetized rotating neutron star in the Crab nebulae (d$\approx$1.7pc[2]).

From the observational point of view type II supernovae are characterized by strong hydrogen lines and low (compared to other supernova types) expansion velocities that keep the most central areas of the envelope optically thick for a few years (Janka 2011; Smartt 2015). Their light curves can be highly diverse, both in brightness and shape, a direct consequence of the varying mass, composition, mass-loss history and other properties of each exploding star. Typically, type II supernovae reach their maximum luminosity 2-3 weeks after the explosion followed by a brightness decline. Some supernovae have light curves showing a characteristic flat stretch; a plateau, and are hence classified as type II-P supernovae. The luminosity plateau is believed to originate from an extended envelope of ionized hydrogen, that traps radiation photons and delaying thus their escape. Explosions showing a steady linear decline after peak maximum are labeled type II-L explosions and are thought to originate from stars that have lost a fraction of their outer hydrogen envelope (for typical SN lightcurves, see left panel of Fig. 2.2).

In general, both the diversity and peculiarity of the observed exploded objects (i.e. SN1987A in the Large Magellanic Cloud), as well as several key uncertainties in the explosion mechanisms, turn the study of core-collapse into a very active and continuously updating research field.

[1] Similar to the electron degeneracy pressure discussed in Sec. 2.3.1, but involving neutrons.

[2] A parsec (short 'pc') is the standard unit of length used in astronomy. It is defined as the distance at which the mean Earth-Sun radius subtends an angle of one arcsecond; equal to $\approx$ 3.26 light years or 3.1×10^{16}m.

2.2.1. Supernovae type Ib, Ic

Supernovae type Ib and Ic were officially declared as separate subtypes of supernovae explosions several decades after their initial categorization as a mixture between type I and type II (Filippenko 1997). They were initially classified as type I, due to the absence of hydrogen in their spectra but lack the characteristic Si and Fe lines seen in type Ia's. In addition, their appearance primarily in late-type galaxies, close to star-forming regions, suggests a correlation with massive stars and type II supernovae.

In fact, type Ib and Ic supernovae are thought to originate from massive stars with strong stellar winds that strip them of their outer hydrogen envelopes (i.e. Wolf-Rayet stars). In consequence, their spectra share large similarities with typical type II spectra but lack completely H lines while their light curves show a faster decline rate compared to regular type II explosions (Janka 2011). The only difference between type Ib's and type Ic's is the fact that the latter also lack He lines, indicating that the progenitor star has lost both its hydrogen as well as its helium envelope. Light curves of supernovae of type Ib and Ic look very similar to those of type Ia's, albeit being $\sim$ 1-2 magnitudes fainter than normal type Ia's. To distinguish between them and sub-luminous type Ia, a spectroscopic analysis is required.

The increase of observational data and the progressively improving data quality has led to observations of several peculiar cases, enriching the so-called 'supernova zoo'. Some of them include (Janka 2011):

- SNe type II can be further categorized according to the width of their hydrogen lines. For instance, incidences with narrow lines are classified as type IIn explosions.
- One exotic subclass of explosions that can be up to 100 times more luminous than normal type II's, are so-called ultra-luminous supernovae explosions. They are characterized by slow luminosity declines and high masses of synthesized ^{56}Ni and are believed to originate from very massive stars, with $M_* \geq 100 M_\odot$.
- Some incidents of type Ib,c can show a considerable degree of asymmetry, combined with large expansion velocities and high explosion energies. These exceptionally luminous explosions, also referred to as 'hypernovae' are sometimes accompanied by Gamma-Ray Bursts (GRB).

2.3. Low-mass stars and their final fate

Low and intermediate-mass stars ($M_* < 8 M_\odot$) do not reach the acquired core temperatures to go through all burning stages and end up with a core containing the nuclear ashes of the last successfully ignited burning stage. The absence of the energy supply to counteract the gravitational force initiates a contraction that halts only after the electrons in the core become degenerate. The star reaches thereby densities of $\rho_c \approx 10^6$ g/cm^3 and shrinks to a radius of a few thousand kilometers. The newly formed object succeeding the former Red Giant that lost its outer envelopes and shrunk to the size of the Earth is called a White Dwarf (WD).

2.3.1. White Dwarfs

A WD is the final evolutionary stage of stars not massive enough to go through all burning stages up to iron. These compact stellar remnants are characterized by high effective surface temperatures and low luminosities, thus populating the lower left corner of the HRD. The strong gravitational force pulls the object together, forcing its atomic electrons to the most compact configuration

allowed. A tighter electron configuration is forbidden by Pauli's exclusion principle, which states that two electrons are not allowed to occupy the same quantum state simultaneously. Pauli's exclusion principle results in a pressure that resists further gravitational collapse, the so-called electron degeneracy pressure, or Fermi pressure. Electrons are denoted 'degenerate electrons' when their Fermi pressure exceeds their thermal pressure. Depending on the mass of their parent star, the resulting WDs can have different compositions:

- Very low mass stars with $M_* < 0.5M_\odot$ that only manage to fuse hydrogen into helium end up as helium WDs. As low mass stars burn their fuel at low rates, He WDs take $\sim 10^9$ Gyr to form and the ones known today presumably accelerated their evolution through binary interaction (Hillebrandt et al. 2013).
- The most common WDs consist of a mixture of carbon and oxygen and are hence called CO WDs. They are formed from stars with initial masses of $0.5M_\odot \leq M_* \leq 8M_\odot$ that are hot enough to fuse helium via the triple-α reaction (Woosley et al. 2002).
- More massive stars with initial masses $8M_\odot < M_* \leq 10M_\odot$ leave WDs composed of oxygen, neon and magnesium behind, provided that they do not collapse into neutron stars (Nomoto 1984; Woosley et al. 2002).

The mass of a WD can vary by more than one order of magnitude, with the lighter ones having a few tenths of a solar mass and the more massive ones reaching a limiting mass, the Chandrasekhar mass.

Chandrasekhar mass limit

For a self-gravitating body supported by degenerate, relativistic electrons a critical mass exists that marks the highest mass a degenerate object can reach before becoming unstable. Increasing masses lead to smaller radii, higher densities and thus higher Fermi energies, ultimately turning a large fraction of the degenerate electrons relativistic. The equation of state for degenerate electrons transforms from $P \propto \rho^{5/3}$ for the non-relativistic case into $P \propto \rho^{4/3}$ for the relativistic case (Janka 2017). As the pressure does not increase fast enough to counter the contraction, gravity ultimately dominates and the WD collapses. The maximum allowed mass is called the Chandrasekhar mass and can be written as (Chandrasekhar 1938):

$$M_{Ch} \approx 5.83 M_\odot Y_e^2 \tag{2.1}$$

For a CO WD consisting of elements with an equal number of protons and neutrons, the proton-to-neutron ratio $Y_e = 0.5$ leads to a Chandrasekhar mass of $1.457M_\odot$.

A single WD is unconditionally stable and doomed to cool forever, radiating gradually its thermal energy away. Due to its low luminosity, it could take several Gyr for a WD to radiate all its internal energy and fade into darkness. A different fate may await the WD if it is born in a binary system. Provided that the separation distance of the two objects is within a certain range, the WD may accrete matter from its companion, reviving thus its ability to undergo nuclear reactions.

2.4. Thermonuclear supernovae

Thermonuclear supernovae are luminous stellar explosions, believed to originate from CO WDs in binary systems (Hoyle and Fowler 1960). They are classified as type Ia due to the lack of hydrogen

lines and the presence of prominent absorptions features of silicon in their early spectra. In the optical, they are characterized by a sudden increase of their light curve, that reaches its maximum $\sim$ 20 days after first light, followed by a rapid decline within the first month and a slower decrease of luminosity lasting several months.

Type Ia supernovae play a vital role in astrophysics. Due to their high intrinsic luminosity and an empirical relation that connects the width of their light curve to their peak brightness (Phillips et al. 1999), Type Ia supernovae are widely used as precise distance indicators in extragalactic cosmology. In addition, their exceptional brightness allows their detection up to several Gigaparsecs (Gpc), offering the opportunity to study the expansion history of the universe (Riess et al. 1998; Perlmutter et al. 1999). Type Ia supernovae also play a fundamental role in the chemical and dynamical evolution of their host galaxies, by heating up cold interstellar gas and triggering star formation through their high-velocity ejecta (Hillebrandt et al. 2013). Other important applications include studies of astrophysical magnetic fields, high-energy particle acceleration, explosive nucleosynthesis and binary evolution.

Despite decades of extensive studies and supernova monitoring campaigns, both the nature of the progenitor system, as well as the explosion mechanism that leads to the thermonuclear runaway, are not unambiguously identified. As the exact nature of type Ia supernovae remains elusive, observations are a vital tool used to constrain progenitor systems and exclude or verify proposed explosion scenarios.

2.4.1. Observational properties

The trademark of type Ia supernovae is the fact that their spectra, absolute magnitudes and light curve shapes look remarkably alike, pointing towards common or at least similar progenitor systems and explosion mechanisms. In contrast to core-collapse supernovae, the ejecta mass of thermonuclear explosions rarely exceeds $2M_{\odot}$, while the average expansion velocity of the ejecta lies at $\sim$ 10000 km/s. These values can be translated into a kinetic energy of $E_{kin} \sim 10^{51}$erg (Janka 2017).

Optical spectra around maximum light, are marked by the absence of hydrogen and sometimes helium but indicate a strong presence of intermediate-mass elements (IMEs) like O, Mg, Si, S and Ca at high velocities. Spectra obtained at later times, when the most inner part of the envelope becomes transparent and the supernova reaches its so-called nebular phase, display a large abundance of IGEs moving at lower velocities. Given the slow exponential decline of the light curve tail, an additional energy source next to the fast decaying thermal energy is required to explain it. This extra energy can be linked with a freshly synthesized radioactive element, whose decay produces γ-rays that are reprocessed inside the ejecta and give rise to the optical emission (Colgate and McKee 1969). The decline of optical Co lines with respect to Fe lines in the nebular phase combined with a lifetime of $\tau_{1/2} \sim 100$ days that matches well with the shape of the light curve tail, reveals ^{56}Co as the radioactive element powering up the light curve at late times. However, the explosive nucleosynthesis of the latter from elements with an even number of protons and neutrons, like C and O, is unfavored. This can be overcome, if it is assumed that practically all ^{56}Co comes from the fast decay of another radioactive element, ^{56}Ni.

Already in the year 1960, British astronomer Sir Fred Hoyle and American astrophysicist William A. Fowler suggested that type Ia supernovae result from CO WD in binary systems that reach the Chandrasekhar mass and explode. The explosive burning of carbon and oxygen to iron peak elements and especially ^{56}Ni yields enough energy to overcome the gravitational binding energy $E_{grav} = \frac{5}{3}\frac{GM}{R^2}$ of a compact star and unbind it.

Owing to their apparent homogeneity, type Ia supernovae expeditiously gained popularity and were used as cosmology distance indicators, becoming so-called 'standard candles', inducing further studies and observations. In the year 1982, Arnett linked the amount of ^{56}Ni synthesized with the SNIa luminosity at the time of maximum light, being thus able to parametrize all thermonuclear supernovae with a single parameter (Arnett 1982). Several years later, the empirical relation between the width of their light curve and the peak brightness Δm_{15} (Phillips et al. 1999) reduced the scatter between individual type Ia supernovae and allowed precise distance measurements that ultimately led to the conclusion that the Universe is in a state of accelerated expansion (Riess et al. 1998; Perlmutter et al. 1999; Leibundgut 2001).

Peculiar events like the super-luminous SN1991T or the sub-luminous SN1991bg showed, however, that this class of explosions is not as homogeneous as it was believed to be in the past. The canonical picture of a WD reaching the Chandrasekhar limit and exploding could not account for all thermonuclear supernovae. Following that, the presence of type Ia supernovae in early-type galaxies, where little or no star formation takes place, as well as in late-type spirals and starburst galaxies, further perplexed the progenitor riddle, suggesting that at least two different progenitor paths could result in a thermonuclear explosion. All observed type Ia supernovae can be roughly categorized into three subtypes, according to their luminosities (Taubenberger et al. 2008; Li et al. 2011b):

- Sub-luminous SNe Ia: These red, dim thermonuclear supernovae are one to two magnitudes fainter than normal supernovae. They are characterized by a rapid luminosity decline and by high abundances of IMEs. Other typical characteristics are low expansion velocities, traces of unburnt material in early spectra, and very low synthesized ^{56}Ni masses $\sim 0.1 M_\odot$. SN1991bg is the prototype of this sub-class that contributes to about 20% of all type Ia SNe.

- Super-luminous SNe Ia: Explosions of this sub-type are roughly one magnitude brighter than normal supernovae and marked by broad light curves and iron lines at maximum light. Arnett's rule suggests that the ^{56}Ni mass synthesized during this sub-type of thermonuclear explosions exceeds the Chandrasekhar mass for WDs. Consequently, it cannot be excluded that an additional source of luminosity powers the light curve. 10% of all type Ia supernovae fall into this class, of which SN1991T is the most representative incident.

- The remaining 70% are considered branch-normal type Ia supernovae. Even within this sub-type, ^{56}Ni masses can vary from $0.3 M_\odot$ to $0.9 M_\odot$ (Stritzinger et al. 2006), while further discrepancies in expansion velocities, spectra and absolute magnitudes cannot be excluded.

Modeling the thermonuclear incineration of a CO WD in a way that it reproduces observations is a complex procedure that implies the correct treatment of hydrodynamics, radiation transport and binary evolution. Several different progenitor scenarios and explosion mechanisms are proposed to explain the progressively increasing number of observed events and the diverging properties among many of them.

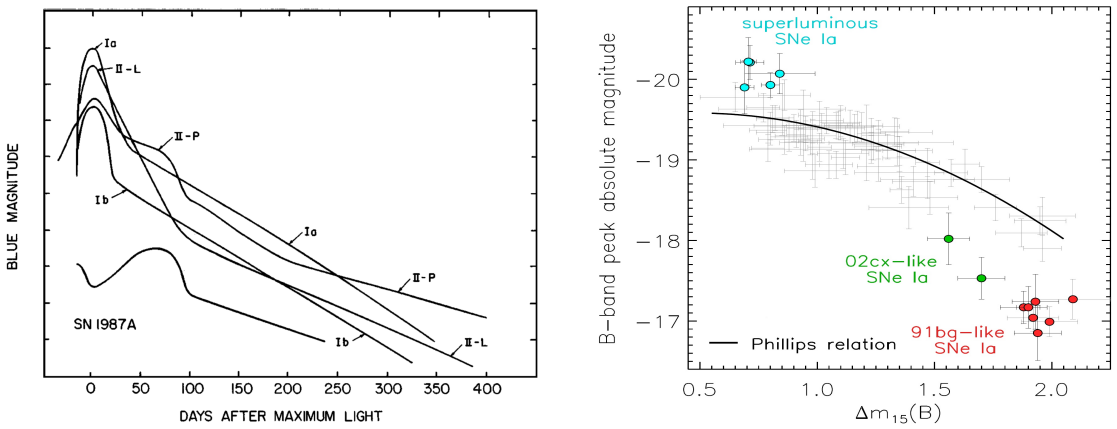

(a) Typical lightcurves of all types of SNe (from Filippenko 1997)

(b) Observational diversity of type Ia supernovae in the optical (from Hillebrandt et al. 2013)

Figure 2.2.: Left: Schematic lightcurves for different types of supernovae (from Filippenko 1997). Right: Observational diversity of type Ia supernovae in B-band decline rate Δm_{15}(B) and B-band peak absolute magnitude. Different subclasses of supernovae are shown with different colors. From (Hillebrandt et al. 2013).

2.4.2. Progenitor Systems and Explosion Mechanisms

A proposed progenitor system must be able to satisfy a large number of criteria, in order to match observations and stand as a viable candidate progenitor model (Hillebrandt et al. 2013; Maeda and Terada 2016).

- Robust explosion mechanism: The progenitor system must naturally reach a state where the thermonuclear runaway becomes inevitable.
- Nucleosynthesis: IMEs are products of incomplete carbon and oxygen burning and can be found in large portions in early supernova spectra. On the contrary, IGEs are seen mostly in nebular spectra, suggesting that in the center of the WD, burning was complete. The explosion mechanism must be able to produce each group of elements at suitable portions and in an appropriate position inside the ejecta.
- Ejecta stratification: Observations of type Ia supernova indicate ejecta stratification, with IME moving at higher velocities in the outskirts and IGE being significantly slower and closer to the center. The explosion mechanism must, therefore, suppress large scale mixing of ejecta.
- Peak luminosity and light curve shape: A candidate progenitor model must be able to reproduce the energy released during a thermonuclear event, as well as the velocity of the ejecta and the amount of radioactive ^{56}Ni synthesized, three parameters that affect the most fundamental optical properties of type Ia supernovae.
- Birth rates and delay times: The progenitor system must be frequent enough to explain the supernova rate per galaxy. It must also be able to yield explosions relatively rapidly, in order to explain events in late-type spirals, but also produce explosions with a longer delay time[3], to account for type Ia supernovae occurring in early-type galaxies.

[3]The delay time is defined as the time passed from the formation of the progenitor system until the explosion.

In general, there exists no single progenitor system that fulfills all the above-mentioned requirements and characteristics.

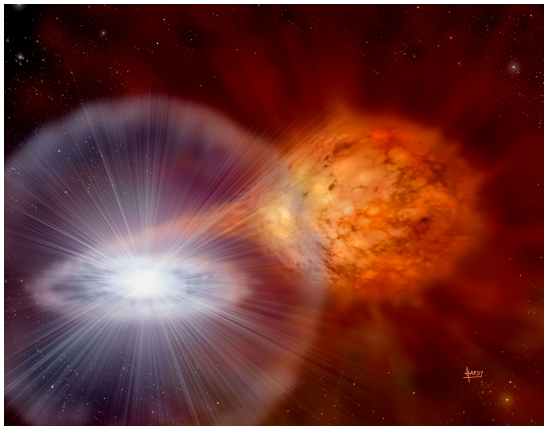

(a) The single-degenerate (SD) model (from David A. Hardy/AstroArt.org)

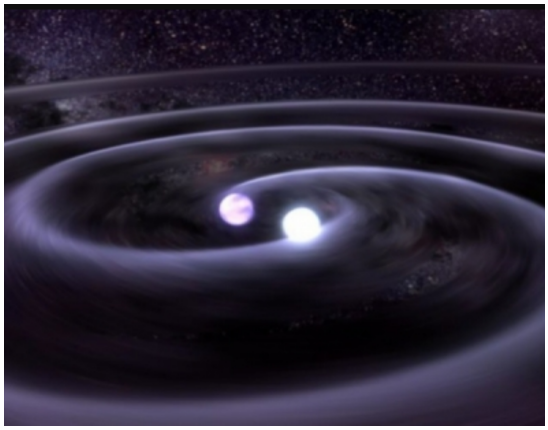

(b) The double-degenerate (DD) model (from GSFC/D. Berry)

Figure 2.3.: Artistic impressions of the two widely accepted progenitor models leading to thermonuclear explosions.

2.4.3. Single Degenerate Models

Chandrasekhar mass models

The single-degenerate (SD) scenario (Whelan and Iben 1973) has long been considered the canonical system that leads to a thermonuclear explosion and was proposed in order to explain the observed homogeneity of type Ia supernovae. This scenario involves a WD with a mass close to the Chandrasekhar limit and a main-sequence or slightly evolved star as a companion. The companion overfills its Roche-lobe[4] and transfers matter (mostly hydrogen) to the WD. If the accretion happens at a certain rate (Badenes et al. 2007), hydrogen accumulates in a stable manner on the surface of the WD, heats up through the release of gravitational binding energy and burns hydrostatically into carbon and oxygen, increasing thereby the density of the compact object that approaches the Chandrasekhar mass limit. Finally, the compressional heat near the center of the WD suffices to initiate carbon burning.

Models suggest though, that the burning of carbon in the center of the WD is not immediately explosive. The released energy is initially transported outwards by convection, a stage that can last several centuries (Röpke and Hillebrandt 2005). The background temperature of the WD increases gradually until the conditions for a thermonuclear runaway are fulfilled, leading to the complete disruption of the WD and to a type Ia supernova explosion. There are two ways to induce an explosion in a degenerate object like a CO WD: Either with a subsonic deflagration or with a supersonic shock-driven detonation.

- Detonations describe a burning front that propagates in the form of shock waves. Their compressional heating is enough to induce ignition. Detonations proceed through the ejecta at supersonic velocities, while the released energy behind the burning front sustains them. In this regime, the star has no time to expand and is completely incinerated within seconds.

[4]Roche Lobe: Region around a star in a binary system, within which orbiting material is gravitationally bound to it. When a star exceeds its Roche lobe, its surface extends beyond that region and the material that lies outside can fall on the companion.

- In a deflagration, the burning front propagates through the star with velocities below the speed of sound. In contrast to detonations, where causal contact between regions ahead and behind the combustion wave is lost, the pressure wave has enough time to move ahead of the front and expand the star, thus decreasing its density. Hence, while propagating outwards, the burning front encounters progressively diluted ejecta. At some point, the density falls below the burning threshold and the explosion stalls. One way to overcome this issue and successfully explode the star is to assume that the burning front expands in a turbulent manner due to Rayleigh-Taylor instabilities[5]. These enlarge the surface area of the burning front, increasing the burning rate and consequently accelerate the speed at which the deflagration propagates.

To first order, the burning products of both detonations and deflagrations depend on the density of the fuel ahead of the combustion front (Röpke and Hillebrandt 2005; Seitenzahl et al. 2013). If the fusion processes happen at densities $\rho \geq 6 \times 10^9$ g/cm3, the burning is complete and proceeds to nuclear statistical equilibrium, producing primarily IGEs. The exact isotopic pattern depends on the proton-to-neutron ratio of the fuel. Lower fuel densities suffice only for the synthesis of IME, such as Mg, Si, S, Ca and below a certain threshold ($T \leq 1.5 \times 10^9$K) burning ceases completely.

Considering the physical laws of the burning front, a pure detonation of a M_{Ch} WD would yield a thermonuclear supernova composed entirely out of IGE (Arnett 1969), which is in strong contradiction to observations of IMEs in early spectra.
Deflagrations (Nomoto et al. 1984) on the other hand would only work if strong turbulence is assumed, otherwise, they produce weak explosions with a large fraction of unburned fuel and low amounts of synthesized ^{56}Ni. An issue though is the large-scale mixing of the ejecta, a direct consequence of the strong turbulence required to successfully explode the WD (Khokhlov 1995; Niemeyer and Hillebrandt 1995).

Since both burning regimes produce explosions inadequate to explain the bulk of type Ia supernovae, an explosion mechanism that can be considered a compromise between the two was suggested, the so-called 'delayed detonation' (Khokhlov 1991). In this case, the explosion starts as a subsonic deflagration, that produces IGEs near the core and allows the star to pre-expand. Under the right conditions, a transition to a supersonic detonation may occur, forming a layer of IMEs, as a direct consequence of lower densities. A delayed detonation of a M_{Ch} WD reproduces many key observational characteristics, including ejecta stratification, the pronounced layer of IME in the outer layers and a sufficient amount of ^{56}Ni near the center. It is considered the only viable explosion mechanism for WDs approaching the Chandrasekhar mass limit, albeit the physics behind the transition process is not yet well understood.

Despite the modeling successes of delayed detonations of a M_{Ch} WD, their major drawback is the fact that too few progenitor systems are observed in nature. In order to explain the galactic type Ia supernova rate with Chandrasekhar mass progenitors, around 10.000 WDs with a mass $M_{WD} \geq 1.25 M_\odot$ should be distributed in a galaxy like the Milky Way (Janka 2011). Most of the known WDs, however, have masses significantly lower than $1 M_\odot$. This issue is supported by the absence of X-ray emission in elliptical galaxies (van den Heuvel et al. 1992). The accretion of hydrogen onto the surface of a WD and the subsequent burning into carbon produces temperatures

[5]Rayleigh-Taylor instability: An inverse density stratification under the influence of a central accelerating force, like the gravitational field of a WD, is subject to buoyancy instabilities, called Rayleigh-Taylor instabilities. In an example of two fluids with different densities, the lighter fluid, situated below the heavier fluid, would form plumes flowing upwards, while portions of heavier fluid sink towards the bottom.

T$\sim 10^6$K that should result in an enhanced galactic X-ray emission not observed in elliptical galaxies (Janka 2011).

Sub-Chandrasekhar mass models

The intrinsic homogeneity motivated the Chandrasekhar mass WD explosion model as the most promising progenitor system to explain type Ia supernovae. Thermonuclear explosions with comparable properties should be triggered by progenitor stars with a very well-defined range of properties. However, advanced observations of type Ia supernovae highlighted the diversity among many of them. The requirement of a WD reaching the Chandrasekhar mass can hence be relaxed, leading to the development of sub-Chandrasekhar mass models (Iben et al. 1987; Woosley and Weaver 1994).

This model involves a sub-Chandrasekhar WD that accretes He from a He-rich star. Under the right conditions for temperature and density and after reaching a limiting mass ($M_{He} \sim 0.1$-$0.2 M_\odot$), this freshly accreted layer of easily burnable He may detonate, generating a shock wave toward the core (Shen et al. 2010). A shock wave passing through degenerate matter can trigger a second detonation ('double-detonation scenario') that finally disrupts the star and leads to a type Ia supernovae (Fink et al. 2007). The advantage of this model lies in the fact that the predicted rates for this progenitor system are high enough to explain the observed type Ia supernovae rates and that the range of WD masses is able to account for the variety among ejecta and ^{56}Ni masses.

At the same time, a large amount of He undergoing detonation on the surface of the WD would leave its imprint as a high-velocity layer of ^{56}Ni in optical spectra that is not in agreement with observations. Besides, simulations of double detonations synthesize further stable IGE at low optical depths, like Cr or Ti (Hoeflich and Khokhlov 1996; Fink et al. 2010) that are efficient radiation absorbers and would redistribute the light in redder parts of the spectrum, also at odds with observational evidence. Further uncertainties involve the retention efficiency of He on an accreting WD, as well as the exact physical requirements that lead to a detonation.

Recent studies tackled these issues and tested whether low-mass ($M_{He} < 0.05 M_\odot$) He shells, polluted with C, can detonate (Ruiter et al. 2014; Kromer et al. 2010). This configuration reproduces observations very well, turning double detonations of sub-Chandrasekhar WDs into a very promising progenitor model able to explain the bulk of type Ia supernovae.

2.4.4. Double Degenerate Model

This scenario involves two CO WDs ('double-degenerate') spiraling each other until they merge (Webbink 1984; Iben and Tutukov 1984). After several hundred Myr (or even Gyr), the gradual loss of angular momentum through the emission of gravitational waves (Peters 1964) ultimately brings the two degenerate objects in contact. If the mass ratio of the objects is close to unity, both stars can avoid tidal disruption and collide, giving rise to the violent merger scenario (Pakmor et al. 2012). It is believed that the temperatures achieved when the objects come in contact suffice to trigger a detonation (Seitenzahl et al. 2009). In order to fuse enough ^{56}Ni, though, the densities must be accordingly high, pointing towards massive CO WD with masses $M_{WD} \geq 0.8 M_\odot$ (Ruiter et al. 2013).

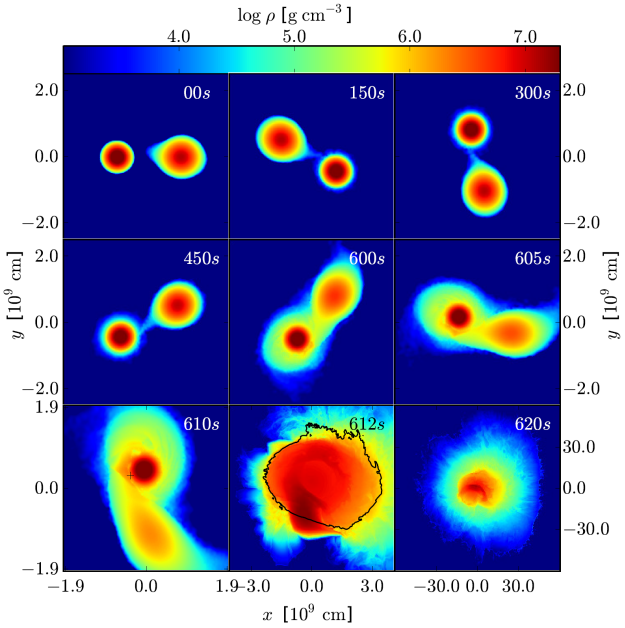

Figure 2.4.: Hydrodynamic evolution and subsequent thermonuclear explosion of a merger of a $0.9M_{\odot}$WD with a $1.1M_{\odot}$WD (from Pakmor et al. 2012).

The most characteristic signatures of DD explosions are the high degree of asymmetry in the ejecta, caused by the rapid rotation in the last moments before the collision (Janka 2011) and the total ejected mass, that exceeds the Chandrasekhar limit. The latter does not necessarily imply a higher ^{56}Ni mass as well. Simulations indicate that only a small volume reaches high enough densities to burn into IGEs. As a result, DD progenitors are only successful in describing sub-luminous type Ia supernovae, a fact that comes in concordance with theoretical rate predictions for this progenitor channel.

2.4.5. Galactic supernova rates

One of the most important constraints for studies involving type Ia supernova progenitor systems are galactic SN Ia rates; the number of events per galaxy within a given time. In particular, SN Ia rates are crucial for the chemical evolution of the galaxies, the production of cosmic rays, the stellar evolution theory, the supply of positrons to the ISM any many more.

A precise determination of the SN Ia rate is of great importance for accurate astrophysical results. Unfortunately, the low number of events per galaxy and century, combined with several observational biases, yield high statistical uncertainties in the derived rates. On the one side, the radiation of events occurring on the far-side of inclined spiral galaxies may never the Earth, on the other side, explosions near the bright nucleus of distant galaxies may pass unnoticed. Finally, it is natural that the detection of sub-luminous supernovae in very distant galaxies is suppressed in comparison to bright events. (Tammann et al. 1994; Cappellaro et al. 1997). Thus, SN rates must be corrected for several biases that make the establishment of a universal value challenging.

Studying the number of events per galaxy, the first remark are their variation for each supernova and galaxy type. Supernovae resulting from the core-collapse of massive stars are believed to trace the star forming sites of their host galaxies. Stars that experience the collapse of their cores are massive and hence short-lived. With lifetimes of a few million years, they do not have enough time to leave their birth site and explode 'in situ'. This is in concordance with the fact that SN II and

SN Ib,c are seen almost exclusively in late-type galaxies with ongoing star formation. On the other side, type Ia supernovae are associated with older stellar populations (WDs) and have enough time to wander off their birthplace. Moreover, some progenitor channels have delay times of the order of Gyrs that fit well with the observations of type Ia supernovae both in early and late-type galaxies.

There are several approaches to derive galactic supernovae rates. Most of them depend on supernovae monitoring campaigns of external galaxies. Another possibility is to take historically observed galactic supernovae into account (Tammann et al. 1994), but as the last galactic supernovae in the Milky Way happened $\sim$ 130 and $\sim$ 400 years ago, respectively (G1.9+0.3 around the year 1890 (Green and Gull 1984) and Kepler's supernova, SN1604), estimates using galactic incidents are highly uncertain.

Tammann et al. 1994 used a sample of 96 SNe from the 330 brightest galaxies within a radius of $\approx$ 20Mpc and obtained SNe rates reported in Tab. 2.1.

Galaxy type	SN Ia [SNe/100yr]	SN Ib/c [SNe/100yr]	SN II [SNe/100yr]
E-S0 (elliptical-lenticular)	0.25	0.00	0.00
S0a-Sa (lenticular-spiral)	0.12	0.01	0.04
Sab-Sb (spirals)	0.12	0.07	0.34
Sbc-Sd (barred-spirals)	0.12	0.19	0.98
Sdm-Im (irregular, dwarf)	0.12	0.23	1.05

Table 2.1.: SNe rates by Tammann et al. 1994

Cappellaro et al. 1997 combined the rates of five SN searches and corrected for the biases mentioned above. Their results are given in Tab. 2.2.

Galaxy type	SN Ia [SNe/100yr]	SN Ib/c [SNe/100yr]	SN II [SNe/100yr]
E-S0 (elliptical-lenticular)	0.15	≤ 0.02	≤ 0.02
S0a-Sb (spiral)	0.20	0.11	0.40
Sbc-Sd (barred-spirals)	0.24	0.16	0.88
Others (irregular, dwarf)	0.27	0.22	0.41

Table 2.2.: SNe rates by Cappellaro et al. 1997

Tab. 2.1 and Tab. 2.2 reflect some discrepancies between several rates. This is reasonable, on the one hand, due to the large uncertainties accompanying those rates and on the other hand, because both studies categorized the galaxy types in a different manner. A final comparison is made with results from Janka 2011:

Galaxy type	SN Ia [SNe/100yr]	SN Ib/c [SNe/100yr]	SN II [SNe/100yr]
E-S0 (elliptical-lenticular)	0.12	0.01	0.01
S0a-Sb (lenticular-spiral)	0.14	0.14	0.18
Sbc-Sd (barred-spirals)	0.15	0.18	0.48
Other (irregular, dwarf)	≤ 0.09	0.12	0.25

Table 2.3.: SNe rates by Janka 2011

The errors of the rates for all approaches range from $\pm$ 0.1 SNe/100yr to $\pm$ 1.0 SNe/100yr depending on the supernova type, galaxy and study. All studies suggest that half of the occurring supernovae are of type II and explode preferably in late-type spirals, marked through their high star formation rate (SFR). SNe Ia on the other hand, explode in all type of galaxies and are the only explosions found in elliptical and lenticular galaxies. Despite large observational efforts, SNe rates still remain uncertain by at least one order of magnitude.

2.5. Observational objectives across the electromagnetic spectrum

Disentangling the fitting progenitor system for an incident thermonuclear explosion is a challenging task. Modeled spectra and light curves can look remarkably similar if some physical parameters of the models are tuned accordingly. Extragalactic distances further perplex the situation, due to the difficulty in achieving the required sensitivity to distinguish between the progenitor paths. Still, every progenitor system and explosion mechanism leaves its own imprint that may be revealed using the advantages of a multi-wavelength study.

Radio observations provide valuable constraints on the circumstellar environment around the binary system, as the two main channels of progenitor systems are predicted to form distinctive circumstellar environments. While in the SD channel a fraction of the accreted mass is lost due to winds and Roche-Lobe overflows, the DD channel is characterized by a very clean circumstellar environment. It is believed that the interaction of the expanding SN ejecta with the circumstellar medium produces strong shocks that accelerate charged particles like electrons. In the presence of an ambient magnetic field, the latter lose a fraction of their energy in the form of synchrotron radiation (Kundu et al. 2017). Its strength is proportional to the strength of the magnetic field. Hence, radio observations examine the densities of the circumstellar material, as well as the strength of the magnetic field (Pérez-Torres et al. 2014).

In the middle-infrared (MIR) the substantially smaller extinction compared to the optical band allows detailed studies of the photosphere evolution from the first days after first light up to the nebular phase. In addition, a wealth of IGE lines that fall in this range can be crucial in disentangling stable from radioactive isotopes and therefore give clues about the explosion mechanism (Telesco et al. 2015).

Further hints about magnetic fields, as well as potential mixing in the innermost region, can give late-time line profiles of iron in the near-infrared (NIR) (Penney and Hoeflich 2014; Diamond et al. 2018). Several atomic transitions of unburned C and O, IMEs and IGEs lie in this band. Thus, infrared spectroscopy in regular time sequences provides a precise 'tomography' of the ejecta, as the photosphere recedes to the center of the explosion.

NIR and optical photometry allow an estimate of the energy deposition by energetic γ-rays from radioactive decay. Peak luminosities are usually given in the blue band, while the UVOIR (ultraviolet-optical-infrared) light curve is fitted to derive the Δm_{15} relation and consequently to allow the use of thermonuclear explosions as standard candles. Optical images of the explosion site years before the explosion can be examined for a bright companion star that would point toward an explosion from the SD channel (Kelly et al. 2014).

X-rays probe the circumstellar environment and the mass-loss rate of the progenitor system. In particular, inverse Compton scattering (see Sec. 3.10) of optical photons by relativistic electrons is believed to give rise to X-ray emission. Observations in the X-ray band put constraints on the circumstellar environment around the explosion (Margutti et al. 2012). Pre-explosion X-ray images provide clues about the progenitor system. In case of the SD progenitor channel, X-ray emission from the explosion site as a consequence of matter accretion would be expected (van den Heuvel et al. 1992).

Finally, γ-ray photons from radioactivity probe directly the mass and distribution of ^{56}Ni and other radioactive elements in the velocity space of the supernova envelope. Through the 511keV positron annihilation line, the number of positrons annihilating in the supernova envelope can be estimated. These objectives are also the main goal of this work. For details, see chapters 5 and 6.

3. Positron and Gamma-ray physics

Positrons are the anti-particle of electrons with the same spin and mass but with the opposite charge.

The existence of positrons, initially as a positive-charge solution of the recently formed Dirac equation, was predicted in 1928 by the English theoretical physicist Paul Dirac (Dirac 1928). A few years later the American physicist Carl David Anderson found the first experimental traces of a particle with the same mass-to-charge ratio as an electron but with the opposite charge while letting cosmic-rays pass through a cloud chamber. (Anderson 1933) Following his publication, many scientists confirmed Anderson's discovery by examining older photographic plates where positron traces were falsely dismissed as protons (Leone and Robotti 2010). Anderson's discovery of the positron was awarded with the Nobel Prize of 1936 and marked the first strong experimental evidence of antimatter particles. The confirmation that this particle is indeed the antiparticle of the electron followed in 1934 by Klemperer and Chadwick, who detected the characteristic electron-positron annihilation line at 511keV (Klemperer and Chadwick 1934).

Thus, positrons and electrons are complementary fermionic particles with a rest mass of $m_{e^\pm} = 9.109 \cdot 10^{-31} = 510.9989 \mathrm{keVc}^{-2}$, a 1/2-spin and a charge of $q_{e^\pm} = \pm 1.6022 \cdot 10^{-10} \mathrm{As} = \pm 1\mathrm{e}$ (Mohr et al. 2016) that obey Pauli's exclusion principle (see Sec. 2.3.1) and follow the Fermi-Dirac statistics.

3.1. Positronium

There are several predicted bound states involving positrons. Some of them, like the anti-hydrogen, consisting of an anti-proton and a positron orbiting around the negative nucleus, were produced artificially in particle accelerator facilities (Baur et al. 1996). Heavier 'anti-elements' require very high velocities and have low lifetimes, making their creation and detection challenging.

However, a more common bound system exists that consists of an electron and a positron orbiting around their common center of mass. This bound system that was theorized by the Croatian physicist Mohorovicic in 1934 (Mohorovičić 1934) and discovered experimentally in 1951 by the Austrian-American experimental physicist Martin Deutsch (Deutsch 1951), became known as the 'Positronium' atom (Ps atom). The Ps atom is very similar to the hydrogen atom, except for the fact that the massive proton is substituted by the $\sim$ 2000 times lighter positron (Karshenboim 2004). Thus, the reduced mass of the Ps atom is almost half the reduced mass of hydrogen, causing all spectral properties as well as the binding energy of Ps to have half the value of the hydrogen atom.

Like every system consisting of a particle and its complementary antiparticle, the Ps atom has a finite lifetime and decays predominantly into two or three photons. The exact number depends on the spin of its constituents. Composed of two fermions with half-integer spin ($S_{e^\pm} = 1/2$), the Ps atom is of bosonic nature, with three possible spins states S_{Ps}={-1,0,1}, that depend on the quantum numbers of the electron and positron.

There are four different configurations for two fermions, whose spin part of the wave function can be written as $|S_{e^\pm}, m_{e^\pm}\rangle$ with spin $S_{e^\pm} = 1/2$ and projections on the spin axis $m_{e^\pm} = \pm 1/2$:

$$
\begin{aligned}
|1/2, +1/2\rangle\,|1/2, +1/2\rangle &\equiv (\uparrow\uparrow)\\
|1/2, +1/2\rangle\,|1/2, -1/2\rangle &\equiv (\uparrow\downarrow)\\
|1/2, -1/2\rangle\,|1/2, +1/2\rangle &\equiv (\downarrow\uparrow)\\
|1/2, -1/2\rangle\,|1/2, -1/2\rangle &\equiv (\downarrow\downarrow)
\end{aligned}
$$

In this notation, '$\uparrow$' stands for $m_{e^\pm} = +1/2$, while '$\downarrow$' for $m_{e^\pm} = -1/2$. Three out of four combinations (triplet) have 'parallel' spins that sum up for a total spin S_{Ps} of 1, while the remaining configuration (singlet) has 'anti-parallel' spins that equal 0. For the bound Ps atom this is translated to:

$$
\text{Triplet state } {}^3S_1\text{: } |S_{Ps}, m_{Ps}\rangle = \begin{cases} |1, +1\rangle = (\uparrow\uparrow) \\ |1, 0\rangle = \frac{1}{\sqrt{2}}(\uparrow\downarrow + \downarrow\uparrow) \\ |1, -1\rangle = (\downarrow\downarrow) \end{cases}
$$

$$
\text{Singlet state } {}^1S_0\text{: } |S_{Ps}, m_{Ps}\rangle = \begin{cases} |0, 0\rangle = \frac{1}{\sqrt{2}}(\uparrow\downarrow - \downarrow\uparrow) \end{cases}
$$

The triplet state with parallel spins and total spin S=1 is denoted as 'ortho-Positronium' (ortho-Ps) and is formed in 75% of the times, while in the remaining 25% the singlet state with anti-parallel spins and total spin S=0 called para-Positronium (para-Ps) appears.

Para-Ps has a lifetime of 1.2×10^{-10}s and releases two photons of 511keV energy in opposite directions. In order to conserve the spin of the two ingoing fermions, ortho-Ps, with a substantially longer lifetime of 1.4×10^{-7}s (Prantzos et al. 2011), decays predominantly in three photons that carry away the total rest mass energy of 1022keV. Momentum conservation ensures that no photon in this process obtains more than 511keV, producing thus a range of photon energies between 0keV and 511keV (Ore and Powell 1949).

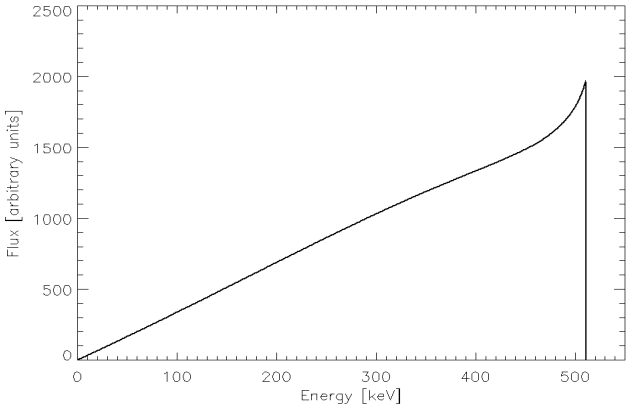

Figure 3.1.: Expected photon spectrum from the annihilation of ortho-Ps, theoretically calculated by Ore and Powell 1949

QED allows the annihilation into a larger number of photons, albeit its realization is heavily suppressed. Para-Ps can decay into multiples of two photons, while ortho-Ps into an odd number of photons. A single-photon annihilation from a free Ps atom is prohibited due to momentum conservation, but may appear in the presence of another particle (see Sec. 3.2).

3.2. Positron production mechanisms

3.2.1. β^+-decay

Positrons are created by the radioactive decay of proton-rich nuclei, located on the proton-rich side of the valley of stability (see Fig. 3.6). Their instability originates from the excessive number of protons. One possibility for a proton-rich nucleus to reach a more stable nuclear configuration is by 'transforming' a proton into a neutron inside the nucleus, while a positron and a neutrino are emitted to conserve energy, charge and momentum.

$$ {}^{A}_{Z}\mathrm{P} \rightarrow {}_{Z-1}{}^{A}\mathrm{D}^{1-} + {}^{0}_{1}\mathrm{e}^{+} + {}^{0}_{0}\nu \tag{3.1} $$

Eq (3.1) can be reduced to the decay of a proton into a neutron.

$$ p^{+} \rightarrow n + e^{+} + \nu \tag{3.2} $$

As a result of the higher neutron mass ($\mathrm{m}_n \approx 939.56\mathrm{MeV/c^2}$) compared to the proton mass ($\mathrm{m}_p \approx 938.27\mathrm{MeV/c^2}$)) (Mohr et al. 2016), this decay can only occur in the presence of a parent nucleus, whose mass is higher than its neutron-richer isobar. The released decay energy during this process is given by the mass difference of parent and daughter nucleus.

$$ Q_{\beta^+} = \Big[m({}^{A}_{Z}\mathrm{P}) - m({}_{Z-1}{}^{A}\mathrm{D})\Big]c^2 \tag{3.3} $$

As the available decay energy is shared between three bodies, the energy spectrum of both the positron and the neutrino is continuous with a well-defined maximum at the maximum available energy Q_β in the decay.
In astrophysical environments most β^+-emitters are created either through explosive nucleosynthesis in stellar explosions (e.g. ^{22}Na, ^{44}Ti, ^{56}Ni), or through hydrostatic burning in the cores of massive stars (e.g. ^{26}Al) (Prantzos et al. 2011). Positrons ejected from β^+-radioactivity have kinetic energies of $\mathrm{E}^{e^+}_{kin} \sim$ MeV (Nadyozhin 1994).

3.2.2. Lepton and Meson decay

In the Standard Model of particle physics, particles are defined as leptons if they have a 1/2-spin. There are two main classes of leptons: The first class includes massive and charged leptons that interact with other particles weakly and electromagnetically, the second class contains neutral, (nearly) massless particles that rarely interact.
Furthermore, charged and neutral leptons are divided into three lepton families:

- The most familiar lepton family has three members; the electron e^- and the positron e^+ that both share a rest mass of $\mathrm{m}_{e^\pm} \approx 0.511\mathrm{MeV/c^2}$ and the electron (anti)-neutrino ($\nu_e, \overline{\nu}_e$).
- A second lepton family consists of muons ($\mu^\pm$) and muon-neutrinos ($\nu_\mu, \overline{\nu}_\mu$). Muons are unstable and have a lifetime of $\tau_\mu = 2.197\mu$s, before they decay into positrons and electrons, emitting thereby neutrinos and anti-neutrinos of both flavors to ensure lepton number conversation.

$$\begin{aligned} \mu^+ &\rightarrow e^+ + \nu_e + \overline{\nu}_\mu \\ \mu^- &\rightarrow e^- + \overline{\nu}_e + \nu_\mu \end{aligned} \tag{3.4}$$

Due to the fact that muons are ~ 200 times more massive than electrons (m_μ=105.658MeV/c^2), muons cannot be generated through radioactivity, where mass differences Δm between nuclei are substantially smaller. Nevertheless, they are created in copious amounts as secondary particles in inelastic collisions between high-energy particles. For instance, when energetic cosmic-rays ($E_{CR} \approx 200$MeV/c^2) hit components of the interstellar medium (ISM) or the atmospheric constituents of the Earth, a large amount of neutral and charged mesons, like pions (π^+, π^-, π^0) and kaons (K^+,K^-,K^0) are produced (Gaisser 2012). Both meson types are more massive and shorter-lived and decay with high branching ratios into muons that further decay into positrons.

$$\begin{aligned} \pi^+ &\rightarrow \mu^+ + \nu_\mu \rightarrow e^+ + \nu_e + \overline{\nu}_\mu + \nu_\mu \\ K^+ &\rightarrow \mu^+ + \nu_\mu \rightarrow e^+ + \nu_e + \overline{\nu}_\mu + \nu_\mu \end{aligned} \tag{3.5}$$

It must be noted that the higher mass of the positively charged kaon ($m_{K^+} \approx 500$MeV/c^2) allows more decay channels. All of them end, however, with the emission of one positron as a consequence of charge conservation.

- The third and final lepton family are the tau leptons and tau neutrinos. Tau leptons (τ^+, τ^-) are the heaviest leptons (m_τ =1776.82MeV/c^2) and are produced artificially in particle acceleration facilities. Their large mass allows several possible decay channels. In most cases, τ^+-decays will end up emitting positrons.

3.2.3. Photon-photon pair production

High-energy γ-rays in strong radiation fields are also able to produce electron-positron pairs. In particular, if the product of the photon energies satisfies $E_\gamma \cdot E_\gamma \geq 2m_e^2c^4/(1\text{-}\cos(\theta))$, electron-positron pair production is feasible from the energetic point of view (Prantzos et al. 2011). The total cross section for this process as a function of a dimensionless velocity $\beta = (|p|/E)_{CM}$ is given by Gould and Schréder 1967:

$$\sigma_{PP,\gamma\gamma} = \frac{1}{2}\pi r_0^2(1-\beta^2)\left[(3-\beta^4)\ln\left(\frac{1+\beta}{1-\beta}\right) - 2\beta(2-\beta^2)\right] \tag{3.6}$$

The total cross section reaches a maximum of $\sigma_{pp,max}$=1.7×10^{-25}cm^2 for an incident photon energy of E_γ=716.5keV. Photon-photon pair production should be a common process if a sizeable fraction of the luminosity is above the electron rest mass energy threshold. The fact that it has never been observed experimentally, suggests that the photon densities realized in terrestrial experiments are too low. Nevertheless, compact objects like neutron stars or black holes may reach high enough photon densities, so that the right conditions for efficient photon-photon pair creation are met (Lightman and Zdziarski 1987).

The decay of ^{56}Ni to ^{56}Co and subsequently to ^{56}Fe yields several transitions above the pair-production threshold. Thus, there is a potential to create additional positrons alongside the β^+-decay of ^{56}Co. An estimate of the number of positrons created through pair-production from high-energy photons in supernovae envelopes can be made with Monte Carlo simulations.

3.2.4. Positron production via E-fields and B-fields

According to Einstein's mass-energy equivalence, $E = mc^2$ (Einstein 1905), a single photon carrying an energy $E_\gamma \geq 1022$MeV could energetically produce electron-positron pairs. However, a $\gamma \rightarrow e^+ + e^-$ interaction would violate the conservation of momentum. The photon needs a partner that can carry away the excess momentum and energy.

Thus, pair-creation from a single photon is possible in the electric field on an atomic nucleus or in highly magnetized objects like pulsars and magnetars (Daugherty and Harding 1983). Both reactions become more probable with increasing photon energies and magnetic field strengths and yield positrons carrying various kinetic energies.

3.2.5. Other positron production mechanisms

There are several other mechanisms that may lead to positron production, albeit most of them have either very low reaction cross-sections and branching ratios or depend on non-physical assumptions and speculations. Therefore, they are irrelevant for positron studies in thermonuclear supernovae and are mentioned for completeness.

Some of them are :

Dark matter annihilation, neutrino-pair annihilation, W^+, Z, H-boson decay, anti-neutron decay (Siegert 2017).

3.3. Positron deceleration

Positrons are ejected with MeV kinetic energies in the environments of different astrophysical objects by a large variety of mechanisms presented in Sec. 3.2. Their final fate and annihilation depend on the properties of the environment they are produced. As charged leptons, they interact with all types of particles, including charged and neutral atoms, electrons, electric and magnetic fields, as well as photons. Since most of the times the energy of the positron exceeds that of the ambient particles, the interactions cause the former to lose energy until they reach a phase, where their kinetic energy approaches the kinetic energy of their ambient medium. They 'thermalize'. Once they thermalize, the cross-sections for annihilation with free or bound electron become dominant and their subsequent annihilation is a matter of time.

The energy loss of positrons is a continuous process that, depending on the surrounding medium, can last from a few seconds up to several million years (Milne et al. 1999; Guessoum et al. 1991). It is, however, competing with the process of positron annihilation during their slowing-down, where the positrons keep a substantial fraction of their kinetic energy. This process is called 'annihilation in flight' or 'direct annihilation'.

3.3.1. Positron energy losses

Depending on the properties of their environment (density of the medium, temperature, ionization grade, chemical composition, the existence of magnetic fields) and on their own kinetic energy, positrons can decelerate by various electromagnetic interactions.

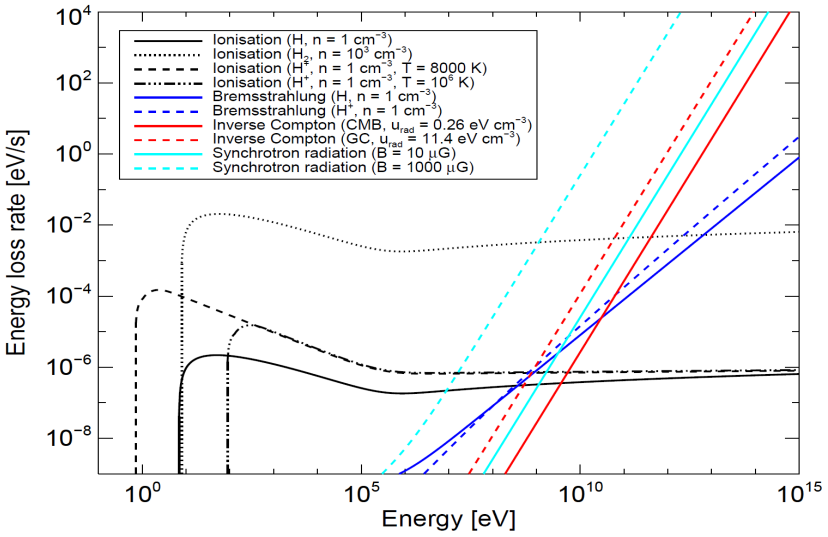

Figure 3.2.: Energy losses of positrons in interstellar space as a function of kinetic energy for different ISM conditions (from Siegert 2017)

Fig. 3.2 displays typical positron energy loss mechanisms for all ranges of possible kinetic energies up to $\sim$ TeV. The energy losses can be split into two energy regimes. For positron kinetic energies $E_{e^+} > 10$MeV, the following Coulomb interactions dominate the energy loss rate of positrons:

- Inverse Compton scattering with photons of the cosmic microwave background (CMB) and other interstellar radiation fields (red slopes). The stronger the radiation field, the higher the energy loss.
- Bremsstrahlung emission through interactions with charged particles like electrons and ions (dark blue slopes). The higher the ionization stage, the more efficient is the medium in stopping positrons.
- In astrophysical environments with magnetic fields B >6.4 μG, synchrotron radiation may dominate the energy loss rate of positrons (light blue slopes). The stronger the magnetic field, the smaller the positron gyroradius $r_g = p_{e^+}/qB$, the higher the positron path through the ejecta and thus the higher the energy loss.

For positrons with kinetic energies $E^{e^+}_{kin} < 10$MeV, the above-mentioned processes become irrelevant and Coulomb interactions such as excitation and ionization of atoms and molecules govern the total energy loss rate for positrons. In case of a high ionization fraction of the medium, plasma losses also gain importance. While in the former processes the energy loss is discrete, as it requires the collision with an individual atom or molecule, interactions with plasma waves can be considered a continuous progress.
The energy loss of positrons per unit length due to ionization and excitation of ambient particles is given by (Heitler 1954; Blumenthal and Gould 1970; Chan and Lingenfelter 1993):

$$\frac{dE}{dx} = -\frac{4\pi r_0^2 m_e c^2 Z}{A m_u \beta^2}\Pi(\gamma), \tag{3.7}$$

,where r^0 is the classical electron radius, m_e the rest mass of the electron, c the velocity of the light in vacuum, Z the nuclear charge of the ejecta, $\beta = v/c$, A the mass of the ejecta and m_u the atomic mass unit. The energy dependent factor $\Pi(\gamma)$ is given by (Berger and Seltzer 1964):

$$\Pi(\gamma) = \ln\left(\frac{\sqrt{\gamma-1}\gamma\beta \mathrm{m_e c^2}}{\mathrm{I(Z)}}\right) + \frac{1}{2}\ln(2) + \Sigma(\mathrm{E}) \tag{3.8}$$

Here, γ denotes the Lorentz-factor and I(Z) the ionization potential, which is approximated empirically Segre et al. 1977 and depends on the chemical composition of the medium and Σ(E) are relativistic corrections.
The formula for ionization losses of positrons is similar to Eq. (3.7), except that the ionization potential I(Z) is replaced by a maximum impact parameter b_{max} and the nuclear charge Z by the number of free electrons per nucleus, χ_e.

3.4. Positron annihilation

Depending on the properties of the ambient medium (e.g. the ionization state) and on their kinetic energy , positrons choose either free or bound electrons to annihilate. After picking up an electron, the annihilation can proceed either directly or through the formation of positronium:

Annihilation with free electrons

- Positrons can pick up a free electron and annihilate 'in flight'. In this case, the resulting γ-rays carry both the rest mass energies, as well as the kinetic energies of the particles, producing thereby a continuum above 511keV.

$$\mathrm{e^+ + e^- \rightarrow \gamma + \gamma} \tag{3.9}$$

- A second possibility for the annihilation of positrons with free electrons offers the formation of Ps via 'radiative recombination', a reaction similar to the recombination of hydrogen (Crannell et al. 1976). During the formation, a photon that carries the binding energy of the newly formed 'atom' is emitted. In the subsequent decay of Ps, either two or three photos are emitted (see Sec. 3.1).

$$\mathrm{e^+ + e^- \rightarrow Ps + \gamma} \tag{3.10}$$

Annihilation with bound electrons

- When positrons reach kinetic energies of $\mathrm{E_{kin}} \sim 100$eV, they can interact with ambient atoms or molecules, stripping off an electron and form Ps. Since the negative charge of the electron moves from the parent atom to the positron to form a neutral compound, this reaction is called 'charge exchange' and is endoenergetic; the binding energy of the Ps (6.8eV) is lower than the ionization energy of atoms. This sets a threshold energy for this reaction, as positrons with lower kinetic energies are not energetic enough to ionize ambient atoms.

$$\mathrm{e^+ + X \rightarrow Ps + X^+} \tag{3.11}$$

- Positrons that are located in neutral environments marked by the absence of free electrons, have evaded all above mentioned processes and managed to slow down to kinetic energies below the threshold energies for charge exchange reactions can only annihilate directly with bound electrons.

$$\mathrm{e^+ + X \rightarrow \gamma + \gamma + X^+} \tag{3.12}$$

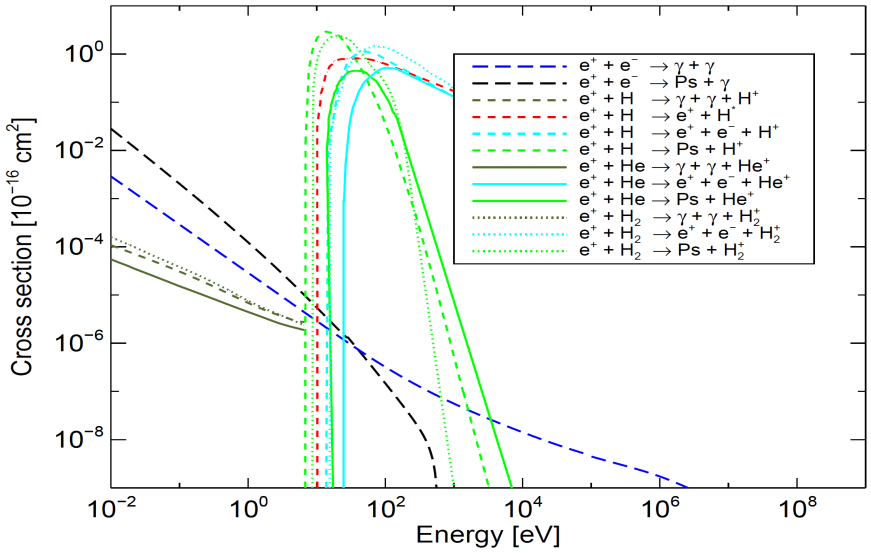

Figure 3.3.: Annihilation cross sections for different reactions of positrons with electrons, molecular and atomic hydrogen and helium as a function of positron kinetic energy (from Siegert 2017).

3.4.1. Direct annihilation

For the whole range between their initial energies and kinetic energies of the order eV, positrons can pick up free or bound electrons and annihilate 'in flight'. In this case, the resulting γ-rays carry both the rest mass energies, as well as the kinetic energies of the particles, producing thereby a continuum above 511keV.
The direct annihilation cross section σ_{da} as a function of the positron energy is given by equation (3.13)

$$\sigma_{\mathrm{da}} = \frac{\pi \mathrm{r}_\mathrm{e}^2}{\gamma+1}\left[\frac{\gamma^2+4\gamma+1}{\gamma^2-1}\cdot\ln(\gamma+\sqrt{\gamma^2-1}) - \frac{\gamma+3}{\sqrt{\gamma^2-1}}\right], \tag{3.13}$$

where r_e is the classical electron radius and γ is the Lorentz factor (Dirac 1930). The direct annihilation cross section is a decreasing function of the positron's kinetic energy, indicating thus that positrons are more likely to annihilate after they have slowed down. However, for all positron kinetic energies, annihilation in flight is a minor process. At high positron kinetic energies, energy loss mechanisms dominate, while at lower kinetic energies σ_{da} lies orders of magnitudes below the cross sections of reactions involving Ps formation.

3.4.2. Positronium formation and annihilation

The cross-sections for 'charge exchange' predominate all other cross sections, provided that the ionization fraction is low. Indeed, several studies that performed Monte Carlo simulations took into account both energy loss and annihilation cross sections for positrons found out that in a neutral medium, the fraction of positrons undergoing charge exchange approaches unity (Bussard et al. 1979; Brown and Leventhal 1987). In the case of a highly ionized medium, however, not only does the abundance of neutral elements decrease but also plasma losses due to the increased number of free electrons slow down the positrons in a faster rate below the charge exchange threshold.

Radiative recombination

At positron kinetic energies below the charge exchange threshold, Ps formation via radiative recombination becomes the dominant process above direct annihilation with free and bound electrons, provided that the number density of free electrons is not zero.

Generally, the number of positrons annihilating via the formation of Ps, the so-called Ps-fraction f, is given by:

$$\mathrm{f} = \frac{8\mathrm{I}_{3\gamma}}{9\mathrm{I}_{2\gamma} + 6\mathrm{I}_{3\gamma}}, \tag{3.14}$$

3.4.3. Line widths

Each of the aforementioned processes leaves a characteristic imprint on the resulting annihilation spectrum. The most striking first-order difference between different annihilation paths is the presence or absence of the ortho-Ps continuum, which infers directly, whether the annihilation took place directly or through the formation of Ps.

Furthermore, line widths can provide valuable clues about the exact path a positron chose to annihilate. Following this idea, widths of the electron-positron annihilation line in processes with free electrons (radiative combination and direct annihilation) were derived by Crannell et al. 1976 taking the thermal broadening of both leptons into account. This results in a width of $\Gamma_{\mathrm{rc,da}} = 1.1\sqrt{\mathrm{T}_4}$ keV, where T_4 denotes the temperature of the medium in 10^4K.

Guessoum et al. 2005 used a Monte Carlo simulation to calculate the widths of the annihilation line when positrons form Ps through charge exchange with H, H_2 and He, the most abundant components of the ISM. In contrast, the widths for direct annihilations with these elements were obtained experimentally (Brown and Leventhal 1987; Iwata et al. 1997).
The corresponding line widths are given in Tab. 3.1.

Process	H	H_2	He
Direct annihilation	1.6keV	1.7keV	2.5keV
Charge exchange	5.8keV	6.4keV	7.4keV

Table 3.1.: Line widths for positron annihilation processes involving H, H_2, He. Values extracted from Guessoum et al. 2005; Brown and Leventhal 1987; Iwata et al. 1997.

It is obvious that the composition of SN Ia ejecta differs substantially from the ISM, which is basically composed of the three constituents H, H_2, He (Ferrière 2001). Nevertheless, the line widths in Tab. 3.1 give insight on the corresponding line broadening purely due to the annihilation process.

3.5. Positron annihilation throughout the Milky Way

The first signatures of galactic positron annihilation were measured in the 1970s with low spectral resolution balloon-borne experiments (Johnson et al. 1972). The peak of the observed flux did not lie precisely at 511keV, the hallmark of positron annihilation, but rather at $\sim$ 470keV.

Subsequent balloon missions with high-resolution germanium detectors verified the observed signal, this time on its nominal position at 511keV and with a line flux of $1.2 \pm 0.2 \times 10^{-3}$ph/cm^2/s. An ortho-Ps continuum was detected, its intensity suggesting that 92% of the annihilations occurred through the formation of Ps (Leventhal et al. 1978). In addition, a time variability of the observed signal was established (Leventhal et al. 1980; Albernhe et al. 1981). This was interpreted ambiguously in the high-energy society, either as an intrinsic variability of the positron annihilation source or as a consequence of an extended emission along the Galactic plane. Since none of the instruments used at that time comprised imaging qualities, the necessity of an instrument with both imaging as well as spectroscopic capabilities became apparent.

A major step towards this direction was made in 1991 with the launch of the Compton Gamma Ray Observatory (CGRO) that carried a collimated scintillation spectrometer on board, named OSSE (Johnson et al. 1989). The obtained data revealed an extended source consisting of a bulge in the center of the Milky Way and a fainter emission from the Galactic plane (Purcell et al. 1994). The morphology of the positron annihilation emission was unique and could not be linked with any other galactic map at longer wavelengths. In addition, it placed several constraints on the candidate positron sources. Until then, the β^+-decay of radioactive ^{56}Co produced in large numbers in type Ia supernovae was the most plausible positron candidate (Guessoum et al. 1991; Chan and Lingenfelter 1993; Kinzer et al. 1996; Milne et al. 2002). Since type Ia supernovae preferably explode in the galactic disk (reference), several studies focused on how to transfer positrons from the galactic disk to the galactic center/bulge (Brown and Leventhal 1987). In addition, the shape of the 511keV line and the measured Ps fraction constrained further the annihilation conditions of positrons near the Galactic center. However, despite considerable improvements in the galactic positron annihilation riddle through CGRO, the exact origin of the positrons remained elusive.

The launch of ESA's INTEGRAL (Winkler et al. 2003) in 2002, an observatory carrying among other instruments the imaging spectrometer SPI (Vedrenne et al. 2003) on-board, was designed to revolutionize γ-ray observations, by combining adequate imaging capabilities with high-resolution spectroscopy. In fact, its excellent spatial and spectral resolution, SPI is capable of not only resolving individual candidate sources but also determining precisely the annihilation conditions through the spectral shape of the 511keV line. One year later, enough data were accumulated to construct the first all-sky maps of positron annihilation. (Knödlseder et al. 2005; Weidenspointner et al. 2006). As progressively more data were accumulated in the passing of the years, it became obvious that the majority of the 511keV line emission was concentrated in the galactic bulge, while a much fainter emission extended throughout the Galactic disk.

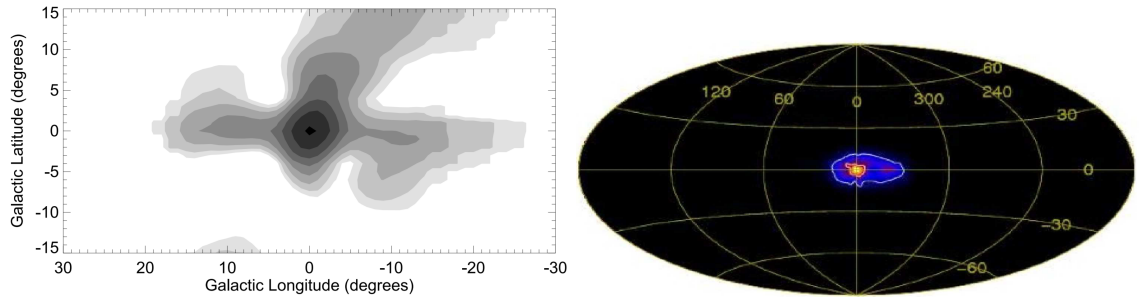

Figure 3.4.: Left first galactic 511keV map measured by OSSE on CGRO. THe contours are exponentially spaced (from Purcell et al. 1994) Right: Galactic 511keV map measured by SPI on INTEGRAL after five years of operation. (from Weidenspointner et al. 2008)

The high-resolution germanium detectors of SPI offered the opportunity to investigate the spectral shape of the 511keV line with higher spatial sensitivity.

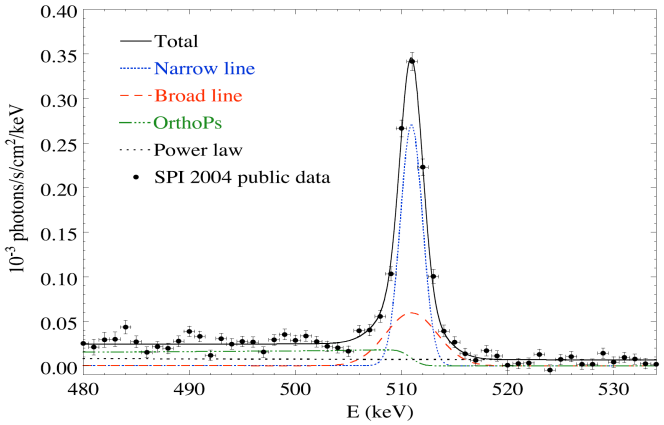

Figure 3.5.: Spectrum of positron annihilation emission from the Galactic Bulge measured by SPI. The spectrum is fitted by a convolution of functions (from Jean et al. 2006).

The 511keV line observed in the Galactic Bulge is best described by two components. A narrow line with a FWHM=1.3±0.4keV containing ≈ 66% of the flux and a broader and fainter line with a FWHM=5.4±1.2keV with the remaining flux. The strong ortho-Ps continuum detected can be converted into a Ps fraction of $f_{Ps} = 97 \pm 2\%$

Finally, Siegert, T. analyzed eleven years of SPI data throughout the Milky Way and performed fine electron-positron annihilation spectroscopy (Siegert 2017). With careful analysis, excellent exposure and detailed background modeling he was able to derive that a total number of 5×10^4 positrons annihilating per second in the Milky Way. ≈ 1/3 of them annihilate in the bulge and ≈ 2/3 in the Galactic disk. The significant emission from the Galactic disk improved significantly the previously puzzling bulge-to-disk ratio to values much closer to the spatial distributions of expected positron sources. Moreover, by comparing several astrophysical tracer maps to the galactic map of positron annihilation, he derived that the positron annihilation signal is similar to the distribution of the stars in the Milky Way. The differing spectral properties of positron annihilation found in different galactic regions suggested that the annihilation conditions in the bulge and the disk can vary.

Finally, he confirmed massive stars, supernovae and microquasars as valid sources of positrons. The former through their synthesis of ^{26}Al and ^{44}Ti, stellar explosion through ^{56}Co γ-rays and microquasars through a variable emission of pair-plasma annihilation.

3.6. Positrons in type Ia supernovae

As presented in Chapter 2, the explosive synthesis of radioactive elements and their subsequent decay establishes thermonuclear supernovae into major sources of positrons. In particular, normal type Ia supernovae produce about 0.5-0.6$M_\odot$ ^{56}Ni that with a lifetime of $\tau_{1/2} \approx 6.1$days decays via EC to ^{56}Co. In 19.58% of all cases, radioactive ^{56}Co decays into stable ^{56}Fe via β^+-decay, emitting thereby a positron and a neutrino. Hence, a normal type Ia supernova that synthesised 0.5$M_\odot$ of ^{56}Ni produces about:

$$N_{e^+}(\text{SNIa}) = \frac{M_{^{56}\text{Ni}}(\text{SNIa})}{m_{^{56}\text{Ni}} \cdot m_u} p_{\beta^+} \approx 2 \cdot 10^{54} e^+ \tag{3.15}$$

In this relation[1] , $M_{^{56}Ni}$(SN Ia) denotes the ^{56}Ni mass (in g) synthesised in a type Ia supernova, $m_{^{56}Ni}$ the atomic mass of ^{56}Ni, m_u the atomic mass unit and p_{β^+} the probability for a β^+-decay of ^{56}Co.

Positrons emitted in the β^+-decay of ^{56}Co possess a kinetic energy distributed within the interval 0 and 1459keV. Their energy distribution is given by equation (3.16). With a mean value of $\overline{E}_{kin}(e^+)$=0.632MeV, a large fraction is highly relativistic (Nadyozhin 1994).

$$N(E) = Cp^2(E_0 - E)^2(2\pi\eta(1 - \exp(-2\pi\eta)))^{-1} \tag{3.16}$$

At this energy domain, the annihilation rate is orders of magnitude lower than the energy loss rate (see Fig. 3.2). Thus, the produced positrons first lose energy in the expanding debris through ionization and excitation interactions with ambient particles, until they thermalize and reach kinetic energies, where Ps formation and annihilation become significant. Unfortunately, many undetermined quantities hinder the correct modeling of positrons and their behavior inside the supernova envelope:

One of the major uncertainties in supernova physics is the size and morphology of the magnetic field. A correct description of it is crucial, as it affects the trajectories of positrons inside the ejecta. A powerful magnetic field would reduce the gyroradius of positrons inside the ejecta, increasing thereby its path length and consequently minimizing their probability of escape. It is believed that WDs possess appreciably strong magnetic fields of $B_{WD} \sim 10^5$-10^9G, that can be described as dipoles (Leibundgut 1995; Penney and Hoeflich 2014). The evolution of the initial magnetic field during the thermonuclear runaway and the enormous expansion though remains a mystery.

Three different configurations are classically considered (Chan and Lingenfelter 1993; Milne et al. 1999; Ruiz-Lapuente and Spruit 1998):

- No magnetic field
- A radial magnetic field
- a turbulent, disordered magnetic field

Each magnetic field configuration specifies the motion of positrons inside the supernova ejecta:

A tangled, disordered magnetic field is believed to be the result of convection in the near Chandrasekhar-mass WD prior to the explosion (Ruiz-Lapuente and Spruit 1998). Such a morphology would cause positrons to meander near their birth site, not allowing them to diffuse to smaller optical depths and forcing them to annihilate in situ. Positron escape from thermonuclear supernovae with tangled magnetic fields is negligible.

The idea of a radial magnetic field originates from the consideration that the expansion of the supernova envelope would comb out any initial dipole field (Colgate et al. 1980). This would result in positrons spiraling along radial magnetic field lines, thus enhancing their probability to escape. The escape probability, though, would still depend on the strength of the magnetic field, the time of emission, the composition of the ejecta and the spatial distribution of ^{56}Ni.

[1]Positrons from pair production of high-energy γ-photons of ^{56}Co decay are neglected. $2 \times 10^{54} e^+$ correspond to $1.8 \cdot 10^{24}$kg $\approx 1/3$ of the mass of the Earth in antimatter produced in a normal type Ia supernova

For supernova arising from objects with weak magnetic fields $B < 10^3$G, the assumption of a negligible post-supernova magnetic field becomes valid. In this case, synchrotron losses can be completely omitted and positrons follow free trajectories and interact only with ions and electrons on their way to the surface.

In either cases, it is believed that the homologous expansion of the ejecta reduces the field strength by $B(t) \propto (rB)_{WD}/(vt)^2$ (Ruiz-Lapuente and Spruit 1998; Milne et al. 2002). Latest considerations of positron annihilation in type Ia supernova envelopes suggest that the magnetic field that the final structure of the magnetic field is very similar to the initial field of the WD, as it is frozen into the expanding ejecta, a direct consequence of homologous assumption (Penney and Hoeflich 2014).

Another considerable uncertainty is the degree of ionization of the ejecta, a parameter that affects the strength of various positron-ejecta interactions. Highly ionized elements are observed in the optical and the NIR through their atomic de-excitation lines, still, the exact ionization fraction of the ejecta remains undetermined. A possible low ionization would enhance the reaction rates of ionization and excitation with bound electrons and after significant deceleration, positrons would form Ps through charge exchange with ambient atoms. The absence of free electrons would minimize the rates for direct annihilation with free electrons and radiative recombination. A high degree of ionization would boost plasma interactions and be more efficient in slowing the positrons down, reducing their probability of escape (Milne et al. 1999).

Last but not least, charge exchange and direct annihilation cross sections for elements other than atomic and molecular hydrogen and helium are highly uncertain. This is rather unfortunate, as type Ia supernovae are one of few astrophysical sites, where hydrogen and helium, the most abundant elements in the Universe are scarce. The composition of the ejecta is far different from the ISM and is dominated by IMEs and IGEs. Experimentally obtained cross sections for IMEs and IGEs are crucial to simulate the propagation of positrons inside a supernova accurately. Despite the fact that there exists no experimental evidence for these cross sections, it is assumed that for heavier elements they are proportional to the Bohr radius $\alpha_0 = \hbar/m_e c\alpha \approx 5.3 \cdot 10^{-11}$m

Motivated by the large positron annihilation flux from the Milky Way and the fact that SNe Ia are considered major candidates for the galactic positron supply, several studies tackled the positron issue and tried to calculate a positron escape fraction for type Ia supernova ejecta.

For instance, Ruiz-Lapuente and Spruit 1998 studied late bolometric light curves to infer whether positrons deposit their kinetic energies and annihilate or are able to avoid thermalization and escape. The first scenario would cause a flattening of the late bolometric light curve, whereas the second scenario would yield a steeper decline. Their results were ambiguous, as some supernovae supported the trapping scenario, while some others indicated an enhanced positron escape. These findings are in accordance with similar studies performed by Colgate 1991; Cappellaro et al. 1997.

Another possibility to derive escape fractions is to run simulations containing all relevant physics. Several assumptions are required concerning the chemical composition of the ejecta, the distribution of the radioactive elements, the supernovae explosion mechanism, the ionization grade as well as the configuration and morphology of the magnetic field.

Chan and Lingenfelter 1993 were also motivated by the diffuse 511keV Galactic emission and the mystery behind the origin of the annihilating positrons and run simulations in order to verify if supernovae could be at least to some extent responsible for the galactic observations. In particular, they tested one delayed-detonation and one detonation model, allowing mixed or central ^{56}Ni dis-

tributions and found out that for certain configurations (radial magnetic fields and ejecta mixing), the positron escape fraction may reach 15%. On the contrary, for supernova envelopes with tangled magnetic fields, the positron escape fraction is negligible and only a minuscule fraction of them may escape ($\sim$ 5%) if ^{56}Ni is considerably mixed.

Another study by Milne et al. 1999 based on the same physical principles generated bolometric light curves and fitted them on a sample of ten type Ia supernovae. The fits suggested that positron escape at late times should be natural for most type Ia supernovae.

Earlier studies by Colgate 1970 and Axelrod 1980; also yielded positron escape fractions between 0% and 10%. Although the differences in the escape fractions might be small, the impact on the high-energy astronomy and astrophysics would be very large, as even a few % would suffice to explain a large fraction of positrons seen to annihilate throughout the Milky Way (Prantzos et al. 2011).

3.7. Radioactive decay

Radioactivity was accidentally found by Antoine Henri Becquerel in 1896, while he was experimenting on phosphorescent materials (Mould 1995). In one of his experiments with uranium polluted photographic plates, he noticed the blackening of the plates. The French scientist soon understood that it was not caused by phosphorescence, but rather by the uranium salts that emitted an unknown type of invisible radiation. Further research by Marie and Pierre Curie, Becquerel and Paul Villard established the physical term of 'radioactivity' for elements that emitted this type of radiation. Ernest Rutherford distinguished between three different kinds of radiation, the α-decay, the β-decay and the γ-decay, which he named after their ability to penetrate matter (Soddy 1913).

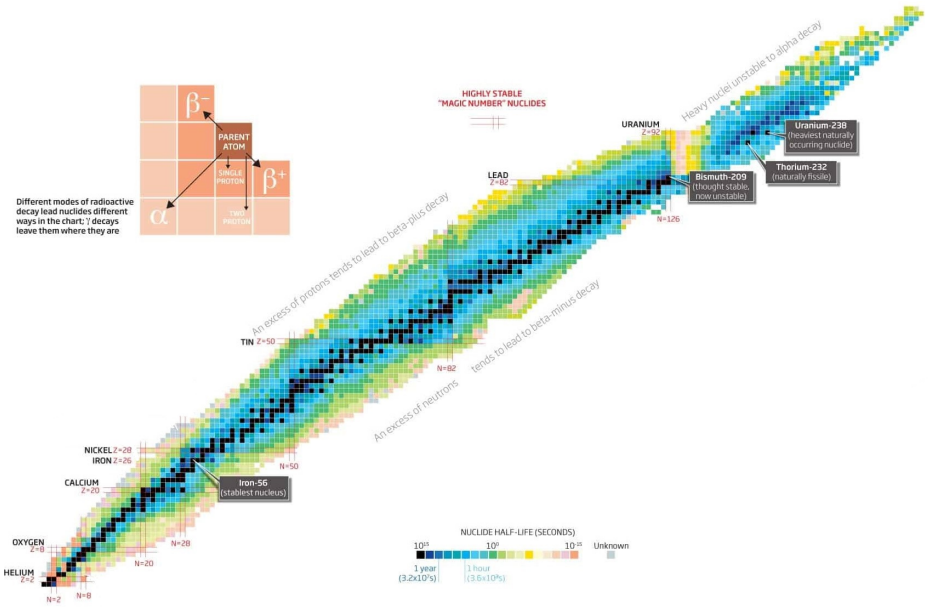

Figure 3.6.: Chart of the known nuclei colored after their half-life. Black squares indicate stable isotopes and mark the valley of stability. Extracted and modified from www.nuclear-power.net

Today it is well established that radioactive decay is driven by nuclear stability. As unstable atomic nuclei attempt to reach a more stable form, they release energy in the form of radiation and matter.

An element ${}^{A}_{Z}\mathrm{X}$ characterized by the number Z of protons needs a certain number $N = A - Z$ of neutrons in order to reach a stable nuclear configuration. As can be seen in Fig. 3.6 the higher Z becomes, the more neutrons are needed to compensate for the continuously growing Coulomb repulsion of the nucleus. This results in a so-called 'valley of stability' in the proton-neutron plane, where stable isotopes of all elements can be found.

As Rutherford realized more than a century ago, radioactive decay is a stochastic process. The probability per unit time for a single radioactive nucleus to decay is not a function of the time, which implies that the rate, at which a radioactive nuclide decays, is constant. The constant rate of decay is thus given by the radioactive decay constant λ:

$$\lambda = \lim_{\Delta \mathrm{t} \to 0} \frac{\Delta \mathrm{N}/\mathrm{N}}{\Delta \mathrm{t}} \tag{3.17}$$

The decay constant λ is defined as the statistically averaged decay probability for an infinitesimal time interval and is a property of each radionuclide. If λ is known, the decrease in the number of radionuclides given an initial amount N of radionuclides is given by:

$$\frac{\mathrm{dN}}{\mathrm{dt}} = -\lambda \cdot \mathrm{N} \tag{3.18}$$

The differential Eq. (3.18) can be solved, yielding a relation for the number of remaining radioactive nuclei N(t) at a given time t of an initial amount N_0, called the decay law:

$$\mathrm{N(t)} = \mathrm{N}_0 \cdot \mathrm{e}^{-\lambda \cdot \mathrm{t}} \tag{3.19}$$

Following Eq (3.19), the concept of half-life can be developed. This is defined by the amount of time a radioactive element needs to lose half of its initial value due to radioactive decay.

$$\mathrm{T}_{1/2} = \frac{\ln(2)}{\lambda} \tag{3.20}$$

Since the half-life of a nucleus depends only on lambda, it is unique for every radionuclide.

3.7.1. Types of radioactive decay

An unstable nucleus has several different possibilities to transform into a stable nuclear configuration and reach the valley of stability.

α-decay

Heavy nuclei with large A tend to cluster into sub-units of He-nuclei, known as α-particles. These consist of two protons and two electrons, have an electric charge of +2e and a high nuclear binding energy, being thus very compact and tightly-bound. Heavy nuclides decay preferably via α-decay, as it is a fast way to reach more stable nuclear configurations. α-decay is caused by the strong nuclear interaction.

$${}^{A}_{Z}\mathrm{P} \rightarrow {}^{A-4}_{Z-2}\mathrm{D}^{2-} + {}^{4}_{2}\mathrm{He}^{2+} \tag{3.21}$$

β-decay

β-decay is caused by the weak interaction. Depending on the charge of the emitted lepton, it appears in two forms, the β^+-decay and the β^--decay.

- β^+-decay:

  Proton-rich nuclei, located on the proton-rich side of the valley of stability, have too many protons in order to be stable. To compensate for that, a proton is transformed into a neutron inside the nucleus, while a positron and a neutrino are emitted in order to conserve charge, energy and momentum.

$$ {}^{A}_{Z}\mathrm{P} \rightarrow {}^{A}_{Z-1}\mathrm{D}^{1-} + {}^{0}_{1}\mathrm{e}^{+} + {}^{0}_{0}\nu \tag{3.22} $$

  Because the available decay energy is shared between two bodies, the energy spectrum of both the positron and the neutrino is continuous with a well-defined maximum at the maximum available energy Q_β in the decay. The β^+-decay is of fundamental interest for this thesis, since radioactive ^{56}Co in type Ia supernova envelopes produces positrons through this decay channel.

- β^--decay:

  Nuclei situated on the neutron-rich side of the valley of stability decay by transforming neutron into protons. Again, in order to respect energy, charge and momentum conservation, an electron and an anti-neutrino are emitted, with a continuous energy spectrum similar to the β^+-decay.

$$ {}^{A}_{Z}\mathrm{P} \rightarrow {}^{A}_{Z+1}\mathrm{D}^{1+} + {}^{0}_{-1}\mathrm{e}^{-} + {}^{0}_{0}\overline{\nu} \tag{3.23} $$

Electron capture decay (EC)

This mode is the second possibility a proton-rich nucleus has to balance its proton-to-neutron ratio, thus competing to the β^+-decay. In particular, EC decays are favorable, when the mass difference between parent and daughter nuclei does not suffice to generate a positron. From the quantum mechanical point of view, electron captures happen, because quantum mechanics assign a non-zero probability for the orbital electrons to be located within the nucleus. As a consequence, EC is the process in which a proton-rich nucleus absorbs one of its inner electrons, emitting thereby a neutrino, that carries the entire decay energy away.

$$ {}^{A}_{Z}\mathrm{P} \rightarrow {}^{A}_{Z-1}\mathrm{D}^{*} + {}^{0}_{0}\nu \tag{3.24} $$

γ-decay

In most of the aforementioned nuclear processes, the daughter nucleus is left in an excited state. In this purely electromagnetic interaction, an excited nucleus relaxes to a lower-lying nuclear state by emitting γ-photons.

$$ {}^{A}_{Z}\mathrm{P}^{*} \rightarrow {}^{A}_{Z-1}\mathrm{P} + \gamma \tag{3.25} $$

Every nuclear stage is characterized by three quantum numbers: The angular momentum J, parity π and isospin T. The differences between quantum numbers of different nuclear stages affect their lifetime. Transitions between different nuclear levels have typical lifetimes of 10^{-9}s and happen usually in cascades, i.e. consecutive γ-ray photons are emitted, until the nucleus reaches a stable nuclear state (i.e. the ground state). Transitions with lifetimes longer than $\tau \geq 10^{-9}$s are denoted 'meta-stable' configurations of a nucleus.

In addition to the β^+-decay of ^{56}Co, the detection of photons from the γ-decay of the same element, as well as its parent nucleus ^{56}Ni, are one of the main scientific targets of this thesis.

3.7.2. ^{56}Ni-decay sheme

As illustrated in Chapter 2, most sub-types of type Ia supernovae produce predominantly ^{56}Ni (Seitenzahl et al. 2009). Depending on the sub-type, between $0.1M_\odot$ and $1.0M_\odot$ of freshly synthesised ^{56}Ni are expected per explosion (Stritzinger et al. 2006).

Situated on the proton-rich side of the valley of stability, ^{56}Ni is forced to convert two of its protons into neutrons, in order to reach stable ^{56}Fe.

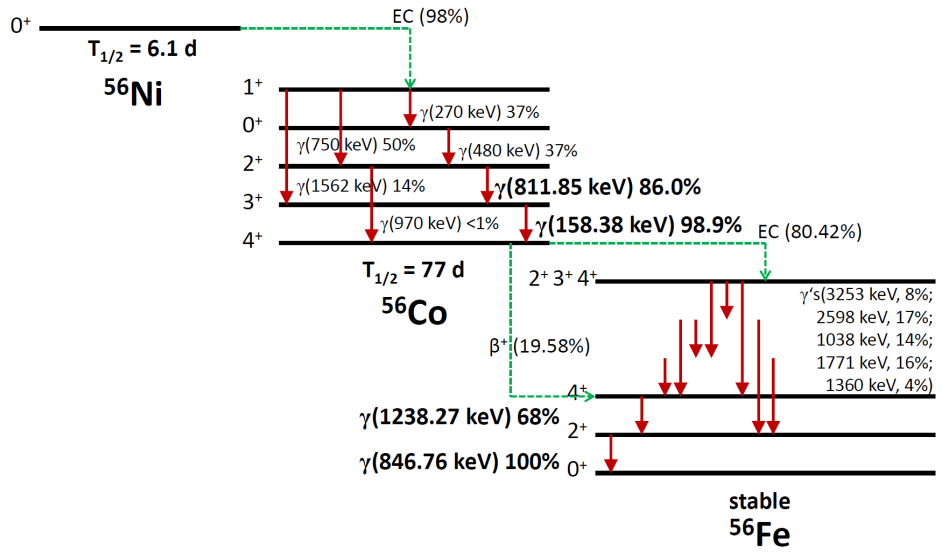

Figure 3.7.: Decay scheme of the ^{56}Ni decay chain.

Fig. (3.7) displays the decay scheme of the ^{56}Ni-decay chain. Unstable ^{56}Ni has a lifetime of $T_{1/2} = 6.1$d and decays with 98% probability via EC to ^{56}Co. The latter is in the $J^\pi=1^+$ excited state and de-excites emitting successive γ-photons with diverse branching ratios. The most prominent transitions yield photons with 158keV (98.9%), 750keV (50%) and 812keV (86%). The total energy released per ^{56}Ni decay can be roughly estimated from the mass difference between ^{56}Ni and ^{56}Co. According to calculations made by Huo et al., the total energy emitted via γ-photons is $Q_\gamma = 1.75$MeV, while the total energy carried away by neutrinos is $Q_\gamma = 0.41$MeV.

Once ^{56}Co reaches its $J^\pi=4^+$ ground state, it decays with a half-life of ^{56}Co of 77.12 days into excited ^{56}Fe either by another EC (80.42%) or by β^+-decay (19.58%)(Nadyozhin 1994). ^{56}Fe has 20 different energy levels, emitting thus a forest of γ-photons with various energies before reaching the ground state. The most prominent of them are located at 847keV (100%), 1040keV (14%) and 1238keV (68%). In the case of the β^+-decay, a positron is emitted, carrying a mean kinetic energy of 0.632MeV, while the resulting ^{56}Fe nucleus lands its $J^\pi=4^+$ nuclear energy level. The total available decay energy of ^{56}Co is split into γ-rays ($Q_\gamma = 3.61$MeV), positrons and neutrinos ($Q_{e^+,\nu} = 1.459$MeV).

3.8. Gamma-rays

Most of the decays described above are associated with the emission of $\sim$ MeV photons that populate the upper end of the electromagnetic spectrum and are called γ-ray photons.

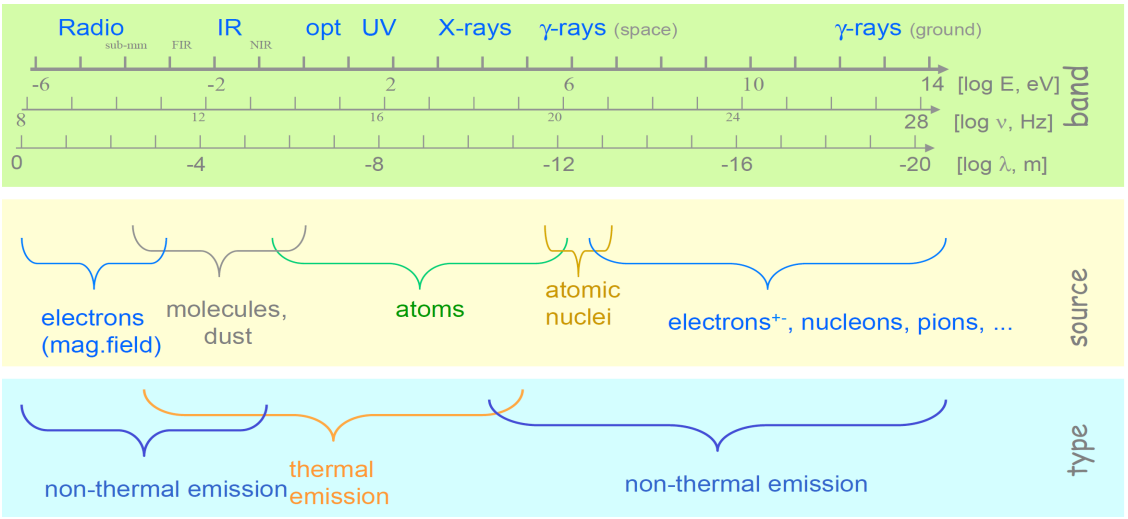

Figure 3.8.: An overview of the electromagnetic spectrum, where γ-rays populate the right part and are subdivided according to their ability to penetrate the atmosphere

γ-photons are no longer described by their wavelength but rather by their energy in units of electron Volts (eV), through $E = h \cdot \nu$. There is a broad overlap between the less energetic γ-rays (called 'soft' γ-rays) and the most energetic x-rays (called 'hard' x-rays), making it hard to differentiate them. A typical border line is set at 100keV. On the other side, there is no upper limit on the most energetic γ-rays reaching energies up to the order of TeV (Aharonian et al. 2004). Thus, the γ-ray spectrum spans over 9 orders of magnitude, being almost as broad, as all other remaining bands together.

γ-rays were discovered in 1900 by the French chemist and physicist Paul Villard, while he studied the radiation emitted during the nuclear de-excitation of radon (Villard 1900). Ernest Rutherford, who experimented on α-rays and β-rays, named these forms of electromagnetic radiation γ-rays, as a consequence of their enhanced ability to penetrate matter, in comparison to the formerly known types of radiation. (D.Sc. 1903).

3.9. Gamma-ray interaction processes

As mentioned above, the γ-ray energy spectrum covers all energies above a few tenths of keV. At these energies, the propagation of photons through matter, regardless of whether the latter consists of the atoms of a γ-ray detector, the ejecta of a thermonuclear supernova, the atmosphere of the Earth, or the constituents of the ISM, is dictated by three basic interaction processes: the photoelectric absorption effect (PE), the Compton scattering effect (CE) and the pair production effect (PP).

3.9.1. Photoelectric effect

At photon energies $E_\gamma >\sim 200$keV photoelectric absorption is the dominant interaction process. This effect occurs, when the energy of an incident photon exceeds the work function of the material it passes through. In this case, the photon is absorbed, and its energy is transferred on an orbital electron, which is kicked out of the atom. Its kinetic energy that can be calculated as the difference between the incident photon energy and the work function of the atom. The cross-section of the photoelectric effect depends on the energy of the photon, the height of the work function and the charge number Z of the material and is given by:

$$\sigma_{\mathrm{PE}} = \kappa \cdot \frac{\mathrm{Z^n}}{\mathrm{E^m}} \tag{3.26}$$

Exponents m and n depend on the incident photon energy E_γ and κ is a dimensionless constant. The strong dependency on Z illustrates that a photoelectric detector is highly efficient when it is built out of materials with a high proton number.

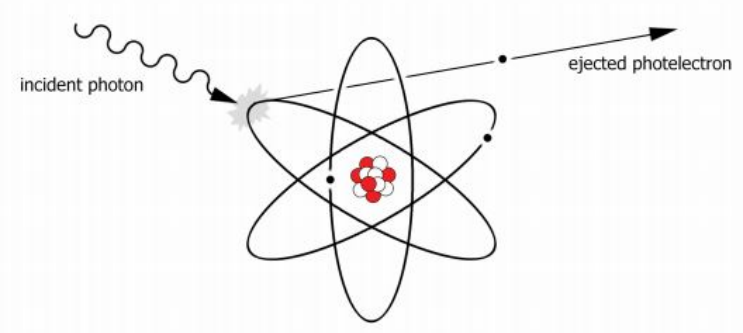

Figure 3.9.: Schematic drawing of the photoelectric effect (from PET's userguide (FOPRA, TUM))

The photoelectric absorption effect destroys the photon but allows the creation of secondary fluorescence photons. For example, if the initial photon is absorbed by a K-shell electron, a vacancy in the innermost shell is created. L- or M-shell electrons may then be transferred to the K-shell, emitting x-ray photons in the process.

Photoelectric effect in a thermonuclear supernova

γ-photons generated inside the envelope of a thermonuclear supernova are subject to photoelectric absorption.

In first order, the ejecta of type Ia supernovae can be categorized into three different types : (i) unburned material (C,O) with low Z, (ii) partially burned material with $Z \sim 14$ (IMEs) and completely burned material with a high Z (IGEs) (Ambwani and Sutherland 1988). For each type of supernova ejecta, Veigele 1973 calculated the corresponding cross-sections that are widely used in Monte Carlo (MC) simulations of γ-ray radiation transport:

$$\sigma_{PE} = \begin{cases} 0.0448 \cdot (\mathrm{E/100keV})^{-3.2} \times 10^{-24}\mathrm{cm}^2, & \text{for Z} = 7 \\ 1.16 \cdot (\mathrm{E/100keV})^{-3.13} \times 10^{-24}\mathrm{cm}^2, & \text{for Z} = 14 \\ 25.7 \cdot (\mathrm{E/100keV})^{-3.0} \times 10^{-24}\mathrm{cm}^2, & \text{for Z} = 28 \end{cases}$$

The high photoelectric absorption cross-sections below 100keV (see Fig. 3.13) result in a cut-off of the γ-ray supernova spectrum at low energies. The position of this cut-off depends on the chemical

composition of the outer layers, making its precise determination a direct probe of the outer ejecta configuration (Isern et al. 2017; Gómez-Gomar et al. 1998).

3.9.2. Compton effect

At higher photon energies the Compton scattering effect dominates photon interactions with matter. Here, a photon is scattered inelastically on an electron, losing thereby a fraction of its energy and changing its direction. The cross section of this process depends on (i) the energy of the incident photon and (ii) the angle of scattering.

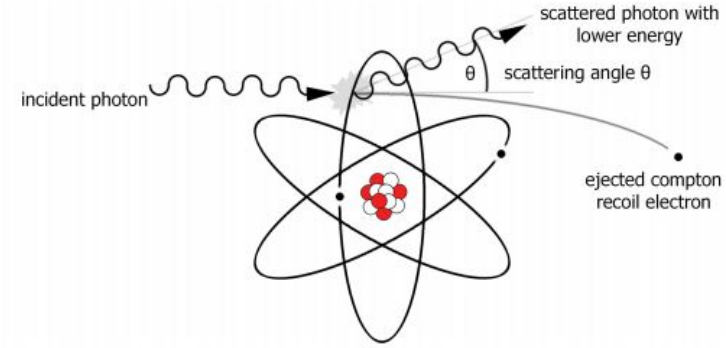

Figure 3.10.: Schematic drawing of the Compton effect (from PET's userguide (FOPRA, TUM))

Since the photon energies relevant for the Compton effect clearly exceed the corresponding work functions of electrons in atoms, whether an electron is bound in an atom or free does not play a significant role in this process (Summa et al. 2013).

For a given scattering angle θ and an initial photon energy E_0 the final-state energy E'of the photon is given by:

$$E' = \frac{E_0}{1 + \frac{E_0}{m_e c^2}(1 - \cos(\theta))} \tag{3.27}$$

The scattering angle θ of a photon that interacted via Compton scattering is widely used in Compton telescopes to determine the origin of the incident gamma-rays. However, the Compton cross-section is not constant for all angles. The angle-dependent Compton cross-section is given by:

$$\frac{d\sigma_{CE}^{KN}}{d\Omega} = \frac{1}{2} r_0^2 \left(\frac{k}{k_0}\right)^2 \left(\frac{k}{k_0} + \frac{k_0}{k} - \sin^2(\theta)\right) \tag{3.28}$$

where $k_0 = E_0/(m_e c^2)$, $k = E/(m_e c^2)$ and $r_0 = (\alpha\hbar c)/(m_e c^2)$. The total cross-section can hence be derived by integrating Eq. (3.28) over the solid angle and is a smoothly varying function of energy (Klein and Nishina 1929).

$$\sigma_{CE}^{KN} = 2\pi r_0^2 \left\{ \frac{1+k}{k^2} \left[\frac{2(1+k)}{1+2k} - \frac{\ln(1+2k)}{k} \right] + \frac{\ln(1+2k)}{2k} - \frac{1+3k}{(1+2k)^2} \right) \right\} \tag{3.29}$$

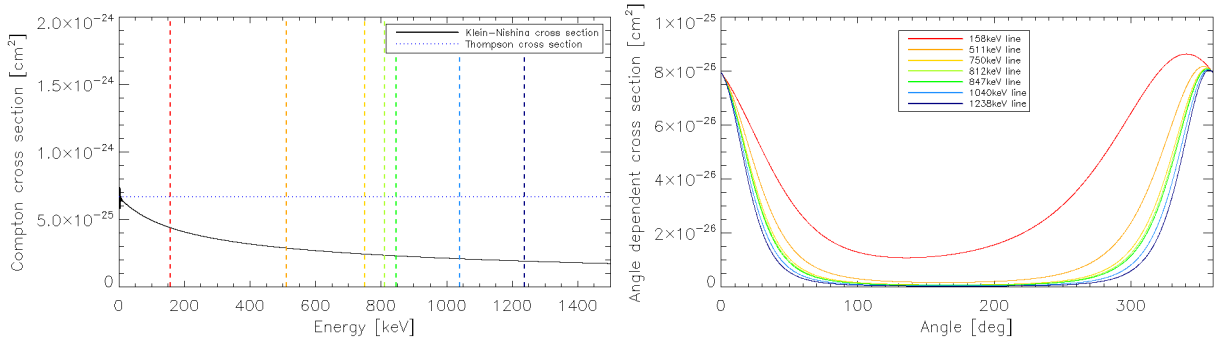

Figure 3.11.: Energy (left panel) and angle (right panel) dependence of the Klein-Nishina cross section. The dashed vertical lines represent important transition energies of ^{56}Ni and ^{56}Co.

For low photon energies ($E_\gamma \leq 100$keV), the Klein-Nishina cross section simplifies to the Thompson cross-section.

$$\sigma_{\mathrm{Th}} = \frac{8\pi}{3}\left(\frac{\alpha\hbar c}{mc^2}\right)^2 \simeq 6.652 \cdot 10^{-25}\mathrm{cm}^2 \tag{3.30}$$

Compton effect in a thermonuclear supernova

For the majority of photon energies coming from the radioactive decays of ^{56}Ni and ^{56}Co, Compton scattering is the dominant interaction process. Since type Ia supernovae originate from objects initially composed of carbon (N=Z=6) and oxygen (N=Z=14), most of the constituents of the ejecta have an electron fraction $Y_e = 0.5$. Hence, Compton scattering in a type Ia supernova is weakly dependent on the composition and depends primarily on the column density n_e of target electrons and the energy E_γ of the incident photon (Milne et al. 2004).

3.9.3. Pair production

Pair-production becomes relevant for photon energies $E_\gamma \geq 1022$keV, which corresponds to two times the rest mass of an electron. As a consequence of the equivalence between mass and energy $E = m \cdot c^2$, the energy of a photon is converted into an elementary particle and its antiparticle, i.e. an electron-positron pair. Conservation of energy and momentum disallow the production of an electron-positron pair from a single photon in vacuum. The presence of an electric field is important in order to carry away excess energy and momentum. Therefore, a single quantum pair-production may happen either within an atom that exhibits an external Coulomb field or simply through an interaction with a free electron.

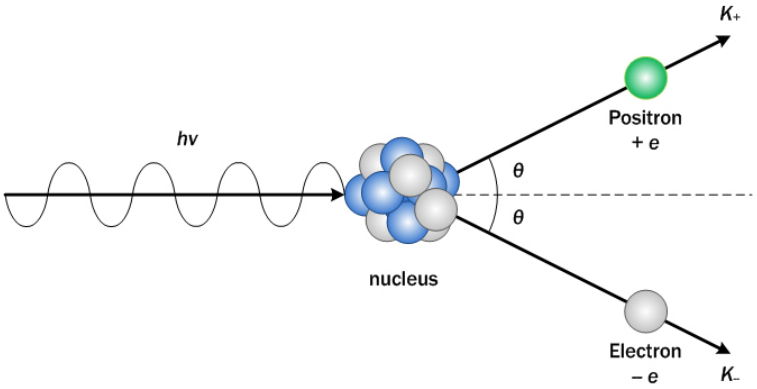

Figure 3.12.: Schematic drawing of the pair production effect (from http://electrons.wikidot.com/)

The cross section for pair production is divided into two regimes, the low-energy, non-relativistic limit and the high-energy relativistic limit (Jauch and Rohrlich 1976):

$$\sigma_{\mathrm{PP}}^{\mathrm{NR}}(\mathrm{E}) = \frac{\pi}{12}\alpha \mathrm{Z}^2 \mathrm{r}_\mathrm{e}^2 \left(\frac{\mathrm{E}}{\mathrm{m}_\mathrm{e}} - 2\right)^3 \tag{3.31}$$

$$\sigma_{\mathrm{PP}}^{\mathrm{UR}}(\mathrm{E}) = \alpha \mathrm{Z}^2 \mathrm{r}_\mathrm{e}^2 \left[\frac{28}{9} \cdot \ln\left(\frac{2\mathrm{E}}{\mathrm{m}_\mathrm{e}}\right) - \frac{218}{27}\right] \tag{3.32}$$

E denotes the energy of the incident photon, α the fine-structure constant, m^e and r^e the mass and the radius of the electron and Z the number of protons of the targeted atom.

Another approach, widely used in radiation transfer simulations for γ-ray spectra of type Ia supernovae, is given by Hubbell 2006.

$$\sigma_{PP} = \begin{cases} 0\mathrm{cm}^2, & \text{for } \mathrm{E} < 1.022\mathrm{MeV} \\ 1.0063(\mathrm{E} - 1.022)\mathrm{Z}^2 \times 10^{-27}\mathrm{cm}^2, & \text{for } 1.022 < \mathrm{E} < 1.5\mathrm{MeV} \\ [0.0481 + 0.301(\mathrm{E} - 1.5)]\mathrm{Z}^2 \times 10^{-27}\mathrm{cm}^2, & \text{for } \mathrm{E} > 1.5\mathrm{MeV} \end{cases}$$

The relative strength of the photoelectric, the Compton scattering and the pair-production effects in supernova-like materials as a function of incident photon energy is displayed in Fig. 3.13. At low γ-energies, the photoelectric effect dominates, while above $\mathrm{E}_\gamma \sim 1300\mathrm{keV}$, the pair-production effect gains importance. In between, the Compton scattering is the dominant interaction process.

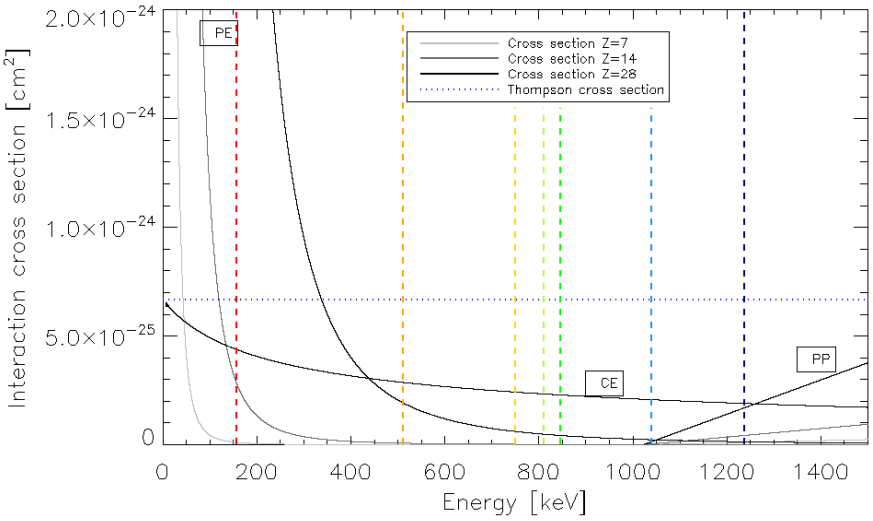

Figure 3.13.: Cross sections of the PP, CE and PP effects in three different types of materials as a function of energy. For the Compton scattering, no dependence on Z is assumed. The dashed colored vertical lines represent the energy position of prominent γ-transitions of ^{56}Ni and ^{56}Co.

Pair-production in a thermonuclear supernova

The decay of ^{56}Ni to ^{56}Co and subsequently to ^{56}Fe yields several transitions above the pair-production threshold. Thus, there is a potential to create additional positrons alongside the β^+-decay of ^{56}Co. An estimate of the number of positrons created through pair-production from high-energy photons can be made with Monte Carlo simulations.

3.9.4. Photon-photon interactions

As already introduced in Sec. 3.2.3, two interacting photons with a total energy $E_\gamma \geq 1.022 MeV/c^2$ can be converted to an electron-positron pair. In compact objects like neutron stars or black holes, the radiation densities are high enough so that the right conditions for efficient photon-photon pair creation are met. Exploded WDs cannot be considered compact objects, but their high luminosities and γ-ray flux may compensate for the linearly increasing radius, turning them into candidate sites for photon-photon pair production.

Photon-photon interactions in thermonuclear supernovae

According to Siegert 2017 and Lightman and Zdziarski 1987, to achieve efficient photon-photon pair-creation, γ-ray photons must be opaque to themselves and their optical depth must satisfy $\tau_{\gamma\gamma} \geq 1$.

$$\tau_{\gamma\gamma} = n_\gamma \sigma_{PP,\gamma\gamma} r \geq 1 \tag{3.33}$$

Here, n_γ denotes the number density of the photons, r the radius of the object and $\sigma_{PP,\gamma\gamma}$ the pair-creation cross-section. The energy density n_γ can be written as:

$$n_\gamma = \frac{L}{4\pi r^2 m_e c^3} \tag{3.34}$$

Where L is the luminosity of the source. Hence, using Eqs. (3.33) and (3.34) the condition for the optical depth can be rewritten:

$$\tau_{\gamma\gamma} = \frac{\mathrm{L}}{\mathrm{r}} \frac{\sigma_{\mathrm{PP},\gamma\gamma}}{\mathrm{rm_e c^3}} \tag{3.35}$$

The relation $\sigma_{PP,\gamma\gamma}/m_e c^3$ is $\approx 10^{-29}$cm s/erg[1]. Hence, the luminosity of the object divided by the radius must be $\approx 10^{29}$ erg cm^{-1} s^{-1}, in order to fullfill the condition for photon opacity. In an expanding type Ia supernova, both the luminosity and the radius are functions of time. In order to estimate the radius, a homologous expansion can be assumed: r=5000km+6000km/s·t. Fig. 3.14 depicts the time evolution of the compactness parameter l in the first 300 days after the explosion.

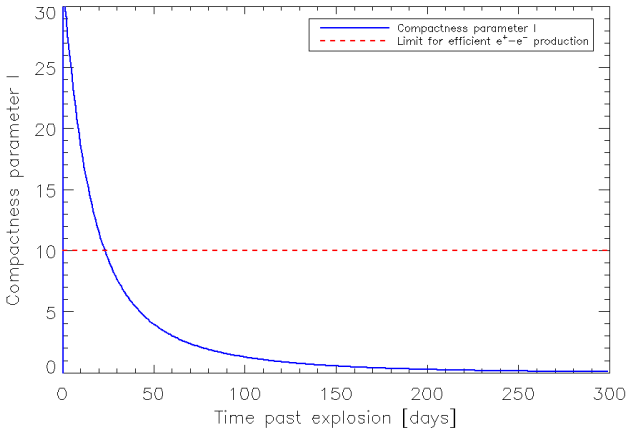

Figure 3.14.: The evolution of the compactness parameter l inside a type Ia supernova envelope as a function of time. The red horizontal line represents the lower limit for efficient photon-photon pair-production. Only the luminosity of the 1238keV line was considered.

In Fig. 3.14 it is apparent that up to ∼day 30 after the explosion and only considering the luminosity of the 1238keV line, l exceeds the canonical value of 10 and the conditions for efficient electron-positron production from photon-photon pair creation are met. Considering also the energetic γ-photons from the ^{56}Ni-decay further increases the probability that type Ia supernovae convert a fraction of their γ-luminosity into electron-positron pairs.

3.10. Gamma-ray production mechanisms

γ-rays are associated mainly with non-thermal emission produced by a large variety of phenomena that involve nuclear and particle physics. In this section, the γ-ray production mechanisms of particular astronomical interest are presented, while other production mechanisms are briefly mentioned.

Radioactivity

As illustrated in Sec. 3.7, radioactivity is one of the most important sources of γ-photons both in space and Earth. Most decay modes leave their daughter nuclei in excited states, thus forcing them to release their excess energy via electromagnetic radiation. Since the energy differences between different nuclear energy levels range between several tens of keV upwards to a few tenths of MeV, these photons mostly fall within the γ-ray band.

Matter-antimatter annihilation

A detailed example of this purely electromagnetic decay was discussed in Sec. 3.4. According to the Standard Model of particle physics, every particle has its respective antiparticle. When they reach zero separation, two photons sharing an energy equivalent to the sum of the rest masses and their kinetic energies are released. If the kinetic energies during the annihilation process are zero, each photon carries the rest-mass energy of the annihilated particle, as dictated by $\mathrm{E} = \mathrm{m} \cdot \mathrm{c}^2$. Alongside electron-positron annihilation that plays a fundamental role in this thesis, there are several other particle-antiparticle annihilations of astronomical interest, such as the proton-antiproton annihilation, muon-antimuon annihilation, pion-antipion annihilation or even the speculated dark matter annihilation.

Besides neutrinos, electrons and positrons are the lightest elementary particles known, with a rest mass of $0.511\mathrm{MeV/c}^2$. Their annihilation provides a minimum total energy of $1.022\mathrm{MeV/c}^2$ that can be carried away by γ-photons. Since the rest masses of most annihilating particles are in the MeV/c^2 regime and the complete energy is carried away by a relatively small number of photons, matter-antimatter annihilations can be considered a major source of γ-rays, as they yield photons in the MeV-regime.

Bremsstrahlung and Synchrotron radiation

Bremsstrahlung and Synchrotron radiation are two examples of continuous spectrum radiation that were briefly discussed as potential energy loss mechanisms of positrons in Sec. 3.2.4. The former is associated with electric fields and the latter with magnetic fields.

Bremsstrahlung occurs when a charged particle is decelerated due to the electric field of another charged particle carrying the same charge from an initial velocity v_i to a final velocity v_f. The difference in kinetic energies is emitted as a photon due to energy conservation in the process. In order to produce high-energy γ-photons from this process, high Z materials are required (Bethe and Heitler 1934; Ginzburg 1979)

Synchrotron radiation is emitted when ultra-relativistic leptons spiral along magnetic field lines. The resulting Lorentz force accelerates them radially with respect to their initial direction, emitting hence photons. According to some studies (Sokolov et al. 1968), high enough magnetic fields and particle energies may suffice to create photons with energies of the order of $\sim$ MeV.

Energetic particle collisions

Another source of γ-ray emission originates from particle-particle collisions. (See Ramaty et al. 1979), where high-energy particles hit targets that can be considered stationary. Particle-particle collision is a common astrophysical process found in numerous astronomical sites:

- γ-ray emission arises when high-energy protons from cosmic-rays hit components of the ISM, producing thereby secondary particles like protons, neutrons, pions of all charges and other spallation products. Many of them have finite lifetimes, decaying or annihilating via γ-emission. Cosmic-rays can also cause nuclear excitation of ISM components like ^{12}C or ^{14}O that de-excite emitting γ-ray photons at specific energies.
- Cosmic-rays can also affect spacecrafts and space-based telescopes. A satellite like INTEGRAL is composed of several different materials, which are activated by the bombardment of cosmic-rays and produce secondary neutrons. These can be captured by most of the nuclei

in the spacecraft, forming new excited isotopes and radionuclides that de-excite and decay via one of the decay-modes described in Sec. 3.7, producing γ-photons at various energies.

- High-velocity ejecta from stellar explosions hitting the surrounding medium can also induce γ-ray emission due to nuclear excitations and spallation processes. The resulting products decay emitting characteristic γ-photons that may be detectable from γ-ray observatories for a nearby supernova remnant (Gómez-Gomar et al. 1998).

Inverse Compton effect

As the name of this process already states, Inverse Compton effect (IC) is the inverse of the Compton scattering and increases the energy of scattered photons instead of decreasing it. The excess energy comes from ultra-relativistic leptons. The higher their energy, the larger the energy they transfer on photons, so that practically photons of arbitrary energies can reach the γ-regime through this interaction, provided that the leptons colliding with them are energetic enough.

Other production mechanisms

There are several other production mechanisms of γ-rays, albeit not of high importance for γ-ray astronomy. Nuclear fusion and fission reactions liberate energy in the form of electromagnetic radiation, as a result of the higher binding energy of their end-products. The emerging radiation is of the order $\sim$ MeV and falls in the γ-ray band. As described in detail in Chapter 2, stars undergo nuclear fusion in their cores. The liberated binding energy is emitted in the form of γ-photons. However, the high densities in the stellar cores cause these γ-rays to diffuse and deposit their energy in their local environment. In nuclear power plants, γ-rays from the fission of fissile nuclei like ^{235}U or ^{239}Pu are converted to heat energy and ultimately to power.

Finally, γ-rays can also be produced thermally, provided that the temperature of the 'black-body' emitting them is high enough. Using Wien's displacement law $\lambda_{\max} = \mathrm{b} \cdot \mathrm{T}^{-1}$ and $\mathrm{E} = \mathrm{h} \cdot \mathrm{c}/\lambda$, one can derive that the spectral radiance of sources with temperatures $\mathrm{T} \geq 2.4{\times}10^{8}\mathrm{T}$ will peak in the γ-ray band. Slightly cooler objects can also emit a small fraction of their thermal radiation in the γ-ray band due to the high-energy tail of Planck's radiation law. Nevertheless, such temperatures can only be found in the cores of stars, where their diffusion length of the resulting γ-rays is too small to reach the surface and escape.

4. INTEGRAL, SPI and Data analysis

In the previous chapter, the production mechanisms and interaction types of γ-radiation and positrons were discussed. In order to receive and decipher successfully the 'messages' sent from cosmic events in form of massless 'energy packages' and thus understand the nature of various astrophysical phenomena better, it is crucial to construct robust and reliable telescopes, capable of detecting radiation from the most energetic part of the electromagnetic spectrum. However, detecting high-energy photons from space can be challenging as it is associated with fundamental problems.

To begin with, the opaqueness of the atmosphere turns the detection of extraterrestrial γ-ray signals on Earth impossible. This might be fortunate for the lifeforms on Earth, but at the same time it is inconvenient for γ-ray observatories, which must be mounted on balloons, rockets and satellites to get access to γ-radiation.

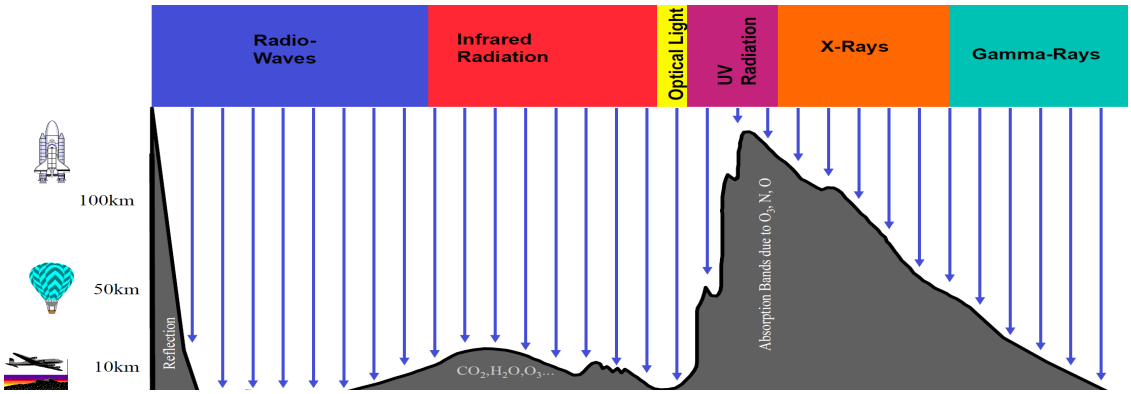

Figure 4.1.: A scheme illustrating the opacity of the atmosphere for different energy bands. Soft γ-rays ($E_\gamma \sim$ MeV) are not able to penetrate the atmosphere. However, at very large photon energies $E_\gamma \sim$ GeV, the atmosphere becomes transparent and allows the detection of γ-rays via Cherenkov telescopes (from Lecture: 'Observational Astrophysics', TUM).

Another problem arises due to the highly penetrable nature of γ-rays that makes their collimation by mirrors impossible. Therefore, to make a γ-ray telescope out of a γ-ray detector, very sophisticated configurations like coded-mask systems or multiple detector layers, are required. In addition, since cosmic γ-ray fluxes are very low and background counts extremely high, γ-ray spectra are typically subject to low statistics. Even the most powerful γ-ray line, the galactic positron annihilation line, emits only a few 10^{-3}ph/cm^2/s. Typical astrophysical sources do not exceed 10^{-5}-10^{-4}ph/cm^2/s (Diehl 2013). GRBs can be considered an exception, but as they are sudden events and their duration short, it is rather unlikely to spot them in time and analyze them spectroscopically.

Further issues are generated by the large intrinsic background, i.e. photons of non-astronomical origin that dominates γ-ray spectra. γ-ray detectors in space, as well as the entire structures carrying them, suffer from high fluxes of energetic radiation, such as cosmic-rays or the Van Allen radia-

tion belts surrounding the Earth. These energetic particles hit the spacecraft, activating thereby all materials onboard and produce secondary particles, radioactive nuclei and prompt γ-radiation. Most of the secondary products de-excite emitting γ-rays in the same energy range as the desired astrophysical targets. In fact, these unsought γ-photons surpass the majority of celestial signals by a factor of ~ 100.

High-energy astronomers and astrophysicists were able to circumvent most of the aforementioned technical and physical issues. In order to bypass the atmosphere, γ-ray detectors were mounted on balloons and satellites. To compensate for the low γ-ray fluxes, modern telescopes are built with large effective areas and the observation strategy involves long observation windows ($t_{obs} \geq$30 min). As mentioned above, to convert γ-ray detectors into γ-ray telescopes, the concept of coded-masks was introduced. These cast characteristic shadows on the detector plane that can be translated through complex algorithms into exact coordinates in the sky. Finally, in order to disentangle the intrinsic background from the true celestial sources, a precise background model that can predict the background counts for every energy channel and pointing accurately is of primary importance.

4.1. Detecting methods

One of the most fundamental problems in γ-ray astronomy is their high penetrability of the incident radiation; it is impossible to collimate γ-photons with mirrors or lenses and challenging even to stop them. In fact, γ-rays are detected rather indirectly through their secondary particles, like electrons and positrons, produced in one of the three interactions presented in Sec. 3.9. Thus, efficient MeV detectors are made out of relatively high-Z materials, able to stop incoming photons. In addition, they must be capable of collecting and processing the secondary particles produced through the primary interactions.
In modern high-energy astronomy, two different detector types are preferred, scintillation detectors and semiconductor (solid-state) detectors.

4.1.1. Scintillation detectors

The physical principle of scintillation is widely used in high-energy astronomy as one possibility to detect $\sim$ MeV γ-rays indirectly. Scintillators can be subdivided into three classes, depending on the material they are made of: Organic scintillators can be either in liquid or solid form and consist mainly of hydrocarbons. Next to organic scintillators also inorganic scintillating crystals like NaI, CsI, BGO, as well as noble gases like xenon, are widely used.

The main idea behind scintillation detectors is the following: When a high-energy photon interacts with a scintillating material, it excites electrons from the valence band to the conduction band, creating electron-hole pairs. After a finite time, these pairs recombine, emitting thereby a multitude of lower-energy photons, whose quantity is directly proportional to the energy of the incident photon. In order to produce efficiently secondary photons in the energy range of visible light and make both the excitation and de-excitation more probable, scintillating materials are usually doped (Hofstadter 1948). The low-energy secondary photons are then headed towards a photocathode, which, using the physical principle of the photoelectric effect, absorbs and converts them to electrons. Since the resulting signal is weak, the resulting electrons are multiplied to produce a detectable electronic signal in photomultiplier tubes (PMTs) or avalanche photodiodes (APDs).

Photomultiplier tubes are able to strengthen the signal produced by scintillation photons enough to become easily detectable e.g. by oscilloscopes. PMTs accelerate the emitted photoelectrons

toward successive electrodes, called dynodes, where progressively more electrons are freed. After passing several dynodes a large number of electrons reach the negatively charged anode producing an easily detectable current pulse.

A second option for multiplying a weak signal are APDs. They are semiconductors with a reverse bias voltage applied. The voltage gradient ensures that incoming electrons gain on the way to the cathode more kinetic energy, enough to free further electrons that on their turn kick more electrons free. The number of freed electrons grows exponentially resulting in an electron avalanche easily detectable by the read-out system.

Scintillation detectors have fast response times but are prone to energetic radiation and have typically low energy resolutions, due to the large band gap ($E_{Gap} \sim$ 4-9eV) that prevents a complete conversion of photon energy into electron-hole pairs. Thus, scintillators are not suitable for fine spectroscopy in space. In addition, organic scintillators are characterized by low densities that make them inefficient as γ-ray detectors, since interaction with incident radiation is not guaranteed. On the other hand, their fast response times make them efficient as anti-coincidence shields that encompass the actual γ-ray detector (Lichti and Georgii 2001). Inorganic scintillators like BGO have higher densities, being thus able to efficiently stop incomings photons, but their light yield and energy resolution is low. In order to fulfill all criteria for efficient γ-ray spectroscopy in space, semiconductor detectors are the best choice.

4.1.2. Semiconductror detectors

Semiconductor (or solid-state) detectors are based on the same physical principles as their early precursors, the ionization chambers. They have small band gaps ($E_{gap} \leq$ 1eV), which result in a higher number of electrons for an incident photon, improving the energy resolution by about one order of magnitude compared to scintillators.

The main working principle of semiconductor detectors shares several similarities to that of APDs. When a high-energy photon penetrates the detector volume, which is embedded between two electrodes, it creates several electron-hole pairs. Their number is proportional to the energy of the incoming photon (Knoll 2000). To make excitation even more probable, semiconductor detectors are usually doped with n-type materials, like lithium. A high voltage of 2-9kV between the electrodes forces both electrons and holes toward the electrodes, where they produce an electric pulse that can be measured with an outer circuit.

Semiconductor detectors are much denser than scintillation detectors, having thus a greater stopping power. Besides, they are relatively compact and their fast response times make them suitable for detection of γ-rays. In addition, their small band gaps (E_{gap}^{300K}(Ge)=0.67eV) lead to a higher probability of excitations and recombinations of electron-hole pairs and hence, to a better energy resolution. On the other hand, this physical property requires intense cooling, as electron-hole pairs can be created by thermal excitation even at room temperature.

4.2. Imaging methods

The above-mentioned detectors provide excellent energy resolutions and fast response times at the cost of insufficient information about the direction of the incident photon. In fact, early γ-ray missions were simply photon collectors with limited or non-existent angular resolution. In order to construct a γ-ray telescope with solid-state or scintillation detectors, more complex configurations

must be developed. Two of the most iconic γ-ray telescopes of the modern high-energy astronomy era used two different techniques to infer the direction of the incoming radiation: COMPTEL on CGRO was a Compton telescope, while SPI aboard INTEGRAL uses the coded-mask principle.

4.2.1. Compton telescopes

A Compton telescope takes advantage of the angle dependency of the Compton effect (for details see Sec. 3.9.2) to infer the celestial origin of the incoming photon. For this reason, two detector layers are required. The detector layer on top is made of a low-Z material that promotes an initial Compton scattering of the incident photon. The scattering interaction causes the photon to lose a fraction of its energy and change its direction by the angle θ. The latter can be calculated if the photon gets absorbed by a second, higher-Z detector layer deeper within the instrument. In order to identify the second interaction as the aftermath of the first, the delay time between the two interactions must match the time-of-flight between the two locations where the interaction took place. Each detector layer reports the energy deposited; the first layer measured the fraction of the photon energy deposited during the scattering process E_1, while the second layer the remaining photon energy E_2. Using these two values, the scattering angle θ can be determined via:

$$\cos(\theta) = 1 - m_e c^2 \left(\frac{1}{E_2} - \frac{1}{E_1 + E_2} \right) \tag{4.1}$$

Angle θ does not infer the exact origin of the photon but rather an event circle in the sky. Typical angular resolutions of Compton telescopes can reach $\sim$ 10arcmin at the cost of the energy resolution ($\sim$5-8% (FWHM)).

4.2.2. Coded-mask apertures

Another possibility to equip a γ-ray detector with imaging abilities is the coded-mask principle, applied on the spectrometer SPI aboard INTEGRAL.
In this imaging method, a mask consisting of several transparent and opaque blocks is positioned above the detector plane, as illustrated in Fig. 4.2. These blocks create a certain shadow pattern ('shadowgram') on the detector plane, which consists of several individual detectors to form a detector camera. By doing so, when a celestial source at a particular sky position irradiates the camera some detectors are completely shadowed, some are partly shadowed and some not shadowed at all. Changing slightly the orientation of the spacecraft causes the mask to cast its shadow on different detectors. This observation strategy is called 'dithering'. Using complex computer-based deconvolution algorithms (Caroli et al. 1987), it is thereby possible to determine the exact location of the source in the sky.

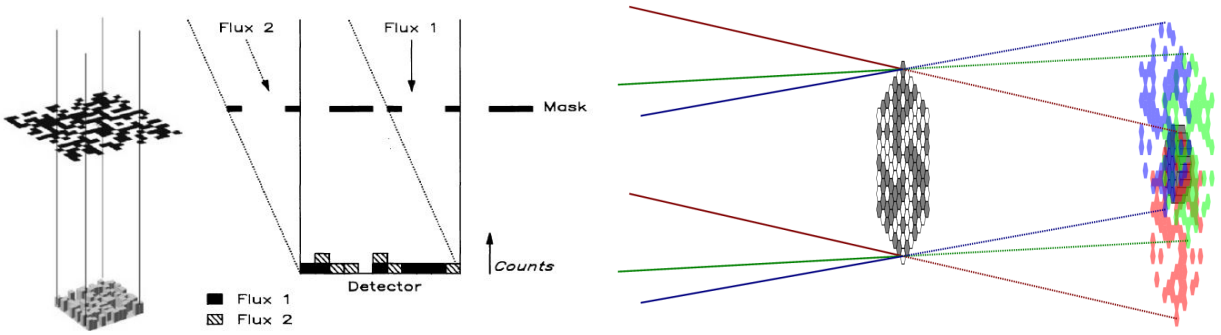

Figure 4.2.: Left: A scheme illustrating the working principle of a coded mask (Caroli et al. (1987)), Right: Shadowgrams of three point sources located at different celestial coordinates (Kretschmer 2013).

Coded-mask systems have large 'fully coded field of views' (FCFV). This is defined as comprising all directions for which the recorded flux is completely modulated by the mask. The 'partially coded field of view' (PCFV) on the other hand is defined as 'comprising al the directions for which only a fraction of the detected flux is coded by the mask' (Caroli et al. 1987).

The angular resolution of a telescope carrying a coded-mask system is characterized by three parameters: the separation l between the camera and the mask, the size m of the transparent elements and the size d of the opaque elements of the mask (Skinner 2004).

$$\Delta\theta = \sqrt{\left(\frac{\mathrm{m}}{\mathrm{l}}\right)^2 + \left(\frac{\mathrm{d}}{\mathrm{l}}\right)^2} \tag{4.2}$$

The separation l between mask and detector plane is limited, as it would lead to bulkier and heavier instruments and consequently to higher launch costs. The size of the mask elements cannot be arbitrarily small, as it would worsen the stopping efficiency of the mask. In fact, it was proven that the best imaging resolution is achieved if the transparent and opaque elements of the mask share the same size (m=d) (Skinner 2008). Typical angular resolutions of coded-mask γ-ray telescopes can reach a few degrees. Coded-mask systems have been very successful tools for determining the location of celestial sources and were therefore used on INTEGRAL, to combine the superb spectral resolution of SPI with imaging capabilities.

Choosing the right combination of materials for the detector array, the anti-coincidence shields, the mask, the electronic systems and further instruments on-board of an astrophysical laboratory in space requires careful consideration. Several additional parameters, like the choice of orbit, the exact position of the detector camera on the spacecraft and the distance between mask and detector can further affect the performance of the telescope. In the following section, the INTErnational Gamma-Ray Astrophysics Laboratory (INTEGRAL) and its spectrometer SPI, along with all physical concepts implemented to efficiently stop γ-radiation, to reduce background and to achieve a decent spatial resolution, are presented.

4.3. The INTEGRAL mission

On the 17^{th} of October 2002 the European Space Agency (ESA) in collaboration with the Russian Space Agency launched INTEGRAL from the spaceport of Baikonur, Kazakhstan.

INTEGRAL was considered the successor of the Compton Gamma Ray Observatory (CGRO), dedicated to fine γ-ray spectroscopy in the 15keV to 10MeV energy domain combined with accurate imaging of celestial γ-ray emission sources (Winkler et al. 2003). It was initially assigned as a two-year mission with possible extensions up to five years. However, its scientific successes, combined with the robustness of the instruments and the spacecraft granted several two-year extensions. In the year 2019, INTEGRAL still orbits the Earth and continues to eye the high-energy Universe.

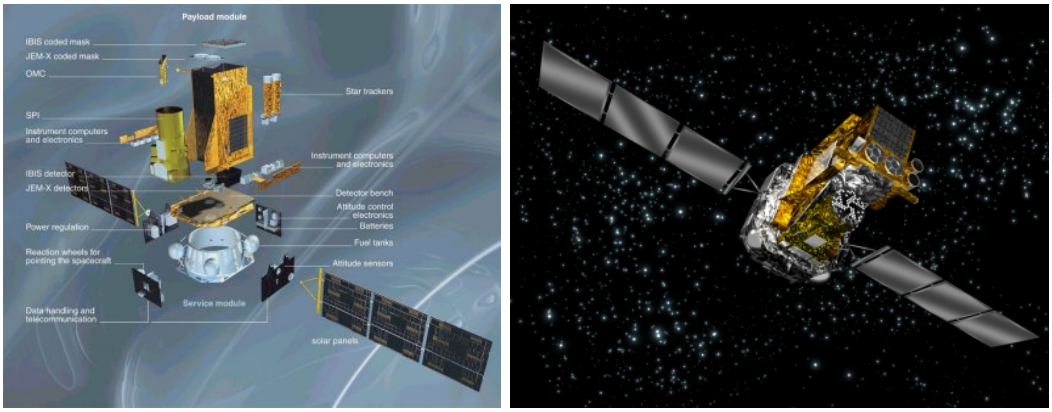

Figure 4.3.: Left: An overview of the components of INTEGRAL (from ESA). Right: An artistic impression of INTEGRAL, with the spectrometer SPI at the front (from ESA).

The launch took place from the spaceport of Baikonur, Kazakhstan, using a PROTON launcher of the Russian Space Agency. The rocket inserted INTEGRAL into a geosynchronous highly eccentric orbit, with an apogee of 153000km, a perigee of 9000km and a period of $t_{orbit} \sim 3$ days (Jensen et al. 2003). This orbit was chosen deliberately to provide long observation periods in stable background environments, away from the Van Allen radiation belts surrounding the Earth.

4.3.1. Instruments aboard INTEGRAL

INTEGRAL carries two main instruments sensitive in γ-rays onboard, the high-energy resolution spectrometer SPI and the imager IBIS. SPI and IBIS are accompanied by two monitoring instruments, the soft X-ray monitor JEM-X and the optical camera OMC. All four instruments are co-aligned, while the three of them targeting high-energy radiation are accompanied by coded masks.

Spectrometer SPI, the high spectral resolution γ-ray telescope of INTEGRAL, is sensitive to photons with energies between 20 keV and 8 MeV. The camera consists of 19 high purity germanium detectors and operates in conjunction with a coded-mask system that provides imaging capabilities. This work evaluates data from SPI and therefore a more detailed description of the instrument is found in Sec. 4.4.

Imager IBIS is the second major γ-ray instrument on board, optimized for high-angular resolution imaging (Ubertini et al. 2003). IBIS observes the γ-ray Universe in the energy range between 15keV and 10MeV. It uses a coded-mask system like SPI to gain information about the direction of the photons and, to operate at the same time as Compton telescope, it comprises two layers of detector arrays. The forward detector plane consists of 128×128 CdTe (cadmium-telluride) tiles accumulating a collecting area of $\approx 2600\text{cm}^2$. Below this detector plane, a second detector plane exists, made of 64×64 CsI (caesium-iodide) tiles with a total area of $\approx 2890\text{cm}^2$. A mask consisting of 95×95 tungsten tiles is situated 3.4m above the detector planes, providing a FCFV of 9°×9° and a PCFV of 19°×19°. The small size of the detectors, combined with the relatively large number of detector and mask pixels provides an excellent spatial resolution of $\sim$ 12 arcmin with a bright point source location below 1 arcmin. However, due to the small size of the detectors, IBIS loses in energy resolution ($\sim$ 10 % (FWHM)). A telescope with excellent spatial and decent energy resolution, like IBIS, is therefore optimal for observations of sources, whose spectrum is characterized by a γ-continuum, complementing by this way SPI, which focuses more on a high-resolution energy

spectrum and discrete lines.

The Joint European X-Ray Monitor (JEM-X) is one of the complementary instruments installed on INTEGRAL, sensitive in the energy range 3-35keV (Lund et al. (2003)). It is an X-ray monitor with an angular resolution of $\sim$ 3arcmin, an effective area of $\approx$500 cm^2 and a FCFV of 10°×10°. It consists of two co-aligned telescopes, both with their own coded masks, recording spectra in the energy range between 3 and 35keV.

The second complementary instrument on INTEGRAL is the Optical Monitoring Camera (OMC), a CCD (1024×1024 pixels) camera observing the optical counterpart of the targeted γ-sources. It has an angular resolution of 25 arcsec, a point source location of $\approx$ 6 arcsec and a field of view of 5°×5°.

4.3.2. Orbit

The orbit of INTEGRAL was chosen very carefully to minimize radiation damage caused by the Van Allen radiation belts surrounding the Earth. The belts consist of two main regions with intense radiation trapped by the Earth's magnetic field (Akasofu and Chapman 1961).

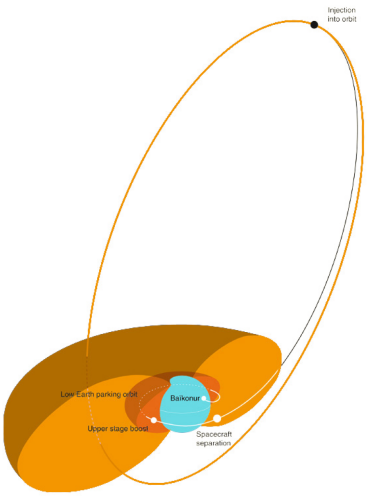

Figure 4.4.: INTEGRAL's eccentric orbit around the Earth, illustrated as a blue sphere. The orange toruses display the Van Allen radiation belts (from ESA).

The inner Van Allen belt is located 1.000-6.000km above the Earth and is characterized by high concentrations of energetic protons and electrons, trapped by its magnetic fields. The outer Van Allen belt contains mostly high energy electrons and is found at altitudes between 13.000km and 60.000km. Its width and particle density can fluctuate, depending on the activity of the Sun.

In order to minimize the passage through the radiation belts, whose particles can cause severe damage to all instruments, cables and electronics mounted on INTEGRAL, a highly eccentric orbit with an inclination of 52.5° in respect to Earth's rotational axis was chosen. With a perigee height of only 9.000 km and an apogee height of almost 154.000km (see Fig. 4.4), INTEGRAL initially needed $t_{\mathrm{orbit}} \approx 72$ hours to complete an orbit around the Earth (Jensen et al. 2003). In January 2015, the orbit was adjusted to 2 days and 16 hours (i.e. $t_{\mathrm{orbit}} \approx 64$ hours) as the first step toward a controlled re-entry in February 2029 (Diehl et al. 2018b).

INTEGRAL's orbit, however, does not bypass the radiation belts completely. To protect the instruments and minimize radiation damages, scientific observations cease at an altitude of 60.000km approaching the belts and commence after the spacecraft has left them behind, at an altitude of 40.000km. Consequently, only $\sim$ 10% of observation time is lost.

4.4. SPI

4.4.1. Main detector array

SPI is the spectrometer aboard INTEGRAL designed for high spectral resolution spectroscopy and the instrument used for the data analysis in this thesis. The core of the instrument consists of 19 high purity germanium detectors ordered in a compact hexagonal structure (illustrated in Fig. 4.5c), covering a geometrical area of 508cm^2. Each detector is numbered from 00 to 18, where 00 is the most central detector (see Fig. 4.5d). In order to create detectors out of hexagonal blocks (side length=3.2cm, height=69.42mm) of Ge, the latter were n-doped and placed inside aluminum capsules. To minimize the distance the holes must cover toward the electrode and avoid thereby possible hole trapping, an external high voltage of 4kV was selected across the detector plane, transforming the Ge blocks into reverse-biased n-type detectors. In order to achieve the best possible energy resolution for γ-ray spectroscopy, an active cryogenic system with the goal to minimize thermal activation was applied. Hence the detector array is cooled down to 85-90K, while in operation. This results in a spectral resolution of 2.5keV at 1.33MeV that depends, however, on the energy of the incident photon (Vedrenne et al. 2003).

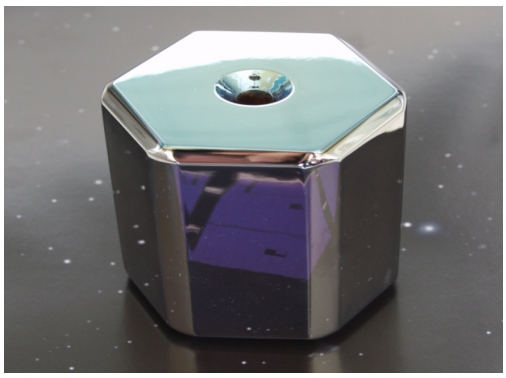

(a) One of the nineteen Ge detectors of SPI

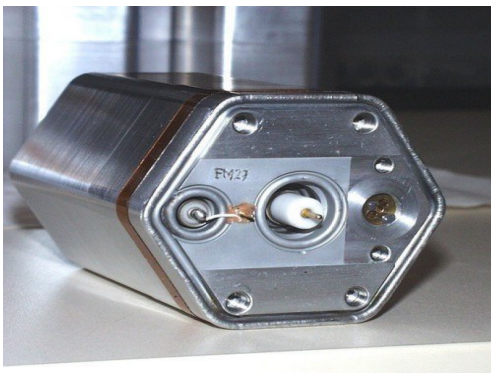

(b) A Ge detector encapsuled and wired

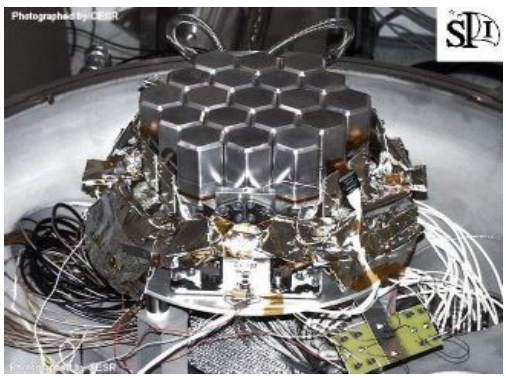

(c) The complete detector array of SPI

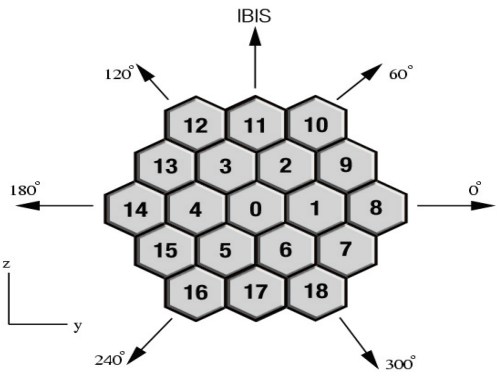

(d) A drawing with the detector numbering

Figure 4.5.: The camera system of SPI (from SPI team).

4.4.2. Coded mask system

SPI is able to image the sky in conjunction with a coded-mask system, mounted 1.71m above the detector array. The 0.72m wide coded mask consists of 127 hexagonal elements, arranged in a particular pattern with 120° symmetry (for details see Fig. 4.6a) . 63 elements of the mask are made of 3cm-thick tungsten and block the penetration of γ-rays, while the remaining 64 elements are transparent. The dimensions of the mask provide a FCFV of 16°×16°, a PCFV of 31°×31° and a spatial resolution of 2.5° and a positioning accuracy of 10arcmin (Vedrenne et al. 2003).

4.4.3. Background reducing systems

As previously stated, the continuous bombardment of energetic cosmic rays activates the materials of the spacecraft, producing secondary neutrons, β-particles and γ-ray photons. These may hit the detector plane from undesirable directions, producing an artificial signal. In order to avoid this, several background reducing components were installed on SPI, fortifying it against undesired radiation.

Anticoincidence shield ACS

The most important background reducing system of SPI is a heavy hexagonal anticoincidence shield (ACS). It consists of 91 scintillating BGO (bismuth germanate, chemical formula: $Bi_4(GeO_4)_3$) crystals surrounding SPI in every direction except for the actual field of view, for a total volume of $\approx 790\text{cm}^3$ and an additional mass of 512 kg. Each BGO crystal is viewed by two photomultipliers that trigger a veto signal, whenever a photon interacts with the ACS. For a short amount of time the Ge detectors do not record registered photons, as they have probably penetrated the telescope from the side. Although the ACS lacks any spectral or directional information about the incoming radiation, its fast response time combined with the large surface can be useful in detecting GRBs (Lichti and Georgii 2001; von Kienlin et al. 2003).

The anticoincidence shield registers an enormous amount of background hits ($\sim$ 66000 counts/s, depending on the solar activity, the distance to the radiation belts, possible solar flares, etc.) and reduces the recorded background by a factor of 20-25 (Roques et al. 2003; Jean et al. 2003). Being, however, one of the most massive structures on INTEGRAL, it produces itself a considerable flux of background photons, which affects most severely the outer detectors.

Plastic scintillator PSAC

Another background reducing system implemented for SPI is the plastic scintillator anticoincidence subassembly (PSAC). As the name states, it is a circular plastic scintillator placed just below the mask, with the goal to reduce the background at the 511keV line (Jean et al. 1997). The scintillator is 5mm thick, has a diameter of 0.80m and is monitored by four photomultipliers. In contrast to Monte Carlo simulations that indicated a significant background reduction at 511keV, in-flight tests have shown that the reduction of the background in the proximity of the 511keV line is only about 5% (Roques et al. 2003).

Pulsed shape discrimination electronics PSD

The inspection of the pulse shape can be considered the final selection test for recorded events in the Ge detectors. The idea behind this background reducing mechanism is based on the physical fact, that β-particles and photons interact in a different manner with Ge detectors. β-particles, penetrating a Ge detector, deposit their energy within a few mm, whereas γ-ray photons interact

multiple times via Compton scattering before their energy is completely absorbed. As a consequence, the former produces a single sharp pulse in the pre-amplifier, whereas the latter yield significantly broader pulse shapes.

The PSD electronics aim to reduce the instrumental background in the 200-2000keV energy band, by rejecting detector events triggered by β-particles (Vedrenne et al. 2003). Pre-launch simulations indicated that employing this background reducing system would improve the sensitivity of the instrument by a factor of two. However, in-flight tests showed that the fraction of β-events in this energy range is lower than predicted, reducing the sensitivity gain to 10-30%.

4.4.4. Cooling system

Ge detectors must be permanently cooled down to T$\approx$ 90K to minimize the creation of electron-hole pairs. Furthermore, a low detector temperature would also slow down the damage caused by energetic radiation and, therefore, maintain the detector array in a better condition.

The cryostat applied for the cooling of SPI, contains four mechanical Stirling coolers located on an external radiator next to the detector plane. The latter is enclosed in a beryllium structure that works as a heat isolator, called the Cold box. Several precautions were taken to minimize the thermal leakage and the microphonic noise between the detector plane and the main body of the cryostat. A second task of the cryostat is to provide the necessary heat for the detector annealing, a detector restoring procedure discussed in Sec. 4.4.5. In overall, the cooling system of SPI operates well within expectations, fulfilling its scientific tasks.

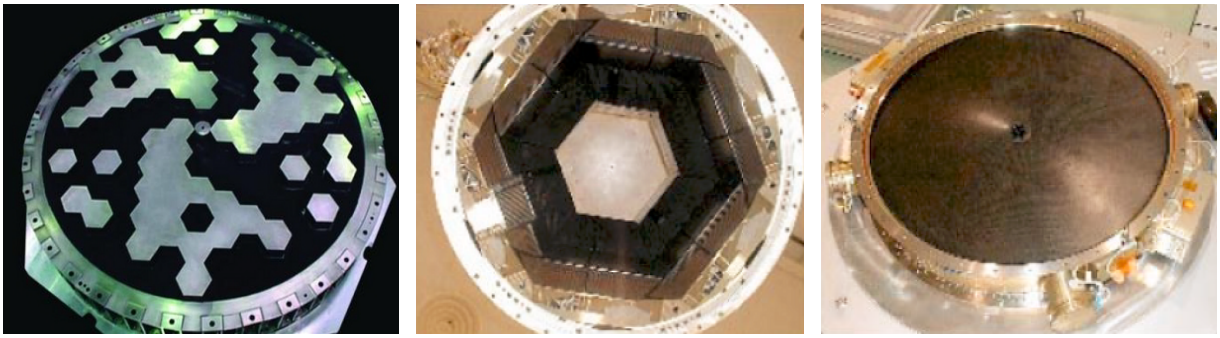

(a) The coded mask of SPI (b) ACS blocks (c) PSAC

Figure 4.6.: Several subsystems of SPI (from SPI team).

4.4.5. After launch performance

INTEGRAL was launched on the 17$^{\text{th}}$ of October 2002 from Baikonur in Kazakhstan and the first nine months of operation were dedicated to the evaluation of the performance of all subsystems, as well as the calibration of the instruments and the determination of several fundamental properties of the telescope.
In summary, all subsystems of SPI operated nominally after launch, in concordance with theoretical predictions and pre-launch tests. The efficiency of a few background reducing systems and consequently the strength instrumental background and the sensitivity of the instrument were more optimistic than they actually.

Detector annealing

As expected, the continuous bombardment of cosmic radiation and the regular passage through the Van Allen radiation belts not only activate the materials of the spacecraft, producing background emission but also cause serious damage to the detector array. In particular, high-energy particle collisions damage the (nearly) perfect lattice structure of Ge, producing additional hole traps and vacancies. They hinder in turn a complete collection of the charged particles created in the detector body, which results in a gradual worsening of the energy resolution. The effects of detector degradation accumulate over time and can substantially worsen the performance of the instrument already within a few months.

The detector degradation effect was expected and as a countermeasure, a detector restoring procedure called 'annealing' was implemented for the first time on a γ-ray mission. SPI's detectors are thus heated twice a year to 105°C for typically two weeks, to remove internal vacancies or interstitials and reform the perfect crystal lattice of the Ge. The annealing process restores the quality of the Ge lattice, purging it of all defects caused by cosmic radiation.

Detector failures

Unfortunately, during INTEGRAL's sixteen-year journey in space, four out of nineteen detectors received irrevocable damage during particular perigee passages and ceased recording data. Consequently, they were switched off and do not contribute any more in the scientific objectives of the instrument, reducing slightly its performance in terms of spatial resolution and sensitivity.

Detector 2 was the first detector to fail in December 2003 (revolution 140), detector 17 followed in July 2004 (revolution 215), detector 5 failed in September 2009 (revolution 776) and detector 1 in May 2010 (revolution 930). This led to the establishment of SPI epochs; epoch 1 comprises all revolutions with 19 working detectors, epoch 2 with 18 working detectors, epoch 3 with 17 working detectors, etc. Since both targeted supernovae explosions in this thesis were detected after the last detector failure, the camera configuration during the supernova observation consisted of fifteen instead of nineteen detectors.

Parameter	Value
Energy range	20keV-8MeV
Energy resolution	2.1keV at 511keV; 2.5keV at 1.33MeV
Narrow line sensitivity (3σ)	5×10^{-5}ph cm^{-2}s^{-1} (at 511keV)
Continuum sensitivity (3σ)	1.5×10^{-6}ph cm^{-2}s^{-1} keV^{-1} (at 511keV)
Angular resolution (FWHM)	2.5°-2.7°
Positioning accuracy	10 arcmin
Fully coded field of view	16°×16°
Partially coded field of view	31°×31°
Detector size (size × thickness)	3.2cm × 6.94cm
Detector area (geometric)	508cm^2
Detector area (effective)	10cm^2-100cm^2
Total mass	1228kg

Table 4.1.: SPI instrument characteristics (Jean et al. 2003; Siegert 2017)

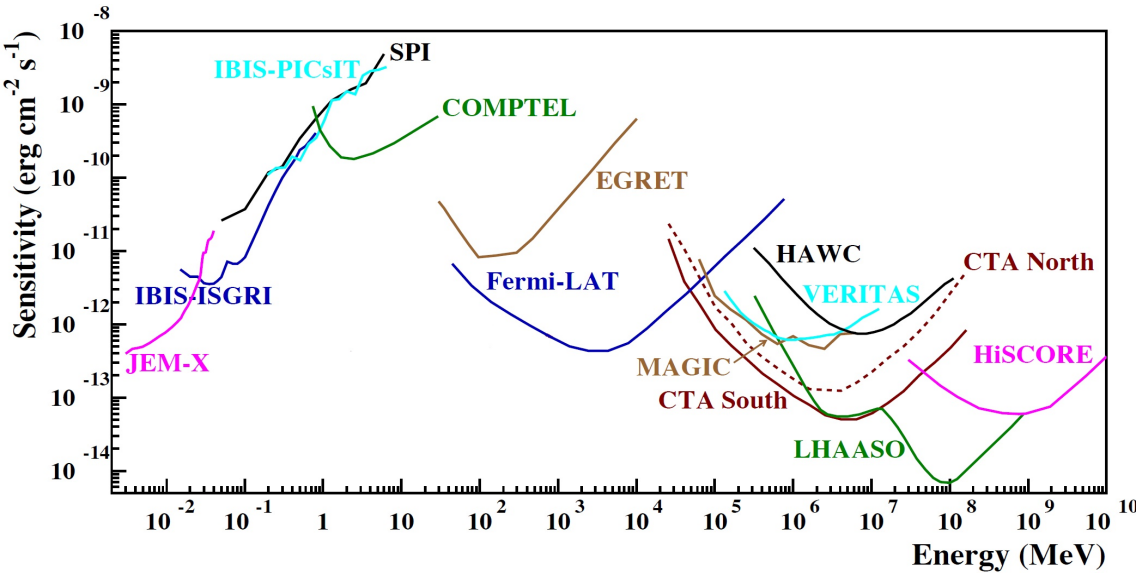

Figure 4.7.: INTEGRAL's sensitivity compared to other ground-based and space-borne γ-telescopes (after De Angelis 2018).

4.5. SPI primary data and spectral response

When a photon interacts with one of the nineteen Ge detectors, a germanium detector event is registered. In the case, however, that the event falls within the time window of a veto-signal coming from an anticoincidence shield (t=725ns), the event is rejected as a potential background interaction. For valid events, the time of the trigger, the signal pulse height of the event and the detector identity are provided by the front-end electronics. If an adjacent detector records a second signal within the coincidence time window of 350ns, a multiple event is registered, both pulse heights are added and its properties are noted as well in a so-called ' multiple event'. For both single and multiple events, a pulse shape discrimination test is performed, to check whether the interaction originates from a photon or a β-particle. Finally, the event is assigned to an energy channel according to its electronic pulse height. The whole photon processing lasts 26μ.

A first-order energy calibration is performed at INTEGRAL's Science Data Centre, by fitting Gaussian lines on six strong isolated lines of the raw spectrum. The relation between energy E [keV] and pulse height p is given by:

$$\mathrm{E} = \mathrm{c}_1 \frac{1}{\mathrm{p}} + \mathrm{c}_2 + \mathrm{c}_3\mathrm{p} + \mathrm{c}_4\mathrm{p}^2 \tag{4.3}$$

This turns a count histogram into a γ-spectrum.

The shortest observation interval of SPI lasts $\sim$ 30min and is called 'pointing'. During a pointing, the telescope is oriented toward a particular sky direction. Typically, the observation strategy of INTEGRAL involves 25 pointings, arranged in a 5×5 grid around the targeted object. After each pointing, the telescope is reoriented by 2.1°. This bears several advantages for the data analysis, as it creates an additional modulation of the sky signal on the detector plane, due to the altering shadowgrams cast by the mask.

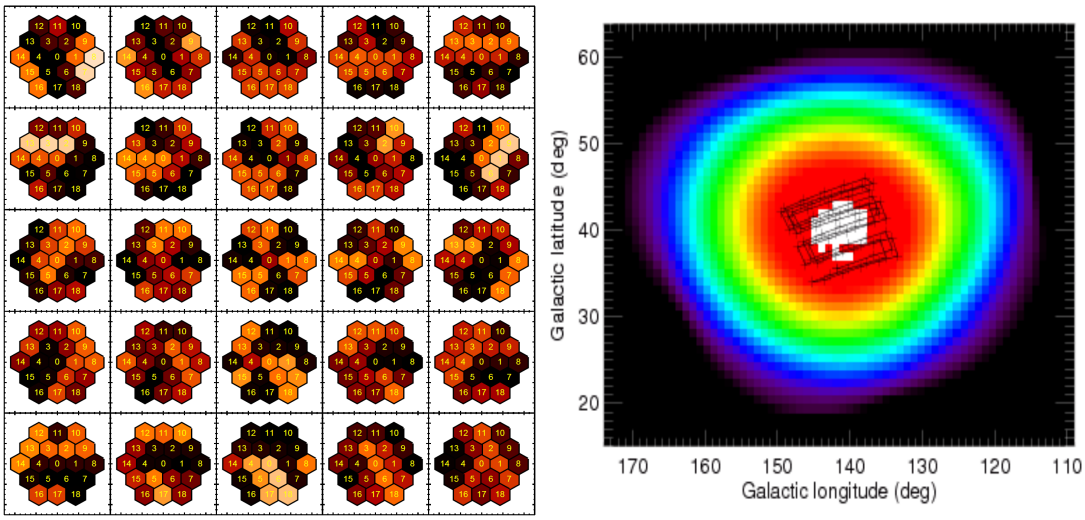

Figure 4.8.: Left: The effect of dithering on the detector camera. The received intensity measured by each detector is color-coded from black (completely shadowed) through red, yellow (partially shadowed) to white (fully exposed). From Diehl et al. 2018b. Right: The dithering of SPI around point source SN2014J ((l,b)=(141.427°, 40.558°)) in revolution 1393 (from INTEGRAL house keeping page).

The modulation of relative counts among detectors, seen in Fig. 4.8 only affects celestial photons and is hence one of the keys to disentangle celestial from background-induced events. However, despite the relatively long duration of single pointings, and the large field of view of SPI, very few celestial photons are expected for typical γ-sources with intensities of the order of $\sim 10^{-5}$ph/cm^2/s. The low number of celestial photons is not reflected in the raw spectra.

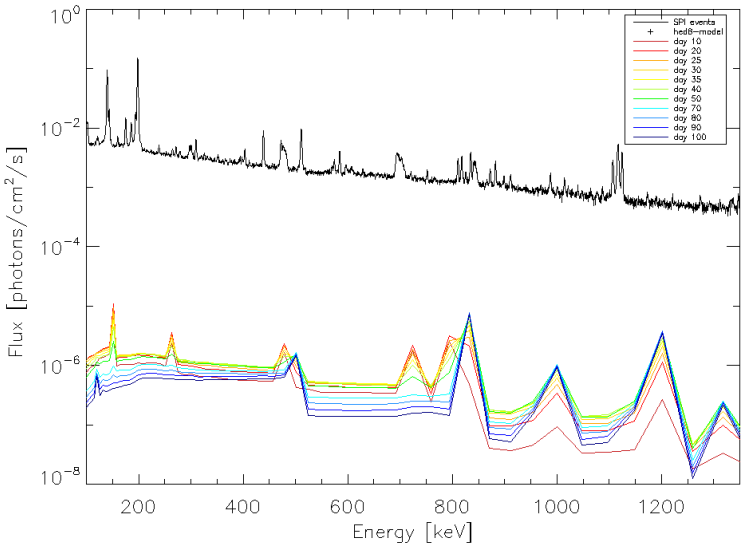

Figure 4.9.: Comparison between the background dominated flux recorded by SPI and a representative type Ia supernovae emission at 3.5Mpc calculated by The and Burrows 2014 for various times after the explosion.

Fig. 4.9 displays a first-order comparison between a typical spectrum recorded by SPI and a representative model spectrum of a type Ia supernova model at a nominal distance of 3.5Mpc. Even at the energies of the strongest emission lines of ^{56}Co and ^{56}Ni, the background events prevail

by $\sim$ 2-3 orders of magnitude. Typical continuum emission of $\sim 10^{-6}$ph/cm^2/s/keV is even more difficult to detect.
As already introduced in Sec. 4.4.3, space-based telescopes suffer from the continuous bombardment of cosmic rays. These energetic particles of various origins have a continuous energy spectrum covering the complete γ-domain. At energies approaching typical nuclear excitation energies, interaction cross sections reach their maximum, affecting instruments measuring MeV photons the most (Diehl et al. 2018a). This explains the decreased sensitivity in this domain (for a comparison to other γ-ray instruments designed for higher γ-energies see Fig. 4.7).

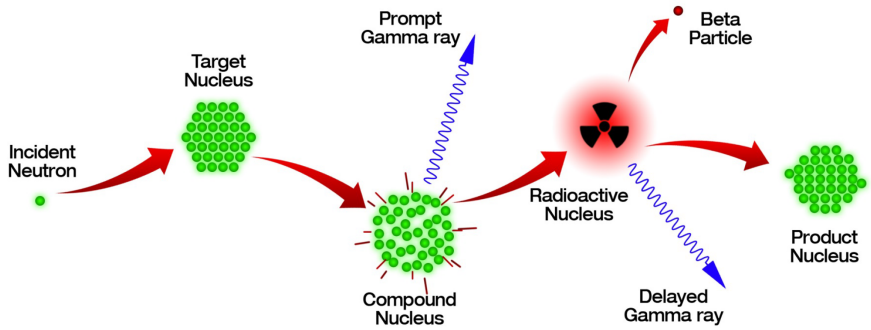

Figure 4.10.: Scheme of possible processes triggered through a secondary neutron in the interior of INTEGRAL (from Siegert 2017).

Energetic particles hit the spacecraft and trigger several activation processes, producing secondary neutrons, prompt de-excitation emission and radioactive isotopes. The neutrons can be captured by all structures of the spacecraft producing further unstable nuclei that de-excite either with prompt or delayed radiation processes, mainly in the MeV domain. If the resulting photons manage to bypass the protective shields of SPI, they are registered as legit celestial photons. The variability of the background emission, due to fluctuations of the cosmic-ray flux, poses further difficulties.

Generally, the events recorded by SPI are analyzed in histograms that count events per data space bin $\mathrm{d}_{i,j,k}$, where the indices i,j,k represent the pointing, j the detector and k the energy bin.

$$\mathrm{d_{i,j,k}} = \sum_{\mathrm{gl,gb}} \mathrm{R^{gl,gb}_{i,j,k}} \sum_{\mathrm{n=1}}^{\mathrm{N_s}} \theta_{\mathrm{s}} \mathrm{S^{gl,gb}_{n;i,j,k}} + \sum_{\mathrm{n=N_s+1}}^{\mathrm{N_s+N_b}} \theta_{\mathrm{b}} \mathrm{B_{n;i,j,k}} \tag{4.4}$$

These can be subdivided in celestial and background counts. In particular, the first part of Eq. (4.4) refers to celestial counts and the second part to background counts. $\mathrm{d_{i,j,k}}$ describes the photon counts in energy bin i, detector j and pointing k. It consists of photons from both cosmic and background sources. The first part of the sum refers to celestial counts and the second part to background counts. $\mathrm{S^{gl,gb}_{n;i,j,k}}$ denotes the sky sources, $\mathrm{B_{n;i,j,k}}$ the background sources and $\mathrm{R^{mn}_{ijk}}$ refers to the instrumental response function, which is relevant only for celestial photons that pass through the coded mask system and cast a shadow on the detector array. The sums over the celestial and background sources allow the contribution of several celestial and background sources. The galactic longitude and latitude are described by the indices gl and gb, respectively. Finally, parameters θ_s and θ_b describe the intensity of the celestial and background sources. They are obtained by fitting an expected background model and an expected sky model to the measured counts. Especially θ_s is of particular interest since it describes the intensity of the celestial source.

The concept of 'fitting' is of vital importance for the correct analysis of γ-ray data and requires a fundamental understanding of its mathematical principles, presented in the following section.

4.6. Statistical methods and modeling of data

In modern astronomy the most appropriate procedure to derive physical conclusions from a given set of N data points y_i, is by fitting a model described by M parameters $y(x_i)=y(x,a_1...a_M)$ to the data set and adjust the parameters to reach maximum agreement. The agreement between data and model is described mathematically by a so-called figure-of-merit function, which is structured in such a way that a small value represents close agreement. However, data recording is subject to statistical and measurement errors, leading to the fact that no model describes the data perfectly. In this context, an indicator of the goodness-of-fit and the likely errors of the best-fitted parameters are required to evaluate whether a particular model is appropriate or not.

The most reliable and easy-to-use procedure providing this information is the maximum likelihood method. Its goal is to reveal the parameter set, for which the probability that the data could have occurred is maximal. The probability that must be maximized is represented by a product of probabilities of each data point:

$$P \propto \prod_{i=1}^{N} \left\{ \exp\left[-\frac{1}{2}\left(\frac{y_i - y(x_i)}{\sigma}\right)^2 \right] \Delta y \right\} \tag{4.5}$$

In Eq. (4.5), Δy, σ and N are constants that allow to reduction of the expression to:

$$\chi^2 = \sum_{i=1}^{N} \frac{(y_i - y_{x_i})^2}{\sigma_i^2}, \tag{4.6}$$

widely known as 'chi-squared'. χ^2 must be minimized in order to obtain the maximum likelihood estimate of model parameters.
The choice of the minimization technique, depends on the linearity of the model. For linear models, it suffices to calculate the partial derivatives of χ^2 and set them zero:

$$0 = \frac{\partial \chi^2}{\partial a_{1...M}} \tag{4.7}$$

Depending on the number M of parameters, a system of M linear equations must be solved to obtain the maximum likelihood values for $a_{1...M}$.
Their errors can be calculated using:

$$\sigma^2_{a_{1...M}} = \sum_{i=1}^{N} \sigma_i^2 \left(\frac{\partial a_{1...M}}{\partial y_i} \right)^2 \tag{4.8}$$

For non-linear models, like Gaussian functions, an iterative optimization algorithm called 'gradient descent' is preferred. This procedure calculates an initial χ^2-value using parameter guesses, then builds the gradient of χ^2 and moves in the direction of the negative gradient, i.e. toward the minimum of the gradient. After several iterations, the desired local minimum and its corresponding parameters are determined. For instance, in the case of a function with two parameters, the algorithm can be presented by Eq. (4.9)

$$\chi^2(\alpha_{i+1}, \beta_{i+1}) \approx \chi^2(\alpha_i, \beta_i) + \nabla\chi^2(\alpha_i, \beta_i) \tag{4.9}$$

The program *curvefit*, used in the entire thesis for fitting γ-ray spectra, uses a very similar fitting method. To evaluate the goodness of a fit, indicator χ_{red}, defined as:

$$\chi^2_{\mathrm{red}} = \frac{\chi^2}{\nu}, \tag{4.10}$$

where ν=N-M are the degrees of freedom, must be approximately one. To test the statistical significance of a model m, a χ^2 comparison with the zero hypothesis is desired. If $\Delta\nu$=1, the statistical significance in units of standard deviation σ is given by:

$$\Delta\chi^2 = \sqrt{\chi^2_{0\mathrm{hyp}} - \chi^2_{\mathrm{m}}} \tag{4.11}$$

Eq. (4.11) gives the probability to reject the null hypothesis. For instance, $\Delta\chi^2 = 1\sigma$ allows the rejection of the zero hypothesis with 68.3%, $\Delta\chi^2 = 2\sigma$ with 95.4% and $\Delta\chi^2 = 3\sigma$ with 99.73% respectively. This quantity is of particular interest in this thesis for evaluating the statistical significance of the observed γ-lines from ^{56}Ni and ^{56}Co.

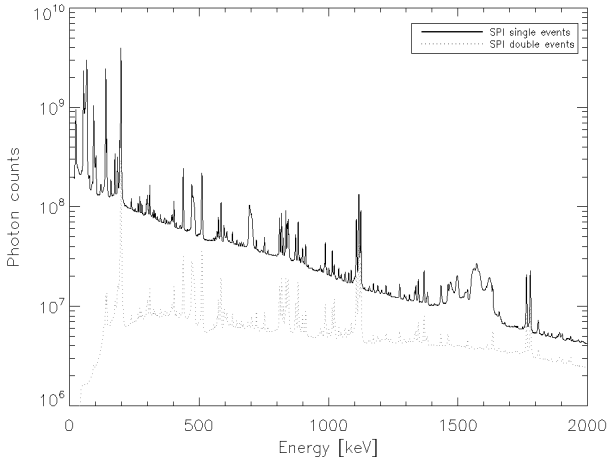

(a) Mission integrated SPI spectrum

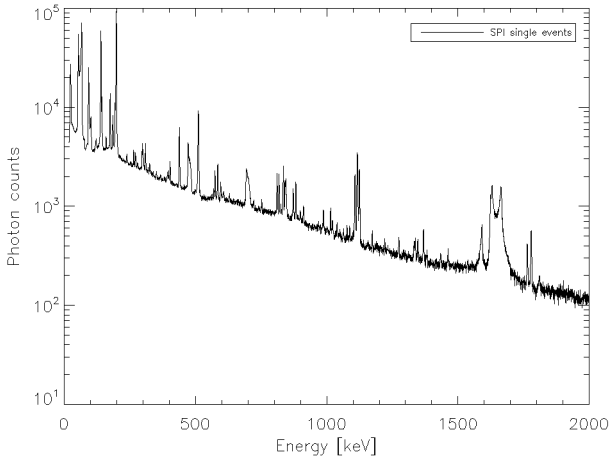

(b) Spectrum of orbit 1380, detector 0

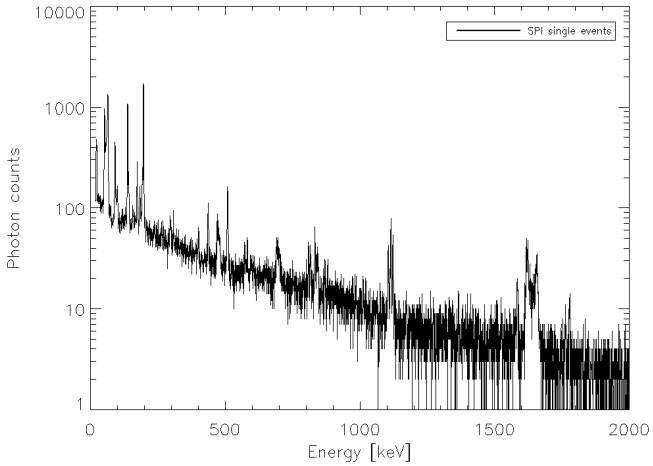

(c) Spectrum of orbit 1380, detector 0, pointing 1

Figure 4.11.: SPI spectra of 20-2000keV. Left: The mission integrated spectrum (orbits 43-2088). The faint grey slope displays the multiple events. Their contribution becomes important with increasing energy. Right: Integrated spectrum of orbit 1380 recorded by detector 0. Bottom: Recorded spectrum of the first pointing in INTEGRAL's SN2014J campaign by detector 0.

Fig. 4.11 displays typical raw spectra obtained by SPI in three different accumulation times. Generally, the spectrum can be described by a multitude of narrow instrumental γ-ray lines on top of a continuum with the shape of a power-law[1].

While the former originate from discrete nuclear reactions of specific nuclei on the spacecraft, the latter is the result of bremsstrahlung emission from secondary particles and Compton tails[2] of higher energy photons. In panels (a) and (b) even the weakest background features are distinguishable from the continuum, but the same cannot be stated for panel (c), clearly reflecting that spectra of individual pointings are statistically limited. In particular, the histogram counts $\mathrm{d}_{i,j,k}$ introduced in Eq. (4.4), consist of celestial and background events and are therefore subject to the Poisson statistics.

$$\mathrm{P(d,m)} = \frac{\mathrm{m^d exp(-m)}}{\mathrm{d!}} \tag{4.12}$$

Eq. (4.12) reflects a probability distribution. It describes the probability that d events occur in a specific interval of time if these events occur independently at a known constant rate m. Counting photons can be considered an independent process and is described accurately by the Poisson distribution.

Hence, simple background subtraction is not appropriate to derive celestial spectra and fitting both the intensity of the celestial sources as well as the background is the correct treatment of γ-ray spectra. To extract the faint celestial emission from heavily background-dominated data, though, a punctilious analysis of all background aspects and a detailed understanding of the properties, the origins and the time evolution of instrumental lines are necessary.

4.7. Background model for SPI

The goal for a background model designed for SPI is to estimate accurately the number of counts per energy bin, pointing and detector originating from non-celestial sources. Throughout the lifetime of INTEGRAL, several distinctive background models were applied on SPI data. A first-order estimate of the background contribution is to observe an area in the sky with no (known) celestial sources, for example at latitudes $b > \pm 30°$. However, as will be shown in the following subsections, photon counts show large temporal variations even in the time scale of subsequent pointings. In addition, the spectral response of SPI changes after each passage through the radiation belts, limiting thus the applicability of this approach. To overcome this issue, the subsequent idea was to predict the temporal evolution of the instrumental background in correlation with instrumental 'tracers' (Vedrenne et al. 2003; Wang et al. 2009). These are count rates of the protective shields or the detectors, e.g. the ACS rate and the saturated events in the germanium detectors GeSatTot[3]. Their advantages lie on their proportionality to the ambient strength of the energetic particle flux and on their superior statistics, due to their large number of counts. Empty field observations are often rescaled using these tracers and used to describe the background in subsequent observations. Their proportionality factor is fitted on the data leading to fairly good descriptions of the instrumental background. However, this method is insensitive to long term variations as radioactive build ups in the structures of the spacecraft or detector degradation (Jean et al. 2003).

[1] The broad feature between 1400-1700keV is considered electronic noise. Other asymmetric features are the result of several closely spaced de-excitation lines, called 'line blends'.

[2] These are photons that deposited only a part of their energy in the detector array through a single Compton scattering.

[3] A saturating Ge event, is an event registered in the germanium detectors, whose energy exceeds 8MeV.

Another approach is based on modeling the instrumental background, treating thereby correctly the instrumental set-up and the radiation environment, as well as implementing all relevant interaction physics. Background modeling in space-borne germanium spectrometers has been studied extensively in the last decades, motivated by the first balloon experiments carrying Ge spectrometers (Gehrels 1985). Several SPI-specified studies were performed before launch, to optimize the properties of the telescope, as well as after launch to analyze the first produced spectra (Jean et al. 1996, Weidenspointner et al. 2003). However, most simulations fall short at explaining accurately the continuum emission, due to shortcomings in specific interactions, like neutron capture reactions, or the contributions from β-decays.

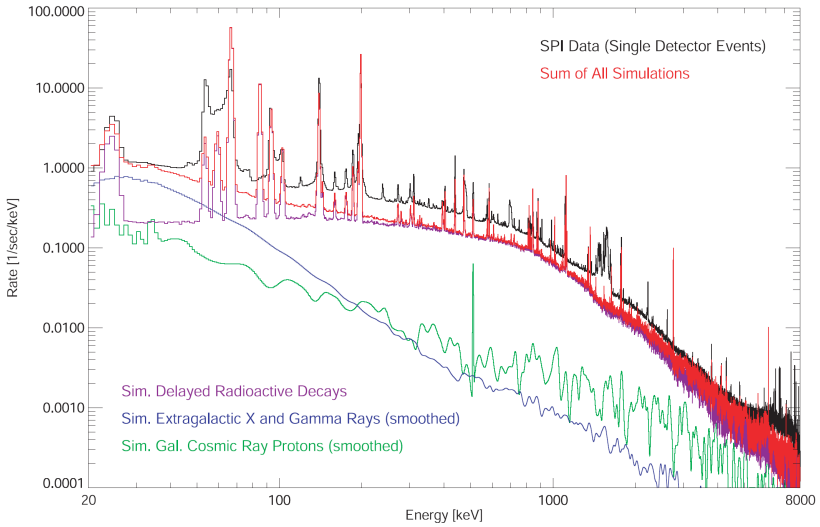

Figure 4.12.: Comparison of a simulated SPI spectrum (red slope) with a raw spectrum obtained during an empty field observation in revolution 13 (black slope). From Weidenspointner et al. 2003.

4.7.1. Current background model

The inadequacy of physical models to describe the background intensity of SPI accurately motivated an empirical background model, developed by Siegert 2013 and used in this thesis for the generation of celestial spectra. This analysis describes the instrumental background of SPI in a self-consistent manner, taking advantage of the instrument's longevity. In particular, by combining data from broad energy ranges and sufficiently long time periods, the spectral response of the instrument and its variation over time and energy is determined precisely. This allows the reduction of underlying systematics and thus the correct modeling of the background features of SPI.

In summary, the treatment exploits the differences in the behavior of celestial and background photons to distinguish between the two signals. The physical assumptions for this analysis approach can be revised as:

1. Celestial photons pass through the mask and contribute to the counts only of non-shadowed detectors, dictated by the imaging response function of the instrument.

2. The background sources of SPI have constant origins. This implies that the relative background intensities between detectors for a particular isotope are constant over time, and independent of the sky direction, where SPI is pointed to. In addition, the spectral shapes of background features remain constant on the time scale of one orbit.

Although the relative background intensities of the background sources are constant over time, the background pattern for single 0.5keV-wide energy bins is not constant, because Ge detectors degrade over time, each of them at its own distinctive rate, causing deviations in the fluxes of single energy bins. Only the relative flux of whole background lines can be considered constant over time. In addition, it is impossible to distinguish the fraction of an instrumental line and the fraction of the instrumental continuum from a single energy bin. Thus, the crucial information required to describe accurately the background and derive the celestial spectrum of a source are the background detector patterns of the instrumental continuum and all instrumental lines as a function of energy and time.

The first step toward the construction of the self-consistent background description is to cut the all-mission spectrum depicted in Fig. 4.11a in smaller bands with a width of $\sim$ 100keV and model them with several distorted Gaussian lines superimposed on a power-law-like continuum.

$$\mathrm{F(E)} = \mathrm{C(E;}\,\alpha, \mathrm{c_0}) + \sum_{\mathrm{i}} \mathrm{L_i(E;\,A_{0,i}, E_{0,i}}, \sigma_{\mathrm{i}}, \tau_{\mathrm{i}}) \tag{4.13}$$

The power law function (Eq. (4.14)) is normalized at the center energy E_m of interest and further described by the index α and the constant scaling factor c_0. The Gaussian lines are modeled with regular Gaussian functions (Eq. (4.15)), convolved with an one-sided exponential tail (Eq. (4.16)), to account for the continuous process of detector degradation:

$$C(E;\alpha, c_0) = c_0 \left(\frac{E}{E_m}\right)^a \tag{4.14}$$

$$G(E;E_0,\sigma) = A_0 \exp\left(-\frac{(E-E_0)^2}{2\sigma^2}\right) \tag{4.15}$$

$$T(E,\tau) = \frac{1}{\tau}\exp\left(\frac{E}{\tau}\right) \tag{4.16}$$

$$\begin{aligned} L(E;A_0,E_0,\sigma,\tau) &= (G \otimes T)(E) \\ &= \sqrt{\frac{\pi}{2}}\frac{A_0\sigma}{\tau} exp\left(\frac{2\tau(E-E_0)+\sigma^2}{2\tau^2}\right) \\ &\times erfc\left(\frac{\tau(E-E_0)+\sigma^2}{\sqrt{2}\sigma\tau}\right) \end{aligned} \tag{4.17}$$

Fitting the all-mission spectrum with Eq. (4.13) delivers well-determined parameters, even for faint lines; a direct consequence of the excellent statistics accumulated over sixteen years. However, as will be shown in the following subsections, the spectral response of the instrument changes significantly throughout the mission, as a consequence of detector degradation, cosmic-ray flux variations, solar activity and radioactive build-ups. The all-mission spectrum is thus the averaged-out response of the instrument throughout the fifteen years and fails in describing the exact background shape in every revolution precisely.

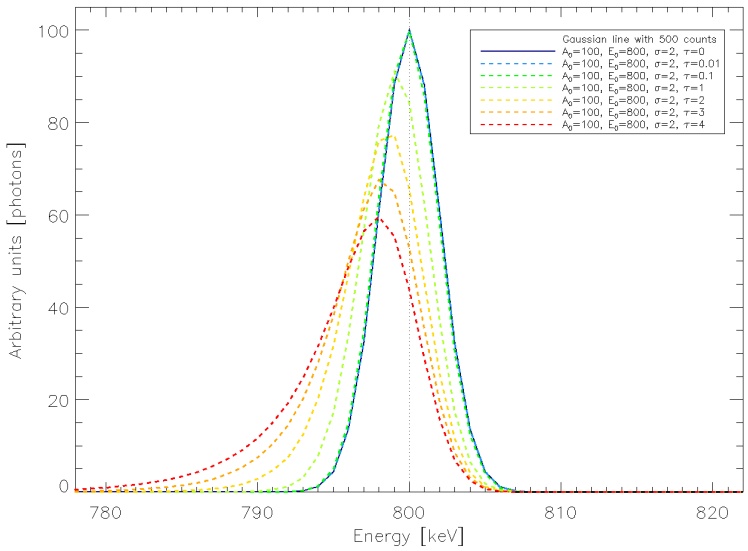

Figure 4.13.: Modeling the instrumental lines of SPI. The line model is a combination of a regular Gaussian, with a line centroid at 800keV and a FWHM of 4.5keV, and a one-sided exponential (see Eq. (4.17)). The shape of the line is shown for several degradation values τ. Even at the worst camera condition (shortly before annealings), τ rarely reaches values above unity. N.B. the distortion of the spectral shape, does not affect the intensity of the line that remains constant.

Shorter time periods are required to describe the spectral response of the instrument at a given time. Fitting spectra from individual pointings, may trace the actual spectral response accurately but the small number of detector counts (see Fig. 4.11c) yields low statistics, increasing the (Poissonian) errors in the derived fluxes. In addition, microscopic deviations in the weight, composition and damages of every individual Ge detector, results in small differences in the spectral responses of each detector that should not be averaged out using the camera-averaged response. A compromise between high statistics and spectral change is needed. It turned out, that fitting the three-day orbital spectra for each individual detector (e.g. Fig. 4.11b) provides the necessary statistics for firmly determined spectral parameters, assuming that the spectral shapes of background features remain constant on the time of one orbit (Diehl et al. 2018b). Using this formalism on the complete energy domain of SPI, an instrumental background database is created, separately for the instrumental lines and the continuum. The final step is to fit Eq. (4.4) to the data. This is done with a maximum likelihood fit, using Poissonian statistics.

In the following subsections, the properties of SPI's spectral response from the first orbits until the year 2019 is presented in order to investigate, whether this empirical approach and its assumptions are justified or not.

4.8. Spectral response properties of SPI

For the exact and successful description of the properties and the features of SPI's instrumental background, a fundamental understanding of its origins, effects and temporal evolution is of crucial importance.
To begin with, before fitting a model to the data, it must be decided, which data are meaningful and which must be rejected. It is important to leave out raw data contaminated by extreme

space weather conditions. For example, even though INTEGRAL observations stop near the Van Allen radiation belts, it was shown that they still influence the photon counts. For this reason, a procedure called 'spiselectsscw' reduces further the observing time, by filtering out data recorded in the proximity of the radiation belts. Further data filtering is implemented after checking it how natural cosmic phenomena, like the activity of the Sun, affect the spectra and hence, the quality of the fitting. Finally, the time-dependence of the detectors degradation is investigated and discussed.

4.8.1. Detector degradation

Ge detectors in space are subject to the continuous bombardment of the energetic radiation in the vicinity of the Earth. This leads to damages in the perfect crystalline structure of the material and consequently to a deterioration of the charge collection properties of the camera. Spectral lines are hence transformed from (nearly) perfect Gaussians to Gaussian-like features with a one-sided exponential (see Fig. 4.13). This transformation worsens the exceptional spectral resolution of SPI and also affects the position of the peak E_0 of the line, which contains important astrophysical information in celestial spectra.
As presented in Sec. 4.4.5, a restoring procedure called annealing was implemented and its effect on the spectral response of the instrument is presented in Fig. 4.14.

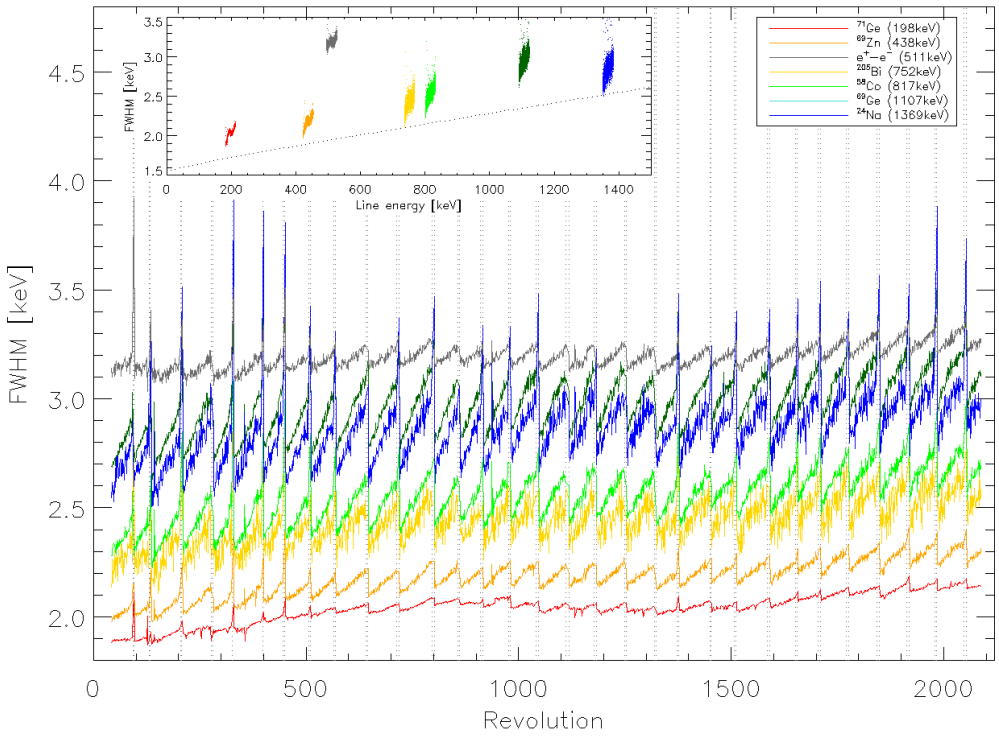

Figure 4.14.: Detector-averaged line widths of several instrumental background lines as a function of INTEGRAL mission time. Dashed grey vertical lines represent semi-annual annealings of the detectors. The inset displays the energy resolution of the instrument as a function of energy compared to SPI's energy resolution function before launch (dashed slope).

Fig. 4.14 leads to the conclusion that the energy resolution of SPI throughout the mission and for all instrumental lines varies in a systematic saw-tooth pattern, dictated by the time of annealings. The linear energy dependence of the energy resolution is apparent, except for the positron-annihilation line that marks an exception. The width of the 511keV-line depends on the annihilation conditions

within the structures of the instrument and as illustrated in Sec. 3.4, it leads to a systematic broadening with respect to other lines.

In summary, the spectral resolution degrades up to 15% within half a year. The degradation rate increases with increasing line energy, and the net degradation between two annealings depends on the overall background intensity. Annealings were proven very successful in restoring the spectral capabilities of the instrument, albeit a minor gradual long term-degradation cannot be avoided completely.

4.8.2. Solar influences

Solar Cycle

Since the 19$^{\text{th}}$ century it is known that the activity of the Sun follows a $\sim$ 11-year periodic change called the Solar Cycle (Schwabe 1843). During this period, the behavior of the Sun, considering the strength of solar radiation and magnetic field, the amount of solar mass ejected, the number of sunspots and solar flares, changes, following a specific pattern. Orbiting the Sun at 'only' 150×10^6km away, the activity of the Sun directly affects the space weather in the proximity of the Earth, including space telescopes, weather and navigation satellites.

The longevity of the INTEGRAL mission offers the opportunity to study the solar influence on γ-ray telescopes. In particular, a first-order test can be made by monitoring the evolution of several SPI count rates over INTEGRAL mission time.

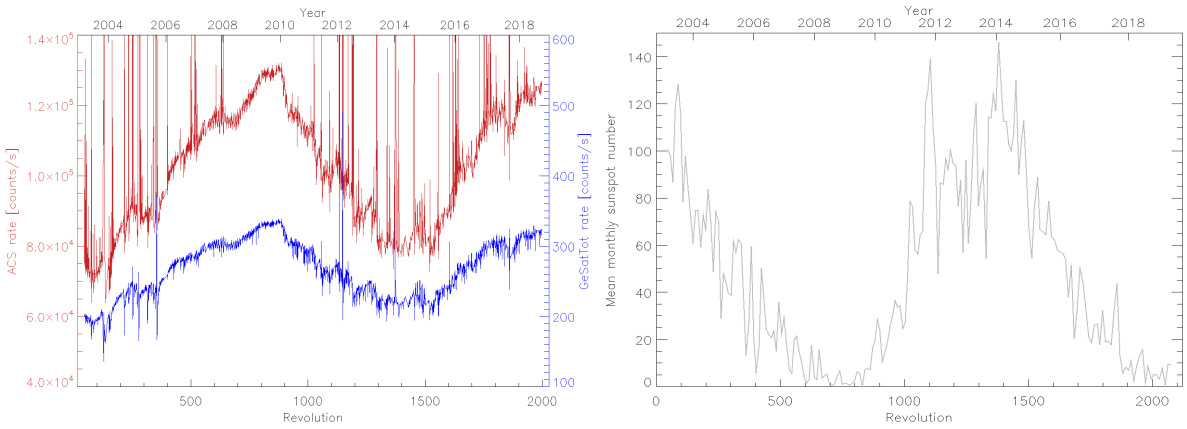

Figure 4.15.: Left: Intensities of the two mostly used 'tracers' of SPI, the ACS rate and the GeSatTot rate as a function of INTEGRAL mission time. Right: Average monthly sunspot number since the launch of INTEGRAL (data from the Solar Influences Data Analysis Center SIDC).

Fig. 4.15 shows the evolution of two important SPI count rates with time. The count rates rise until revolution $\sim$ 900 that corresponds to the year 2010 and then decline until revolution $\sim$ 1500, corresponding to the year 2015, before they start rising again in a harmonic-like manner. Comparing the detector rates and the mean monthly number of sunspots, a temporary phenomenon on the surface of the Sun that correlates with the solar cycle, indicates that the intensity of charged-particle interactions in the detector anti-correlates with solar activity. A high solar activity drives a reinforced solar magnetic flux that reaches out to the inner planets of the Solar System and deflects charged cosmic-ray particles, protecting thereby the Earth along with its orbiting satellites. As a result, the solar maximum coincides with the minimum of the recorded SPI count rates and vice versa.

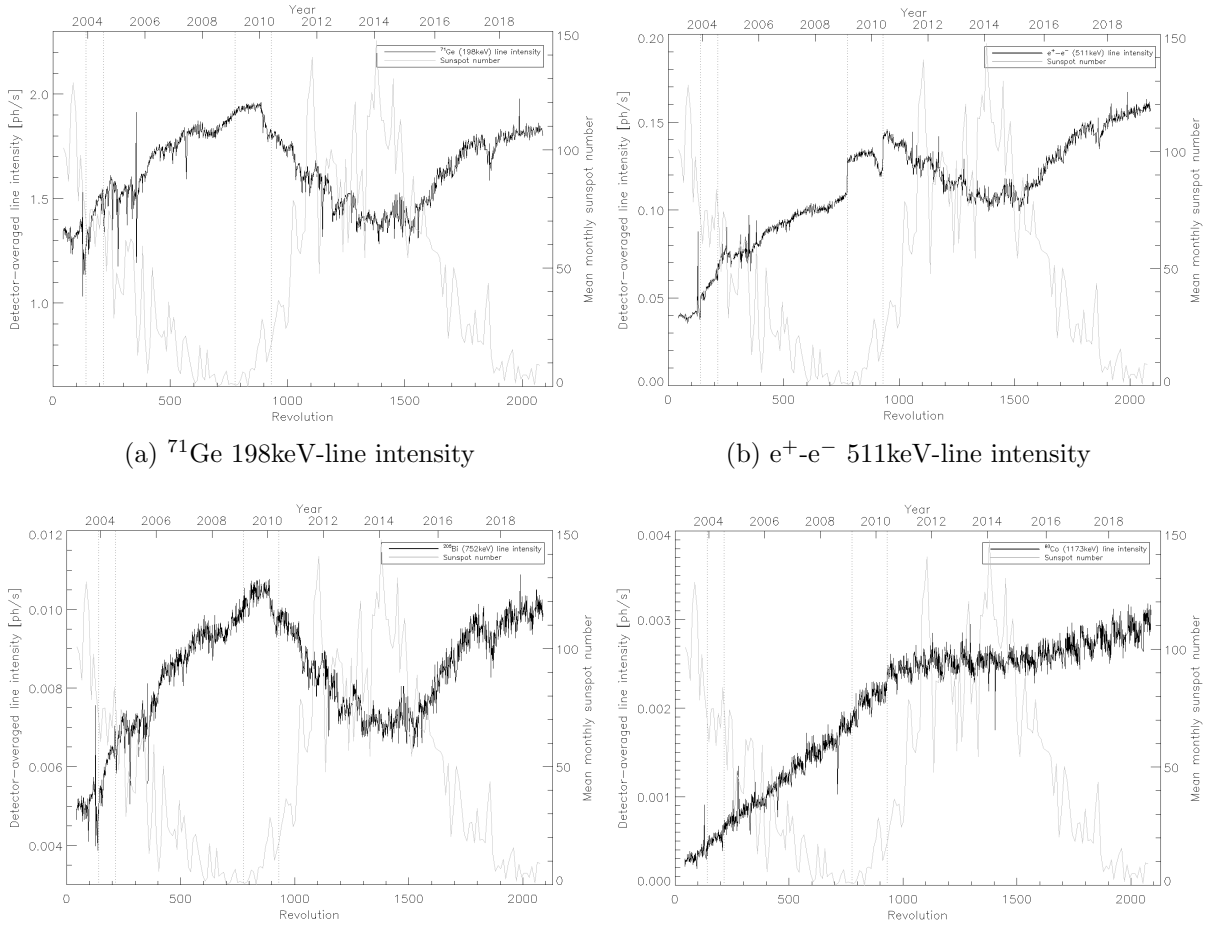

(a) ^{71}Ge 198keV-line intensity

(b) e^+-e^- 511keV-line intensity

(c) ^{205}Bi 752keV-line intensity

(d) ^{60}Co 1173keV-line intensity

Figure 4.16.: Time evolution of the fluxes of several background lines recorded by SPI compared with the monthly averaged number of solar spots throughout INTEGRAL's lifetime.

In panels (a)-(d) of Fig. 4.16 the time evolution of four distinctive background lines of SPI are shown. The number of solar spots is overplotted with faint grey lines, while vertical dashed lines mark the revolutions with detector failures. Panel (a) displays the temporal evolution of the strongest Ge line of the spectrum, the 198keV neutron capture line of ^{71}Ge. Its temporal behavior resembles closely that of the tracers in Fig. 4.15 and clearly anti-correlates with solar activity. Panel (b) represents the same for the positron annihilation line, which marks an exception, as it cannot be attributed to a single background source, but rather includes components of physically different origins (e.g. β^+ decays, pair productions, etc.). This line also anti-correlates with solar activity and shows a particular sensitiveness to detector failures. Panel (c) presents a background line originating from the ACS shield surrounding SPI, the 752keV Bi line, that follows the trends of panels (a) and (b). Finally, panel (d) presents a special case and illustrates the diversity of the physics involved in understanding and explaining the background in an astrophysical laboratory like INTEGRAL: Cobalt is mostly found in the electronic cables of the instrument. Neutron captures by stable Co isotopes produce ^{60}Co, a radioactive isotope with a half-life of $T_{1/2} \approx 5.27$years. For the first years of the mission, the neutron capture rate exceeded the decay rate, resulting in a radioactive build-up and in a linear increase of the line intensity. After ~ 6 years, the rates became equal, stabilizing the line intensity. The behavior of the line intensity in the last two years, suggests an anti-correlation with the solar cycle that could be confirmed in the following years.

Solar flares

The outliers in the count rates of the tracers, shown in the left panel of Fig. 4.15 are caused by solar flares. They are characterized by sudden and unpredictable increases in the brightness of the Sun, emitting large amounts of energy and charged particles. It is believed that solar flares occur when a phenomenon called 'magnetic reconnection' takes place. The Sun's surface contains numerous loops of magnetic lines, connected with the surface of the Sun. When they reconnect far above the Sun's surface, the yield large outbursts of charged particles and photons covering the whole electromagnetic spectrum is released, forming a so-called coronal mass ejection (Reames 1999; Antiochos et al. 1999). However, the mechanisms involved in this procedure, as well as the conversion of the magnetic energy in kinetic energy, are not well understood.

The produced particles and photons of solar flares hit SPI and interact mostly with its main protective shield, the ACS. A large fraction of them is stopped by the ACS shield that shows an increased count rate by a factor of $\sim$ 2-3. The remaining fraction may pass the shield without interactions and reach the Ge camera giving rise to the GeSatTot rate or may interact with the structures of the spacecraft and produce a large and unpredictable flux of secondary neutrons. These undergo the reactions depicted in Fig. 4.10, producing thus background photons that they do not follow the regular source pattern, as in regular space weather conditions but rather show an irregular flux distribution. This violates a key assumption of the background model described in Sec. 4.7.1 that the background sources have constant origins and reduce the power of detector patterns. Hence, data recorded during solar flares include contaminations and must either be completely excluded from the analysis or handled carefully using other background scaling techniques.

4.8.3. Detector Ratios

A key aspect of the background model used for the data analysis is the constancy of the spatial distribution of the background sources and the relative background intensities between detectors for both lines and continuum. All background features should show a source-specific, robust and invariable intensity ratio among detectors. In other words, detectors should always measure the same intensity of a specific background feature in respect to other detectors, as long as the number of functioning detectors stays the same. If a detector fails, multiple events are registered as single events and the ratio must be determined once more.

Detector ratios are defined as the relative intensity of one detector compared to all other operating detectors of the camera. Ideally, without any background contribution, this ratio should only depend on the shadow of the coded mask and the direction of the celestial sources, which would cause some detectors to measure photons and some not. However, the background that dominates over all celestial sources imprints its own pattern on the detector plane that does not depend on the orientation of the instrument but rather on the spatial distribution of the background sources on the spacecraft and the solid angle between them and every individual detector. It can even be assumed that over the course of one revolution, the dithering strategy of the instrument results in approximately equal exposure time for each detector, thus smearing out the revolution-integrated celestial intensity for each detector.

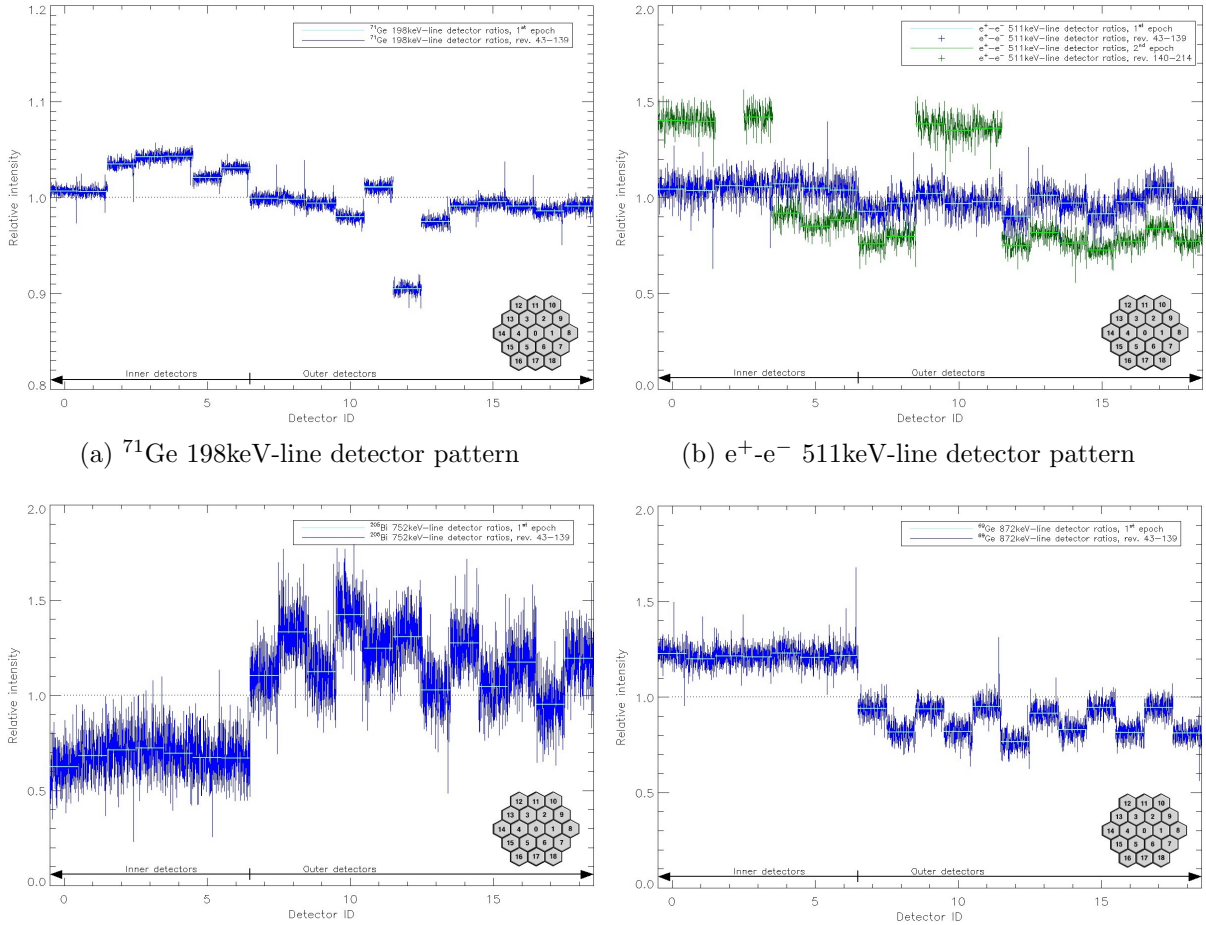

(a) ^{71}Ge 198keV-line detector pattern

(b) e^+-e^- 511keV-line detector pattern

(c) ^{205}Bi 752keV-line detector pattern

(d) ^{69}Ge 872keV-line detector pattern

Figure 4.17.: Background detector patterns for different classes of background lines in epoch 1. The light horizontal lines serve as secondary time axes from revolution 43 until revolution 140. For the positron annihilation line, also the detector ratios of epoch 2 are shown with green color.

Fig. 4.17 displays characteristic background ratios for different classes of background lines. Panel (a) displays the background pattern of the strongest background line of SPI. The high count rate of the line results in superb statistics and very small errors for the fitted parameters of the line. It is apparent that most detectors register a similar amount of photons, with a slight increase in the relative intensities of the inner detectors. Panel (b) presents the unique positron annihilation line. Generally, this line has contributions from several sources on the spacecraft and shows a balanced detector pattern. However, the effect of detector failures on adjacent detectors is clearly visible. Following the failure of detector 2, all neighboring detectors (i.e. detectors 0, 1, 3, 9, 10, 11) experienced a major increase in their intensities. Panel (c) depicts the detector pattern of a line originating from the ACS shield surrounding SPI. As expected the outer detectors measure an increased intensity with respect to the inner detectors. The weakness of the line compared to the prominent background features of the other panels results in a higher variation in the intensities measured for each revolution. Finally, panel (d) presents another Ge line that shows an almost perfect regular pattern. The inner detectors 0-6, each of them surrounded by six neighboring detectors register the highest intensities. Detectors 7, 9, 11, 13, 15 and 17 are surrounded by four neighbouring detectors and register an intensity ratio close to unity, while detectors 8, 10, 12, 14,

16, 18 are positioned at the edges of the honeycomb structure and register the lowest intensity, being adjacent only to three detectors.

The examples of detector ratios presented above illustrate that the relative intensities of instrumental background lines between detectors change only marginally in the time scale of one epoch and highlight the robustness and validity of the empirical background approach used to derive the celestial spectra. Most importantly, they are direct proof of the fact that the background intensities of SPI can be predicted, by taking into account the spectral behavior of the instrument over the last sixteen years.

4.9. SPI data analysis

SPI's raw data are provided by using a program called '*spiselectscw*'. This program sorts the raw data in several fits-files. One fits-file contains generic information about the instrument for each individual pointing, i.e. the recorded rates, temperatures, exact coordinates, time information and many more. The actual spectra along with the precise temporal information and coordinates of each pointing can be found in separate fits-files.
In this section several parameters that affect the final celestial spectra are investigated and tuned accordingly, to achieve maximum sensitivity and an acceptable background fit.

4.9.1. Data cleaning and filtering

Data correction

One small occasional 'glitch' of the program '*spiselectscw*' is an occasional mismatch between the science window files containing generic information about the instrument and the actual spectra. In particular, for some revolutions, the number of pointings in the generic fits-file does not match with the actual number of pointings in the spectra. Since the intensity of the background is usually scaled to one of the instruments tracers, this leads to the false use of the tracer, as for instance, the tracer recorded in pointing four is used to scale pointing three. This glitch originates from the fact that there are several sub-pointings lasting a few hundred seconds.

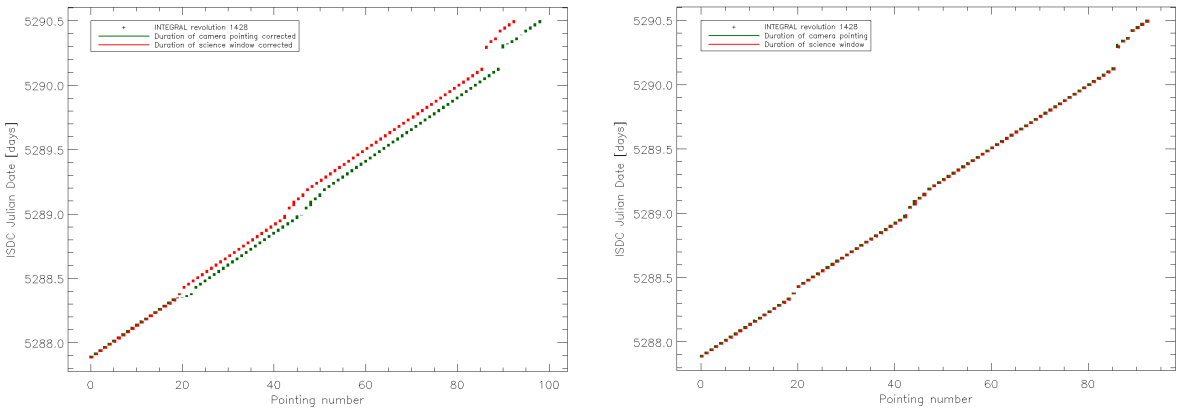

(a) Temporal discrepancy between 'detector pointing' and 'tracer pointing' in revolution 1428

(b) Discrepancy amendment after deleting several sub-pointings

Figure 4.18.: Matching of both detector pointings and instrument pointings. The camera pointings are illustrated through green lines, while the science window pointings are shown in red color.

To amend this discrepancy and match the pointings, the superfluous sub-pointing are removed. This is done for most revolutions evaluated in this analysis.

Treating solar flares and tracers

As already mentioned in Sec. 4.8.2, solar flares cause an outbreak of secondary neutrons and photons with irregular distributions that distort line shapes and violate the relative detector intensities. Thus, detector patterns are distorted, reducing the predictive power of the background model.
A useful procedure to evaluate how well does the fitted background model match with raw SPI data is to check the residuals of the fit. As the name states, residuals are defined as the difference between data points and model fitted points, normalized to the statistical fluctuations of the background counts, that should follow the Poisson statistics. In case of SPI data, where the assumption of complete background domination is valid, it suffices to check the difference between $B_{i,j,k} \equiv \sum_{n=N_s+1}^{N_s+N_b} \theta_b B_{n;i,j,k}$ and $d_{i,j,k}$.

$$Res_{i,j,k} \equiv \frac{d_{i,j,k} - B_{i,j,k}}{\sqrt{B_{i,j,k}}}, \tag{4.18}$$

In case of a good data description, the residuals should follow a normal distribution around μ=0 with a standard deviation of σ=1. A small shift towards the positive axis is expected, as it indicates the presence of a celestial signal in the data.

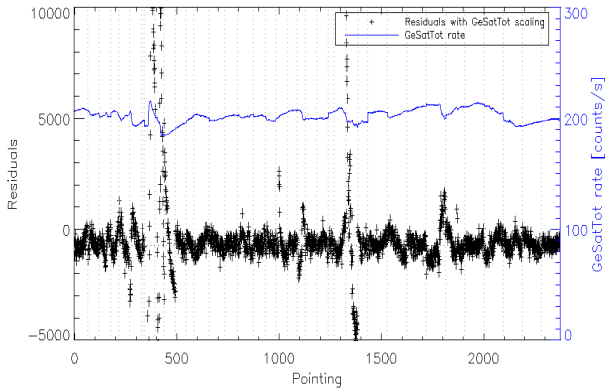

(a) Residuals with GeSatTot scaling

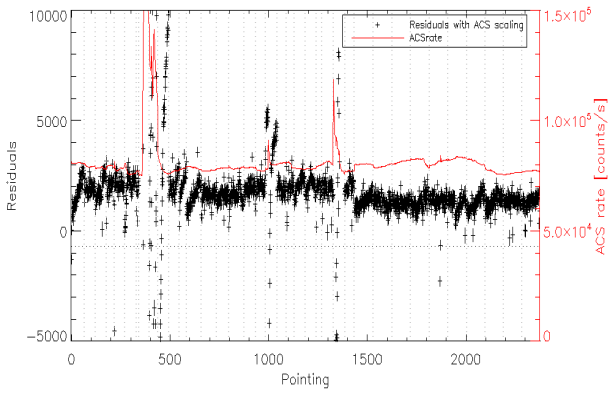

(b) Residuals with ACSRate scaling

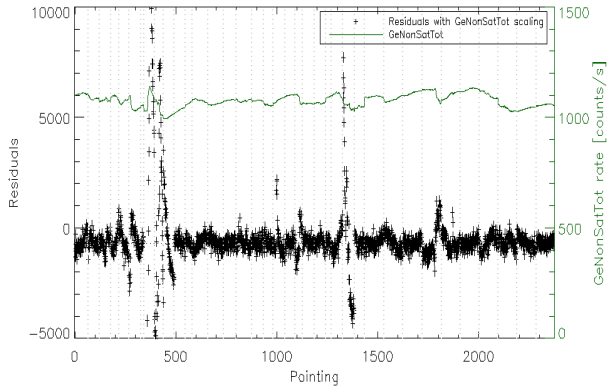

(c) Residuals with GeNonSatTot scaling

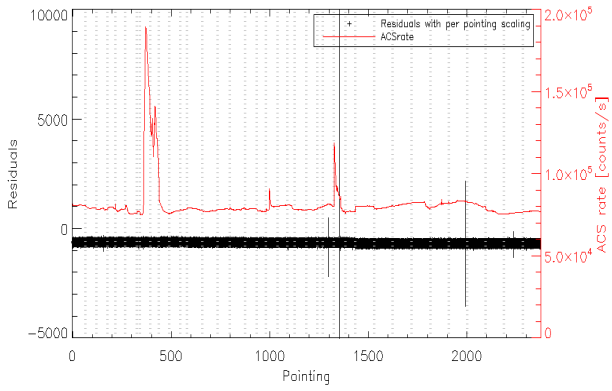

(d) Residuals with background scaling per pointing

Figure 4.19.: Detector-integrated residuals of the SN2014J observation campaign for the 100-1350keV energy range, with four different background scaling techniques. The grey vertical lines mark the different revolutions.

Fig. 4.19 displays the time evolution of the residuals of INTEGRAL's SN2014J campaign, integrated over all detectors and energy bins and with four different background scaling techniques. The rates of the tracers used to scale the background intensities are overplotted with color. In general, two main periods with intense solar activity occurred during SN2014J observations. The first covered revolutions 1386-1390 and the second revolutions 1405-1406. In these periods, the residuals of panels (a),(b),(c) deviate significantly from the zero-line, indicating that the background model fails to describe the data sufficiently. Hence, data recorded during solar flares include contaminations and must either be completely excluded from the analysis or handled carefully using other background scaling techniques.

Panel (d) displays the residuals when the background line shapes are determined independently for every single pointing and detector. This method delivers the residuals closest to zero, even in periods of solar flares, but produces a very large number of parameters that can be avoided in periods of quiet space weather. In addition, by fitting the background separately for every pointing and detector, possible celestial contribution may be included in the background modeling.

The efficiency of the background modeling for the whole SN2014J mission can be evaluated by the following procedure: A background model that describes the data adequately produces residuals close to zero. Integrating the absolute values of the residuals of all 2375 pointings yields a Res_{tot} that must be close to zero for a good background description. Doing this for all four panels of Fig. 4.19 yields:

Tracer	GeSatTot [10^6]	ACSrate [10^6]	GeNonSatTot [10^6]	Per pointing [10^6]
|Total residuals|	2.432±0.010	9.058±0.010	2.266±0.010	1.413±0.028

Table 4.2.: Total absolute residuals of SN2014J for the four different background scaling methods

Tab. 4.2 proves that the residuals of the whole SN2014J campaign are minimized when the background is scaled in every pointing. GeSatTot and GeNonSatTot are two correlated tracers and yield similar residuals, albeit the background scaled with the tracer GeNonSatTot describes the data more accurately. Finally, the background scaled with the ACS rate clearly underestimates the background intensity and consequently, the ACS rate can be safely rejected as an efficient background tracer for the SN2014J campaign.

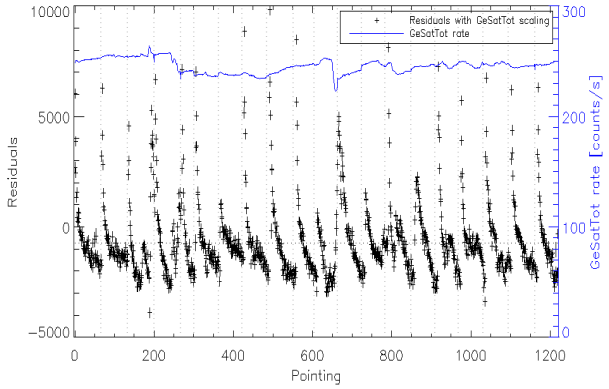

(a) Residuals with GeSatTot scaling

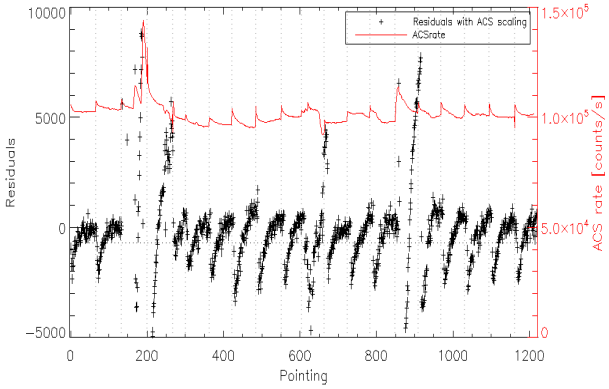

(b) Residuals with ACSRate scaling

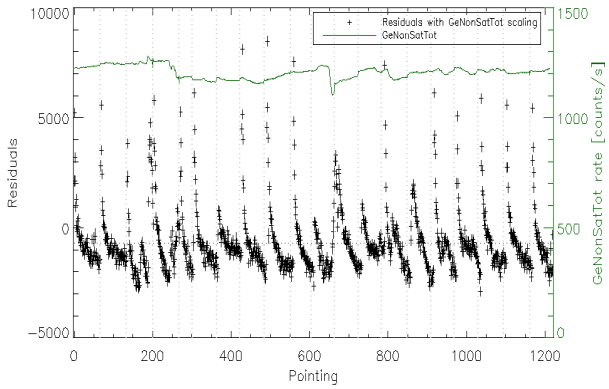

(c) Residuals with GeNonSatTot scaling

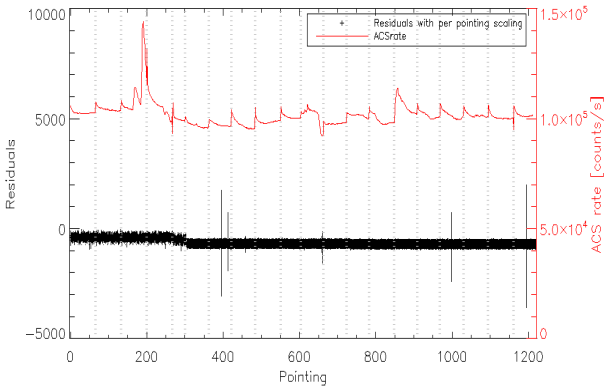

(d) Residuals with background scaling per pointing

Figure 4.20.: Detector-integrated residuals of the SN2011fe observation campaign for the 100-1350keV energy range, with four different background scaling techniques. The grey vertical lines mark the different revolutions.

Fig. 4.20 presents the detector averaged residuals for the SN2011fe observations with four different background scaling techniques. In panels (a), (b) and (c) a systematic saw-tooth pattern is apparent, indicating that the tracers are unable to trace the background properly. Scaling the background features per pointing delivers the most accurate background description.

Tracer	GeSatTot [10^6]	ACSrate [10^6]	GeNonSatTot [10^6]	Per pointing [10^6]
|Total residuals|	1.520±0.007	2.443±0.007	1.350±0.007	0.739±0.008

Table 4.3.: Total absolute residuals of SN2011fe for the four different background scaling methods

The values reported in Tab. 4.3 follow the same trend as the ones of the SN2014J analysis. Scaling the background in every pointing minimizes the residuals, while GeSatTot and GeNonSatTot have similar values, albeit the background scaled with the tracer GeNonSatTot has lower residuals by $\approx 10\%$. Similar to Tab. 4.2, the background scaled with the ACS rate yields the highest residuals and is inappropriate for background intensity scaling.

The final inference from the residual analysis is that at periods with normal space weather, the background can be scaled using GeNonSatTot or GeSatTot. Datasets recorded during periods of

strong solar activity should be evaluated using a background model scaled anew for each individual pointing, due to the failure of detector patterns and hence, of the complete background modeling. For the SN2011fe campaign, the analysis of the residuals favors a background scaling for each individual pointing throughout the campaign.

Filtering of extra pointings

Part of the standard data filtering strategy of our group is to omit pointings near the radiation belts (for t $\leq$ 0.1 and t $\geq$ 0.9 of the orbit). This provides a first-order data filtering that 'purges' the dataset from possible spikes in the rates. In an attempt to exploit the complete exposure of both supernovae, this measure is relaxed and pointings near the radiation belts are initially included to the dataset. They become subject to inspection and are added to the final dataset, after checking that both space weather tracers (e.g. GeSatTot, ACSrate) and residuals for these particular pointings do not take any peculiar values.

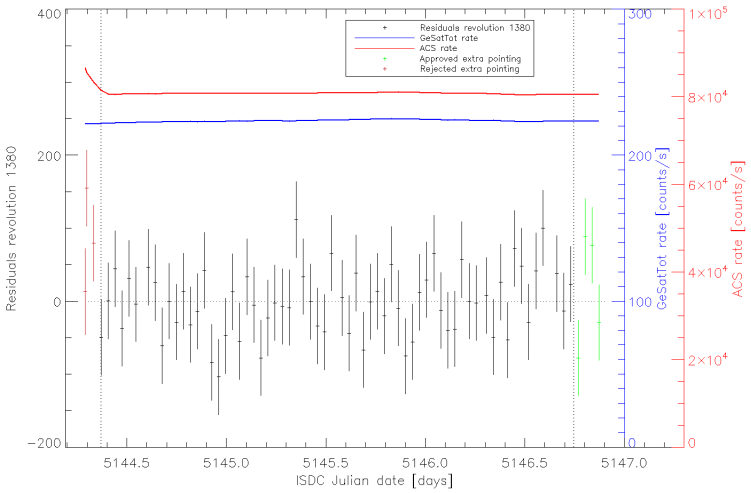

Figure 4.21.: Residuals and tracer rates of revolution 1380. The area between the two dashed vertical lines marks the borders set by the standard filtering procedure. Green data points mark accepted pointings, while red data points mark rejected pointings.

The inspection of the individual 'extra' pointings is illustrated in Fig. 4.21. After fitting the spectrum, the residuals for every detector, pointing and the complete energy range are calculated using Eq. (4.18). Pointings, whose residuals lie within the acceptable range and tracer rates remain constant, are added to the dataset.

Nearby sources

While looking toward SN2014J, the large field of view (16°×16°) and angular resolution (2.5°(FWHM)) of SPI may allow a flux contribution of nearby sources. This could cause contaminations in the spectra of SN2014J, and falsify the intensities of the targeted object.

Extragalactic galaxies, stars and supernovae are faint γ-ray sources. For instance, assuming that in M82, the host galaxy of SN2014J, $\sim 10^{43} e^+$ annihilate per second, producing always two 511keV photons, the resulting positron annihilation line would reach the Earth with a flux of $\sim 10^{-8}$ ph/cm^2/s. This is several orders of magnitude below the 3σ sensitivity limit of SPI for narrow lines (for details, see Tab. 4.1). Concerning the geometry of extragalactic γ-sources, it is clear that even the largest galaxies at Mpc distances have radii of a few arcsec. Hence, in γ-ray observations of

extragalactic sources, located far below or above the galactic plane to avoid nearby galactic sources, a single point source is a good approximation for the celestial emission model.

In the general source catalog of INTEGRAL, three sources in the celestial neighbourhood of SN2014J are registered:

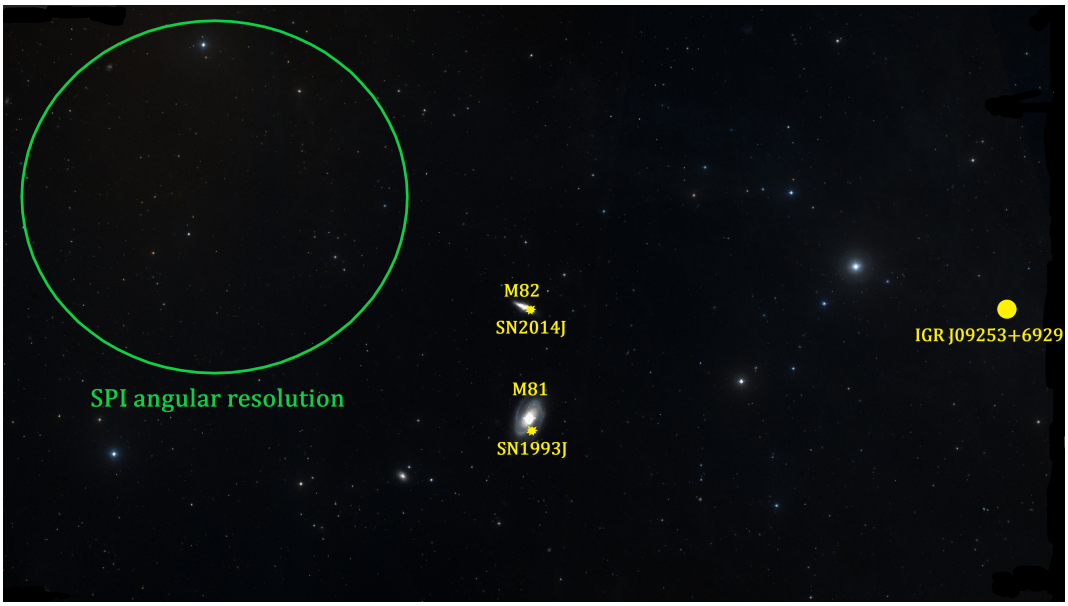

Figure 4.22.: Sources within the field of view of SPI during the SN2014J campaign (original sky picture from http://simbad.u-strasbg.fr).

1. M82, the host galaxy of SN2014J. Since the distance between the nucleus of the galaxy and the supernova on the sky is no more than a few arcseconds, the two sources practically coincide and are indistinguishable for SPI.

2. M81 and its supernova remnant SN1993J. M81 is the closest galaxy to M82 and the elite member of the M81 group. M81 houses a core-collapse supernova remnant, SN1993J, which was the second brightest supernova ever observed at its time. However, sixteen years after first light, it is considered a faint γ-ray source, as most of its radioactive material, should have already decayed. The two objects are $\approx 1^\circ$ away from SN2014J and consequently indistinguishable for SPI.

3. IGR J09253+6929 is an object identified with JEM-X on INTEGRAL and was also observed in the optical by other instruments. Follow-up spectral analysis allowed its classification as a type I Seyfert galaxy (Masetti et al. 2010). Its separation from SN2014J is larger than the angular resolution of SPI, which should allow distinguishing between the two sources. However, the γ-emission of a type I Seyfert galaxy at an unknown distance cannot be safely estimated and is highly uncertain.

Sources	(gl | gb)
IGR J09253	(143.42° | 38.44°)
SN1993J (M81)	(142.15° | 40.92°)
M82	(141.41° | 40.57°)
SN2014J	(141.43° | 40.56°)

Table 4.4.: Galactic coordinates of the four sources in the field of view of SPI.

A method to evaluate to what extent one source X influences a nearby source Y, while fitting their corresponding celestial intensities θ_s from Eq. (4.4), is given by studying their correlation ρ_{XY}. This is given by:

$$\rho_{\mathrm{XY}} = \frac{\sigma_{\mathrm{XY}}}{\sigma_{\mathrm{X}} \cdot \sigma_{\mathrm{Y}}}, \tag{4.19}$$

where $\sigma_{\mathrm{XY}} = \mathrm{cov}_{\mathrm{XY}}$ is the covariance of the two sources. ρ_{XY} takes values between ± 1. A negative correlation value means that two sources X and Y are anti-correlated; one source gains in intensity at cost of the other. A correlation near zero reflects the independence of the intensities of the two sources. Applying Eq. (4.19) on all combinations of sources in the field of view of SPI, results in a 4×4 matrix displayed below:

Correlation ρ_{XY}	IGR J09253	SN1993J (M81)	M82	SN2014J
IGR J09253	1.00	0.14	0.34	-0.34
SN1993J (M81)	0.14	1.00	0.41	-0.43
M82	0.34	0.41	1.00	-0.99
SN2014J	-0.34	-0.43	-0.99	1.00

Table 4.5.: Correlation of the four sources in the field of view of SPI

The values in Tab. 4.5 are averaged over 2500 energy bins. Their corresponding standard deviations are of the order of 10^{-3}.

4.9.2. Differences in the spectra

After discussing potential factors that could influence the celestial fluxes, the next step is to investigate up to what extent they actually do affect them and the quality of the fit. This is presented below with some illustrative examples for selected spectra and selected revolutions. Additional examples can be found in the Appendix.

Data correction

To test the influence of the pointing adjustment presented in Fig. 4.18, the SN2014J spectrum obtained in revolution 1428 in the energy range between 780 and 920keV is depicted in Fig. 4.23. The selection of this particular revolution comes from the fact that it contains a large number of mismatched pointings and of several sub-pointings of a few hundred seconds. In particular, six detector pointings and nine instrument pointings were removed to equate detector and instrument pointings.

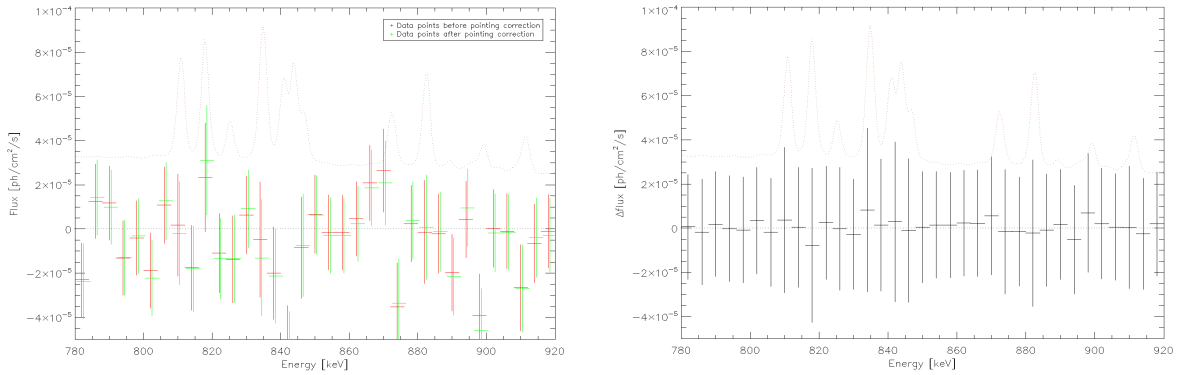

(a) Comparison of the spectra before and after correcting the time sequence of the pointings

(b) Flux differences between the two approaches

Figure 4.23.: Comparison of the celestial intensities of revolution 1428 before correcting (red data points) and after correcting (green data points) the time sequence of the pointings. The data are given in 4keV energy binning. Note that for illustration purposes, the green data points are shifted by 0.5keV.

In Fig. 4.23 it is apparent that adjusting detector and instrument pointings only affects marginally the flux intensities. As a next step, the residuals of the two approaches were compared. In fact, integrating the absolute values of the residuals of all pointings and all detectors for the selected energy range showed no particular improvement.

Solar flares

While INTEGRAL approached the apogee of revolution 1388, a strong solar flare commenced, accelerating a large flux of particles toward the Earth and INTEGRAL. The rate of the ACS shield jumped abruptly to 2.5 times the regular value, recording thus $\sim 120{\times}10^4$ more counts/s compared to regular solar activity. The particle flux reached its peak near the middle of revolution 1388 and declined during revolution 1389 until it reached its nominal value at the beginning of revolution 1390.

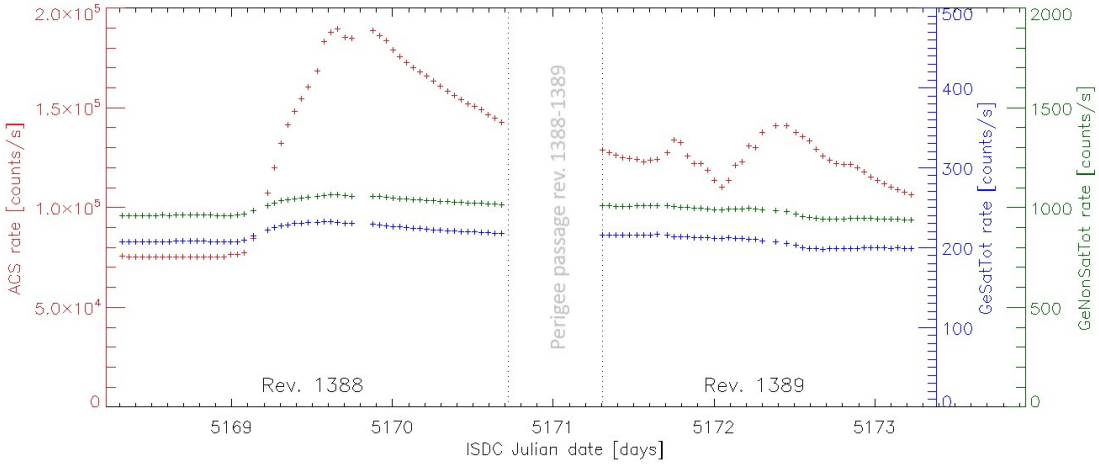

Figure 4.24.: Count rates of the tracers ACSrate, GeSatTot and GeNonSatTot during a solar flare in revolutions 1388-1389.

Solar flares are unfortunate events for γ-observations, however, their appearance in revolutions 1388-1389 can be exploited to check the response of the background model during times with intense ambient particle flux.

Most importantly, the influence of one of the most fundamental considerations of the background model, the stability of line shapes throughout one revolution, can be tested. For the red data points, the line shapes of the raw spectrum were determined once for the whole revolution. For green data points, the background line shapes were determined for each individual pointing anew.

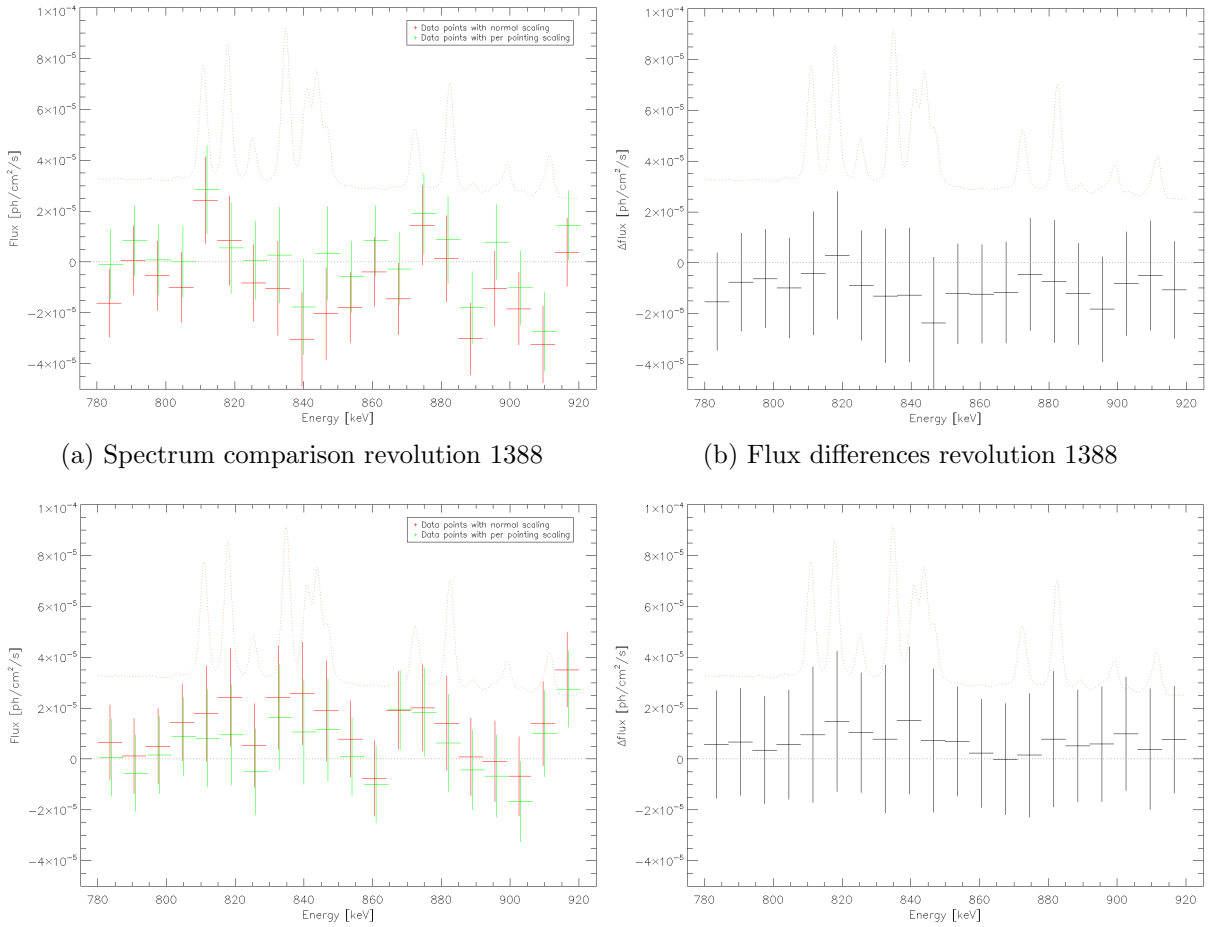

(a) Spectrum comparison revolution 1388

(b) Flux differences revolution 1388

(c) Spectrum comparison revolution 1389

(d) Flux differences revolution 1389

Figure 4.25.: Comparison of the celestial intensities with two different background scaling techniques in observations made during a solar flare. For red data points the background features were determined from the accumulated spectrum of the whole revolution and scaled using GeSatTot, while for green data points, the background spectrum was determined for each individual pointing and detector anew. The background shape in this energy range is drawn with a faint brown slope.

Solar flares cause major distortions in the celestial spectra and this is clearly depicted in Fig. 4.25. Depending on whether the tracer rates rise or decline within the observation window, celestial intensities from regular background modeling are either underestimated (panels (a) and (b)) or overestimated (panels (c) and (d)). The poor quality of the fit during solar flare events was already illustrated in Figs. 4.19 and 4.20. Apart from removing the affected datasets completely from the analysis, the only viable countermeasure is to scale their background in every pointing anew.

Nearby sources

To test the influence of nearby sources on the spectra of SN2014J, two datasets, one obtained during revolution 1428 and one by binning revolutions 1424-1428 together were analyzed including nearby celestial sources.

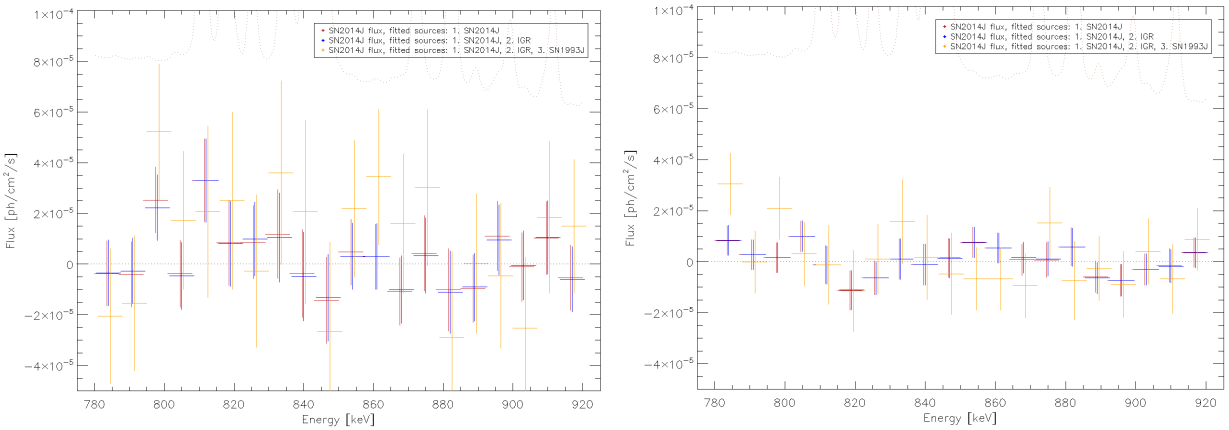

(a) Spectra of revolution 1428

(b) Spectra of revolutions 1424-1428

Figure 4.26.: Comparison of the SN2014J flux for one (only SN2014J), two (SN2014J and IGR J09253+6929) and three (SN2014J, IGR J09253+6929, SN1993J) fitted celestial sources. Note that for illustration purposes, blue data points are shifted by 0.5keV and orange points by 1.0keV.

As expected, the separation of the sources on the sky plays a fundamental role in the spectra of SN2014J and the error bars of the data points. Including Seyfert galaxy IGR J09253+6929 next to SN2014J in the fit (blue data points) influences the spectra of SN2014J to a minimal extent. This is illustrated in both panels, as red and blue data points almost coincide in all energy ranges. Adding, SN1993J, a source with a sky separation of $\sim 1^\circ$ in the fit, not only affects the fluxes but almost doubles its error bars, reflecting the difficulty of SPI to distinguish the two sources. The case, where all four sources, including M82, were fitted, is not displayed in Fig. 4.26, as the statistical errors of the fluxes rise to $\sim 10^{-3}$ph/cm^2/s instead of the typical $\sim 10^{-5}$ph/cm^2/s (Additional material on this test can be found in the Appendix).

4.10. Fitting the celestial fluxes

Once a celestial spectrum is obtained, a suitable model is required to draw physical conclusions about the observed target. γ-ray photons that originate from radioactive decay and avoided any scattering interactions with ambient particles have discrete energies that correspond to the energy differences between nuclear energy levels. An ideal detector measuring decay photons from a stationary source would measure a spectrum resembling a Dirac delta-function centered at the laboratory energy of the transition. However, the instrumental resolution, as well as possible source kinematics, broaden the energy distribution of the photons and enables the use of Gaussian functions to model the spectra. Gómez-Gomar et al. 1998 simulated the γ-emission of ^{56}Ni and ^{56}Co for different ejecta configurations and points that the received fluxes do not have exactly Gaussian shapes. However, at Mpc distances the difference between the theoretical model shapes and Gaussian lines regarding the width of the line are below $\sim 3\%$.

Since both targeted supernovae are located at extragalactic distances and their flux is expected to be broadened, both by their expansion velocities of ^{56}Ni and ^{56}Co, and the instrumental resolution of SPI, a Gaussian line is sufficient to model the decay spectra:

$$\mathrm{f(E;C,A,E_0,\sigma) = C + A\exp\left(-\frac{(E-E_0)^2}{2\sigma^2}\right)} \tag{4.20}$$

In Eq. (4.20), C is a constant off-set and accounts for the underlying continuum, A is the amplitude of the line, E_0 the line centroid and σ the standard deviation of the line. The latter can be related to the FWHM using:

$$\mathrm{FWHM_{line} = 2\cdot\sqrt{2ln(2)}\sigma \approx 2.35\sigma} \tag{4.21}$$

In several cases throughout the thesis, a model consisting of two lines was fitted to the data:

$$\mathrm{f(E;C,A_{1,2},E_{0;1,2},\sigma_{1,2}) = C + A_1\exp\left(-\frac{(E-E_{0;1})^2}{2\sigma_1^2}\right) + A_2\exp\left(-\frac{(E-E_{0;2})^2}{2\sigma_2^2}\right)} \tag{4.22}$$

Once a Gaussian line is fitted on the celestial spectrum, its flux can be calculated using:

$$\mathrm{F_{line} = \sqrt{2\pi}\cdot A\cdot\sigma} \tag{4.23}$$

Parameters E_0 and σ contain important information about the kinematics of the decaying material in the supernova ejecta. In particular, the motion of the γ-ray source toward or away from the observer causes a blue-shift or a red-shift, respectively. This velocity, called 'bulk velocity' is given by:

$$\mathrm{v_{bulk} = \frac{E_0 - E_{lab}}{E_{lab}}\cdot c,} \tag{4.24}$$

where E_0 denotes the fitted line centroid, E_{lab} the laboratory energy of the line and c the speed of light.
Assuming a homologous expansion, the spread velocity of the ejecta toward all directions causes a so-called Doppler broadening of the line next to the broadening due to the finite instrumental resolution FWHM$_{res}$ of SPI. The spread velocity of the radioactive material is given by:

$$\mathrm{v_{spread} = \sqrt{FWHM_{line} - FWHM_{res}}\cdot\frac{c}{E_0},} \tag{4.25}$$

Finally, another model to capture the shape of the continuum is given by a logistic function:

$$\mathrm{f(E;C,L,E_0,k) = C + \frac{L}{1+\exp(-k(E-E_0))}} \tag{4.26}$$

This model allows the continuum to have a cut-off at a given energy E_0. On the one side of the cut-off, the flux of the continuum is given by parameter C, on the other side, by parameter L. Parameter k represents the steepness of the curve at E_0.

^{56}Co spectrum simulation

To illustrate the importance of the branching ratios and the energy dependence of the Doppler broadening in the form of the resulting γ-ray spectrum of the supernova, a Monte Carlo simulation was run to generate model spectra. 10^4 decays of ^{56}Co were followed, which produced 511keV, 847keV, 1040keV and 1238keV line photons according to their branching ratios (see Fig. 3.7). The radioactive source was allowed to expand with $\sim$ 5000km/s, yielding a FWHM$\approx$ 15keV for the 847keV line. In addition, to treat the extremes of positron-annihilation correctly, the two limiting Ps-fractions of f=0.0 and f=1.0 were used. To visualize the effect of Compton scattering on the

spectra, the simulation was performed twice: Once assuming complete transparency and once forcing 50% of the 511keV photons to undergo one single Compton interaction. The interaction probability of the other line photons was scaled using the angle-independent Klein-Nishina formula (see Eq. (3.29)). No other interactions were included in the simulation. Motivated by the shape of the ortho-Ps continuum in Galactic spectra (see Fig. 3.5), the shape three-photon annihilation flux in the 0-511keV energy range was assumed to resemble a constant line.

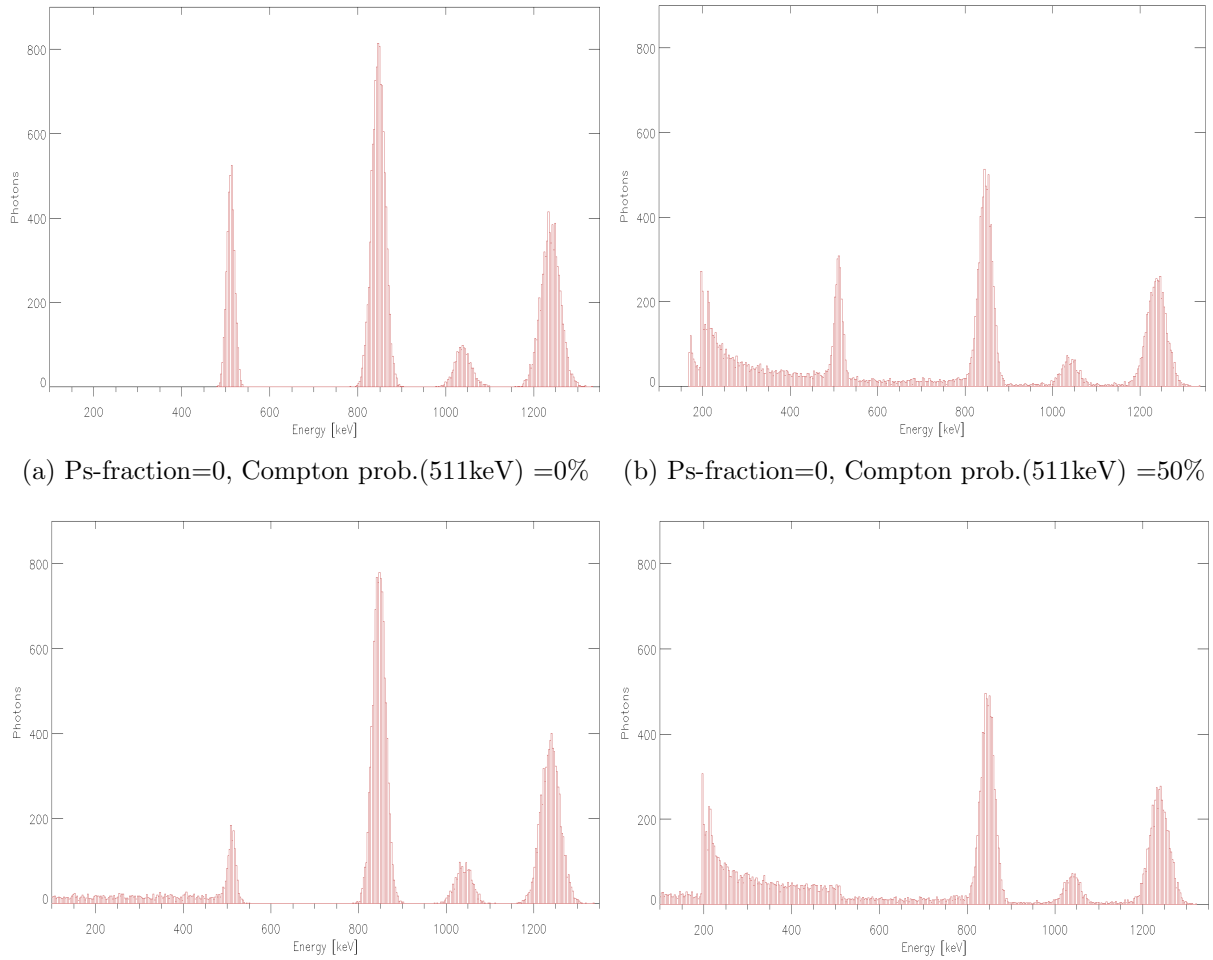

(a) Ps-fraction=0, Compton prob.(511keV) =0%

(b) Ps-fraction=0, Compton prob.(511keV) =50%

(c) Ps-fraction=1, Compton prob.(511keV) =0%

(d) Ps-fraction=1, Compton prob.(511keV) =50%

Figure 4.27.: Modeled spectra of the ^{56}Co emission assuming Ps-fractions of 0.0 and 1.0. The panels on the left present the spectra without Compton interactions, while in the left panels, $\sim$ 50% of all photons undergo one Compton scattering interaction.

The simulated spectra in Fig. 4.27 may be subject to major simplifications, albeit they allow drawing some useful conclusions regarding the analyses of SN2014J and SN2011fe:

The weak energy-dependence of the Klein-Nishina formula at these energies shows that the various lines are almost equally dependent by Compton scattering, with the normalized flux differences being less than 10%. On the other hand, the line broadening reduces the detection probability of the most energetic lines, as their fluxes are spread over more energy bins. A characteristic example is shown in panel (a). Despite the fact that the 1238keV line has a higher branching ratio in respect to the 511keV line (0.68 to 2×0.19), the 511keV line has a higher amplitude. The 1040keV line has small probabilities of detection, as it is both moderately broadened and faint, due to its relatively

low branching ratio of 0.14. In some cases (panels on the right), its intensity is lower than the continuum intensity in the 200-500keV energy band. Finally, the most important parameter for the detection of the 511keV line is the Ps-fraction in the supernova ejecta. Assuming that the spectral shape of the 511keV line is broadened only according to the kinematics of ^{56}Co, it has the potential to be the second brightest candidate for detection (f=0, panels (a) and (b)), or to become not significant at all (f=1, panel (d)).

5. SN2014J

On the 21st of January 2014, astronomer Stephen J. Fossey and a group of undergraduate students at the University of London Observatory discovered a rise in luminosity on the south-west side of the nearby starburst galaxy M82 (Fossey et al. 2014). Immediate follow-up observations providing early spectra classified it as a type Ia supernova (Cao et al. 2014), later named SN2014J. At a distance of 3.5Mpc (Karachentsev and Kashibadze 2006), it was the closest type Ia supernova in the last four decades and offered a rare opportunity for detailed studies of supernova physics over a wide range of the electromagnetic spectrum, including the γ-ray band.

Zheng et al. 2014 reconstructed the inferred explosion date to be January 14.75+-0.21 UT, by fitting a broken power law on the early time rise of the SN. The full moon on the 16th of January 2014 allowed SN2014J to elude detection by major SN surveys, thus remaining concealed for almost a week after first light.

5.1. Host galaxy M82

Messier 82 or the Cigar galaxy is a spiral galaxy in the M81 Group with intense star-forming activity. Being a member of the constellation of Ursa Major, tidal interactions of M82 with its neighbor M81 approximately 10^8 years ago is believed to have triggered star-forming activity (Barker et al. 2008). Its canonical distance from the Milky Way varies between 3.3Mpc and 3.5Mpc (Karachentsev and Kashibadze 2006; Dalcanton et al. 2009). Throughout the thesis, a distance of 3.5Mpc $\pm$ 0.3Mpc is adopted.

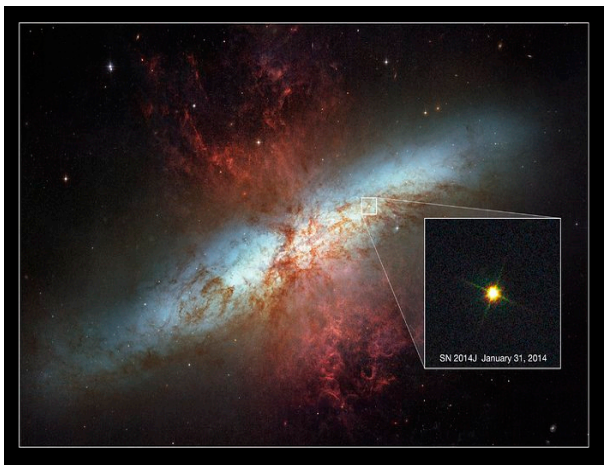

Figure 5.1.: Hubble's image of M82 and the location of SN2014J. From www.esa.int

SN2014J is located at galactic coordinates (l,b)=(141.427°, 40.558°), 55”2 west and 20”.0 south of the nucleus of M82. Observations in the optical suggest that SN2014J is a spectroscopically normal type Ia SN that suffers from absorption and reddening caused by dust particles in the host galaxy along the line of sight (Amanullah et al. 2014).

5.2. Analyses in other wavelengths

Soon after detection, an ensemble of ground-based and space telescopes, sensitive in a wide range of the electromagnetic spectrum, turned their fields of view towards SN2014J to use this unique opportunity and obtain high-quality spectra with high SNR of a nearby thermonuclear supernova.

Zheng et al. 2014 found that the rise of SN2014J cannot be explained adequately by the t^2-model. This model predicts that the early luminosity is proportional to the surface area of an expanding fireball and holds for the majority of early discovered explosions. Instead, an uncommon varying power-law seems to describe the early luminosity better, yielding an explosion time of January 14.75±0.21 UT. The physical explanation of this phenomenon is unclear, with the most plausible explanations being either changes in the photospheric temperature during expansion or perhaps a possible ^{56}Ni distribution in outer layers. Also Goobar et al. 2015 found hints of additional luminosity in the very early light curve indicating either shock heating of the SN2014J ejecta, interaction with circumstellar matter or the companion star, or the presence of radioactive elements at the outskirts.
The majority of early optical and NIR photometric and spectroscopic observations, though, classify SN2014J as a spectroscopically normal, heavily reddened supernova, with slightly high-velocity features and a layered structure with limited mixing. IMEs (Mg, S, Si) elements, as well as IGEs, were found at relatively high velocities with the only peculiarity being the absence of unburned carbon in the outer layers. These properties are consistent with models of a M_{Ch} explosion undergoing a deflagration to detonation transition (Zheng et al. 2014; Goobar et al. 2014; Marion et al. 2015; Goobar et al. 2015; Galbany et al. 2016).

Parameters	Marion et al. 2015	Goobar et al. 2014
$E(B\text{-}V)_{M82}$	1.23 ± 0.01mag	2.5 ± 1.3mag
R_{VM82}	1.46	1.4 ± 0.15
A_{VM82}	1.80	2.5 ± 1.3
$E(B\text{-}V)_{MW}$	0.05mag	0.14mag
R_{VMW}	3.1	3.1
A_{VMW}	0.155	0.43
m_{Bmax}	11.68 ± 0.01mag	–
M_{Bmax}	-19.19 ± 0.10mag	–
t_{Bmax}	Feb1.74 ± 0.13UT	–
Δm_{15}	1.11 ± 0.02mag	–

Table 5.1.: SN2014J optical properties

Tab. 5.1, presents the key parameters derived from optical spectra, determined by various groups. SN2014J was extensively studied also in other energy bands. No-detections in the X-rays and radio were useful to place upper limits in the density of the circumbinary medium and the mass loss of the progenitor system in its pre-supernova evolution (Margutti et al. 2014, Pérez-Torres et al. 2014). In particular, these studies suggest a tenuous medium around SN2014J and favor the DD scenario, known for its clean environment around the SN. However, cavities could also be formed by recurrent novae.

Kelly et al. 2014 analyzed optical, pre-explosion images of the region where SN2014J exploded and excluded a bright red giant and a symbiotic recurrent nova system. Goobar et al. 2014 found the

closest object located 0".2 from the SN location, but exclude it as the companion star, due to its brightness, displacement and the lack of radio emission.

Kundu et al. 2017 modeled the radio emission of SN2014J and concluded that a few not very well constrained parameters, like the magnetic field strength of thermonuclear supernovae, do not allow stringent results for the nature of the progenitor system. Nonetheless, radio observations point toward DD progenitors, spin-up-spin-down models, or even a few SD binaries, like a He star under certain conditions.

Diamond et al. 2018 studied the emission lines of iron group elements of SN2014J in the NIR and drew conclusions about the progenitor WD, possible mixing in the central regions and the magnetic field strengths. In particular, they concluded that the exploded object was a Chandrasekhar WD with $\rho = 0.7 \times 10^9$ g/cm^3 that underwent delayed detonation and might have ignited off-center. They also found evidence of some limited mixing of stable and radioactive iron group elements in the central regions and suggested the existence of a magnetic field.

Lundqvist et al. 2015 found no evidence of a non-degenerate companion star based on late phase optical observations, thereby favoring a degenerate companion star or a WD merger. However, in case of a large orbital separation, hydrogen or helium companion stars are also plausible as companions of the exploded WD. Srivastav et al. 2016 investigated ionized iron lines in the nebular phase and proposed a certain degree of clumpiness in the ejecta.

Finally, Yang et al. 2017 used very late time HST images to investigate the processes that power the light curve after the majority of ^{56}Ni and ^{56}Co has decayed. They found that one year after the explosion, the SN dims more rapidly than the light curve powered solely by the energy deposition of positrons. They suggest that a fraction of positrons may avoid thermalization and escape the supernova ejecta. By estimating the abundance of ^{57}Ni needed to explain the flatness of the lightcurve three years after the explosion, they favor a Chandrasekhar mass explosion.

5.3. Analyses in the gamma-regime

The relatively short distance to M82 made SN2014J a unique target to study the emitted γ-radiation of a thermonuclear supernova for the first time since the advent of γ-ray astronomy. SPI turned its field of view towards SN2014J on January 31, approximately 16.6 days after the inferred explosion date and around maximum light. The observations continued from this time forward until February 18, covering revolutions 1380-1386, $\approx$ 35 days after the explosion. In revolution 1388 a giant solar flare commenced. Despite the enhanced solar activity, SPI resumed observations 40.6 days after the explosion, that lasted until April 24, more than three months after first light, accumulating thereby 2.8Ms of exposure. This time window offers the opportunity to search for early ^{56}Ni lines in the first few orbits and shed light on the presence of radioactive isotopes on the outskirts of the ejecta, as predicted by some models. The following weeks cover the epoch, where the γ-ray emission is expected to peak. Finally, after an observation gap of approximately one month, additional 1.4Ms of exposure were accumulated in a period, when the supernova envelope is expected to be completely transparent to γ-rays. At this time, the complete bulk of the radioactive material should allow estimates of the total radioactive mass synthesized during the explosion.

Three studies, using three independent approaches for the background treatment, analyzed the data accumulated during INTEGRAL's SN2014J campaign:
Isern et al. 2016 focused on the emission near maximum optical light and found evidence of a broad redshifted feature that corresponds to the 158keV emission of ^{56}Ni decay, as well as a flux

excess in the 720-870keV energy band. In more detail, by analyzing the averaged spectrum of revolutions 1380-1381, they were able to fit a Gaussian line on the 158keV line, yielding a flux of $1.59 \pm 0.57 \times 10^{-4}$ ph/cm^2/s, a line centroid at 154.0 ± 0.64keV and a width of 3.7 ± 1.5keV with a statistical significance of 2.8σ. In analogy, a similar fit produced a flux of $1.5 \pm 0.7 \times 10^{-4}$ ph/cm^2/s, a line centroid at 733.4 ± 3.8keV and a FWHM of 16.9 ± 9.0keV with a statistical significance of 2.1σ for the 750keV line. The line blending of the 812keV line of ^{56}Ni with the 847keV line of ^{56}Co prevented any spectroscopic analysis for these lines. This unusually broad redshift was interpreted as a plume of ^{56}Ni, transparent in γ-rays, that was detached from the main bulk of the ejecta with an expansion velocity of 30.000 km/s[1]. The plume had a mass of $0.08 M_\odot$, a dispersion velocity of 10.000 km/s and receded from the observer with a velocity of 6000 km/s. They concluded their analysis by suggesting models with radioactive material in the outermost layers to describe SN2014J.
Another study by Churazov et al. 2015 focused on the ^{56}Co emission lines 50-100 days after the explosion. This group reports broad lines features at 847keV and 1238keV and by converting the line fluxes to ^{56}Ni mass, could derive a total synthesized ^{56}Ni mass of $0.61 \pm 0.13 M_\odot$. Their best-fit parameters for the two most prominent ^{56}Co lines are given in Tab. 5.2.

Line	Flux [10^{-4} ph/cm^2/s]	Bulk velocity [km/s]	Spread velocity [km/s]
847keV	2.23 ± 0.74	-1900 ± 1600	3600 ± 1300
1238keV	2.78 ± 0.74	-4300 ± 1600	4700 ± 1300

Table 5.2.: Spectral properties of the ^{56}Co lines of SN2014J from the analysis of the SPI data by Churazov et al. 2015

By averaging the velocities of both lines, they report an average blue-shift of -3100± 1100 km/s and a Doppler broadening of 4.100±1650 km/s for the radioactive ^{56}Ni in the supernova ejecta. They conclude that the SN2014J γ-ray spectrum broadly agrees with the predictions of a nearly-Chandrasekhar WD that underwent deflagration or a delayed detonation.

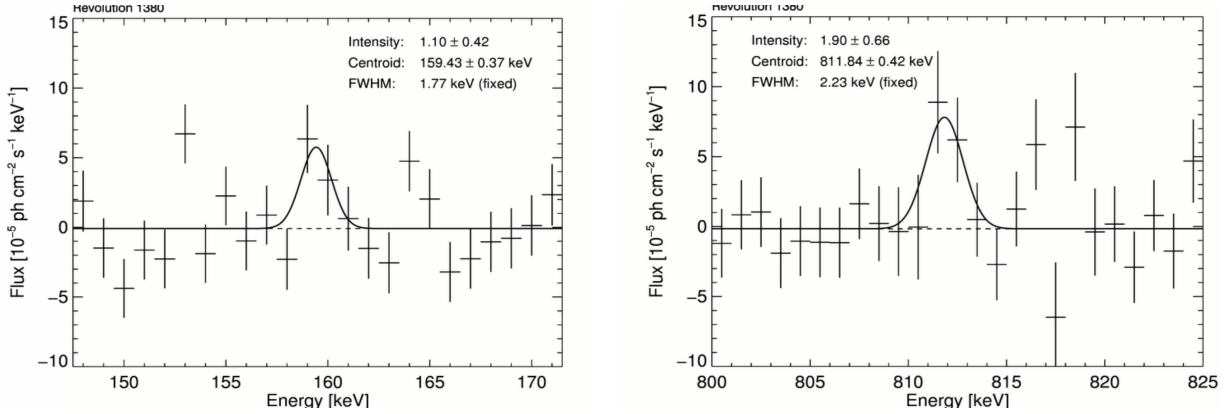

Figure 5.2.: Spectra in the energy ranges of the 158keV and 812keV ^{56}Ni lines, obtained 16.6-19.0 days after the explosion. (From Diehl et al. 2014).

Our high-energy group also examined the SPI data accumulated in the first revolution of the SN2014J campaign and detected early unshifted ^{56}Ni lines in the very first orbit of the SN2014J campaign (days 16.6-19.0 past explosion, Diehl et al. 2014). As narrow as the instrumental res-

olution of SPI allows, the two strongest ^{56}Ni lines at 158keV and 812keV were detected close to their laboratory energies (E_0=159.4±0.4 and E_0=811.8±0.4keV) with fluxes 1.10±0.42×10^{-4} ph/cm^2/s and 1.90±0.66e×10^{-4} ph/cm^2/s, respectively, corresponding to an initial ^{56}Ni mass of 0.06±0.03$M_\odot$ near the surface. Tab. 5.3 reports the fitted parameters of the two prominent lines of ^{56}Ni.

Line	Flux [10^{-4} ph/cm^2/s]	Bulk velocity [km/s]	Spread velocity [km/s]
158keV	1.10 ± 0.42	≤ 2000	≤ 2000
812keV	1.90 ± 0.66	≤ 2000	≤ 2000

Table 5.3.: Spectral properties of the ^{56}Ni lines of SN2014J from the SPI data analysis by Diehl et al. 2014

The values given in Tab. 5.3 stand in contrast with most explosion models containing a shell of ^{56}Ni in their outer envelopes and predict blue-shifted ^{56}Ni lines. To explain the observed properties, a configuration consisting of a WD having an equatorial He belt, accreted from a He star was proposed. If the accretion satisfies certain conditions (Law and Ritter 1983), this belt could remain constrained close to the equator of the WD and not spread in a shell around the object. Following the thermonuclear runaway, most of the accreted He belt would be converted into an optically thin equatorial ^{56}Ni belt. If this configuration is observed pole-on, it can explain qualitatively the properties of the ^{56}Ni lines and simultaneously not violate observations in other wavelengths.

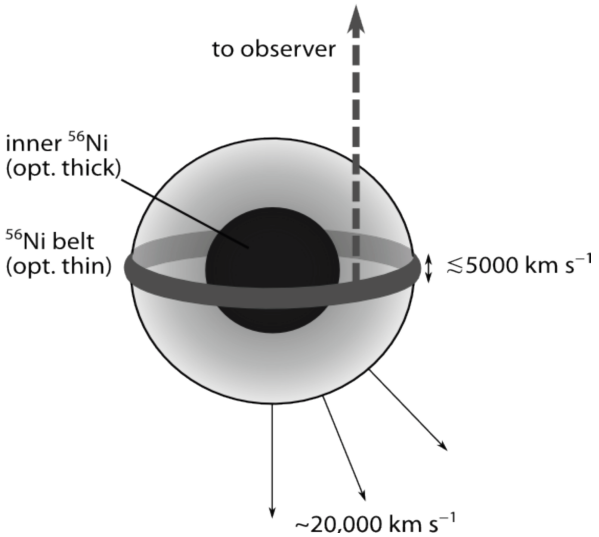

Figure 5.3.: Sketch of an ejecta configuration of SN2014J compatible with SPI observations. For details, see text. From Diehl et al. 2014.

In a follow-up study, our group examined the entire observation set of SN2014J searching for the two dominant ^{56}Co decay lines Diehl et al. 2015. For this, the entire observation dataset was subdivided into four epochs and Gaussian lines were fitted, in an attempt to construct a γ-ray light curve. Epoch one covered days 16.3-41.3, epoch two 41.3-66.3, epoch three 66.3-99.1 and epoch four 134.8-164.0 days after the explosion. Tab. 5.4 presents the fitted parameters of the 847keV and 1238keV lines for each epoch.

Epoch	$Flux_{847}$	$Centroid_{847}$	$Width_{847}$	$Flux_{1238}$	$Centroid_{1238}$	$Width_{1238}$
Epoch 1	2.34	827.2	14.3	0.91	1259.1	17.7
Epoch 2	2.74	851.3	11.1	1.11	1259.1	17.7
Epoch 3	3.65	851.3	20.4	2.27	1259.1	17.7
Epoch 3	1.90	846.6	12.9	0.38	1244.9	18.8

Table 5.4.: Fitted parameters of the ^{56}Co lines of SN2014J in four epochs. The fluxes are given in units of [10^{-4} ph/cm^2/s]. Line centroids and widths in units of [keV]. A few parameters were fixed to values obtained from the fitting of the 847keV line. For more details, see Diehl et al. 2015.

Using the fluxes from the brightest epoch (epoch three) and assuming complete transparency, the analysis of our group estimates a model-independent initial ^{56}Ni mass of 0.50±0.12M$_\odot$. However, the data also suggest transient irregular, narrow line emission in the spectra of the first three epochs, indicating an asymmetric explosion. Another possibility to derive the ^{56}Ni mass synthesized during the explosion is by comparing the 847keV lightcurve to models provided by The and Burrows 2014 specifically made for SN2014J. By scaling the intensity of the best fitting light curves to the observations, a ^{56}Ni mass of 0.49±0.09M$_\odot$ was derived, which is consistent with the model-independent estimate.

Finally, an attempt to detect possible instantaneous positron annihilation in the supernova ejecta was made as part of my bachelor thesis in the year 2016 (Christodoulou 2016). Using the entire observation set, I detected a blue-shifted 511keV line with a detection significance of $\sim 2\sigma$. An ortho-positronium continuum was not found. Additionally, similar to the analysis of the ^{56}Co lines, I constructed a 511keV line light curve and compared it with model predictions of The and Burrows 2014.

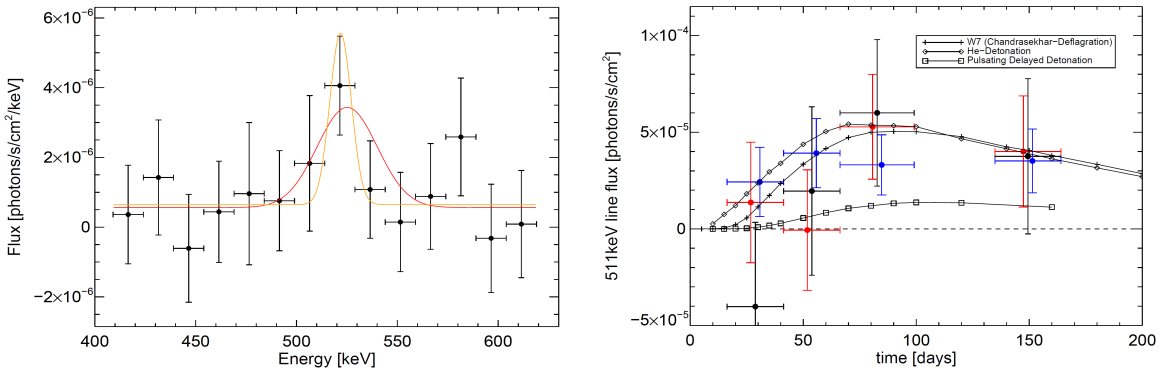

(a) 511keV mission integrated spectrum of SN2014J

(b) 511keV line light curve of SN2014J, divided in four epochs

Figure 5.4.: Left: Spectrum of the 420-630keV band over the entire observation period in 15keV energy binning fitted with Gaussian lines models: red corresponds to a free Gaussian line fit, orange to a Gaussian line with a fixed width. Right: 511keV line light curve of SN2014J for three different Gaussian line shape assumptions compared with the canonical deflagration model W7, the He-detonation model and the pulsating delayed detonation model from The and Burrows 2014. From Christodoulou 2016.

Tab. 5.5 summarises the fitted parameters obtained by fitting two different Gaussian line models to the data: a free Gaussian line fit (red) and a Gaussian line with a fixed width calculated from the ^{56}Co lines (orange).

Epoch	Flux [10^{-4} ph/cm^2/s]	E_0 [keV]	σ [keV]
red	1.08 ± 0.95	525.1 ± 9.1	14.9 ± 8.8
orange 2	0.66 ± 0.25	521.8 ± 3.3	5.3 ± 0.0

Table 5.5.: Fitted parameters of the positron annihilation line for the whole observation window. From Christodoulou 2016.

Based on the flux of the positron annihilation line, Siegert 2017 derived a positron escape fraction of η=0.06 ± 0.33 that can be converted into a galactic positron annihilation rate of $R^{e^+}_{SNIa}$=1.9 ± 11.9×10^{43} e$^+$/s[1], using a SNIa rate of one event per 200 years and a ^{56}Ni yield of 0.49±0.09$M_\odot$ per thermonuclear supernova.

5.4. This work

In my master thesis I examined the same SPI dataset our group used for analysis, with some modifications and extensions regarding the data analysis:

- I used the empirical modeling background approach, described in Sec. 4.7.1 and in detail in Siegert 2013 and in Diehl et al. 2018b, to derive the relevant SN2014J data.
- In order to exploit the complete dataset as much as allowed, the standard analysis procedure of our group; to neglect pointings near the radiation belts ($\leq$0.1 and $\geq$0.9 of the orbit) is relaxed. However, pointings are only added to the dataset, after careful inspection of both the space weather tracers (e.g. GeSatTot, ACSrate) and the residuals. This leads to an average additional observation time of $\sim 1.5\times10^4$ s per revolution[1].
- In observation windows including pointings with high background rates (e.g. rev. 1388-1390 or rev. 1405-1406), the background line parameters are scaled per pointing, instead of the standard scaling per orbit.
- A Seyfert galaxy named IGR J09254750+6929 located at (143.42°/38.44°) is added as a possible celestial source in addition to SN2014J located at (141.43°/40.56°). This source is not expected to produce emission in the aforementioned energy range yet is added for completeness.
- In addition to the ^{56}Ni and ^{56}Co lines detected in other analyses, a coherency check is performed by looking for expected spectral features in the energy bands of weaker lines, like the 750keV line of ^{56}Ni or the 1040keV line of ^{56}Co. Finally, a final consistency test is made, by fitting the lines of each isotope simultaneously.
- Since most of the γ-ray emission of a type Ia supernova lies between 100keV and 1250keV, the focus of this thesis is restricted in the energy range between 100 and 1350keV and includes only single detector events.

[1]This can be translated into $\sim$ 100 additional supernova photons per revolution, for a flux of 1×10^{-4}photons/cm^2/s and an effective area of 80cm^2.

The analysis is split into three main parts:

1. The first six revolutions of INTEGRAL's SN2014J campaign (rev.1380-1386) are inspected for possible ^{56}Ni decay emission in the energy ranges 140-180keV, 730-770keV and 800-840keV, searching for the 158keV, 750keV and 812keV lines; the three prominent lines of ^{56}Ni decay. Two different time windows were chosen:
   - The ^{56}Ni emission was traced in time scales of single revolutions, producing a time series of six spectra.
   - For data with a higher SNR, the emission of ^{56}Ni was studied by binning two revolutions together. The observation windows for this case are:
     a) Orbits 1380-1381, 16.6-22.0 days after the explosion
     b) Orbits 1382-1383, 22.6-28.0 days after the explosion
     c) Orbits 1384-1385, 28.6-34.0 days after the explosion
2. The whole observation data set, is used to explore the variability and the properties of the brightest ^{56}Co lines at 847keV, 1040keV and 1238keV in two different time scales.
   - In four epochs similar to the analysis of Diehl et al. 2015
   - In a 4-revolution time-scale, searching for the optimum between a high SNR ratio and the variability of the signal due to the decay of ^{56}Co
3. The energy range between 250 and 550keV is investigated for a possible positron annihilation signal in the supernova envelope. Possible detection of the ortho-Ps continuum would give insights into the annihilation conditions in the ejecta, while the width of the 511keV line could give clues on whether positrons annihilate instantaneously after creation or are able to propagate inside the supernova envelope before annihilating.

The whole exposure window consists of 2375 telescope pointings with a duration of typically ∼2000s. Multiplying this number with 15 working detectors at that time results in 35625 individual spectra for a total 4.2Msec of exposure. During this period, SN2014J was always within the field of view, while the telescope reorientated by 2.1° in every new pointing, in order to shift the shadowgram of the source in the detector plane.

5.5. Nickel lines

The short half-life of ^{56}Ni ($\tau_{1/2} \approx 6.1$days) leads to a high amount of γ-ray luminosity inside the young supernova remnant. The escape fraction of the ^{56}Ni decay γ-rays is a function of the expansion rate and the distribution of the radioactive material in the supernova ejecta (Gómez-Gomar et al. 1998). In supernova models with considerable amounts of ^{56}Ni at low optical depths, a considerable fraction of early ^{56}Ni γ-ray photos are expected to escape without interactions. Therefore, looking for possible early ^{56}Ni emission is considered a key diagnostic tool for the determination of the progenitor system that led to the thermonuclear runaway. Analyses of early SPI data (Diehl et al. 2014; Isern et al. 2016) detected significant ^{56}Ni emission and it is worth checking if this approach confirms their results.

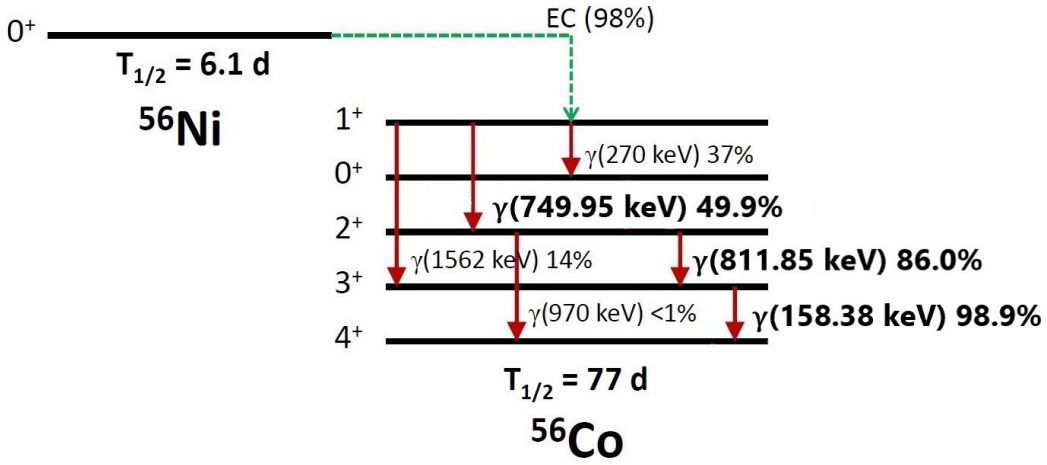

Figure 5.5.: Decay scheme of ^{56}Ni. The lines investigated in this analysis are marked with bolted font. The values next to the photon energies are the branching ratios of each transition. They give the probability of emitting a photon with the corresponding energy.

The decay of ^{56}Ni to ^{56}Co is followed by a cascade of nuclear de-excitation photons of the highly excited daughter nucleus. Five nuclear transitions in the energy range between 158keV and 812keV have a branching ratio higher than 30%, offering a variety of γ-ray lines for detection and analysis (see Fig. 5.5). In this thesis, the bands around the most prominent 158keV, 750keV and 812keV nuclear transitions were studied in time scales of ~ 3 and ~ 6 days for a possible signal from early ^{56}Ni decay γ-rays.

The best outlook for detection offers the 812keV line, due to its optimal energy positioning and high branching ratio of 86%. The transition of the $J^{\pi}=3^{+}$ nuclear level to the ground state ($J^{\pi}=4^{+}$) yields a 158keV photon with a branching ratio of almost 100%. The relatively low energy of the transition results in a modest line broadening due to ejecta expansion that leads to a high number of counts per energy bin. On the other hand, the relative high cross-section for photoelectric absorption at these energies (for details see Sec. 3.9), may reduce the number of escaping photons substantially, even if they are emitted near the surface. Two additional factors that complicate the analysis of this line are the intrinsic continuum of SN2014J, that reaches its maximum in the 100-200keV band, and the respectively increased background rate at these energies. A 750keV photon is emitted in $\approx 50\%$ of all ^{56}Ni decays, making its corresponding line a viable candidate for detection and important for direct comparisons with its neighboring 812keV line.

The first step is to investigate the spectrum around the 812keV line, which has according to models the highest detection probability. If the line is detected, the band around the less energetic 158keV line will be investigated for possible emission. The large energy difference ($\Delta E \approx 700$keV) between the two lines yields different Compton opacities and allows, therefore, a mass estimate of the overlying materials. Finally, by treating the 750keV line, a line that shares similar spectral features and opacities with the 812keV line, a coherency test is made.

5.5.1. 812keV line

The spectra presented in Fig. 5.6 focus on the γ-emission near the 800-840keV energy band and were fitted with a single Gaussian on top of an offset, a model able to describe accurately nuclear transitions in the keV regime. They show a clear flux excess in the vicinity of the 812keV line.

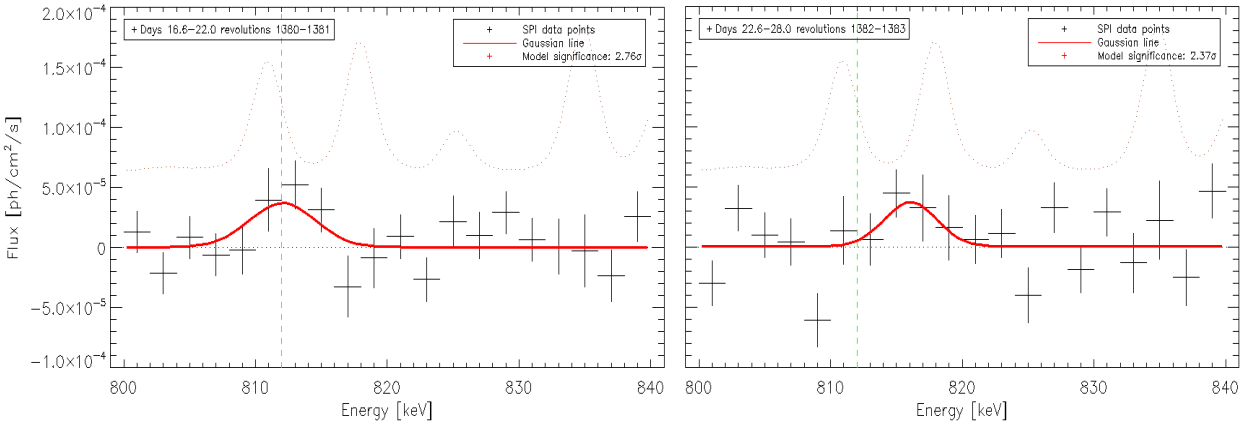

(a) 812keV line, epoch 1

(b) 812keV line, epoch 2

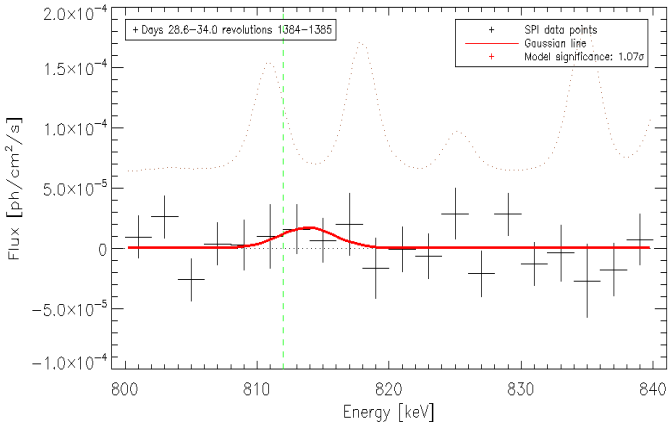

(c) 812keV line, epoch 3

Figure 5.6.: Time series of the 800-840keV band for revolutions 1380-1385. Every data point corresponds to an energy bin of 4keV.

The fitted line declines in strength and becomes broader with time(Tab. 5.6). This is consistent with the decay of ^{56}Ni and the gradual emergence of deeper layers of radioactive material.

Epoch	Flux [10^{-4} ph/cm^2/s]	E_0 [keV]	Bulk velocity [km/s]	σ [keV]	Spread velocity [km/s]
Rev 1380-1381	2.31 ± 1.42	812.0 ± 0.6	20 ± 250	2.5 ± 0.6	2000 ± 600
Rev 1382-1383	1.84 ± 1.71	816.1 ± 0.8	1500 ± 300	2.0 ± 0.7	1550 ± 750
Rev 1384-1385	0.88 ± 1.64	813.8 ± 2.9	660 ± 1080	2.1 ± 3.2	1620 ± 3100

Table 5.6.: 812keV line fitted parameters of SN2014J, three epochs

The bulk velocity of the line in the first observation window is negligible. This supports the configuration suggested in Diehl et al. 2014 of a ^{56}Ni-belt located near the equator of the WD. Using Eq. (5.1) the measured flux of the first epoch can be converted into an initial mass of:

$$\begin{aligned} M(^{56}\mathrm{Ni}, t = 0) &= 4 \cdot \pi \cdot d_{M82}^2 \cdot F_{812keV} \cdot m_{Ni} \cdot \exp\left(\frac{t}{\tau_{Ni}}\right) \cdot \frac{1}{p_{812keV}} \\ &= 0.13 \pm 0.07 M_\odot, \end{aligned} \tag{5.1}$$

where $F_{812\mathrm{keV}}$ denotes the flux of the 812keV line, d_{M82} is the distance between the instrument and M82, τ_{Ni} the mean lifetime of ^{56}Ni, m_{Ni} the atomic mass of ^{56}Ni and $p_{812\mathrm{keV}}$ the branching ratio of the 812keV line.

The derived ^{56}Ni mass is twice the amount found in Diehl et al. 2014. However, with a statistical significance of $\sim 3.3\sigma$, its detection is firm. To test the robustness of the signal, an 812keV light-curve was constructed and compared to explosion models from The and Burrows 2014.

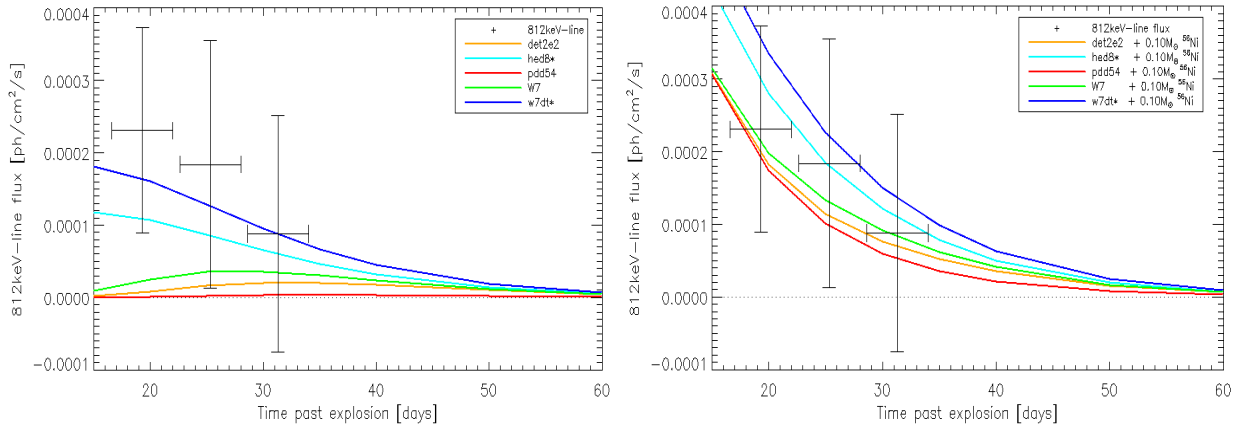

(a) 812keV line light curve compared to models of The and Burrows 2014

(b) 812keV line light curve compared to the same models with additional 0.1M$_\odot$ ^{56}Ni

Figure 5.7.: Left: 812keV-line lightcurve of SN2014J compared with representative models from The and Burrows 2014. Right: A completely transparent ^{56}Ni shell with a total mass of 0.1M$_\odot$ was placed on the surface of the models from The & Burrows. Models with an asterisk indicate the presence of ^{56}Ni in the outer layers.

Fig. 5.7 shows the calculated line fluxes as a function of time. Despite the large error bars, most data points stand higher than the ones from the models (left). Even models with the highest amount of ^{56}Ni in their surface, like w7dt or hecd lie 50% below the fitted fluxes. In order to visualize quantitatively the amount of additional ^{56}Ni needed to explain the fitted fluxes, a completely transparent shell of 0.1M$_\odot$ was placed on the surface of the models (panel on the right). This simplified approach to enhance the flux of the 812keV-line certainly violates the structure of the explosion, as well as optical spectra, opacities, etc., but indicates that a considerable amount of additional ^{56}Ni is needed to explain the observed fluxes in all observation windows.

Evolving further this idea, the amount of additional transparent ^{56}Ni needed to match the fluxes was fitted for all 15 models (for details, see Appendix).

Model	Additional ^{56}Ni mass [$M_\odot$]	Total ^{56}Ni mass [$M_\odot$, outer layers	Significance [σ]
dd202c	$0.11\pm0.07M_\odot$	$0.11\pm0.07M_\odot$	1.57
dd4	$0.12\pm0.07M_\odot$	$0.12\pm0.07M_\odot$	1.79
det2	$0.10\pm0.07M_\odot$	$0.10\pm0.07M_\odot$	1.49
det2e2	$0.13\pm0.07M_\odot$	$0.13\pm0.07M_\odot$	1.87
det2e6	$0.14\pm0.07M_\odot$	$0.14\pm0.07M_\odot$	1.98
hecd	$0.05\pm0.07M_\odot$	$\geq0.05\pm0.07M_\odot$	0.75
hed6	$0.12\pm0.07M_\odot$	$\geq0.12\pm0.07M_\odot$	1.64
hed8	$0.07\pm0.07M_\odot$	$\geq0.07\pm0.07M_\odot$	1.03
m36	$0.11\pm0.07M_\odot$	$0.11\pm0.07M_\odot$	1.66
pdd54	$0.13\pm0.07M_\odot$	$0.13\pm0.07M_\odot$	1.97
W7	$0.12\pm0.07M_\odot$	$0.12\pm0.07M_\odot$	1.72
W7A	$0.11\pm0.07M_\odot$	$\geq0.11\pm0.07M_\odot$	1.55
w7dn	$0.10\pm0.07M_\odot$	$0.14\pm0.07M_\odot$	1.40
w7dt	$0.04\pm0.07M_\odot$	$\geq0.22\pm0.07M_\odot$	0.55
W7E	$0.06\pm0.07M_\odot$	$\geq0.06\pm0.07M_\odot$	0.89

Table 5.7.: Fitted masses of additonal ^{56}Ni for SN2014J

The masses given in Tab. 5.7 are consistent with the mass derived in Eq. (5.1) showing that, with a significance around $\sim 2\sigma$, a considerable amount of the synthesized ^{56}Ni is visible around the maximum optical light of the supernova.

812keV line source grids

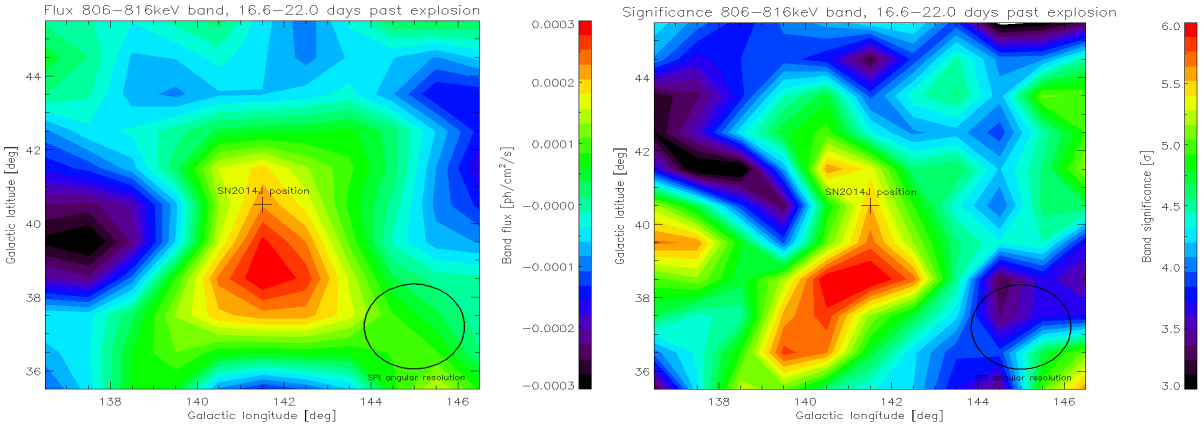

(a) Flux map, rev. 1380-1381

(b) Significance map, rev. 1380-1381

Figure 5.8.: Flux and significance maps in a $10°\times10°$ grid around SN2014J for revolutions 1380-1381. Left: The flux in the 806-816keV band is integrated and color-coded for every grid of the map. Right: The significance of the emission for each grid is calculated by comparing the χ^2-values of spimofit-runs with and without a fitted source. The circle on the bottom right shows the angular resolution of SPI at these energies ($\sim 2.3°$)

Source grids are valuable in order to check whether the observed emission comes indeed from source or it is subject to systematic uncertainties of the strong background of SPI. A point source resembling SN2014J is fitted in steps of 1° for galactic longitudes between 136.5° and 146.5° and

galactic latitudes between 35.5° and 45.5°. Should the maximum emission come from the area where SN2014J is located, it would provide additional evidence that the signal comes indeed from the explosion.

The source grids presented in Fig. 5.8 show that most of the emission in this energy range comes from the area in the sky where SN2014J is located. The exact SN2014J was assumed to be at (141.43° | 40.56°). The small offset between the coordinates of SN2014J and the coordinates of the highest significance is smaller than the angular resolution of the instrument. In contrast to other studies of SPI data (Diehl et al. 2014; Churazov et al. 2015) a 10° x 10° instead of a 20° x 20° source grid was chosen, in order to avoid artificial emissions in areas of the sky far away from SN2014J, where the observation time is limited and the resulting SNR low.

5.5.2. 158keV line

After the detection of the 812keV line, it is worth analyzing the 158keV line and inspect, whether 158keV photons from the ^{56}Ni decay are able to avoid absorption.

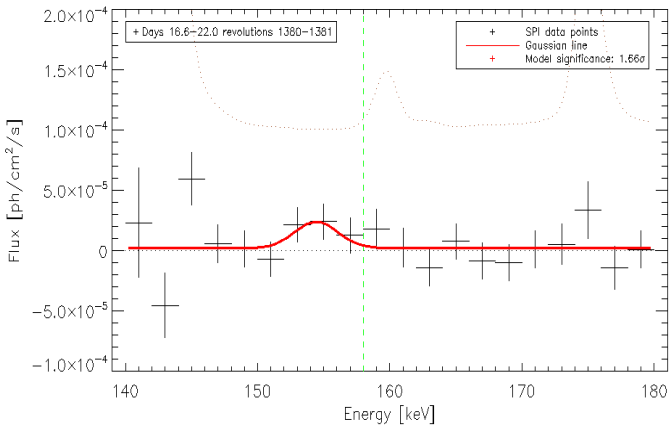

(a) 158keV line, epoch 1

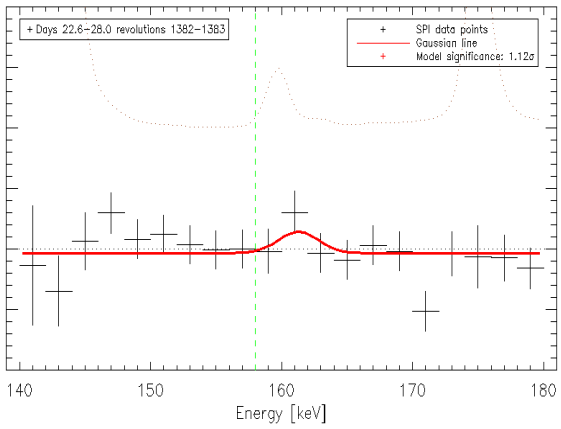

(b) 158keV line, epoch 2

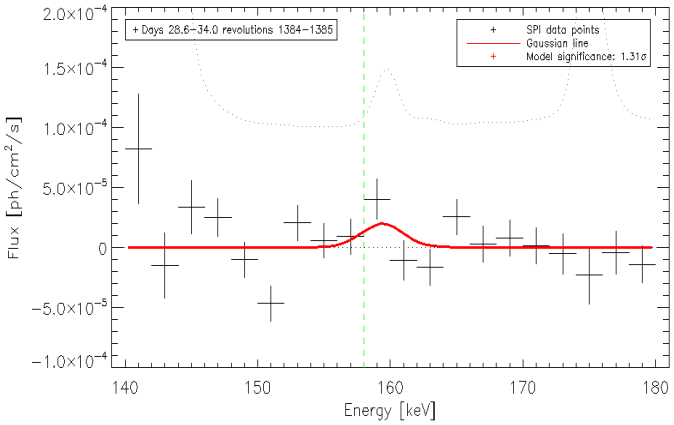

(c) 158keV line, epoch 3

Figure 5.9.: Time series of the 140-180keV band for revolutions 1380-1385. Every data point corresponds to an energy bin of 4keV.

Fig. 5.9 depicts the spectra in the vicinity of the 158keV line of ^{56}Ni. An excess flux is apparent, albeit not as significant as for the more energetic 812keV line.

Epoch	Flux [10^{-4} ph/cm^2/s]	E_0 [keV]	Bulk velocity [km s^{-1}]	σ [keV]	Spread velocity [km s^{-1}]
Rev 1380-1381	0.88 ± 0.57 [0.64]	154.4 ± 0.9	6750 ± 1800	1.6 ± 0.8	6400 ± 2100
Rev 1382-1383	0.68 ± 1.21 [0.93]	161.3 ± 1.3	6250 ± 2400	1.6 ± 1.3	6150 ± 6400
Rev 1384-1385	0.76 ± 1.03 [1.17]	159.4 ± 1.7	2700 ± 3300	1.6 ± 1.7	6150 ± 8600

Table 5.8.: 158keV line fitted parameters of SN2014J, three epochs. Flux values in square brackets present the 2σ upper limits in units of [10^{-4} ph/cm^2/s]

The fitted parameters displayed in Tab. 5.8 result from a free Gaussian fit in the energy band of the 158keV line. Since the significances of the fits do not exceed 1.7σ, no firm conclusions can be drawn from this line. Comparing Tabs. 5.6 and 5.8 indicates a discrepancy between the two lines emitted from the same radioactive isotope. The broad and highly red-shifted line observed in the first observation window is similar to the result from Isern et al. 2016. However, its statistical significance is low and the spectra may be influenced by the Compton down-scattered photos of higher energy lines.
In order to remain consistent with the results of Sec. 5.5.1, 2σ upper limits were calculated, thereby fixing the line width and centroid to the values obtained from the 812keV-line analysis.

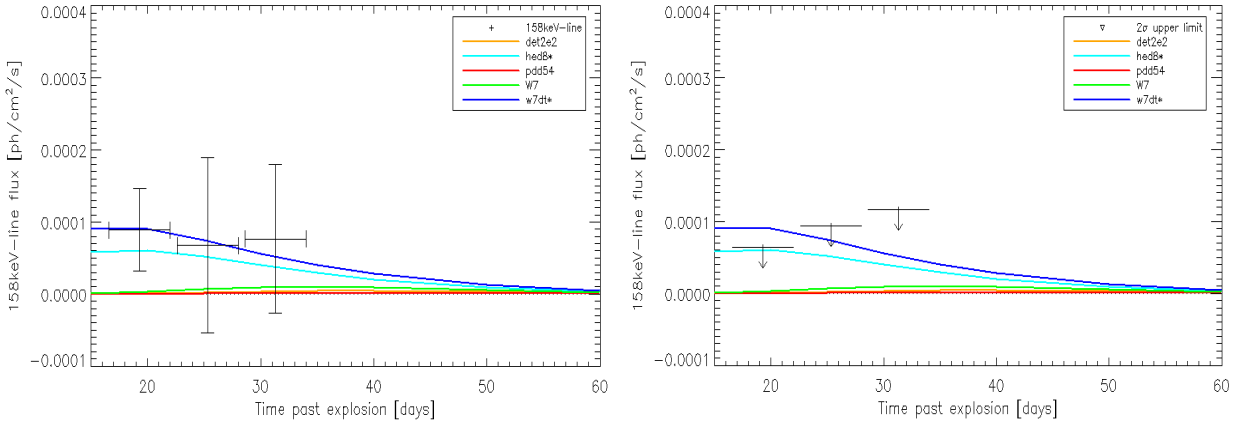

(a) 158keV line light curve compared to models of The and Burrows 2014

(b) 158keV line upper limits compared to models of The and Burrows 2014

Figure 5.10.: Left: 158keV-line lightcurve of SN2014J compared with models from The and Burrows 2014. Right: Right: 158keV line 2σ upper limits. Models with an asterisk indicate the presence of ^{56}Ni in their outer layers.

Both light curves and upper limits are consistent with the existence of radioactive material in low optical depths. However, due to large error bars and a low statistical significance, firm conclusions can not be made. It is clear, though, that the 158keV emission is substantially lower than the corresponding 812keV emission. This suggests that the radioactive source is not located directly on the surface, but further inside at an optical depth, where only 812keV line photons can freely escape and a large fraction 158keV line photons do not.

5.5.3. 750keV line

A 750keV photon is emitted in ≈ 50% of all ^{56}Ni decays, making its corresponding line a viable candidate for detection and important for direct comparisons with the spectral properties of its neighboring 812keV line.

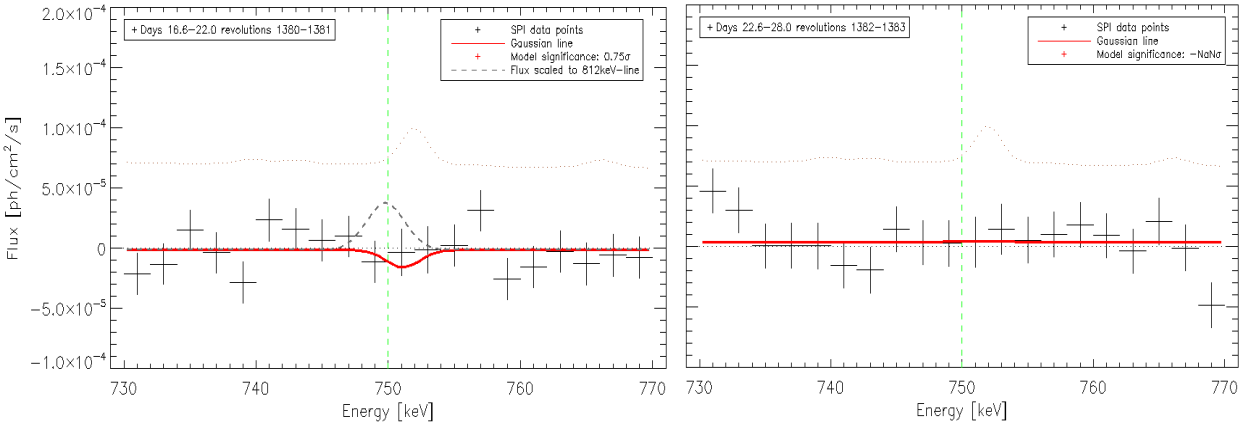

(a) 750keV line, epoch 1

(b) 750keV line, epoch 2

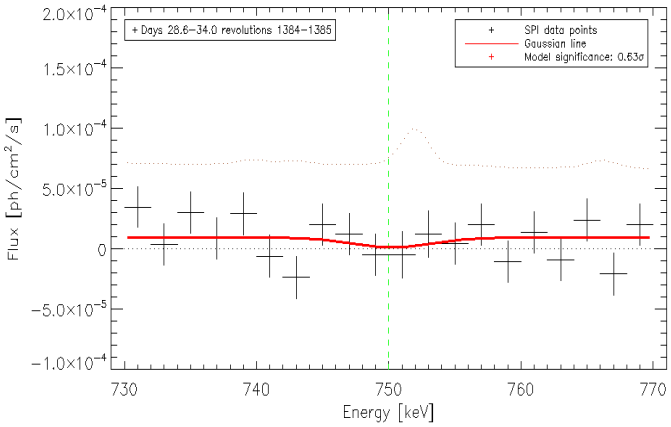

(c) 750keV line, epoch 3

Figure 5.11.: Time series of the 730-770keV band for revolutions 1380-1385. Every data point corresponds to an energy bin of 4keV. In epoch 1, the dashed grey line indicates the form of the spectral feature of the 750keV line, according to the corresponding detected 812keV line.

In Fig. 5.11, no spectral feature corresponding to the 750keV line emission can be identified. In fact, the dashed grey line depicted on panel (a) represents the 750keV emission expected from the 812keV line and can be rejected with a significance of $\sim 3.06\sigma$. Being only ∼60keV apart from the 812keV line, the Compton cross-section for the two lines should be nearly the same, thus resulting in comparable escape fractions and line shapes for both lines. Since no significant emission was found in the spectra, 2σ upper limits were calculated. The line centroids and widths of the lines were drawn from the analysis of the 812keV line.

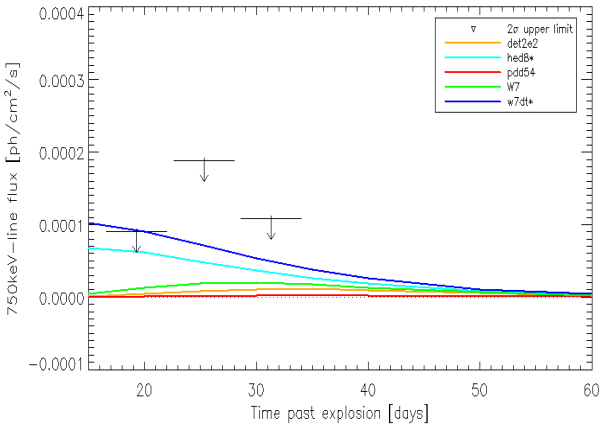

Figure 5.12.: 750keV line 2σ upper limits if SN2014J in three epochs.

Epoch	2σ upper limits [10^{-4} ph/cm^2/s]
Revolutions 1380-1381	0.90
Revolutions 1382-1383	1.89
Revolutions 1384-1385	1.08

Table 5.9.: 750keV line upper limits of SN2014J, three epochs

The derived upper limits do not exclude the presence of radioactive material in the outskirts, as they are above the light curves of the brightest models. However, all three limits are in contrast with the measured fluxes of the other two lines that report an even higher amount of ^{56}Ni in the outskirts.

5.5.4. Simultaneous fit of ^{56}Ni

The most reliable verification of the ^{56}Ni-decay emission is to fit the strongest lines simultaneously and check the consistency of the signal. A fitting model consisting of three Gaussian lines depends on five parameters: three independent line amplitudes, one common line width, and one common line centroid, both of them adjusted for the energy of each line (for details, see Appendix). The model allows different intensities between the lines but constrains them to share the same spectral shapes, relying on the argument of common origin. Scaling the amplitudes to the branching ratios of the lines too could yield difficulties, as the 158keV line and the higher energy lines share different Compton opacities and photoelectric absorption cross sections. Allowing them to have different intensities, intensity ratios can be produces that may be compared to models. A simultaneous fit contains several advantages:

The energy differences between the three lines allow additional emission validity checks. Most importantly, the 750keV line and the 812keV line should share approximately the same Compton opacity and their line flux ratio is expected to be compatible with their branching ratios. The 158keV line, on the other hand, should be affected by increased Compton scattering photoelectric absorption cross sections, as already illustrated in Fig. 3.13. If the 158keV photons escape and appear in the spectrum, this implies that also the two higher-energy lines should be present in their corresponding energy ranges and line broadenings.

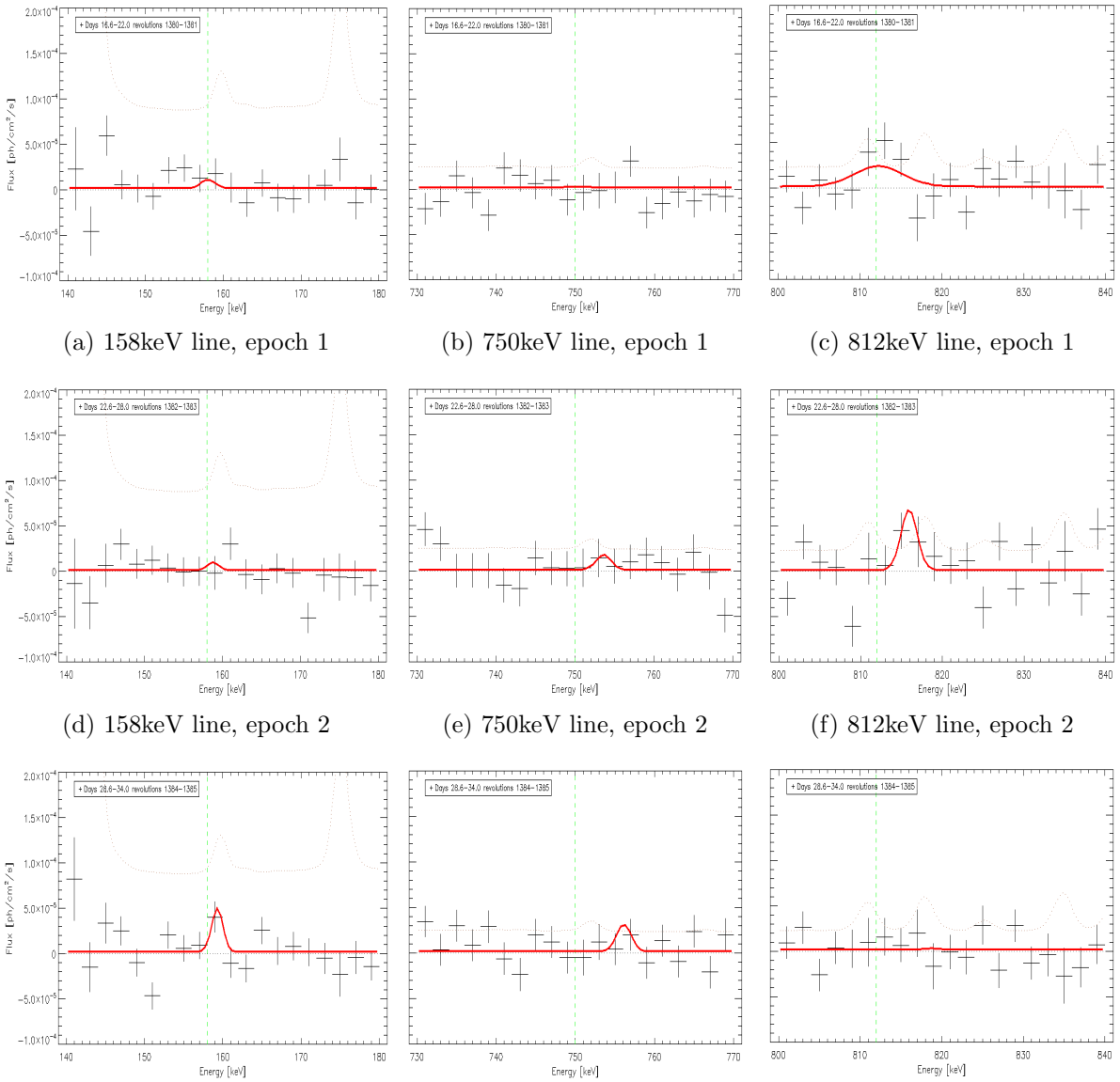

(a) 158keV line, epoch 1 (b) 750keV line, epoch 1 (c) 812keV line, epoch 1

(d) 158keV line, epoch 2 (e) 750keV line, epoch 2 (f) 812keV line, epoch 2

(g) 158keV line, epoch 3 (h) 750keV line, epoch 3 (i) 812keV line, epoch 3

Figure 5.13.: Simultaneous fits of the ^{56}Ni lines for all three epochs. Each data point corresponds to an energy bin of 4keV

Epoch	Significance of fit [σ]	Bulk velocity [km/s]	Spread velocity [km/s]
Epoch 1	2.48	90 ± 800	2500 ± 1600
Epoch 2	3.04	1450 ± 150	300 ± 1200
Epoch 3	2.60	2450 ± 200	50 ± 750

Table 5.10.: Properties of the simultaneous ^{56}Ni line fitting

Fig. 5.13 presents the simultaneous fitting of the 158keV, 750keV and the 812keV lines of 56Ni for the three studied epochs. The spectral properties of the lines are inconsistent with each other. In particular, spectral features seen in one energy band cannot be identified in other bands nor in

following observation windows.

The inconsistency of the emission is not only apparent in the low significance of the fits, but also in the variation of the fitted velocities. The parameters presented in Tab. 5.22 trigger two key questions:

- Why do the lines become bluer with time? Relying on the argument of homologous expansion, the bluer parts of the line should be the first to escape the expanding material. With progressive time, the line should gradually move back to the laboratory value, as a consequence of the increased transparency due to ejecta expansion.
- Why do the line widths decrease with time? This is also inconsistent with theoretical expectations. As time passes, emission from a progressively larger fraction of the ejecta and at different velocities should be able to escape. This would cause a gradual broadening of the line.

Even if an exotic model with a high degree of asymmetry and clumpiness may be able to explain the above-displayed emission, it would fail in explaining the derived line flux ratios:

Line fluxes	Epoch 1	Epoch 2	Epoch 3
F_{158keV} [10^{-4} ph/cm^2/s]	0.22 ± 0.28	0.15 ± 0.28	0.87 ± 0.27
F_{750keV} [10^{-4} ph/cm^2/s]	0.06 ± 0.53	0.41 ± 0.38	0.69 ± 0.29
F_{812keV} [10^{-4} ph/cm^2/s]	1.66 ± 1.14	1.68 ± 0.93	0.03 ± 0.39
F_{812keV}/F_{158keV} (nom. 0.87)	7.71 ± 11.3	11.1 ± 21.5	0.03 ± 0.45
F_{750keV}/F_{812keV} (nom. 0.58)	0.03 ± 0.32	0.24 ± 0.27	22.3 ± 282

Table 5.11.: ^{56}Ni line fluxes and ratios, simultaneous fitting.

In Tab. 5.22 the F_{812keV}/F_{158keV}-ratios of the first two epochs are reasonable. 158keV-line photons are trapped in the ejecta. However, the large deviation of the F_{750keV}/F_{812keV}-ratio in respect to the nominal value, lowers the validity of the 812keV signal. In epoch three, while the spectra near the 158keV and 750keV lines could be fitted with Gaussian lines, the non-detection in the 812keV-line questions their validity.

Redshifted 847keV line test

An exotic explanation of the flux excess seen in the vicinity of the 812keV line in connection to the complete absence of 750keV photons is to assign the former to red-shifted ^{56}Co 847keV photons. In particular, a red-shifted ^{56}Co clump, with low expansion velocities and receding from the observer with velocities between 10000-12000km/s could produce the observed emission.

$$\begin{aligned} \mathrm{M}(^{56}\mathrm{Co}, \mathrm{t} = 19.3\mathrm{d}, \mathrm{SN2014J}) &= 4 \cdot \pi \cdot \mathrm{d}_{\mathrm{M82}}^2 \cdot \mathrm{F}_{847\mathrm{keV}} \cdot \mathrm{m}_{\mathrm{Co}} \cdot \exp\left(\frac{\mathrm{t}}{\tau_{\mathrm{Co}}}\right) \cdot \frac{1}{\mathrm{p}_{847\mathrm{keV}}} \\ &= 0.19 \pm 0.11 \mathrm{M}_{\odot} \end{aligned} \tag{5.2}$$

If the flux near 812keV is assigned to a redshifted 847keV line, $0.19\mathrm{M}_{\odot}$ of ^{56}Co are visible 19.3 days after the explosion, as dictated by Eq. (5.2). This amount of ^{56}Co could be available at that time, as a large fraction should already have been produced through the decay of ^{56}Ni. However, most

explosion models do not predict large abundances of radioactive material at low optical depths, especially receding from the observer with $\sim$ 10000km/s. It would indicate large asymmetries that were not reported in studies of other energy bands.

One model-independent method to judge this possibility is to search for the corresponding red-shifted flux excess in the vicinity of the 1238keV line (for details on the γ-ray photons from ^{56}Co, see Fig. 5.17). By scaling the fitted parameters of the redshifted 847keV line to the energy and the branching ratio of the 1238keV line, the shape of the latter can be reconstructed and tested on the data.

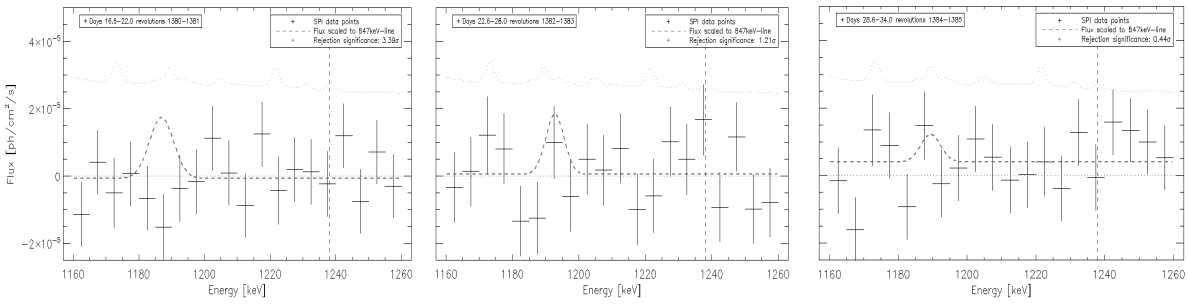

(a) Expected 1238keV line, epoch 1

(b) Expected 1238keV line, epoch 2

(c) Expected 1238keV line, epoch 3

Figure 5.14.: Gamma-ray spectra between 1160-1260keV. The laboratory position of the 1238keV is represented by a dashed blue vertical line. The dashed grey slope marks the expected 1238keV signal, under the assumption that the flux excess at 812keV originates from red-shifted 847keV line photons. Each data point corresponds to an energy bin of 10keV.

Panels (a), (b) and (c) of Fig. 5.14 dismiss the possibility that the emission at 812keV originates from a bulk of receding ^{56}Co, with a significance of 3.39σ, 1.21σ and 0.44σ for epochs 1,2 and 3, respectively.

Destruction of 750keV photons

Another possibility to explain the observed spectra in the early revolutions of INTEGRAL's SN2014J campaign and the inconsistency between the spectral features is to assign the observed flux excess at $\sim$ 812keV to ^{56}Ni and presume a destruction mechanism that affects predominantly 750keV photons over 812keV photons. Compton scattering and photoelectric absorption affect 750keV and 812keV photons almost equally and can be ruled out. One candidate interaction could be the photon-photon pair production mechanism, presented in Sec. 3.2.3.

According to Eq. (3.6) this interaction has its maximum cross-section at $\sigma_{pp,max} \approx 1.70\times10^{-25}$cm^2 for an incident photon energy of $E_\gamma \approx$ 716.5keV that drops to $\sigma_{pp,750keV} \approx 1.69\times10^{-25}$cm^2 for 750keV photons and to $\sigma_{pp,812keV} \approx 1.63\times10^{-25}$cm^2 for 812keV photons, respectively. Whether this difference of $\sim 3\%$[2] suffices to explain the difference in the fluxes of the 750keV and the 812keV lines, depends on the distribution of the radioactive materials in the supernova ejecta, the ambient density and the time.

[2] N.B. $\approx 3\%$ is also the difference between the Compton cross sections of the two lines: $\sigma_{CE,750keV} \approx 2.42\times10^{-25}$cm^2 and $\sigma_{CE,812keV} \approx 2.33\times10^{-25}$cm^2

Analyzing the background near 750keV

Since none of the above approaches provide a firm explanation of the missing 750keV line, the background in the vicinity of the 750keV line is investigated. In contrast to other γ-ray bands, the 730-770keV band does not have a multitude of background lines and only one feature with a centroid at $\approx$ 752keV can be found (see faint dashed brown slope in Fig. 5.11). This background line was identified by our group as a transition line originating from ^{204}Bi (Diehl et al. 2018b).

^{204}Bi can be predominantly found in the ACS shield surrounding the instrument and has a half-life of $\approx$ 11.22 hours. Its meta-stable form ^{204m}Bi decays emitting a photon with an energy of 752.1keV (from nucleardata.nuclear.lu.se). The exact nuclear process that produces ^{204}Bi remains unknown, however, a useful test is to check whether the time variability of the line in the course of one revolution disrupts somehow the detector ratios and consequently the predicting power of the background model in this narrow energy band.

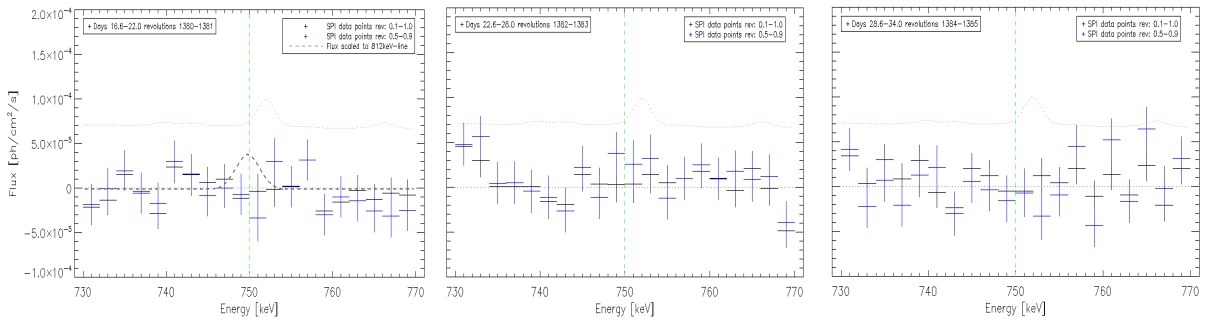

(a) 730-770keV spectra epoch 1 (b) 730-770keV spectra epoch 2 (c) 730-770keV spectra epoch 3

Figure 5.15.: Time series of the 1160-1260keV for revolutions 1380-1385. The black data points correspond to the data used for the analysis of the 750keV line. The blue data points originate from a dataset that only covers the last 40% of the orbit. The background shape in this energy range is drawn with a faint brown slope Every data point corresponds to an energy bin of 10keV.

In Fig. 5.15 a comparison between two different dataset filtering methods is depicted. The black data points correspond to the standard filtering procedure used in this thesis, described at the beginning of the chapter. The blue data points correspond to a filtered dataset, which is composed of a smaller number of pointings. In particular, the first half of the revolution is completely set aside, as well as the last 10%. This is done in order to check, up to what extent the radioactivity of the 752.01keV instrumental line and its modeling affects the celestial spectra. While it is true, that the data points near the line deviate the most between the two approaches, no significant emission can be found in the blue dataset. The reconstructed 750keV line modeled after the detected 812keV line of the first epoch can still be rejected with a 2.64σ statistical confidence.

5.5.5. Nickel lines in 1-revolution time bins

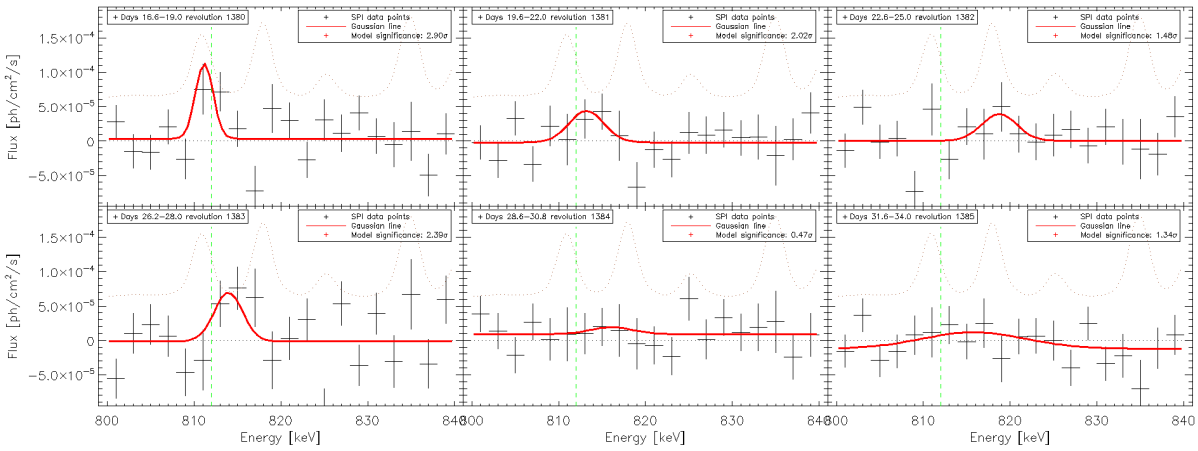

(a) 800-840keV spectra rev. 1380-1385

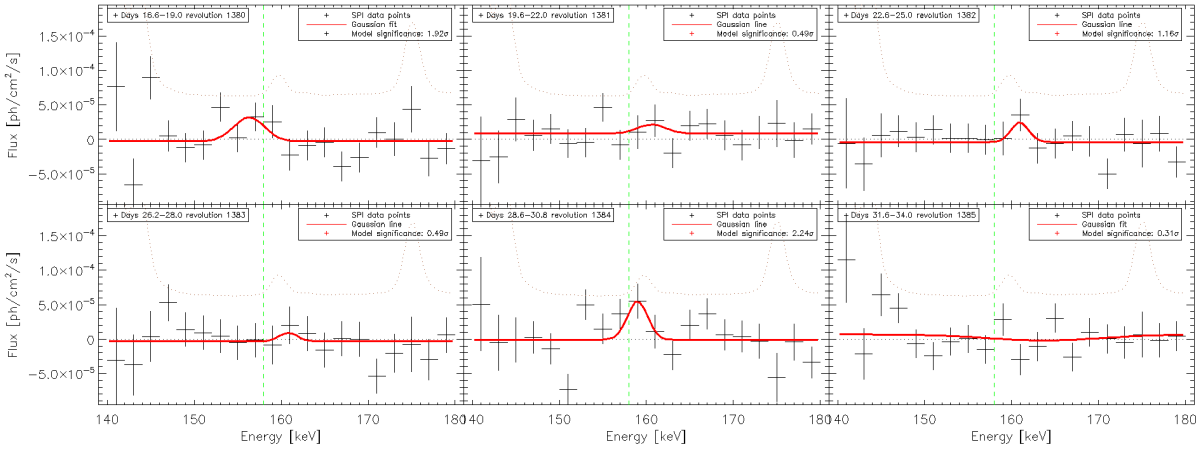

(b) 140-180keV spectra rev. 1380-1385

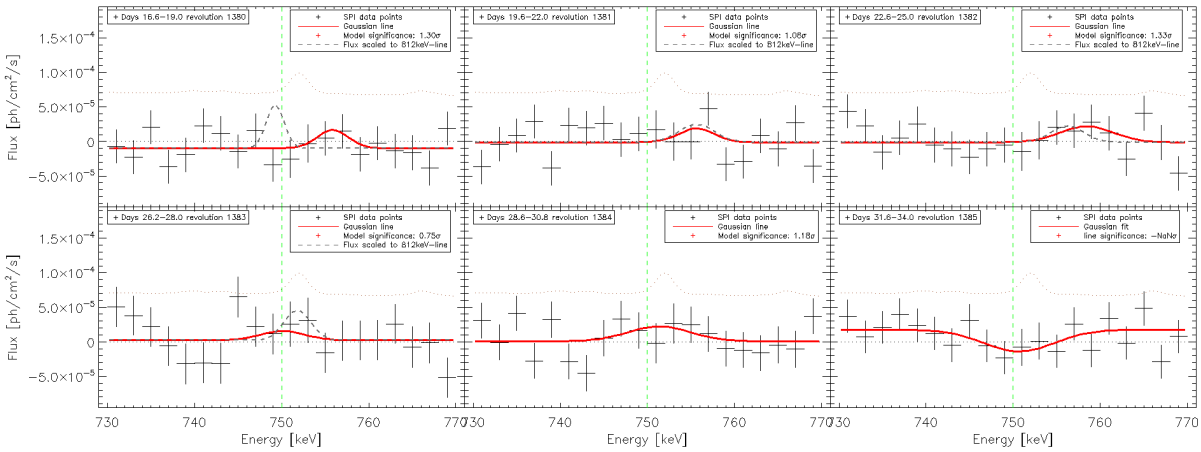

(c) 730-770keV spectra rev. 1380-1385

Figure 5.16.: Time series of the bands around the three major ^{56}Ni lines in 1-revolution time binning. For the 750keV line, the flux corresponding to the 812keV line is displayed with a dashed grey slope.

The ^{56}Ni emission around the three strongest lines of the decay was studied for each revolution between 1380 and 1385 separately. It is worth noting that all 2-revolution spectra presented in the previous subsections are a time average of the individual spectra presented in Fig. 5.16. The goal of this analysis is to test the coherency between the lines and the revolutions.
The spectra were therefore fitted with single Gaussian line fits using optimized starting parameters to avoid local χ^2-minima in the four-dimensional parameter space. While no parameters were fixed, the fit was only accepted if the resulting Gaussian line was broader than the energy resolution of SPI at this energy range.

5.6. Cobalt lines

As mentioned in Sec. 3.7.2, the three major lines from the decay of ^{56}Co to ^{56}Fe are located at 847keV, the 1040keV and the 1238keV line, with a branching ratio of 100%, 14% and 68% respectively. A fourth line coming from the same decay is the positron annihilation line that may, however, show different spectral properties and is therefore discussed in a separate section.

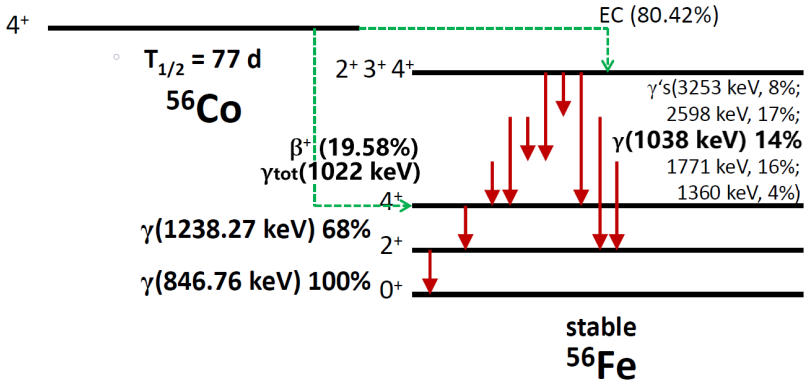

Figure 5.17.: Decay scheme of ^{56}Co. The lines investigated in this analysis are marked with bolted font.

A possible expansion velocity of ^{56}Co inside the supernova ejecta would cause a line broadening proportional to the energy of the lines, decreasing the number of counts per energy bin of interest, and spreading them over a larger number of energy bins. The branching ratios and the line broadening make the 847keV line into the most promising line for detection. On the other hand, the existence of a few respectively strong background lines in the vicinity of the celestial line, in contrast to the other two lines that are situated in energy ranges with stabler background activity, may produce artificial fluxes that could affect the derived fluxes for the 847keV line. In addition to that, higher energy photons have a lower probability of Compton interactions with the ejecta, albeit the energy dependence of Compton scattering at these energies is small. Combining all these parameters, the 847keV line still offers the best detection probabilities, as stated by many authors that modeled the γ-ray emission of a thermonuclear supernova (Ambwani and Sutherland 1988; Milne et al. 2004; Sim and Mazzali 2008; Summa et al. 2013; The and Burrows 2014 and others).

5.6.1. 847keV line

A photon carrying the energy of 847keV is emitted when the excited ^{56}Fe nucleus de-excites from the 2^+ nuclear energy level to its ground state. As Fig. 5.17 shows all transitions occur via the 2^+ nuclear energy level, and hence a 847keV photon is emitted in every ^{56}Co decay. Being the most prominent line of the ^{56}Co decay scheme, fluxes, positron yields, fitted parameters and calculated

masses derived from this line are used as a benchmark in this work.

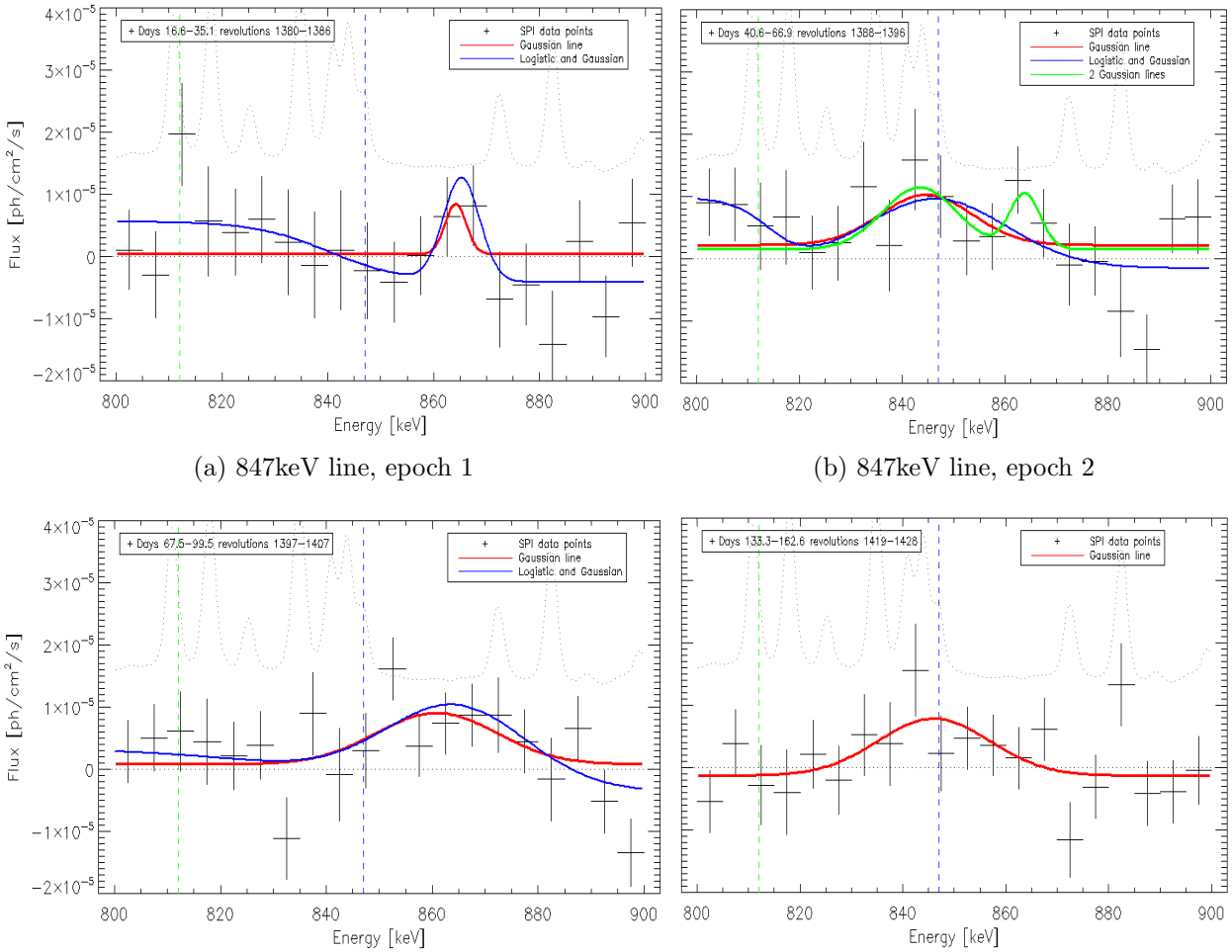

(a) 847keV line, epoch 1

(b) 847keV line, epoch 2

(c) 847keV line, epoch 3

(d) 847keV line, epoch 4

Figure 5.18.: Time series of the 800-900keV band for four epochs. Every data point corresponds to an energy bin of 10keV.

The emission of SN2014J in the 800-900keV band was initially studied in the four epochs mentioned in Sec. 5.4, to ensure a relatively high SNR. If these broadly time-averaged spectra agree with model predictions, a more detailed analysis in finer time bins will be done, attempting to trace the variability of the signal due to the decay of ^{56}Co more efficiently. Isern et al. 2017 suggest that a ten-day time scale ($\sim$ three INTEGRAL revolutions) would be optimal for the detection of the emission of a radioactive element with a half-life of $\tau_{1/2} \approx 70$ days, however, the resulting SNR for a faint γ-source like SN2014J would be low. For this reason, a time-binning of four revolutions was selected, as a compromise between the smallest possible time interval and an acceptable SNR.

Fig. 5.18 presents the spectra of the 847keV line analyzed in 10keV energy bins for the four epochs used also in Diehl et al. 2015. The spectra were initially fitted with a single Gaussian on top of an offset. In the three earliest epochs an alternative model was tested; a logistic function and a Gaussian, taking into account that the flux on the low-energy side of a line appears higher than in the high-energy part (blue slope). This model was used in order to catch the Compton continuum on the red part of the line more efficiently than a simple offset. By this way, an estimate of the

847keV photons that interacted via Compton-scattering can be made. In this case, the continuum is broadly consistent with expectations: Present in epoch one, reaching its maximum in epoch two, becoming less and less significant in epoch three and completely absent in the last epoch. This model yields higher statistical significances and results in a better description of the spectra. A third possibility to measure the ^{56}Co emission within a given energy range is by integrating all emission within the area of interest. In this case, photons between 834-872keV were selected, corresponding to a maximum blueshift of 9000 km/s and a maximum redshift of 4500 km/s. This approach sets aside the opportunity to obtain spectral information by fitting a model to the data, yet may provide the best flux estimate, given that the energy range is chosen suitably.

In the first epoch, a narrow blue-shifted line at $E_0 \approx 865$keV can be identified. This feature may correspond to an outer shell of ^{56}Co with a bulk velocity of 6000 km/s toward the observer. The line feature is located away from background lines, which reduces the possibility that the observed flux originates from inadequate line modeling. A relatively high flux around the 812keV line (vertical green line at 812keV) can be attributed to the 812keV line of the ^{56}Ni, as discussed in Sec. 5.5. The differing spectral properties of the two neighboring lines suggest that they may come from different locations of the ejecta, and be emitted at different times.

Epoch two displays an asymmetry in the ^{56}Co flux, as suggested by Diehl et al 2014. In particular, a blue-shifted feature at $E_0 \sim 862$keV can be identified, possibly corresponding to the same bulk of ejecta found in the first epoch. Additional features can be found at around $\sim$ 845keV and $\sim$ 833keV. The observed emission could point towards several blobs of radioactive material moving at different velocities. This would support the idea of an asymmetric distribution of the radioactive elements in the ejecta. Despite the narrow features, a broad line near the laboratory energy can be fitted to the data, yielding a Doppler broadening of 7500±3000 km/s and a statistical significance of 1.8σ. A two line model (green fit), with a blue-shifted part corresponding to ^{56}Co in the outskirts and an unshifted counterpart for a more massive concentration of ^{56}Co further inside was tested on the data and yields a higher statistical significance. Similar to epoch one, the model with the alternative treatment of the Compton continuum (blue slope) describes the data more accurately.

In the third epoch, irregularities are still present and the whole emission is shifted to the blue. The spread velocity of ^{56}Co, however, remains constant. The continuum emission in the red part of the line becomes less significant, consistent with the idea that at this time (67.5-99.5 days after the explosion) fewer photons are comptonised within the ejecta.

Epoch four encompasses the time when the total bulk of ^{56}Co is expected to be visible since the ejecta should be completely transparent to γ-photons and Compton scattering should be negligible. In this epoch, a broad line with a spread velocity of $\sim$ 9000 km/s describes the data best. This points toward relatively high expansion velocities of the radioactive material inside the ejecta.

Epoch	Flux [10^{-4} ph/cm^2/s]	E_0 [keV]	Bulk velocity [km/s]	σ [keV]	Spread velocity [km/s]
Epoch 1	0.39 ± 0.71	864.2 ± 3.8	6100 ± 1350	2.0 ± 3.4	1450 ± 3200
Epoch 2	1.82 ± 1.64	844.7 ± 5.2	-800 ± 1850	9.0 ± 5.8	7450 ± 4850
Epoch 3	2.36 ± 1.77	860.8 ± 6.4	4900 ± 2250	11.4 ± 7.5	9500 ± 6250
Epoch 4	2.5 ± 2.07	846.0 ± 5.6	-350 ± 2000	10.9 ± 7.9	9000 ± 6650

Table 5.12.: 847keV line fitted parameters for four epochs, red fit (Gaussian line on constant offset)

Epoch	Flux [10^{-4} ph/cm^2/s]	E_0 [keV]	Bulk velocity [km s^{-1}]	σ [keV]	Spread velocity [km s^{-1}]
Epoch 1	1.43 ± 1.06	865.2 ± 1.9	6450 ± 660	3.4 ± 2.0	2750 ± 1750
Epoch 2	3.90 ± 2.63	846.4 ± 5.8	-200 ± 2050	2.0 ± 3.4	11550 ± 6500
Epoch 3	2.36 ± 1.77	864.4 ± 2.7	6200 ± 950	2.0 ± 3.4	11500 ± 2050
Epoch 4	-	-	-	-	-

Table 5.13.: 847keV line fitted parameters for four epochs, blue fit (Logistic function and Gaussian line

Tabs. 5.12 and 5.13 present the fitted parameters of both fits.
By calculating the flux of the 847keV-line for each epoch and fitting model, an 847keV-line light curve was constructed and compared to the predictions from The & Burrows 2014.

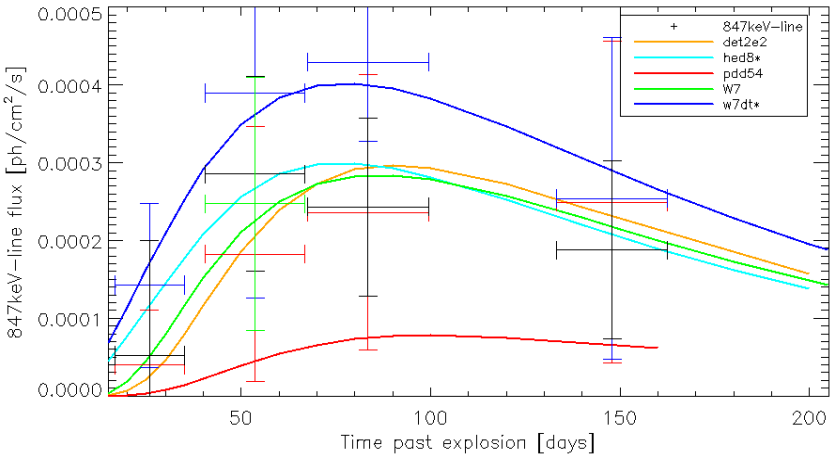

Figure 5.19.: 847keV light curve compared to the simulated light curves of the most representative models constructed by The and Burrows 2014.

As can be seen in Fig. 5.19, the fluxes for each epoch are broadly consistent with most models. The large 1σ error bars of the fluxes do not allow a firm rejection of particular models since all model light curves lie within the 1σ uncertainty. The blue model (logistic and Gaussian) produces higher fluxes than the simple Gaussian fit (red slope) and the black model (integration of the flux in an specific energy band). All models seem to reach a maximum in epoch three, though the red model does not decline significantly in epoch four. The suitability of the light curve of each model was tested in two different ways:

1. By comparing the calculated fluxes to the corresponding flux values of each model of The and Burrows 2014 in the same period, a value similar to χ^2 was calculated.

2. In order to test the evolution of the light curve, three ratios were calculated for all 15 models of The and Burrows 2014:

   - $\Delta R_{1-2} = \dfrac{F2}{F1} = \dfrac{\text{Flux at epoch 2}}{\text{Flux at epoch 1}}$
   - $\Delta R_{2-3} = \dfrac{F3}{F2} = \dfrac{\text{Flux at epoch 3}}{\text{Flux at epoch 2}}$

- $\Delta R_{3-4} = \frac{F4}{F3} = \frac{\text{Flux at epoch 4}}{\text{Flux at epoch 3}}$

These ratios describe the relative flux gain/decline for each model between subsequent epochs and were then compared to the corresponding flux ratios calculated for the three models (red, blue, black). Again, a χ^2-similar value was calculated (see Appendix); the smaller the value, the higher the match between the predicted fluxes and the calculated fluxes from the fits.

Model	$\Delta\chi^2$ red	ΔR^2 red	$\Delta\chi^2$ blue	ΔR^2 blue	$\Delta\chi^2$ black	ΔR^2 black
dd202c	**0.82**	**0.58**	1.49	1.34	**0.79**	1.90
dd4	**0.07**	**0.56**	3.73	6.79	**0.60**	**0.17**
det2	**0.99**	1.31	1.43	**0.59**	**0.50**	3.04
det2e2	**0.17**	12.56	3.54	29.03	**0.49**	8.50
det2e6	1.00	2086.59	10.02	2258.21	3.93	2028.03
hecd	3.66	5.75	**0.44**	**0.30**	1.75	9.11
hed6	**0.95**	3.24	10.57	**0.02**	3.57	5.82
hed8	1.58	5.32	2.04	**0.19**	**0.25**	8.52
m36	**0.18**	**0.45**	3.34	1.58	**0.25**	1.65
pdd54	2.58	45.13	16.51	73.48	7.93	37.15
W7	**0.19**	**0.12**	3.26	2.79	**0.22**	**0.77**
W7A	**0.23**	1.34	3.40	**0.57**	**0.24**	3.20
w7dn	**0.69**	2.22	2.10	**0.19**	**0.28**	4.47
w7dt	5.48	6.15	**0.20**	**0.39**	3.18	9.60
W7E	2.00	6.61	2.09	**0.51**	**0.37**	10.20

Table 5.14.: Compatibility test of the three approaches (red, blue, black models) to the 15 supernova models of The and Burrows 2014. A low value indicates high resemblance between the calculated flux and the respective model. Bold indicates a high degree of compatibility.

Tab. 5.14 presents the results of the two tests explained above. Columns with $\Delta\chi^2$-values show how well the calculated fluxes match the light curves of the models. Columns with ΔR^2-values show how well fits the evolution of the calculated light curve with the evolution of the light curves of the models.

For the red fit, intermediate ^{56}Ni mass models, such as the delayed detonation models m36 and dd4, the merger detonation models det2, det2e2 and det2e6, the delayed detonation model dd202c and the standard deflagration models W7 and w7dn seem to describe the light curve most accurately. On the other hand, most superluminous or subluminous models fail to resemble the data, consistent with the studies that define SN2014J as a normal type Ia explosion.The blue model yields higher fluxes and suits better to models with a higher ^{56}Ni mass, i.e. the superluminous helium-detonation model hecd, or the deflagration model w7dt, with an extra outer layer of $0.18 M_\odot$. The black model, a sum of fluxes between 834-872keV, is an intermediate case. However, its fluxes lie closer to the red model, favoring intermediate ^{56}Ni mass models. To sum up, for the red fit, models dd202c, dd4, m36 and W7 yield a value <1 for both tests, with the latter having the lowest combined chi-squared of all. Models with a high production of ^{56}Ni, like w7dt and hecd represent the data best for the blue fit, while the black fit favors W7 and dd4.

To assure that the observed emission originates indeed from SN2014J, source grids similar to Sec. 5.5.1 for each epoch were constructed.

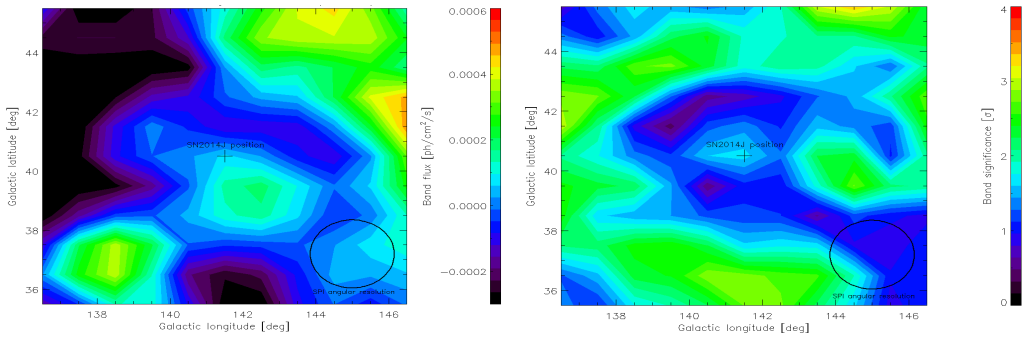

(a) Flux map, epoch 1 (b) Significance map, epoch 1

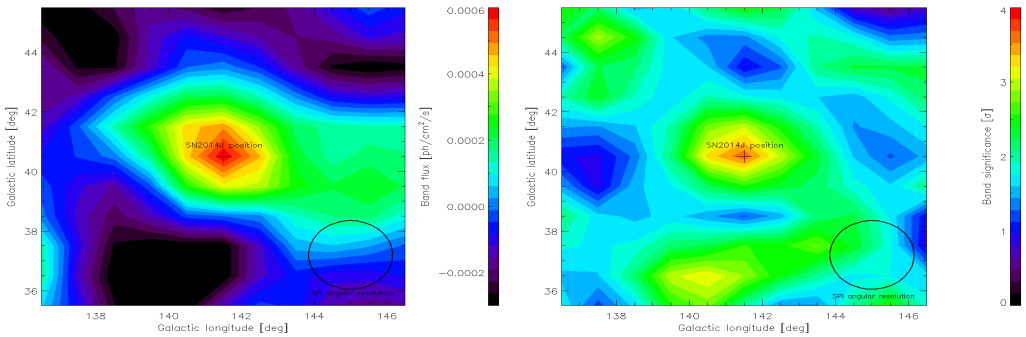

(c) Flux map, epoch 2 (d) Significance map, epoch 2

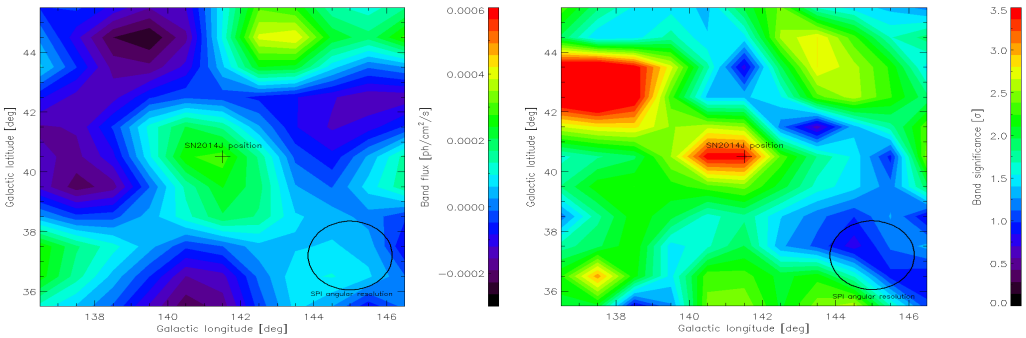

(e) Flux map, epoch 3 (f) Significance map, epoch 3

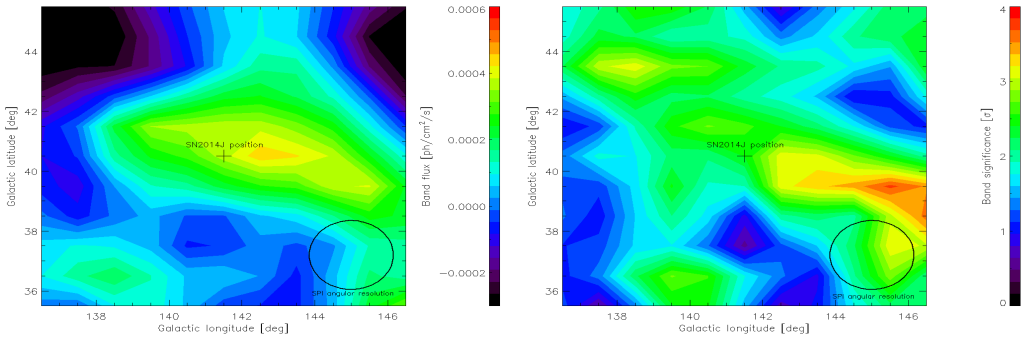

(g) Flux map, epoch 4 (h) Significance map, epoch 4

Figure 5.20.: Flux and significance maps in a 10°×10° grid around SN2014J for revolutions 1380-1381. Left: The flux in the 830-870keV band is integrated and color-coded for every grid of the map. Right: The significance of the emission for each grid is calculated by comparing the χ^2-values of spimofit-runs with and without SN2014J. The circle on the bottom right shows the angular resolution of SPI at these energies ($\sim 2.3°$).

In the source grid depicted in Fig. 5.20, a considerable amount of flux can be seen from the direction of SN2014J. In some cases, emission from other areas can be seen (see left panels), albeit with a much lower significance (compare with right panels). This hints SN2014J as the only γ-ray source in this direction of the sky.

^{56}Ni mass estimates

One approach to derive the initially synthesized ^{56}Ni mass from the 847keV line flux uses the fact that the measured flux of a γ-line is directly proportional to the mass of its corresponding radioactive element at the time of observation. For an estimate of the ^{56}Ni mass from the 847keV line flux, however, the formula becomes more complex, due to the fact that ^{56}Co is the intermediate nucleus in the decay chain of ^{56}Ni. Using Eq. (5.3), an estimate of the ^{56}Ni mass synthesized during the explosion can be made:

$$\mathrm{M}(^{56}\mathrm{Ni}, \mathrm{t}=0) = \frac{4 \cdot \pi \cdot \mathrm{d}^2 \cdot \mathrm{F}_{847\mathrm{keV}} \cdot \mathrm{m}_{\mathrm{Ni}} \cdot \tau_{\mathrm{Co}}}{\left(\frac{\tau_{\mathrm{Co}}}{\tau_{\mathrm{Co}}-\tau_{\mathrm{Ni}}}\right) \cdot \left(\exp\left(-\frac{\mathrm{t}}{\tau_{\mathrm{Co}}}\right) - \exp\left(-\frac{\mathrm{t}}{\tau_{\mathrm{Ni}}}\right)\right) \cdot \mathrm{p}_{847\mathrm{keV}}} \tag{5.3}$$

Parameter $\mathrm{F}_{847\mathrm{keV}}$ denotes the flux of the 847keV line, d is the distance between the instrument and M82, τ_{Ni} and τ_{Co} the mean lifetimes of ^{56}Ni and ^{56}Co, respectively, m_{Ni} the atomic mass of ^{56}Ni and $\mathrm{p}_{847\mathrm{keV}}$ the branching ratio of the 847keV line. Eq. (5.3) is valid for completely transparent ejecta, which is not an appropriate assumption for all observation windows.

As ejecta expansion proceeds, more and more radioactive mass becomes visible and at day 100 the supernova envelope is considered completely transparent to γ-rays. Measurements before that day must be corrected with a γ-ray escape fraction or left out of the mass estimate. Churazov et al. 2015 derived an escape fraction 60% for day 75 after the explosion to calculate Nickel masses. Our group (Diehl et al. 2015) assumed complete transparency in epoch three, the brightest epoch in this analysis.
In this work the derived ^{56}Ni mass is calculated from the line flux measurement of epoch four for the following reasons:

- Using fluxes of earlier epochs would underestimate the ^{56}Ni mass yield, as at times before day 100, a substantial fraction of the radioactive material could remain hidden from the observer. In contrast, at t$\sim$ 5 months after the explosion (i.e. epoch four), the whole bulk of the radioactive material should be observable.

- Using an escape fraction to correct for earlier fluxes would turn a model-independent estimate, into a model-dependent result.

The flux measured in epoch four, yields a synthesized ^{56}Ni mass of $0.57\pm0.48\mathrm{M}_{\odot}$ for the red fit and $0.43\pm0.27\mathrm{M}_{\odot}$ for the black fit (see Appendix for the error estimate). Assuming complete transparency in epoch four, an estimate of the escape fraction of 847keV line photons can be made, by extrapolating its flux to earlier epochs and compare it with the measured fluxes. Using this technique, the following γ-ray escape fractions are given for SN0214J.

847keV escape fractions	red fit	blue fit	black sum	average
Epoch 1	0.05±0.11	0.21±0.24	0.09±0.29	0.12±0.13
Epoch 2	0.32±0.38	0.66±1.07	0.65±0.89	0.54±0.48
Epoch 3	0.73±0.60	0.96±0.86	0.72±0.57	0.73±0.40

Table 5.15.: Calculated escape fractions for 847keV photons in SN2014J, assuming complete transparency in epoch 4.

Another approach to derive the initial ^{56}Ni mass synthesized in SN2014J is by fitting the light curves of the models of The and Burrows 2014 to the observations with a scaling parameter α. The goal thereby is to achieve maximum matching between the fitted 847keV line fluxes found in the first column of Tabs. 5.12 and 5.13 and the light curves of the supernova models of The and Burrows 2014. By multiplying then the ^{56}Ni mass of the model with α, a new scaled mass, for every model from The and Burrows 2014, was derived.

It is assumed thereby that the intensity of the flux is directly proportional to the ^{56}Ni mass at all observation times. Tab. 5.16 presents the ^{56}Ni mass fits for the fifteen explosion models from The and Burrows 2014.

Model	^{56}Ni mass [$M_\odot$] red	^{56}Ni mass [$M_\odot$] blue	^{56}Ni mass [$M_\odot$] black
dd202c	0.52±0.08	0.91±0.05	0.60±0.04
dd4	0.55±0.11	0.93±0.06	0.60±0.04
det2	0.44±0.07	0.80±0.04	0.53±0.03
det2e2	0.57±0.11	0.93±0.06	0.62±0.04
det2e6	0.90±0.31	1.43±0.17	0.85±0.11
hecd	0.39±0.05	0.81±0.04	0.54±0.03
hed6	0.41±0.15	0.79±0.10	0.52±0.08
hed8	0.34±0.06	0.72±0.04	0.48±0.03
m36	0.52±0.10	0.91±0.06	0.60±0.05
pdd54	0.61±0.48	0.97±0.25	0.64±0.19
W7	0.51±0.10	0.88±0.06	0.58±0.04
W7A	0.51±0.10	0.91±0.06	0.60±0.05
w7dn	0.47±0.08	0.87±0.05	0.57±0.04
w7dt	0.37±0.04	0.78±0.03	0.52±0.03
W7E	0.37±0.06	0.81±0.05	0.54±0.04

Table 5.16.: Calculated ^{56}Ni masses by scaling the ^{56}Ni mass of each model of The and Burrows 2014 with scaling factor α. For details, see text.

To estimate a final ^{56}Ni mass, the calculated ^{56}Ni masses of the models with $\Delta\chi^2, \Delta R^2 < 1$ were averaged and weighted according to their compatibility with the data. For details on this procedure, see Appendix. The final ^{56}Ni mass yield for SN2014J using this method is given in Tab. 5.17.

Epoch	red fit	blue fit	834-872keV
^{56}Ni mass	$0.53 \pm 0.07 M_\odot$	$0.81 \pm 0.06 M_\odot$	$0.59 \pm 0.03 M_\odot$

Table 5.17.: ^{56}Ni mass estimates derived from the models with the highest compatibility

Positron production

As already shown in Fig. 3.7 the decay of ^{56}Co can either take place via EC or via β^+-decay. Both channels end up emitting an 847keV photon. Using the fitted fluxes of the 847keV lines, a minimum production rate of positrons, using Eq. (5.4), can be calculated :

$$N_{e^+}^{847keV} = 4 \cdot \pi \cdot d^2 \cdot F_{847keV} \cdot p_{\beta^+} \tag{5.4}$$

Here, p_{β^+} denotes the probability of 56Co to decay through the β^+ decay channel. Only in epoch four does the positron production reflect the true number of produced positrons, though. The values at earlier epochs should be considered lower limits of the true number of positrons created per second, due to the fact that a considerable amount of 847keV photons remains hidden from the observer and do not contribute to the observed flux.

Epoch	red fit [$10^{46}e^+/s$]	blue fit [$10^{46}e^+/s$]	black sum [$10^{46}e^+/s$]
Epoch 1	1.14±2.04	4.09±3.08	1.49±4.22
Epoch 2	5.24±4.75	11.18±7.69	8.20±3.72
Epoch 3	6.78±5.14	12.32±3.25	6.97±3.40
Epoch 4	7.15±6.00	-	5.39±3.36

Table 5.18.: Lower limits of produced e^+ in each epoch

847keV line in 4-revolution time bins

The robust detection of the 847keV line in long epochs covering several weeks, offers the opportunity to study this emission in smaller observation windows, e.g. in 4-revolutions averaged spectra ($\sim$ 12 days). The main goals of this approach are to determine precisely the time of maximum emission and to investigate, whether the emission in epochs two and three show the same irregularity as in the analysis with coarser time-binning.

Fig. 5.21 presents the spectra in 5-revolution time binning.

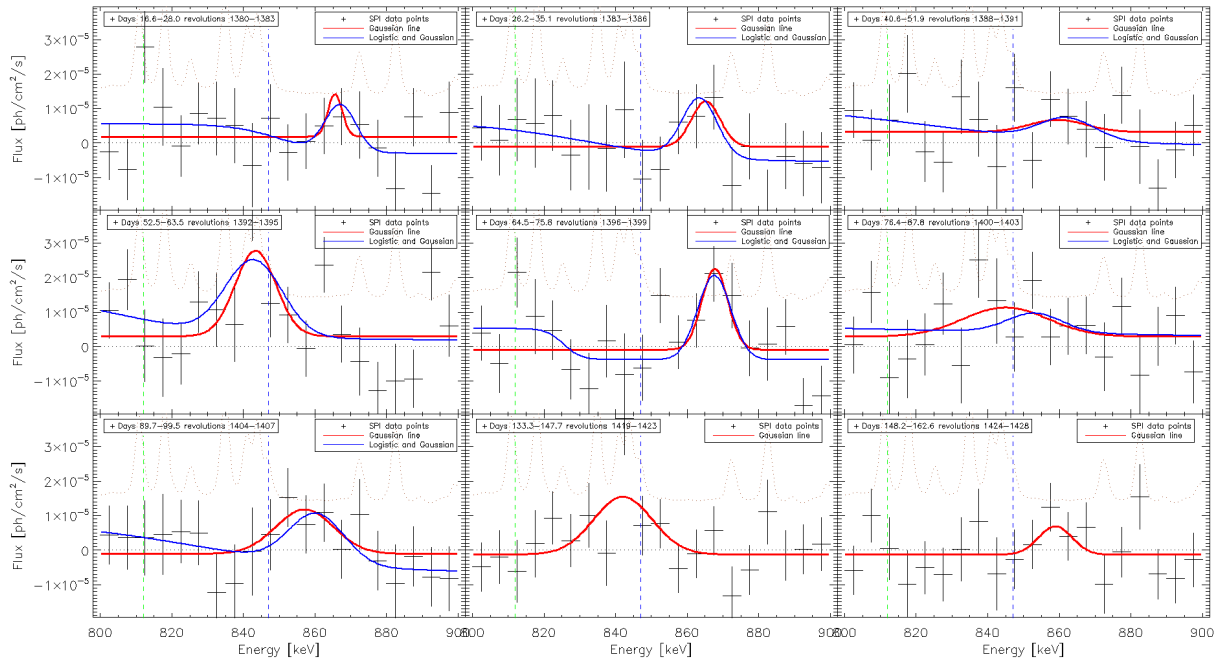

Figure 5.21.: Time series of the 800-900keV band for nine epochs.

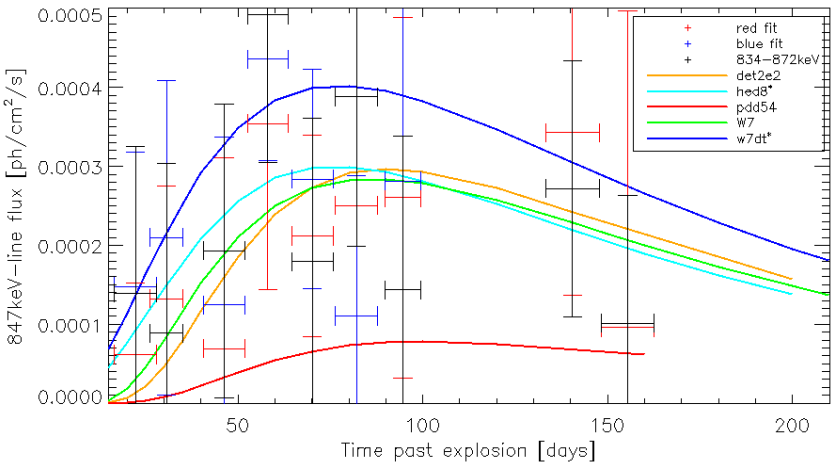

Figure 5.22.: 847keV light curve in nine epochs compared to models of The and Burrows 2014. Note that the last two plots comprise the spectra of five revolutions instead of four.

In all epochs depicted in 5.21, a flux excess in the vicinity of the 847keV line is observable. All three approaches to determine the line flux remain consistent with models, despite the fact that the fluxes of the red and the blue fit differ by a factor of ~ 2. The results of the black approach lie in between. The red fit reaches its maximum at $t_{max} \sim$ 60-70 days after the explosion, the black sum ten days later and the blue fit at days 90-100 days after the explosion. The blue fit overestimates the flux in the first two observation windows, pointing towards early blue-shifted ^{56}Co emission. In the following observation windows, the line centroid shifts between 845keV and 865keV. This supports once again the hypothesis of irregular distribution of radioactivity in the ejecta.

5.6.2. 1238keV line

A 1238keV photon is emitted when the excited ^{56}Fe nucleus de-excites from the $J^{\pi}=4^{+}$ nuclear level to the $J^{\pi}=2^{+}$ nuclear level, a transition with a probability of 68% per decay. The relatively high branching ratio, combined with the fact that this transition is situated at a more quiescent background environment turns this transition into a promising target for detection by SPI. On the other hand, the higher the energy of the incoming photon, the lower the probability of interaction with the detector camera and hence the lower the effective detector area of SPI. In addition to this, the fact that the Doppler broadening is proportional to the energy of the lines, spreads the photons over a larger number of energy bins, thus decreasing the sensitivity in every energy bin, as shown in Fig. 4.27.
If it is assumed that the fluxes and spectral parameters reported in Tabs. 5.12 and 5.13 mirror the true spatial distribution and properties (spread and bulk velocities etc.) of ^{56}Co, then the 1238keV γ-ray photons should show the same (within uncertainties) widths, energy-shifts and fluxes, scaled to the energy and the branching ratio of the 1238keV line.

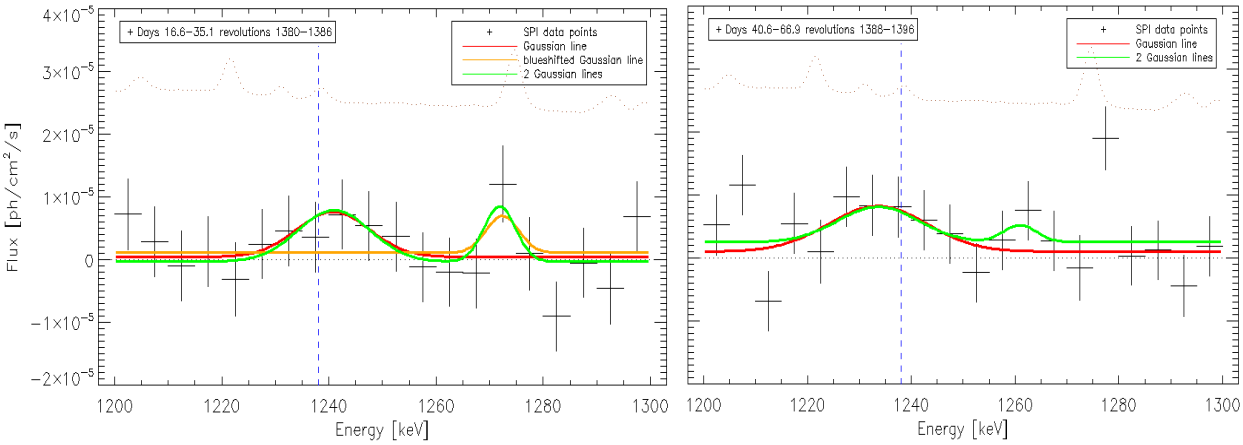

(a) 1238keV line, epoch 1

(b) 1238keV line, epoch 2

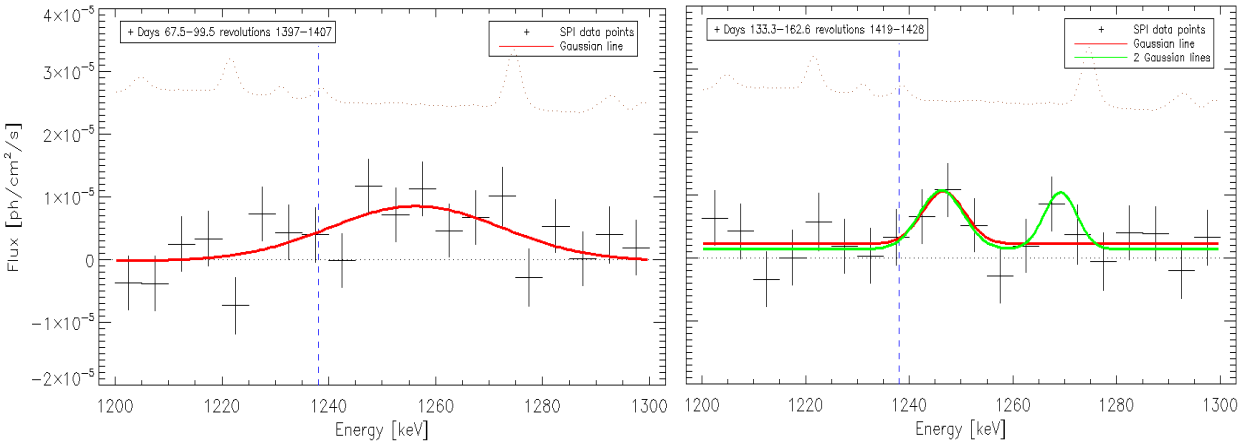

(c) 1238keV line, epoch 3

(d) 1238keV line, epoch 4

Figure 5.23.: Time series of the 1200-1300keV band for four epochs. Every data point corresponds to an energy bin of 10keV.

In Fig. 5.23, the flux in the energy band between 1200-1300keV in the same epochs and energy binning like for the 847keV line is depicted. The spectra show clear emission features in the vicinity

of the 1238keV line, as expected from the analysis of the 847keV line. For this energy range, three approaches for estimating the fluxes have been used. The red slope corresponds to a free fit of a Gaussian line model, while the green fit consists of two Gaussian lines, to capture a blue-shifted part and a main bulk of radioactive ^{56}Co in the ejecta. The third approach (black data points) sums up all emission in the energy range between 1219-1275keV, corresponding to a maximum blueshift of 9000km/s and a maximum redshift of 4500km/s, in the same manner as the black model in Sec. 5.6.1.

Epoch	Flux [10^{-4} ph/cm^2/s]	E_0 [keV]	Bulk velocity [km s^{-1}]	σ [keV]	Spread velocity [km s^{-1}]
Epoch 1	1.23 ± 1.23	1240.8 ± 4.8	650 ± 1150	6.8 ± 5.3	3850 ± 3050
Epoch 2	1.72 ± 1.19	1233.6 ± 5.1	-1050 ± 1250	9.5 ± 5.1	5400 ± 2950
Epoch 3	3.55 ± 1.88	1256.3 ± 4.8	4400 ± 1160	16.2 ± 6.8	9200 ± 3900
Epoch 4	0.85 ± 0.71	1246.6 ± 2.5	2100 ± 600	4.1 ± 2.6	2250 ± 1550

Table 5.19.: Fitted parameters of the main 1238keV line

Epoch	Flux [10^{-4} ph/cm^2/s]	E_0 [keV]	Bulk velocity [km s^{-1}]	σ [keV]	Spread velocity [km s^{-1}]
Epoch 1	0.65 ± 1.19	1272.4 ± 1.5	8350 ± 350	3.1 ± 1.4	1650 ± 400
Epoch 2	0.22 ± 0.17	1261.0 ± 2.5	5550 ± 600	3.2 ± 2.1	1750 ± 1250
Epoch 3	-	-	-	-	
Epoch 4	0.72 ± 0.64	1269.2 ± 2.1	7550 ± 500	3.2 ± 2.2	1700 ± 1350

Table 5.20.: Fitted parameters of the blue-shifted 1238keV emission

In the epoch one, a narrow blue-shifted line with a line centroid at $E_0 \sim 1270$keV is present. Its blue-shift can be converted into a portion of ^{56}Co with a bulk velocity of ∼8000 km/s towards the observer. The spectral properties of this feature are broadly consistent with the blue-shifted feature in the first epoch of the 847kev analysis. A symmetric flux excess near the laboratory energy, which was absent in the 800-900keV band analysis, was detected as well. The significance of this line is $\sim 1.75\sigma$, while the fainter blue-shifted line has a statistical significance of $\sim 1.27\sigma$. Since Compton transparency is enhanced with increasing γ-ray energy, the observed emission near the laboratory energy might be at the position inside the envelope, where a fraction of 1238keV photons can escape but 847keV photons are not energetic enough to avoid absorption.

In epoch two, the blue-shifted emission becomes weaker and less significant. In contrast to the blue-shifted line, the feature near the laboratory energy grows stronger. As ejecta expansion proceeds, progressively more radioactive material gets uncovered and a progressively higher fraction of γ-ray photons should be able to escape. The energy position of both lines is consistent within uncertainties with the results obtained in the 800-900keV band. This highlights the stability of the analysis using the background approach described in Sec. 4.7 and the adjustments made in this work.

The spectrum of epoch three displays an irregular blue-shifted emission. An asymmetric blue-shifted ^{56}Co emission was also detected in the corresponding spectrum of the 847keV line in the same epoch. As both spectra follow the same trend, the spectral analysis of the two major ^{56}Co lines support an asymmetric and irregular distribution of the radioactive material.

In epoch four, when complete transparency is expected, a double feature similar to the first epoch reappears, with a blue-shifted narrow feature at $E_0 \approx 1270$keV and a slightly blue-shifted broader line at $E_0 \approx 1245$keV. The form of the spectral features does not match the corresponding one of the 800-900keV energy band, as no similar spectral feature was found in panel (d) of 5.18.

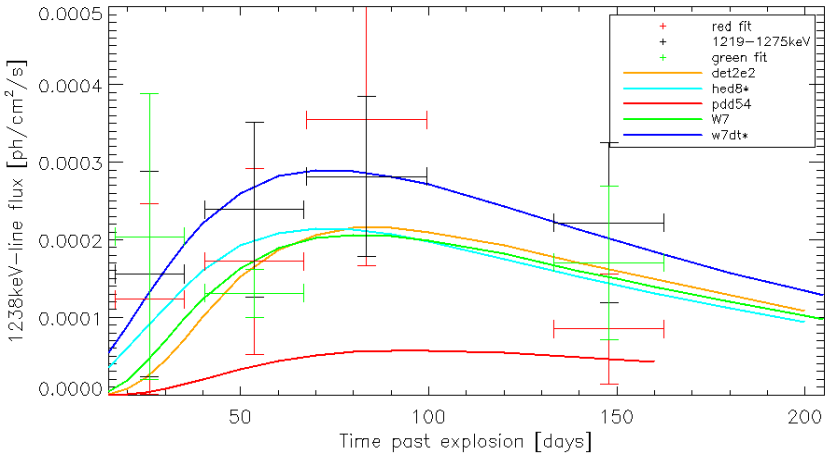

Figure 5.24.: 1238keV light curve compared to models of The and Burrows 2014

It is clear that the flux of the 1238keV line is consistent with most models. The light curve shows a gradual flux increase in the first weeks of the supernova evolution, a maximum reached in epoch three and a slower decline incline in epoch four (see Fig. 5.24).

The same procedure used in Sec. 5.6.1 to derive ^{56}Ni masses was also followed for the 1238keV line. The ^{56}Ni yields calculated from epoch four are $M_{^{56}Ni} = 0.29 \pm 0.24 M_\odot$ for the red fit, $M_{^{56}Ni} = 0.57 \pm 0.35 M_\odot$ for the green fit, and $M_{^{56}Ni} = 0.75 \pm 0.37 M_\odot$ for the black sum. The derived ^{56}Ni masses are consistent within 1σ error bars with the ^{56}Ni mass derived from epoch four of the 800-900keV band.

1238keV line in 4-revolution time bins

In a similar manner to the 847keV line, the 1238keV line was studied in four-revolutions time-averaged spectra. The spectra were fitted with two different models. A free fit of a Gaussian line and a model featuring two Gaussian lines. The latter was motivated by the detection of narrow blue-shifted in three out of four epochs in the 4-epoch analysis (see Fig. 5.23).

Fig. 5.25 presents the spectra in four-revolution time binning. The last two spectra correspond to a time binning of five revolutions since the late observation window consists of ten revolutions in total.

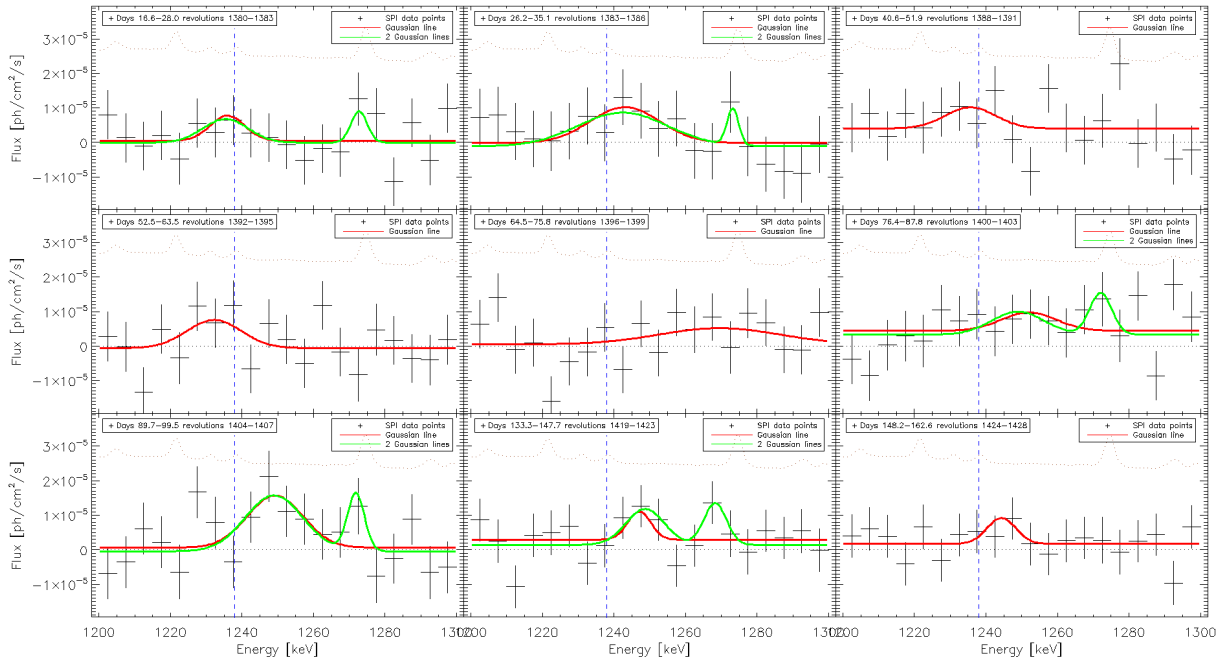

Figure 5.25.: Time series of the 1200-1300keV band for nine epochs.

All epochs depicted in Fig. 5.25 display a significant emission around the 1238keV line. The statistical significances of the main line vary between 1-3σ. For several spectra with blue-shifted emission, a two-line model was fitted on the data.

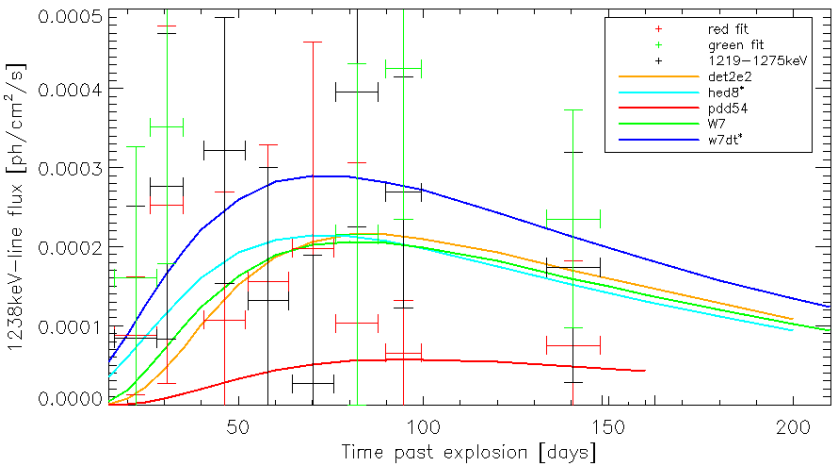

Figure 5.26.: 1238keV light curve in nine epochs compared to models of The and Burrows 2014. Note that the last two data points comprise five revolutions instead of four.

The red fit reaches its maximum at $t_{max} \sim$ 60-70 days after the explosion, the black sum ten days later and the blue fit at days 90-100 days after the explosion. The green fit registers the highest flux, as the fit is flexible enough to fit two lines on the same spectrum. For some observation windows, it overestimates the registered flux, pointing towards early blue-shifted ^{56}Co emission. Similar to the analysis of the 847keV line, the line centroid of the main 1238keV line oscillates between 1235keV and 1260keV. This supports once again the hypothesis of the irregular distribution of the radioactive material in the ejecta.

5.6.3. 1040keV line

The detection of photons from this transition of the excited ^{56}Fe nucleus is suppressed, due to their relatively low branching ratio of 14%. For the analysis of the 1040keV line, the energy band between 1000-1100keV was investigated. Due to the low expected fluxes, only two approaches to measure the flux of the line were made.

1. A simple Gaussian line on top of a constant offset (red slope).
2. A sum of all energy bins between 1024-1071keV (black data points), similar to the analyses of the other ^{56}Co lines.

As an additional flux estimate, 2σ upper limits were derived for all epochs, using averaged widths and energy shifts of the two prominent lines of the ^{56}Co decay.

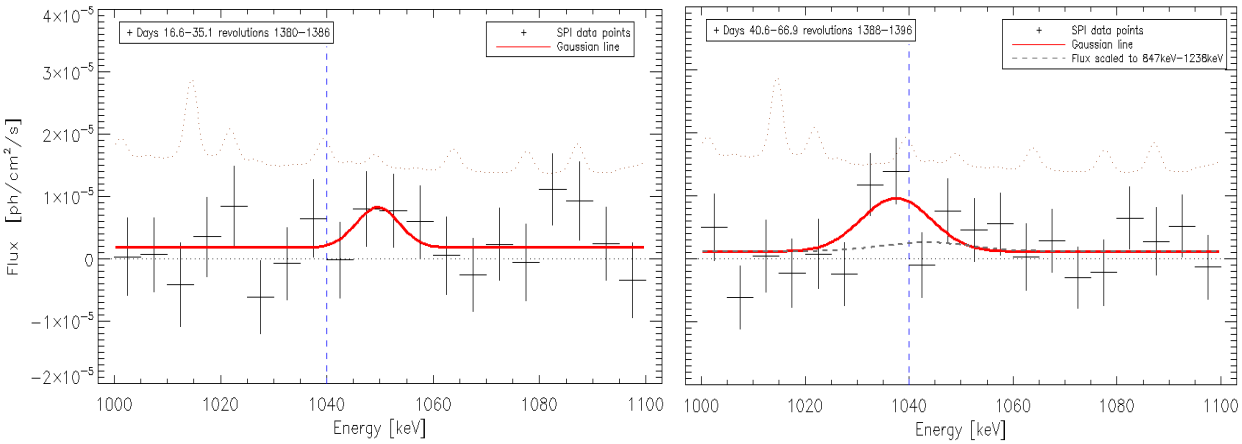

(a) 1040keV line, epoch 1

(b) 1040keV line, epoch 2

(c) 1040keV line, epoch 3

(d) 1040keV line, epoch 4

Figure 5.27.: Time series of the 1000-1100keV band for four epochs. Every data point corresponds to an energy bin of 10keV.

The panels of Fig. 5.27 show indeed flux excess near the laboratory energy of the line. However, the spectral shapes do not match with the results reported from the analyses of the 847keV and the 1238keV lines. On panels (b) and (c), the expected emission of the 1040keV, based on the

847keV and 1238keV lines, is depicted. In these epochs, the consistent detection of the other the aforementioned lines places strict constraints on the spectral form of the 1040keV, that are not depicted in the spectra. However, as the awaited fluxes are of the order of 10^{-5} ph/cm^2/s and broadened by $\sim$ 20keV, the weak 1040keV-line lies below the sensitivity limit of SPI. As a countermeasure, 2σ upper limits based on the line widths and shifts of the other two lines were derived.

Epoch	Flux [10^{-4} ph/cm^2/s]	E_0 [keV]	Bulk velocity [km s^{-1}]	σ [keV]	Spread velocity [km s^{-1}]
Epoch 1	0.65 ± 1.05 [1.33]	1049.6 ± 2.2	2750 ± 650	4.0 ± 2.2	2650 ± 1600
Epoch 2	1.43 ± 1.17 [3.12]	1037.5 ± 4.0	-700 ± 1150	6.7 ± 4.5	4500 ± 3100
Epoch 3	0.46 ± 0.65 [2.48]	1046.2 ± 4.0	1800 ± 700	4.1 ± 4.5	2700 ± 1450
Epoch 4	0.69 ± 0.57 [1.03]	1050.9 ± 1.7	3150 ± 500	2.5 ± 1.7	1550 ± 1250

Table 5.21.: 1040keV line fitted parameters for four epochs, red fit. 2σ upper limits are given in square brackets.

The most striking value reported on 5.21 is the flux measured in epoch two. In this epoch, a spectral feature at $E_0 \approx 1035$keV with a statistical significance of 2.3σ is detected. The line flux of this feature is a factor of $\sim$ 5 higher than the expected one from the analysis of the other two lines. Assuming complete transparency in the ejecta, the flux can be translated into an synthesized ^{56}Ni mass of $M(^{56}\mathrm{Ni}, t = 0) = 1.00 \pm 0.83 M_\odot$. In an analogous manner the integrated flux between 1024-1071keV yields $M(^{56}\mathrm{Ni}, t = 0) = 1.59 \pm 0.81 M_\odot$. If this amount of ^{56}Ni was synthesized during the explosion, SN2014J would be a super-luminous type Ia supernova, and fluxes $\sim 10^{-3}$ ph/cm^2/s would have been expected for the 847keV line.

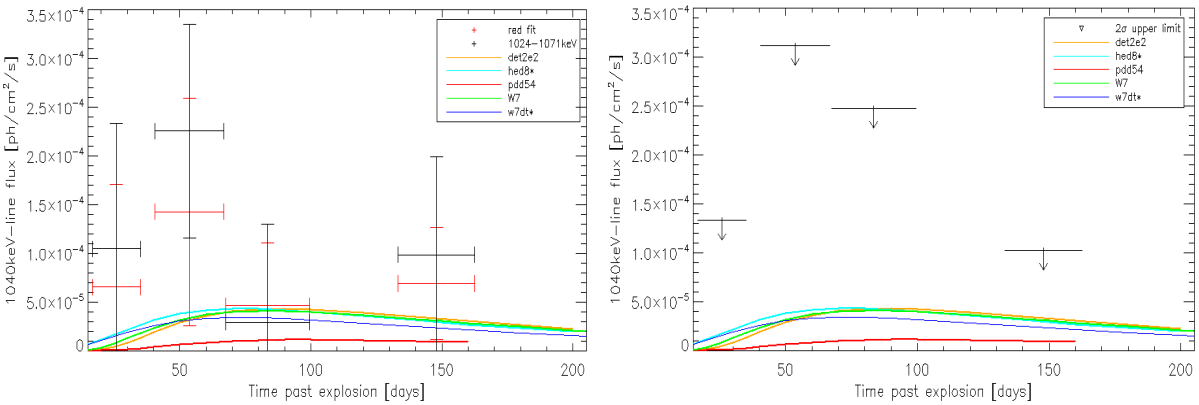

(a) 1040keV line light curves

(b) 1040keV line 2σ upper limits

Figure 5.28.: Left: 1040keV line light curve compared to the light curves of models from The and Burrows 2014. The red data points correspond to a free Gaussian fit, while the black data points sum all flux within a given energy range. Right: 2σ upper limits, using the spectral properties of the 847keV and 1238keV lines.

The upper limits reported in Tab. 5.21 do not allow the rejection of any progenitor model based on the flux of the 1040keV line.

5.6.4. Simultaneous fit of ^{56}Co

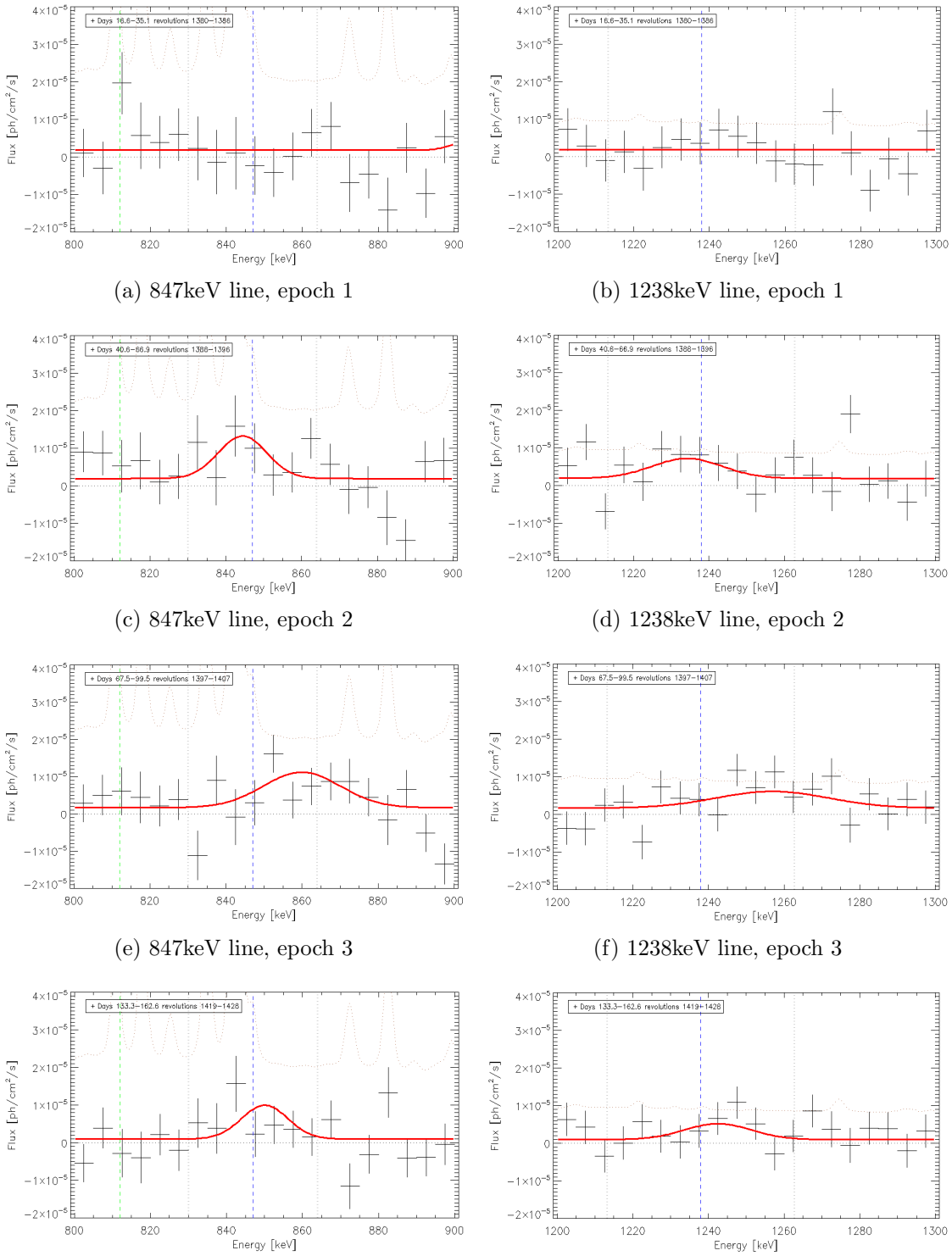

(a) 847keV line, epoch 1

(b) 1238keV line, epoch 1

(c) 847keV line, epoch 2

(d) 1238keV line, epoch 2

(e) 847keV line, epoch 3

(f) 1238keV line, epoch 3

(g) 847keV line, epoch 4

(h) 1238keV line, epoch 4

Figure 5.29.: Simultaneous fits of the ^{56}Co lines for all four epochs. Each data point corresponds to an energy bin of 10keV. Blue vertical lines indicate the laboratory energy of the ^{56}Co lines, green vertical lines of the ^{56}Ni lines. The grey vertical lines represent the shift of the line for an expansion velocity of ±6000km/s.

In order to check the consistency of the ^{56}Co line emission, a simultaneous fit, similar to the one for the ^{56}Ni emission, is applied for the ^{56}Co lines. However, I fitted only the two strongest lines, the 847keV and the 1238keV lines, simultaneously and linked all their parameters according to their branching ratios and energies, including their amplitudes. The reason for doing this lies in the firm detection of both lines, and the small energy separation between them. This implies that both the lines are approximately equally affected by all interaction cross-sections. The 1040keV is omitted from the fit, since the 1040keV line fluxes are below the sensitivity limit of SPI, as shown in Fig. 5.27. Finally, the positron annihilation line could show a completely different spectral shape compared to the ^{56}Co kinematics.

The spectra displayed in Fig. 5.29 present the analogon of Fig. 5.13 for the two lines of ^{56}Co with the highest branching ratios. As indicated by the source grids of Fig. 5.20, the lines of epoch two and three are compatible with each other, within measurement errors. However, the blue-shifted emission detected in the vicinity of the 847keV line in the individual analysis is not accompanied by the 1238keV line. An apparent flux excess around $\sim$ 1275keV is located exactly on top of a background feature and could contain residual fluxes from insufficient line modeling (see faint brown dashed slope in the spectra).

Epoch	Significance of fit [σ]	Bulk velocity [km/s]	Spread velocity [km/s]
Epoch 1	1.15	19400 ± 22500	2800 ± 55500
Epoch 2	3.13	-900 ± 950	5300 ± 2300
Epoch 3	4.15	4600 ± 1250	8450 ± 3050
Epoch 3	2.96	1100 ± 300	5000 ± 2700

Table 5.22.: Properties of the simultaneous ^{56}Co line fitting

The co-detection of both lines in epochs two, three and four support the asymmetry of the explosion suggested by other studies, as both lines move from a slightly red-shifted to a blue-shifted position and back to the laboratory value within this period. In epochs, when the flux is expected to be lower, the fit cannot reproduce Gaussian lines in the relevant energy band. Assuming complete transparency in epoch four, a ^{56}Ni mass from the simultaneous fit can be derived. Inserting the line fluxes of the epoch four into Eq. (5.3) yields $M_{^{56}Ni}=0.31\pm0.21 M_{\odot}$.

5.7. Positron annihilation in SN2014J

In 19.58% of all cases, radioactive ^{56}Co decays into stable ^{56}Fe via β^+-decay. Positrons emitted in this process possess a mean kinetic energy of 0.632MeV, being thus highly relativistic. At this regime of energies, the annihilation rate is orders of magnitude lower than the energy loss rate (for details see chapter 3). Thus, the produced positrons first lose energy in the expanding debris through ionization and excitation interactions, until they thermalize and reach the energy regime, where annihilation and Ps formation become dominant.

Most groups that tackled the positron propagation and annihilation in a thermonuclear supernova suggest that all positrons thermalize and annihilate locally, up to day 200 past explosion. In this sense, INTEGRAL's SN2014J observation campaign ends too soon to directly observe positron escape. Even if observations would cover the relevant time for this scientific target, the distance to M82 combined with the small fraction of decaying material still remaining, would result in fluxes

below the sensitivity limit of the instrument.

Nonetheless, the present observational window may give clues on whether this assumption is justified or not. In addition to that, by determining the width of the positron annihilation line and the strength of the ortho-Ps continuum, conclusions about the annihilation sites and conditions can be drawn. If positrons thermalize and annihilate locally, the 511keV line is expected to have the same profile as the ^{56}Co lines. If they are able to migrate to smaller or larger radii, the line width will follow the ejecta velocity distribution of the annihilation site. The strength of the ortho-Ps continuum is useful to determine the Ps fraction of a thermonuclear supernova.

Early ^{56}Ni and ^{56}Co lines were detected in this work (see Secs. 5.5 and 5.6) establishing the presence of radioactive material in low optical depths. This implies that a fraction of positrons produced near the surface of the supernova envelope may avoid thermalization, escape the expanding ejecta and diffuse in the ISM. Thus, a careful analysis of the positron annihilation signal at early times could provide information on the fate of these positrons and estimate the escape fraction of positrons produced in the first weeks after the explosion.

For the positron annihilation study of SN2014J, the effort was put in the energy range between 250keV and 550keV to cover both the 511keV line, as well as the energy range where the o-Ps continuum is dominant. The spectra were split in the same observational windows used for the studies of the other ^{56}Co lines, in order to directly link the number of produced positrons $N_{e^+}^{847keV}$, deduced from the 847keV line and the number of annihilating positrons, from the 511keV line and the ortho-Ps continuum $N_{e^+}^{511keV}$.

The 511keV line:
The 511keV line was fitted using a free Gaussian line model. Being considerably less energetic than the dominant ^{56}Co lines, it is less broadened and shifted. For this reason and in order to capture the spectral features of the line accurately, a narrower energy band was chosen for the analysis of the line. In epochs with no significant flux, 2σ upper limits were derived.

The ortho-Ps continuum:
Modeling the ortho-Ps contribution is challenging, due to the fact that it is located in the energy range where the Compton continuum from higher-energy lines should reach its maximum. This hampers an independent and trustworthy estimate of the ortho-Ps flux. Assuming complete transparency at late times allows assigning the measured continuum flux to the three-photon annihilation. Another issue is the shape of the continuum. The theoretical spectrum of the ortho-Ps continuum shown in Fig. 3.1 yields a poor fit, as the spectra do not resemble it. A logistic function similar to the one used for the ^{56}Co lines also does not represent the measured data adequately. One possibility is to fit single or double Gaussian functions on the data, with no meaningful physical implications drawn from the fitted parameters other than flux estimates. Another approach to estimate the continuum flux is to simply add the flux in a given energy range, which already used in previous sections for other line studies. In both cases, the continuum is defined as the energy band between 270-470keV for two reasons:

- Below $\approx$ 250keV a multitude of instrumental background lines with high rates distort the spectra and lead to contamination of the measured fluxes.
- In the 270-470keV band a precise estimate of the flux of all explosion models calculated by The and Burrows 2014 is feasible. The authors do not provide light curves for continuum bands. Therefore they must be estimated from their γ-spectra. A continuum light curve allows a comparison between different explosion models and the data.

In all epochs, 2σ upper limits for the continuum were calculated.

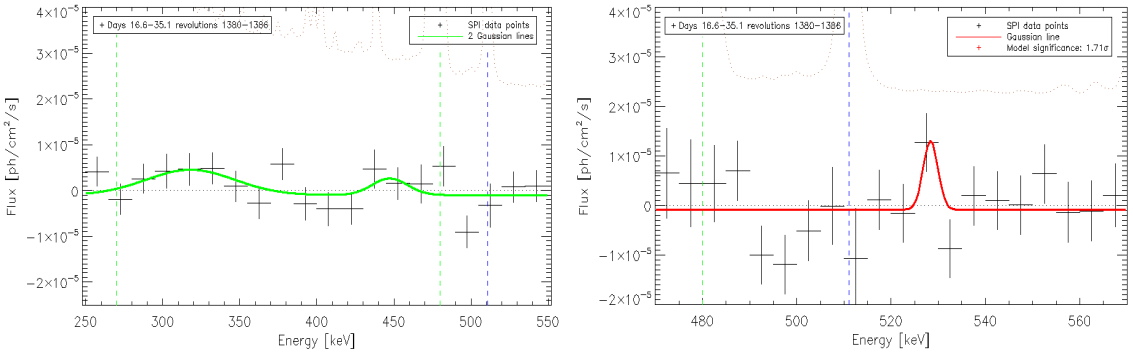

(a) 847keV line, epoch 1

(b) 1238keV line, epoch 1

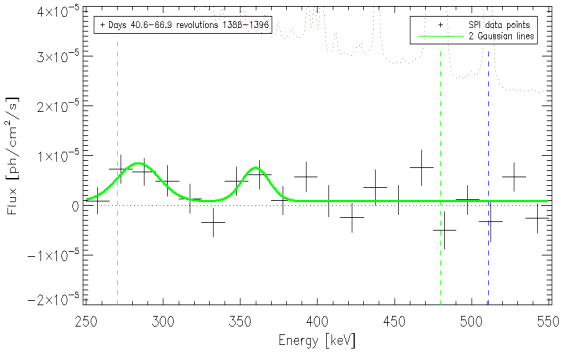

(c) 847keV line, epoch 2

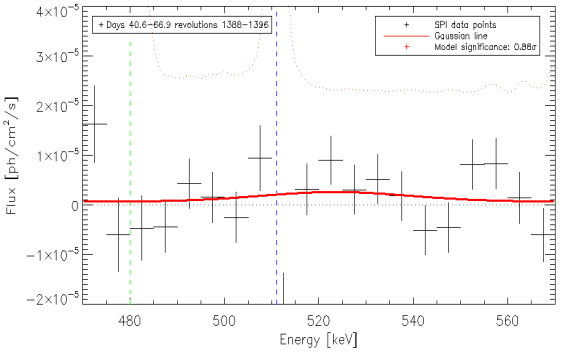

(d) 1238keV line, epoch 2

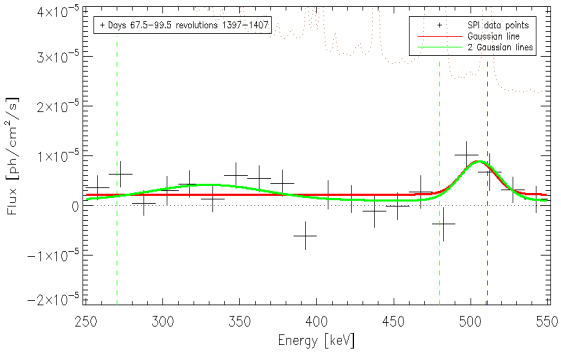

(e) 847keV line, epoch 3

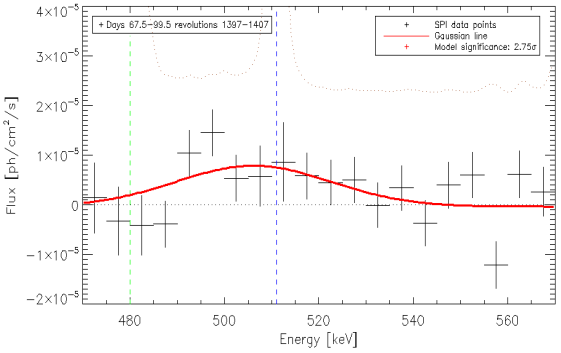

(f) 1238keV line, epoch 3

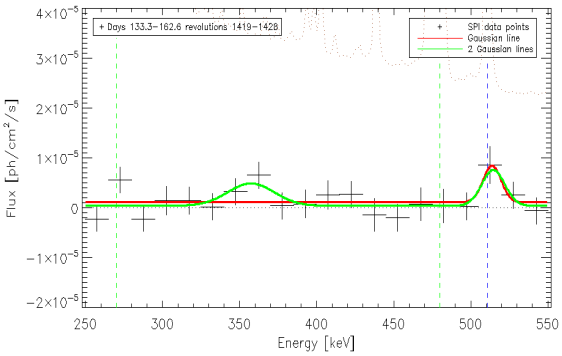

(g) 847keV line, epoch 4

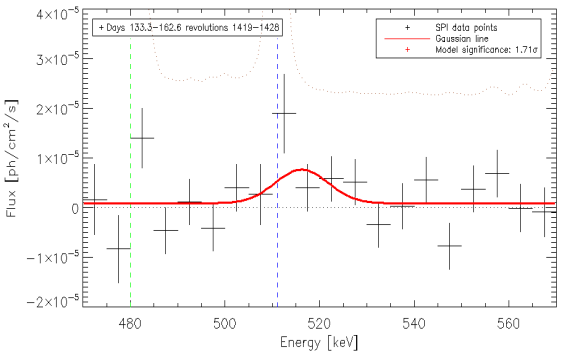

(h) 1238keV line, epoch 4

Figure 5.30.: Left: Gamma-ray spectrum of the 250-550keV band with 24keV energy bin width. Right: The same spectrum presented in 10keV energy bins and only between 470-570keV, for a more detailed inspection of the positron annihilation line. The blue vertical dashed line marks the laboratory energy of the 511keV line, while dashed green vertical lines mark important transitions of ^{56}Ni.

The spectra focusing on positron annihilation are displayed in Fig. 5.30. The panels of the left column depict the whole energy range relevant for positron annihilation in broad 24keV energy bins, while the spectra on the right depict a smaller energy range, from 470-570keV, in order to analyze the 511keV annihilation line with 10keV energy binning.

In epoch one (first row of Fig. 5.30) an enhanced flux between 250-350keV, which can be interpreted as Compton edges of early ^{56}Ni and ^{56}Co lines. Emission from the positron annihilation into two photons is not observed. In early spectra of ^{56}Co (see Fig. 5.18), a narrow blue-shifted flux excess near 870keV was found, corresponding to a bulk velocity of $\sim$ 6000-6500 km/s and a spread velocity of $\sim$ 2000 km/s. Attempting to identify a feature with similar spectral properties on panel (b), a narrow blue-shifted line can be found. Its fitted parameters can be translated into a spread velocity of $\sim$ 1800 km/s, consistent with the velocity of the ^{56}Co line. Its bulk velocity of $\sim$10000 km/s is considerably higher than the one found in Sec. 5.6.

In epoch two, the continuum grows in strength with a peak flux at $\sim$ 280keV. The corresponding spectrum in the vicinity of the 511keV line does not display significant 511keV emission. A 2σ upper limit of 0.80×10^{-4} ph/cm^2/s was calculated.

The continuum intensity declines in epoch three. In contrast, an excess flux in the vicinity of the 511keV line emerges. Fitting it yields a broad red-shifted line with a line flux that exceeds the corresponding one from the ^{56}Co lines. If the line broadening σ and the shift of the peak E_0 are associated with the spread and bulk velocity of ^{56}Co, the emission originates from a region in the ejecta expanding with 22700$\pm$7850km/s and receding from the observer with -2850$\pm$2650km/s. The peculiar spectral properties of this result and the inconsistency both with the same spectrum in other epochs as well as the corresponding spectra of the ^{56}Co lines are noted.

In epoch four, only a small flux excess around E$\sim$ 360keV is observed as continuum emission. The 511keV line is detected with a statistical significance of $\sim 1.7\sigma$. In this epoch, the ejecta can be considered transparent to γ-ray photons and the assumption that the whole emission measured between 270keV and 470keV originates from the annihilation via ortho-Ps is valid. This results in a Ps fraction f=0.62$\pm$1.03 using the flux of the 511keV line and the fitted intensity of the continuum (column 1, epoch 4 in Tab. 5.23) and 0.77$\pm$1.23 choosing the integrated flux of the band (row 4, epoch 4). This value is a lower limit of the actual Ps fraction since only the continuum flux between 270 and 470keV was considered.

Epoch	270-470keV flux green	270-470keV flux black [10^{-4} ph/cm^2/s]	270-470keV 2σ upper limit
Epoch 1	5.04 ± 3.43	2.21 ± 2.74	6.15
Epoch 2	4.11 ± 1.90	5.79 ± 2.32	9.39
Epoch 3	2.92 ± 2.86	4.16 ± 2.12	7.57
Epoch 4	1.70 ± 1.65	2.59 ± 2.12	6.07

Table 5.23.: Fluxes and upper limits of the 270-470keV band of SN2014J, in four epochs. All values are given in units of [10^{-4} ph/cm^2/s].

Epoch	Flux [10^{-4} ph/cm^2/s]	E_0 [keV]	Bulk velocity [km/s]	σ [keV]	Spread velocity [km/s]
Epoch 1	0.54 ± 0.49	528.3 ± 0.9	10200 ± 550	1.6 ± 0.9	1800 ± 1450
Epoch 2	0.78 ± 1.14	523.6 ± 20.3	7400 ± 11900	16.0 ± 19.1	13300 ± 26400
Epoch 3	3.40 ± 1.85	506.2 ± 4.5	-2850 ± 2650	16.4 ± 5.7	22700 ± 7850
Epoch 4	0.95 ± 1.27	516.2 ± 6.3	3050 ± 3700	5.6 ± 5.5	7650 ± 9400

Table 5.24.: 511keV line parameters of SN2014J derived from a more detailed analysis of the 470-570keV energy band.

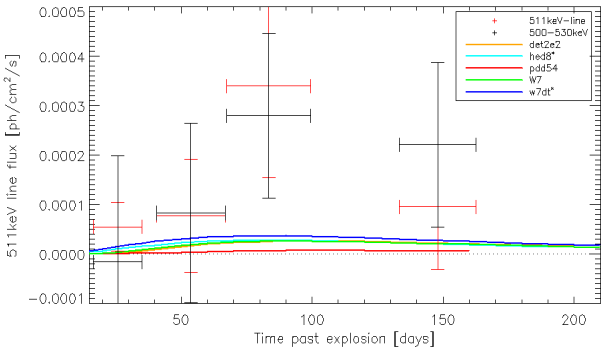

(a) 511keV line light curve, Ps-fraction f=1.0

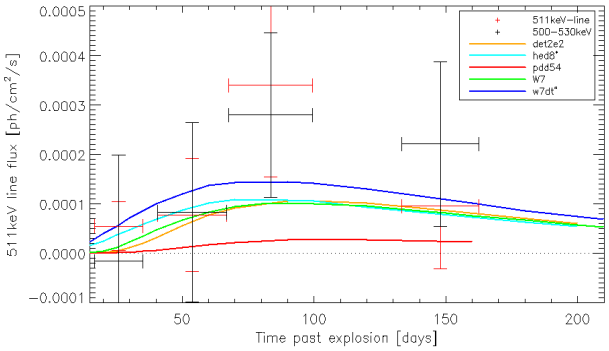

(b) 511keV line light curve, Ps-fraction f=0.0

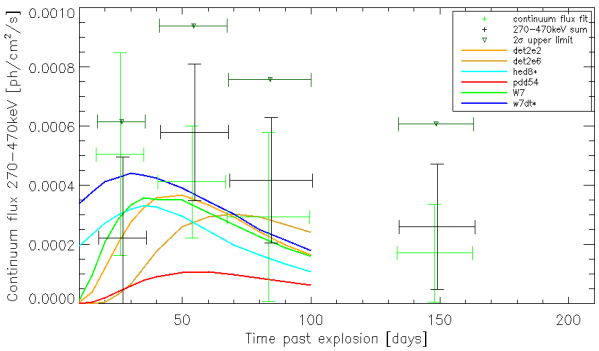

(c) 270-470keV energy band light curve

Figure 5.31.: Left: 511keV light compared light curves of the most representative models constructed by The and Burrows 2014. For all models, a Ps fraction of f=1.0 was assumed. Right: The same plot as left but assuming a Ps-fraction of f=0.0. Below: 270-470keV energy band light curve compared to model light curves calculated from the spectra provided by The and Burrows 2014.

The panels in Fig. 5.31 present the flux evolution of both the 511keV line and the continuum at 270-470keV. The colored slopes in panel (a) display the light curve evolution of a few representative models constructed by The and Burrows 2014, who assumed a Ps-fraction of f=1.0 in their simulations. In panel (b), the light curves were multiplied by a factor of 4 to simulate the case without Ps formation (f=0.0). The panel on the bottom displays the evolution of the continuum between 270 and 470keV. No spectra to derive continuum fluxes were provided for any model after day 100 (for details, see Appendix). To analyze the positron-annihilation line, a free Gaussian line model was fitted to the data (see right panels of Fig. 5.30. The derived fluxes are given in Tab. 5.24

represented by the red data points in Fig. 5.31. The black data points correspond to a sum of the flux in the 500-530keV band, where most of the 2-photon annihilation is expected. The continuum of the green fit in the left panels of Fig. 5.30 is represented by the green data points in Fig. 5.31c, whereas the black data points were calculated by summing the flux in the 270-470keV. Finally, the data points with arrows are 2σ upper limits of the continuum.
While the flux of the 511keV line can be safely assigned to electron-positron annihilation, the fluxes measured in the continuum are a superposition of Compton scattered photons from higher energy lines and possible emission from ortho-Ps annihilation. Model and calculated light curves for both the line and the continuum were compared to all 15 available models with a χ^2-similar technique that was also used in the analysis of the 847keV line and is described in detail in the Appendix. The results are reported on Tab. 5.25.

Model	511keV$_{f=1}$ red	511keV$_{f=1}$ black	511keV$_{f=0}$ red	511kev$_{f=0}$ black	270-470keV green	270-470keV black
dd202c	4.33	3.74	1.90	**1.46**	**0.25**	1.62
dd4	4.62	3.91	2.55	1.85	0.67	**1.73**
det2	4.31	3.77	1.83	**1.56**	0.34	2.31
det2e2	4.65	3.90	2.64	1.82	0.85	**1.75**
det2e6	5.12	4.26	3.97	2.88	2.41	2.63
hecd	3.96	3.67	**1.35**	**1.41**	**0.28**	2.16
hed6	4.98	4.34	3.42	3.16	3.67	6.14
hed8	4.25	3.88	**1.72**	1.87	1.08	3.32
m36	4.56	3.93	2.34	1.92	0.61	2.11
pdd54	5.35	4.55	4.69	3.89	4.95	7.12
W7	4.56	3.91	2.37	1.88	0.58	2.21
W7A	4.54	3.94	2.27	1.97	0.77	2.25
w7dn	4.36	3.84	1.90	1.72	0.52	2.10
w7dt	3.80	3.59	3.80	3.59	**0.12**	**2.07**
W7E	4.20	3.87	**1.67**	1.86	0.93	2.98

Table 5.25.: χ^2 test of the 511keV line (red and black data points) and the continuum (green and black data points in Fig. 5.31c to the 15 supernova models of The and Burrows 2014. A low value indicates high resemblance between the calculated flux and the respective model. Bolded values indicate a high degree of compatibility compared to other models.

The values reported in Tab. 5.25 show that the derived fluxes match better with the modeled light curves that assumed no PS formation. However, the improvement in the χ^2 values is small. The 270-470keV continuum flux calculated from the model with two broad Gaussian lines (green data points) also matches better with the model light curves compared to the integrated continuum fluxes. Model discrimination from the analysis of the 250-550keV energy band is not possible, due to the small differences in the derived χ^2-values.

The relatively low statistical significances of the measured signals and the unknown Ps fraction in the first three epochs do not permit a precise determination of the positron escape fraction. An estimate of the ortho-Ps continuum at these epochs, where the Compton-continuum dominates would lead to a highly uncertain intensity. For this reason, the two limiting cases of f=0.0 and f=1.0 were accepted as possible Ps fractions. The number of annihilating positrons can be derived from the flux of the 511keV line via Eq. (5.5):

$$N_{e^+}^{511keV} = 4 \cdot \pi \cdot d^2 \cdot F_{511keV} \cdot \frac{1}{2} \cdot \mu \tag{5.5}$$

where

$$\mu = \begin{cases} 4, \text{ for Ps fraction f= 1} \\ 1, \text{ for Ps fraction f= 0} \end{cases}$$

These considerations lead to the following values of annihilating positrons from the analysis of the 511keV line:

Epoch	$N_{e^+,f=0}^{511keV}$ [10^{46}e/s]	$N_{e^+,f=1}^{511keV}$ [10^{46}e/s]
Epoch 1	3.98±3.65	15.92±14.62
Epoch 2	5.69±8.42	22.75±33.67
Epoch 3	24.90±13.90	99.59±55.59
Epoch 4	6.97±9.34	27.90±37.36

Table 5.26.: Annihilating e^+ of SN2014J calculated from the flux of the 511keV line in four epochs.

The positron escape fraction is defined as the number of positrons seen to annihilate per second in 511keV γ-rays, divided by the positron production rate calculated through the analysis of the 847keV line.

$$\eta = 1 - \frac{N_{e^+}^{511keV}}{N_{e^+}^{847keV}} \tag{5.6}$$

An escape fraction of η=1.0 implies that all positrons produced through the decay of ^{56}Co are able to escape the ejecta. This is the case for $N_{e^+}^{511keV} = 0$. On the other hand, η=0.0 indicates that the line fluxes of the 847keV line and the 511keV line are compatible to each other and all positrons produced in the decay of ^{56}Co annihilate in the ejecta and give rise either to the 511keV line or the ortho-Ps continuum. In this case, $N_{e^+}^{847keV} = N_{e^+}^{511keV}$. A negative escape fraction indicates that the positron annihilation rate exceeds the positron production rate derived from the 847keV line. In other words, the line intensity of the 511keV line is higher than the one from the 847keV line, scaled to their respective branching ratios ($N_{e^+}^{847keV} \leq N_{e^+}^{511keV}$). Inserting the values reported in Tabs. 5.18 and 5.26, the following escape fractions for INTEGRAL's SN2014J campaign are reported:

Epoch	$\eta_{f=0}$, red fit	$\eta_{f=0}$, blue fit	$\eta_{f=1}$, red fit	$\eta_{f=1}$, blue fit
Epoch 1	-2.49 ± 7.02	0.03 ± 1.15	-12.96 ± 20.08	-2.89 ± 4.62
Epoch 2	-0.08 ± 1.88	0.49 ± 0.82	-3.34 ± 7.54	-1.03 ± 3.32
Epoch 3	-2.67 ± 3.46	-1.02 ± 1.25	-13.69 ± 13.83	-7.08 ± 4.99
Epoch 4	0.02 ± 1.54	-	-2.90 ± 6.17	-

Table 5.27.: Calculated e^+ escape fractions of SN2014J for all epochs using column 1 and 2 of Tab. 5.18.

The domination of negative escape fractions in Tab. 5.27 indicates no positron escape from a type Ia supernova for days 16.6-162.6 after the explosion. In other words, the measured 511keV-line is strong enough to account for all produced positrons, for both limiting cases of possible Ps fractions. However, the positrons measured in the 511keV line appear to annihilate at higher expansion

velocities than the corresponding velocities of their parent isotope. Either they are capable of migration inside the ejecta, before annihilating in areas with higher expansion velocities, or they do not completely thermalize and annihilate with some residual kinetic energy of a few keV. However, the low statistical significances of the positron annihilation line indicate that the derived escape fractions and spread velocities should be handled with caution.

5.7.1. Mission-integrated e^+ escape fraction for SN2014J

One way to circumvent the low statistics and derive the positron escape fraction of SN2014J with a smaller error is to use the mission integrated spectra. The first step is to fit the spectra with free Gaussian lines. Consequently, the mission-averaged positron production rate is calculated for the 847keV and the 1238keV lines $\overline{N}_{e^+}^{^{56}Co}$ and the mission-averaged positron annihilation rate $\overline{N}_{e^+}^{511keV}$ for the 511keV line. The derived rates should have the lowest possible error bars, due to the excellent exposure time of 2.8Ms. Last but not least, the averaged positron escape fraction of SN2014J during the time t=16.6-162.6 after the explosion is derived.

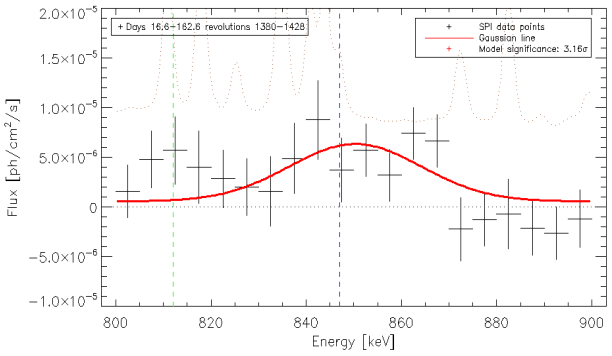

(a) 847keV line, entire mission spectrum

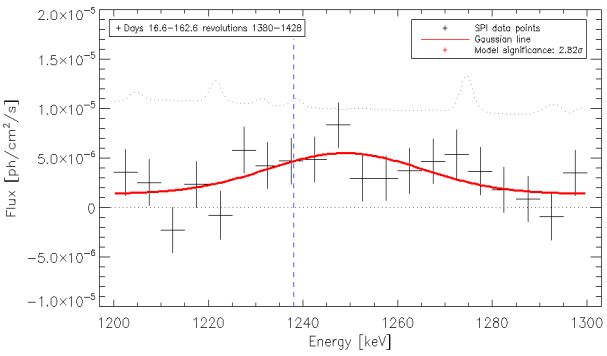

(b) 1238keV line, entire mission spectrum

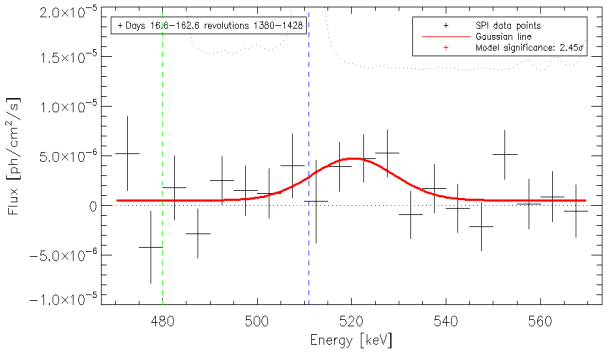

(c) 511keV line, entire mission spectrum

Figure 5.32.: Gamma-ray spectra of SN2014J in the energy band near the three major ^{56}Co lines at 847keV, 1238keV and 511keV band. The spectra are determined over the entire observing period. Every data points corresponds to an energy bin of 10keV.

The fluxes depicted in Fig. 5.32 are determined over the entire observing period and should have the lowest possible error bars. The spectra show significant flux excess in all three energy bands that can be associated with the γ-emission of ^{56}Co.

Epoch	Flux [10^{-4} ph/cm^2/s]	E_0 [keV]	Bulk velocity [km/s]	σ [keV]	Spread velocity [km/s]	$\overline{N}_{e^+}$ [$10^{46}e^+$/s]
847keV line	2.01 ± 1.03	850.3 ± 4.5	1150 ± 1600	13.9 ± 5.5	11550 ± 4550	5.8 ± 3.0
1238keV line	1.70 ± 1.15	1248.9 ± 5.5	2650 ± 1350	16.4 ± 9.3	9350 ± 5300	7.2 ± 4.9
511keV line	0.92 ± 0.69	520.3 ± 4.9	5500 ± 2900	8.7 ± 5.3	11950 ± 7400	6.7 ± 5.2

Table 5.28.: Fitted parameters of the three main ^{56}lines over the entire mission

The fitted parameters presented in Tab. 5.28 are consistent to each other. The only discrepancy between the lines is that the positron annihilation line shows a higher blue-shift, which suggests that positron annihilate either keeping a small fraction of their kinetic energy, or migrate to larger radii and subsequently at higher expansion velocities. The right column of Tab. 5.28 reports the positron production rates for the 847keV and 1238keV lines and the positron annihilation rate for the 511keV line, assuming an Ps-fraction of f=0. Multiplying this number with the factor 4 gives the number of annihilating positrons for a Ps-fraction of f=1 ($\overline{N}^{511keV}_{e^+,f=1.0} = 26.8 \pm 20.8$).
Using the average of the two values from the 847keV and the 1238keV line and inserting it into 5.6, the positron escape fraction of SN2014J is:

$$\eta = 1 - \frac{N^{511keV}_{e^+,f=0.0}}{N^{^{56}Co}_{e^+}} = -0.03 \pm 1.21, \tag{5.7}$$

which is less constraining than the positron escape fraction Siegert 2017 derived but does not rely on the assumption that the 511keV and the 847keV lines should share the same broadening and comes completely from the data itself.

To sum up, the positron annihilation line of SN2014J was detected with a maximal significance of 2.45σ over the entire mission. During this time (Δt=145.6d), $8.45 \pm 6.54 \times 10^{53}$ positrons are seen to annihilate. This number is higher than the total number of positrons produced, as derived from the analysis of the two major ^{56}Co lines ($n^{^{56}Co}_{e^+} = 8.17 \pm 7.17 \times 10^{53}$). The data are best described assuming a Ps-fraction of f=0.0, albeit the low statistics do not allow a firm rejection of f=1.0. The positron annihilation signal was also observed in the four-epoch analysis, albeit with a lower significance and less constrained spectral parameters. In most of the cases, negative escape fractions indicate that more positrons are annihilating, than they are produced from the analysis of the two major ^{56}Co lines.

6. SN2011fe

SN2011fe was discovered on the 24th of August 2011 by the Palomar Transient Factory (PMT) in the well-studied Pinwheel Galaxy (M101) (Nugent et al. 2011). At a distance of 6.4Mpc (Shappee and Stanek 2011), it was the closest supernova in 25 years and the fifth brightest in the century, becoming thus a prime target for detailed studies and high-quality data of a type Ia supernova. Early spectra, announced the explosion as a normal type Ia supernova (Nugent et al. 2011). Pre and post-discovery imaging placed the explosion date at August 23.687+-0.014 UT, implying that the supernova was discovered only $\approx$ 12 hours after first light.

6.1. Host galaxy M101

Messier 101 or the Pinwheel galaxy, is a face-on spiral galaxy in the constellation of Ursa Major. Similar to M82, M101 shows strong star formation activity and several bright star-forming regions (Waller et al. 1997). Its canonical distance from the Milky Way is estimated at 6.4Mpc $\pm$ 0.7Mpc (Shappee and Stanek 2011), which is also adopted throughout the thesis.

Figure 6.1.: Optical image of SN2011fe in M101 (by Rick Johnson)

SN2011fe is located at galactic coordinates (l,b)=(102.03°, 59.77°), well at the outskirts of M101 (more than four arcseconds south of the galactic nucleus). Observations in the optical classify SN2011fe as a spectroscopically normal type Ia SN with minor absorption and reddening probably due to the fortunate fact that M101 is observed face-on from the Milky Way (Pereira et al. 2013).

6.2. Analyses in other wavelengths

Due to its early detection and proximity to M101, SN2011fe became a primary target of interest for investigating theoretical predictions concerning thermonuclear supernovae for the first time with high-quality data and across the electromagnetic spectrum.

The early luminosity was described accurately by the expanding fireball model, constraining the radius of the exploded object to less than $0.1R_{\odot}$ (Nugent et al. 2011; Bloom et al. 2012). Follow-up spectra near the maximum light suggested the synthesis of 0.5-0.6$M_{\odot}$ of radioactive ^{56}Ni (Bloom et al. 2012; Röpke et al. 2012).

Early spectra were dominated by neutral and singly ionized IMEs like O, Mg, S, Ca, with features of unburned C and O. Combining all spectroscopic evidence, SN2011fe was the first explosion to confirm the long-standing hypothesis, that supernovae type Ia originate from CO WDs (Nugent et al. 2011; Bloom et al. 2012). Time series of early optical spectra confirmed the fact that SN2011fe was a spectroscopically normal type Ia supernova but also showed the presence of a considerable fraction of IGE throughout the ejecta (Parrent et al. 2012; Piro and Nakar 2014).

Parameters	Values and reference
m_{Bmax}	9.94mag (Pereira et al. 2013)
M_{Bmax}	−19.13 (Röpke et al. 2012)
t_{Bmax}	Sep10, 18.3d past explosion (Parrent et al. 2012)
Δm_{15}	1.11mag (Pereira et al. 2013)

Table 6.1.: SN2011fe optical properties

SN2011fe was also observed by instruments sensitive in other energy bands. Radio and X-ray data yielded non-detections and allowed strict upper limits in the density of the circumbinary medium and the mass loss of the progenitor system in its pre-supernova evolution.

In particular, radio non-detections placed an upper limit on the mass loss rate at $\dot{M} \leq 6\times 10^{-10} M_{\odot}/yr$, excluding most candidate companions other than double degenerates and a few single degenerate systems (Chomiuk et al. 2012). Similar results came from X-ray data that set an upper limit at $2\times 10^{-9} M_{\odot}/yr$ (Margutti et al. 2012). Four years after first light, no excess flux could be measured in the radio, suggesting that the explosion took indeed place in a very tenuous medium with a particle density $n \leq 1 cm^{-3}$ (Kundu et al. 2017). Röpke et al. 2012 compared optical spectra of SN2011fe with simulated spectra of one delayed detonation model and one WD merger model and concluded that the level of agreement was slightly better for the merger, especially around maximum light.

Further evidence for a double degenerate system provided the analysis of pre-explosion HST images by Li et al. 2011a. No bright source was identified at the location of SN2011fe, ruling out several luminous binary companions such as red giants and allowing only fainter main sequence stars or sub-giants of $M_{*} \leq 4M_{\odot}$ as candidate companion stars.

6.3. Analyses in the gamma-regime

The distance between M101 and the Milky Way was close to the maximal distance for studies of the γ-radiation emitted by a thermonuclear supernova. The potential detection of SN2011fe depends on the explosion mechanism, the amount of synthesized ^{56}Ni and the progenitor system, offering thus the opportunity either to detect directly the explosion, or place strict upper limits and constrain the progenitor and explosion scenarios. SPI started its SN2011fe campaign on Aug 29, only $\sim$ 6 days after detection. The first run of observations ended on Sept 12, near maximum optical light, due to the unfavorable position of the Sun relative to M101. After a gap of $\sim$ 25 days, the observations continued until November 20, $\approx$ 88 days after the explosion, covering revolutions

1097-1111 and accumulating thereby a total of 2.8Ms of exposure. The first observation window offers the opportunity to search for early ^{56}Ni emission, in an earlier time window compared to SN2014J. The second part of observations includes fifteen revolutions and should capture the gradual strengthening of the ^{56}Co lines. Unfortunately, observations stopped when the γ-ray emission is expected to peak.

Isern et al. 2013a analyzed the SPI data and found no significant excess in the SN2011fe spectra. In particular, the analysis of the pre-maximum phase yielded 2σ upper limits on the two main ^{56}Ni lines; $7.1\times\ 10^{-5}$ pm/cm^2/s for the 158keV line and $2.3\times\ 10^{-4}$ pm/cm^2/s for the 812keV line.

A complementary study of the second observation window between days $\sim$ 45-88, allowed the placement of the following upper limits on broader energy bands (Isern et al. 2013b).

Energy band [keV]	2σ Upper limit [ph/cm^2/s]
505-525	1.1×10^{-4}
830-875	1.4×10^{-4}
835-870	1.2×10^{-4}
1215-1275	1.2×10^{-4}
1220-1270	1.1×10^{-4}
1225-1265	1.0×10^{-4}

Table 6.2.: 2σ Upper limits from the analysis of SPI data by Isern et al. 2013b

I re-analyzed SPI's SN2011fe dataset using our improved background modeling approach.

6.4. This work

Two minor modifications compared to the SN2014J analysis were made: First, I omitted the analysis of the 1040keV line, which should be well below the sensitivity limit of SPI, and second, I only fitted one source in the field of view, SN2011fe, since no other γ-ray source could be found in the general source catalog of INTEGRAL. Finally, for spectra with no significant emission, 2σ upper limits were calculated.

The analysis of SN2011fe is split into three main parts, similar to SN2014J:

1. The first five revolutions of the SN2011fe observation campaign (rev.1084-1088) are analyzed for the ^{56}Ni lines at 158keV, 750keV and 812keV lines in time scales of single revolutions
2. The whole observation data set, consisting of 20 revolutions, is used to explore the properties of the two brightest ^{56}Co lines at 847keV and 1238keV in two different time scales.
   - In three epochs:
     a) Revolutions 1084-1087, 6.3-17.7 days after the explosion
     b) Revolutions 1097-1103, 45.2-65.6 days after the explosion
     c) Revolutions 1104-1111, 66.3-68.5 days after the explosion
   - In case of a firm detection in the three-epoch analysis, the variability of the signal will be analyzed in time bins of four revolutions ($\sim$ 12 days).

3. The energy range between 250 and 550keV is investigated for a possible positron annihilation signal in the supernova envelope, using the same observations windows as for the ^{56}Co lines.

The whole exposure window consists of 1101 telescope pointings with a duration of typically $\sim$ 2000s. This can be translated into 16515 individual spectra for a total 1.7Msec of exposure.

6.5. Nickel lines

The analysis of SN2014J's ^{56}Ni emission showed some discrepancies regarding the fluxes of its lines. While the 812keV line showed a firm detection, at least for the first two epochs, the total absence of its neighboring 750keV line challenged the validity of detection. Depending on the distribution of ^{56}Ni in the supernova ejecta, each individual explosion can show diverse spectral properties during the first weeks of its evolution. However, due to the increased distance compared to M82, only a supernova with a considerably higher ^{56}Ni mass in the outer ejecta than SN2014J would produce a detectable flux in the first weeks of its evolution.

The analysis sequence is identical to the one for SN2014J: First, the 812keV line is investigated. If the line is detected, both the 158keV and the 750keV lines will be analyzed for consistency.

6.5.1. 812keV line

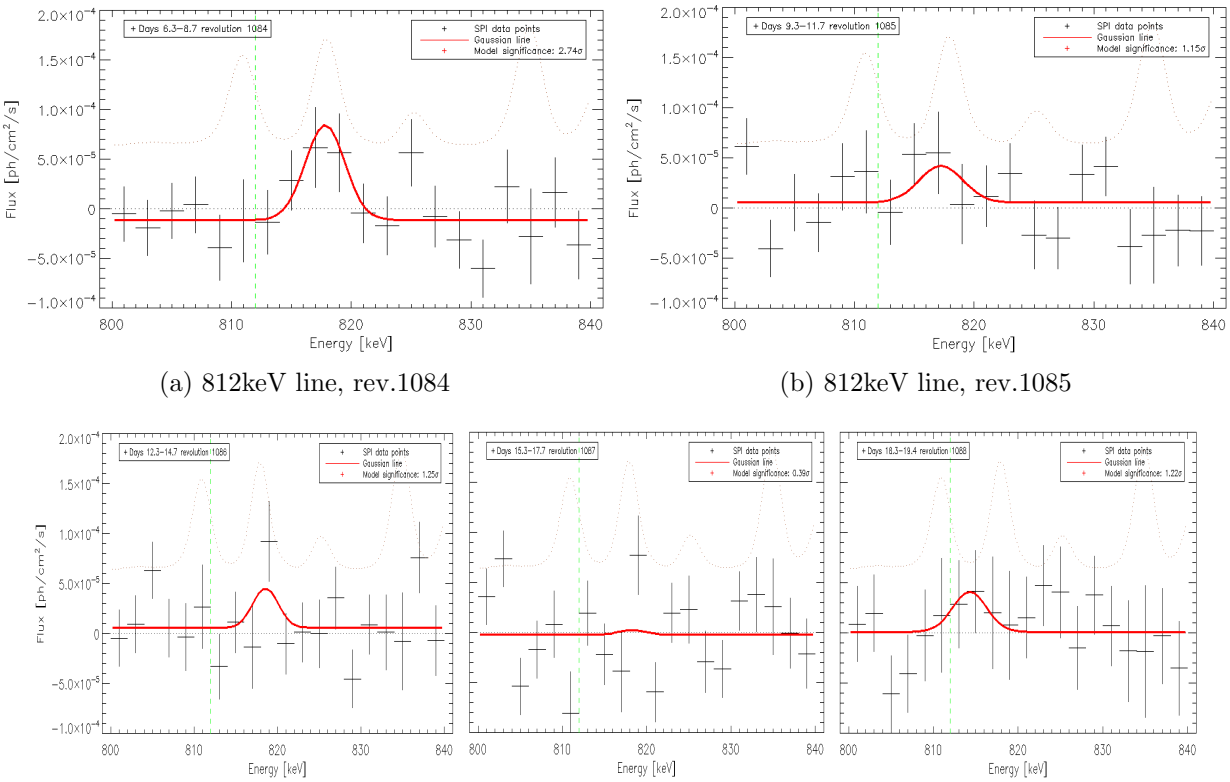

(a) 812keV line, rev.1084 (b) 812keV line, rev.1085

(c) 812keV line, rev.1086 (d) 812keV line, rev.1087 (e) 812keV line, rev.1088

Figure 6.2.: Time series of the 800-840keV band for revolutions 1084-1088. Every data points corresponds to an energy bin of 4keV.

The spectra presented in Fig. 6.2 focus on the 812keV line and were fitted with a free Gaussian line fit on top of a constant. In most panels and a blue-shifted feature around $E_0 \approx 818$keV that

gradually declines in intensity is detected. The spectral feature at $E_0 \sim 818$keV has consistent spectral properties throughout the first run of observations. It can be assigned to ^{56}Ni, expanding with a velocity of ~ 2000km/s. In panel (a), the line has a statistical significance of $\sim 2.7\sigma$ and indicates an unexpectedly high amount of ^{56}Ni at low optical depths.

Epoch	Flux [10^{-4} ph/cm^2/s]	E_0 [keV]	Bulk velocity [km/s]	σ [keV]	Spread velocity [km/s]
Revolution 1084	3.96 ± 2.43	817.8 ± 0.7	2100 ± 300	1.7 ± 0.7	1200 ± 750
Revolution 1085	1.67 ± 1.51	817.2 ± 1.2	2000 ± 450	1.8 ± 1.0	1400 ± 1000
Revolution 1086	1.51 ± 4.13	818.6 ± 0.9	2400 ± 300	1.5 ± 0.8	1100 ± 850
Revolution 1087	0.19 ± 0.18	818.3 ± 1.4	2300 ± 500	1.6 ± 1.1	1100 ± 1150
Revolution 1088	2.01 ± 3.40	814.3 ± 2.6	850 ± 950	2.0 ± 2.7	1550 ± 2700

Table 6.3.: 812keV line parameters

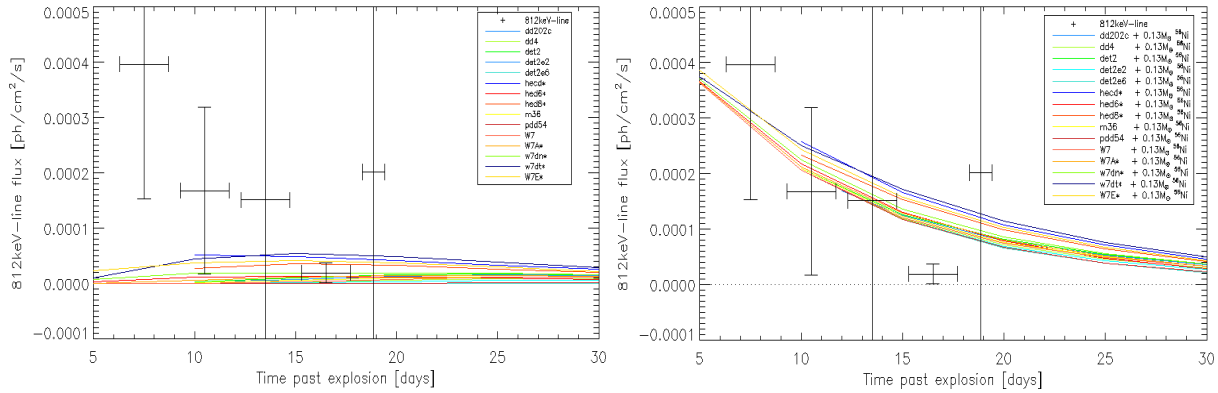

Figure 6.3.: Left: 812keV-line light curve of SN2011fe compared with models from The and Burrows 2014, scaled to a distance of 6.4Mpc. Right: A completely transparent ^{56}Ni shell with a total mass of $0.13M_\odot$ was placed on the surface of the models from The and Burrows 2014. Models with an asterisk indicate the presence of ^{56}Ni in their outer layers.

The flux reported in the first row of Tab. 6.3 can be converted to an initial ^{56}Ni mass near the surface with Eq. (6.1):

$$\begin{aligned} M(^{56}\mathrm{Ni}, t = 0) &= 4 \cdot \pi \cdot d_{M101}^2 \cdot F_{812\mathrm{keV}} \cdot m_{\mathrm{Ni}} \cdot \exp\left(\frac{t}{\tau_{\mathrm{Ni}}}\right) \cdot \frac{1}{p_{812\mathrm{keV}}} \\ &= 0.19 \pm 0.12 M_\odot \end{aligned} \tag{6.1}$$

The above derived ^{56}Ni mass is $\sim 40\%$ of the mass predicted by observations in other wavelengths. This amount of visible radioactive mass only one week after the explosion is not predicted by any model, even by those with fully mixed ^{56}Ni distributions.
Fig. 6.3 compares the fitted 812keV line flux with the flux predicted by models from The and Burrows 2014, scaled to a distance of 6.4Mpc. The fluxes derived in revolutions 1084 and 1085 lie well above the brightest models with a considerable amount of ^{56}Ni at low optical depths. In the right panel, the model light curves were enriched with an extra completely transparent layer of ^{56}Ni with a total mass of $M_{^{56}Ni}$=$0.13M_\odot$. The constructed light curve explains the observed data points more accurately. The exact amount of extra ^{56}Ni required to reach maximum match was fitted to the models and is presented in Tab. 6.6, along with the statistical improvement compared to the unmodified models achieved in the fit.

6.5.2. 158keV line

Following the example of the SN2014J analysis, the detection of the 812keV line can only be verified as a valid celestial signal in connection to the analysis of the remaining prominent lines of the ^{56}Ni decay. The energy of the 158keV line, though, does not allow a direct comparison with the properties of the 812keV line, as it can be seriously affected by both photoelectric absorption and Compton scattering. However, if $0.19 \pm 0.12 M_{\odot}$ ^{56}Ni are located near the surface, a small fraction of it could be on the surface of the expanding envelope producing a blue-shifted flux excess close to the 158keV line.

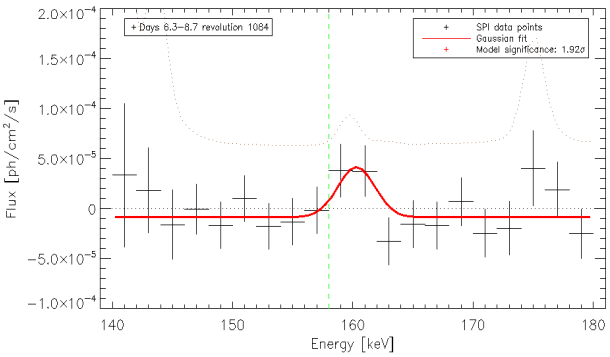

(a) 158keV line, rev.1084

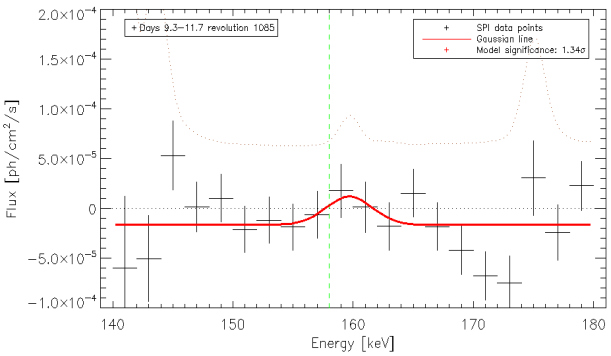

(b) 158keV line, rev.1085

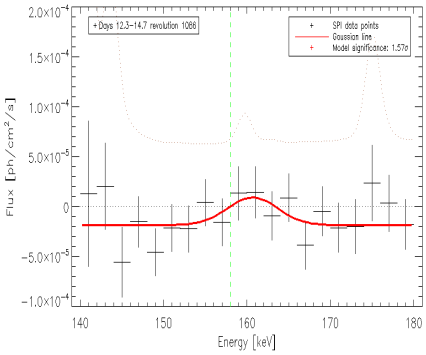

(c) 158keV line, rev.1086

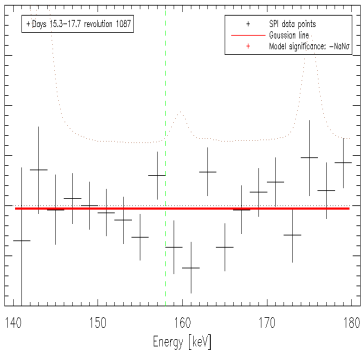

(d) 158keV line, rev.1087

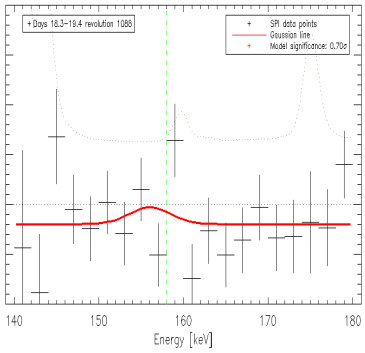

(e) 158keV line, rev.1088

Figure 6.4.: Time series of the 140-180keV band for revolutions 1084-1088. Every data points corresponds to an energy bin of 4keV.

Epoch	Flux [10^{-4} ph/cm^2/s]	E_0 [keV]	Bulk velocity [km/s]	*sigma* [keV]	Spread velocity [km/s]
Revolution 1084	1.96 ± 1.78	160.3 ± 1.0	4300 ± 2000	1.5 ± 1.0	6100 ± 5200
Revolution 1085	1.37 ± 1.98	159.7 ± 2.1	3100 ± 3900	1.9 ± 2.3	7900 ± 11000
Revolution 1086	2.09 ± 2.60	160.7 ± 2.8	5100 ± 5200	3.0 ± 3.4	13000 ± 15500
Revolution 1087	≤ 0.01	–	–	–	–
Revolution 1088	1.02 ± 3.34	156.0 ± 1.9	3700 ± 3600	2.4 ± 1.9	10400 ± 8700

Table 6.4.: 158keV line parameters

The results of the 158keV line fits are consistent with the ones obtained from the 812keV line analysis. Inserting the 158keV line flux measured in revolution 1084 into Eq. (6.1) yields an initial ^{56}Ni mass of $M(^{56}Ni, t = 0) = 0.08 \pm 0.07 M_{\odot}$. The significance of this result is low, albeit it suggests that about half of the observed ^{56}Ni is located at the surface, while the other half is located slightly deeper in the envelope so that only 812keV photons escape.

6.5.3. 750keV line

A 750keV photon is emitted in 50% of all ^{56}Ni decays, making its corresponding line a potential candidate for detection.

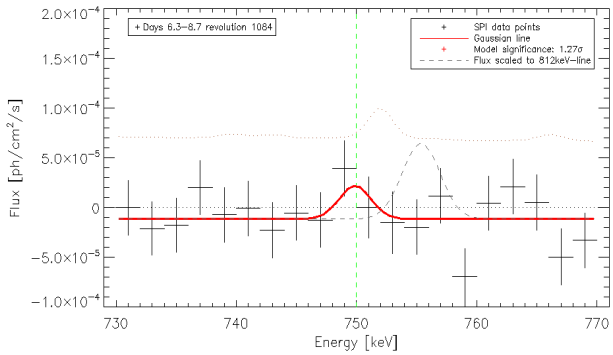

(a) 750keV line, rev.1084

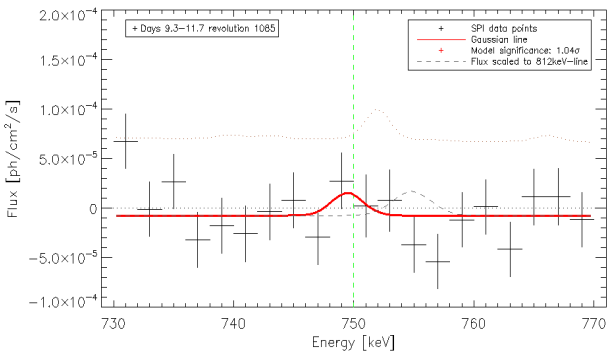

(b) 750keV line, rev.1085

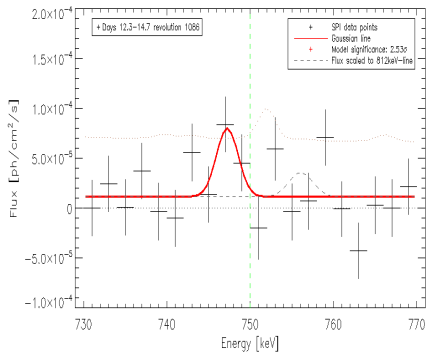

(c) 750keV line, rev.1086

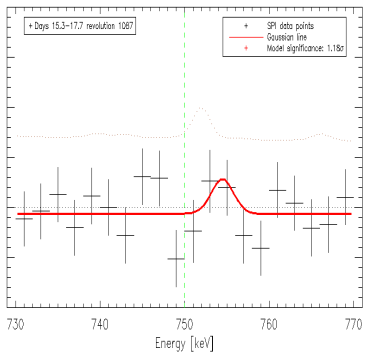

(d) 750keV line, rev.1087

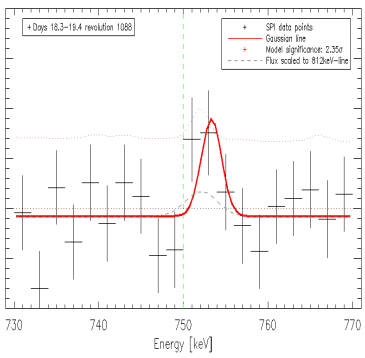

(e) 750keV line, rev.1088

Figure 6.5.: Time series of the 730-770keV band for revolutions 1084-1088. Every data point corresponds to an energy bin of 4keV. Dashed grey slopes display the Gaussian line expected from the results of 812keV line analysis.

Similar to the ^{56}Ni line analysis of SN2014J, the analysis of the 750keV lines yields no particular flux excess in the energy range where it is expected. Dashed grey lines represent the analogous 750keV line features as calculated from the 812keV line and are rejected with significances of $\sim 3.23\sigma$, 1.04σ and 1.35σ for revolutions 1084, 1085 and 1086 respectively. In revolution 1087 no significant emission was observed near the 812keV line, while for revolution 1088, the two lines may coincide, but the intensity of the 750keV line is twice that of the 812keV line.

Epoch	Flux [10^{-4} ph/cm^2/s]	E_0 [keV]	Bulk velocity [km/s]	σ [keV]	Spread velocity [km/s]
Revolution 1084	1.10 ± 1.05	749.9 ± 1.1	-50 ± 400	1.3 ± 0.9	850 ± 1200
Revolution 1085	0.76 ± 1.45	749.5 ± 1.1	-200 ± 450	1.3 ± 1.0	900 ± 1350
Revolution 1086	2.26 ± 1.62	747.2 ± 0.7	-1100 ± 250	1.3 ± 0.7	900 ± 900
Revolution 1087	0.11 ± 0.95	754.5 ± 0.8	1800 ± 300	1.3 ± 0.7	900 ± 900
Revolution 1088	2.94 ± 2.36	753.3 ± 0.7	1300 ± 300	1.2 ± 0.8	700 ± 1100

Table 6.5.: 750keV line fitted parameters, 5 epochs

^{56}Ni mass yields

In an analogous manner to the 812keV line analysis, the exact amount of ^{56}Ni required to explain the observed emission was fitted to the data and the reported masses are presented below in Tab. 6.6.

Model	Extra $M_{^{56}Ni}$(812keV) [$M_\odot$]	Significance [σ]	Extra $M_{^{56}Ni}$(158keV) [$M_\odot$]	Significance [σ]
dd202c	$0.13 \pm 0.07 M_\odot$	1.88	$0.08 \pm 0.06 M_\odot$	1.41
dd4	$0.13 \pm 0.07 M_\odot$	1.90	$0.08 \pm 0.06 M_\odot$	1.41
det2	$0.13 \pm 0.07 M_\odot$	1.87	$0.08 \pm 0.06 M_\odot$	1.40
det2e2	$0.13 \pm 0.07 M_\odot$	1.91	$0.08 \pm 0.06 M_\odot$	1.41
det2e6	$0.13 \pm 0.07 M_\odot$	1.92	$0.08 \pm 0.06 M_\odot$	1.42
hecd	$0.10 \pm 0.07 M_\odot$	1.40	$0.06 \pm 0.06 M_\odot$	1.08
hed6	$0.12 \pm 0.07 M_\odot$	1.81	$0.08 \pm 0.06 M_\odot$	1.37
hed8	$0.11 \pm 0.07 M_\odot$	1.63	$0.07 \pm 0.06 M_\odot$	1.31
m36	$0.13 \pm 0.07 M_\odot$	1.89	$0.08 \pm 0.06 M_\odot$	1.41
pdd54	$0.13 \pm 0.07 M_\odot$	1.92	$0.08 \pm 0.06 M_\odot$	1.42
W7	$0.13 \pm 0.07 M_\odot$	1.90	$0.08 \pm 0.06 M_\odot$	1.41
W7A	$0.13 \pm 0.07 M_\odot$	1.84	$0.08 \pm 0.06 M_\odot$	1.39
w7dn	$0.12 \pm 0.07 M_\odot$	1.75	$0.07 \pm 0.06 M_\odot$	1.33
w7dt	$0.10 \pm 0.07 M_\odot$	1.48	$0.07 \pm 0.06 M_\odot$	1.24
W7E	$0.11 \pm 0.07 M_\odot$	1.54	$0.07 \pm 0.06 M_\odot$	1.21

Table 6.6.: Fitted masses of additional ^{56}Ni needed to match the light curves of the 812keV and the 158keV line of SN2011fe. The significances show the improvement of the light curve fit, compared to the original models by The and Burrows 2014.

The values reported in Tab. 6.6 suggest that $M_{^{56}Ni} \approx 0.13 M_\odot$ are needed to explain the 812keV line luminosity, and half as much to explain the 158keV line. Models with lower fitted ^{56}Ni masses contain ^{56}Ni in the outer envelopes in their initial design.

6.5.4. Simultaneous fit of ^{56}Ni in SN2011fe

To verify the ^{56}Ni-decay emission, a fitting model consisting of three Gaussian lines is fitted to the data.

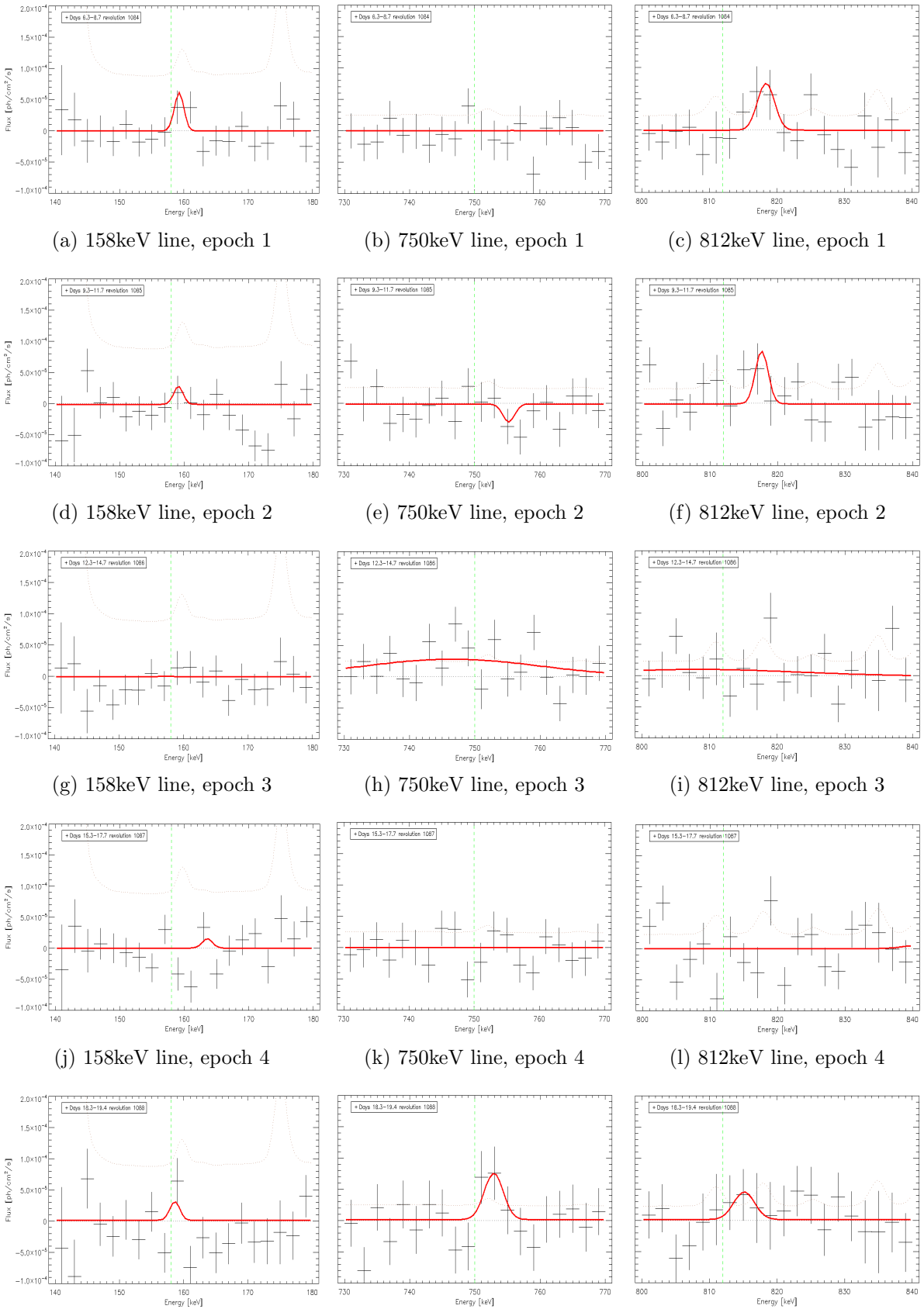

(a) 158keV line, epoch 1 (b) 750keV line, epoch 1 (c) 812keV line, epoch 1

(d) 158keV line, epoch 2 (e) 750keV line, epoch 2 (f) 812keV line, epoch 2

(g) 158keV line, epoch 3 (h) 750keV line, epoch 3 (i) 812keV line, epoch 3

(j) 158keV line, epoch 4 (k) 750keV line, epoch 4 (l) 812keV line, epoch 4

(m) 158keV line, epoch 5 (n) 750keV line, epoch 5 (o) 812keV line, epoch 5

Figure 6.6.: Simultaneous fits of the ^{56}Ni lines for all five revolutions of INTEGRAL's early SN2011fe campaign. Each data point corresponds to an energy bin of 4keV.

Fig. 6.6 displays the results of the simultaneous fitting of the ^{56}Ni lines at 158keV, 750keV and the 812keV for the three epochs used to investigate the ^{56}Ni-decay.

Epoch	Significance of fit [σ]	Bulk velocity [km/s]	Spread velocity [km/s]
Epoch 1	2.88	2350 ± 250	750 ± 1100
Epoch 2	2.52	2080 ± 70	80 ± 750
Epoch 3	4.00	1400 ± 1600	13000 ± 3800
Epoch 4	2.32	10550 ± 1400	1600 ± 3450
Epoch 5	2.48	1150 ± 200	1050 ± 750

Table 6.7.: Properties of the simultaneous ^{56}Ni line fitting

Line fluxes	Epoch 1	Epoch 2	Epoch 3	Epoch 4	Epoch 5
F_{158keV} [10^{-4} ph/cm^2/s]	1.15 ± 0.63	0.52 ± 0.18	–	–	0.57 ± 0.58
F_{750keV} [10^{-4} ph/cm^2/s]	0.02 ± 0.88	-0.7 ± 0.22	–	–	2.74 ± 1.17
F_{812keV} [10^{-4} ph/cm^2/s]	2.37 ± 2.19	2.00 ± 0.38	–	–	1.72 ± 1.38
F_{812keV}/F_{158keV} (nom. 0.87)	2.07 ± 2.23	3.83 ± 1.52	–	–	3.01 ± 3.91
F_{750keV}/F_{812keV} (nom. 0.58)	0.01 ± 0.37	-0.3 ± 0.13	–	–	1.59 ± 1.45

Table 6.8.: ^{56}Ni line fluxes and ratios

Tabs. 6.7 and 6.8 present the properties of the simultaneous fits for all revolutions before maximum optical light. While some parameters correlate well with expectations, others completely fail to reproduce a comprehensible picture of the explosion.

First, the free fail to fit γ-ray lines in the corresponding energy bands in revolutions 1086 and 1987. Thereafter, the complete absence of the 750keV line in revolutions 1084-1086 challenges the robustness of the detection of the 158keV and 812keV lines. On the other hand, the pronounced 750keV feature in revolution 1088 is inconsistent both with expectations, as well as the other two lines.

In conclusion, while focusing only on the two ^{56}Ni lines with the highest branching ratios would yield detections of radioactive material in the outer ejecta with enough statistical significance, including the third strongest ^{56}Ni line in the analysis and fitting all three lines simultaneously, questions the detection of the other two lines. Taking into account that this phenomenon is observed in both supernovae, in addition to the fact, that the lines 158keV and 812keV are located very close to registered background lines (the 158keV line near a ^{47}Sc line at 159.74keV; the 812keV line near the ^{58}Co lines at 810.91keV and 817.90keV) , the above analysis opens up the question of residuals fluxes from these background features.

Redshifted 847keV line test

Similar to the analysis of SN2014J, the possibility to explain the flux excess seen in the vicinity of the 812keV line as a red-shifted ^{56}Co 847keV line is inspected. To begin with, assigning the 812keV line flux from revolution 1084 to ^{56}Co, yields:

$$\begin{aligned} \mathrm{M}(^{56}\mathrm{Co}, \mathrm{t} = 9.0, \mathrm{SN2011fe}) &= 4 \cdot \pi \cdot \mathrm{d}^2_{\mathrm{M101}} \cdot \mathrm{F}_{812\mathrm{keV}} \cdot \mathrm{m}_{\mathrm{Co}} \cdot \exp\left(\frac{\mathrm{t}}{\tau_{\mathrm{Ni}}}\right) \cdot \frac{1}{\mathrm{p}_{847\mathrm{keV}}} \\ &= 0.87 \pm 0.54 \mathrm{M}_{\odot}, \end{aligned} \tag{6.2}$$

which is considerably higher than model predictions and would have left a characteristic signature on optical and NIR spectra. Despite the inconsistency in the ^{56}Co mass, the spectra around the 1238keV are investigated for a corresponding red-shifted emission.

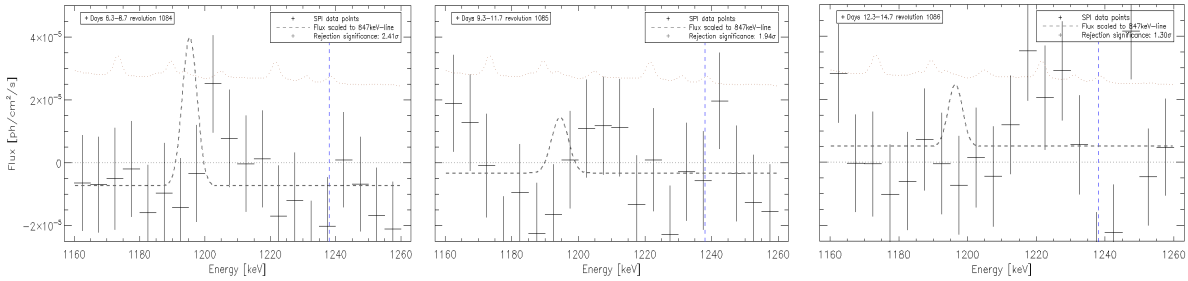

(a) Expected 1238keV line, epoch 1

(b) Expected 1238keV line, epoch 2

(c) Expected 1238keV line, epoch 3

Figure 6.7.: Gamma-ray spectra of SN2011fe between 1160-1260keV. The laboratory position of the 1238keV is represented by a dashed blue vertical line. The dashed grey slope marks the expected 1238keV signal, under the assumption that the flux excess at 812keV originates from red-shifted 847keV line photons. Each data point corresponds to an energy bin of 10keV.

The reconstructed 1238keV lines are inconsistent with the data depicted Fig. 6.7, dismissing the possibility that the emission at 812keV originates from a bulk of receding ^{56}Co, with a significance of 3.39σ, 1.21σ and 0.44σ for revolutions 1084, 1085 and 1086 respectively.

6.6. Cobalt lines

The detection of SN2014J's ^{56}Co emission in epochs two and three (i.e. days $\sim$ 40-100 past explosion) motivates a similar analysis for SN2011fe. In a first-order approximation, neglecting that two individual explosions can have different γ-ray fluxes, the observed flux is expected to be a factor $\sim 3.5^2/6.4^2$ lower in comparison to SN2014J, due to the larger distance to M101. INTEGRAL's SN2011fe campaign successfully covers the period, where the SN2014J ^{56}Co emission was maximal. Only the two strongest ^{56}Co lines, the 847keV and the 1238keV lines are treated in the analysis. The 1040keV line was well below the sensitivity limit for SPI even for distances of $\sim$ 3.5Mpc. If the sequent analysis does not yield well-defined line features, 2σ upper limits will be calculated using line parameters, like the spread velocity, from the SN2014J analysis.

6.6.1. 847keV line

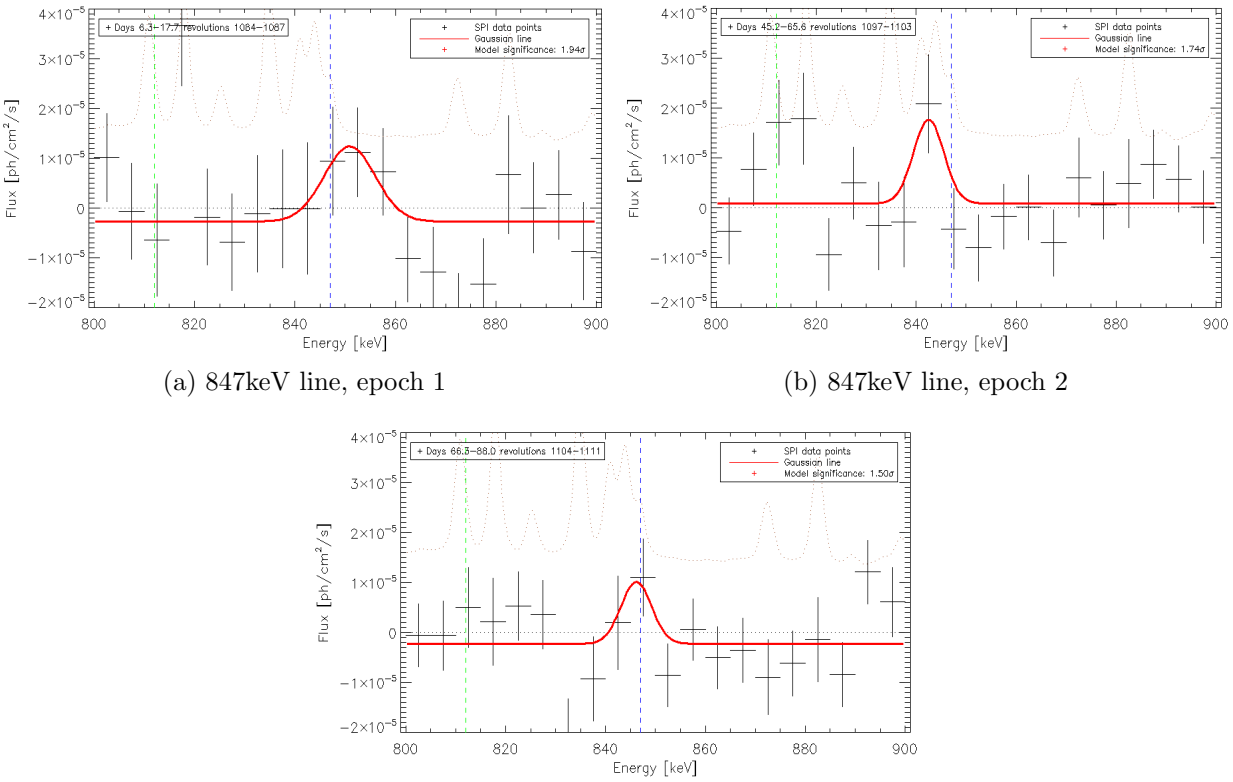

(a) 847keV line, epoch 1

(b) 847keV line, epoch 2

(c) 847keV line, epoch 3

Figure 6.8.: Time series of the 800-900keV band for three epochs. Every data points corresponds to an energy bin of 10keV.

The spectra of SN2011fe in the 800-900keV γ-ray band are presented in Fig. 6.8. Each data points corresponds to an energy bin of 10keV, while the background features are overplotted with a faint brown dashed slope.

In epoch one, only 6.3-17.7 days after the explosion, a blue-shifted feature is present in the spectrum. It was fitted with a Gaussian line model, without any constrictions and yielded a significance of $\sim 2\sigma$. The fitted line parameters indicate a bulk velocity of $\approx 1400 \pm 900$km/s and a spread velocity of 4200 ± 1900km/s. Taking the detection of the 158keV and the 812keV lines into account and neglecting for the time the peculiar behavior of the 750keV, this line confirms the detection of radioactive material at low optical depths with a statistical significance of $\sim 2\sigma$.

In epoch two, about one month later, the blue-shifted feature disappears and a narrow red-shifted feature emerges. A relatively significant flux at $\approx$ 815keV cannot be assigned to ^{56}Ni, since at that time only $\sim 10^{-3} M_\odot$ of 56Ni should have survived. The peak of that feature lies on two strong background features and may be affected by residual background line counts.

The absence of a similarly red-shifted feature in epoch three supports this idea. In this epoch, the maximum flux can be found near the laboratory energy of 847keV line. In general, the fitted fluxes decline with progressive time. This is in contrast with most models, that predict a gradual increase of the ^{56}Co flux for the first three months of supernova evolution.

Epoch	Flux [10^{-4} ph/cm^2/s]	E_0 [keV]	Bulk velocity [km/s]	σ [keV]	Spread velocity [km/s]
Epoch 1	1.94 ± 1.07	850.9 ± 2.5	1400 ± 900	5.1 ± 2.2	4200 ± 1850
Epoch 2	1.28 ± 1.22	842.5 ± 1.4	-1600 ± 500	3.0 ± 1.5	2400 ± 1300
Epoch 3	0.95 ± 1.12	846.2 ± 2.0	-300 ± 700	3.0 ± 2.0	2400 ± 1700

Table 6.9.: Fitted 847keV line parameters of SN2011fe

Upper limits

The values reported in Tab. 6.9 suggest that the radioactive isotopes in SN2011fe are predominantly found at low velocities. The fitted velocities are similar to the ones obtained from the analysis of the ^{56}Ni lines. However, the possibility exists that the observed emission corresponds only to the peak of broader lines, whose wings are too faint to become undetectable by SPI. For this reason, 2σ upper limits for epochs 2 and 3 were calculated. The line centroid was obtained from the free fit (see Tab. 6.9, column 2), assuming that it corresponds to the peak flux of a broader line. In order to cover a broad range of possible spread velocities, the line width σ was varied between σ=1-15keV, corresponding to a maximum spread velocity of $\approx$ 12000 km/s.

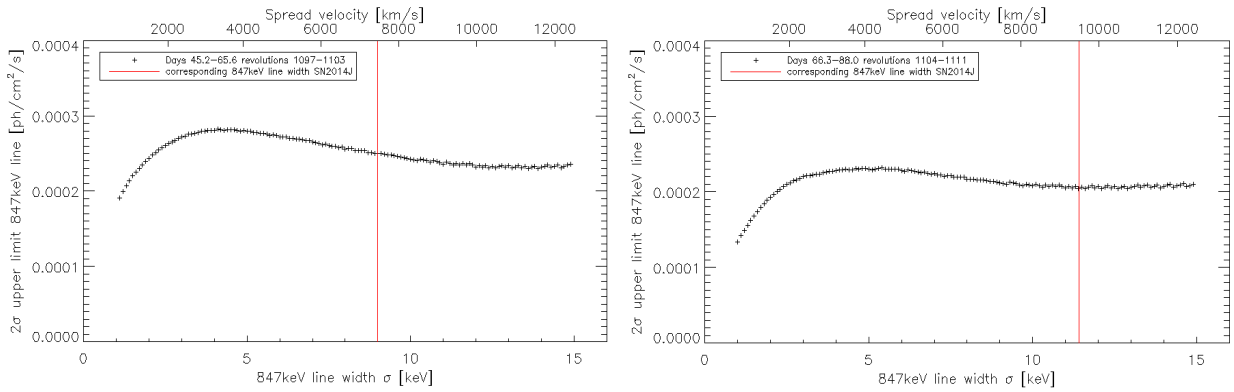

(a) 847keV line, epoch 2

(b) 847keV line, epoch 3

Figure 6.9.: 2σ upper limits as a function of line width for the 847keV line of SN2011fe in epoch 2 and 3. The red vertical line marks the fitted line width of the same line and epoch in the SN2014J analysis.

The derived upper limits as a function of line width are presented in Fig. 6.9. Obviously, the highest upper limit is reached for a line width of $\sigma \approx$3, which is the value obtained from the fit. The exact value of the upper limit depends on the width of the line and, therefore, on the assumed spread velocity. However, the derived limits are higher than the most luminous explosion models, that reach a maximum 847keV line intensity of $F_{847keV,max} \approx 1.2 \times 10^{-4}$ ph/cm^2/s. A few representative values for different spread velocities and both lines are given in Tab. 6.11.

6.6.2. 1238keV line

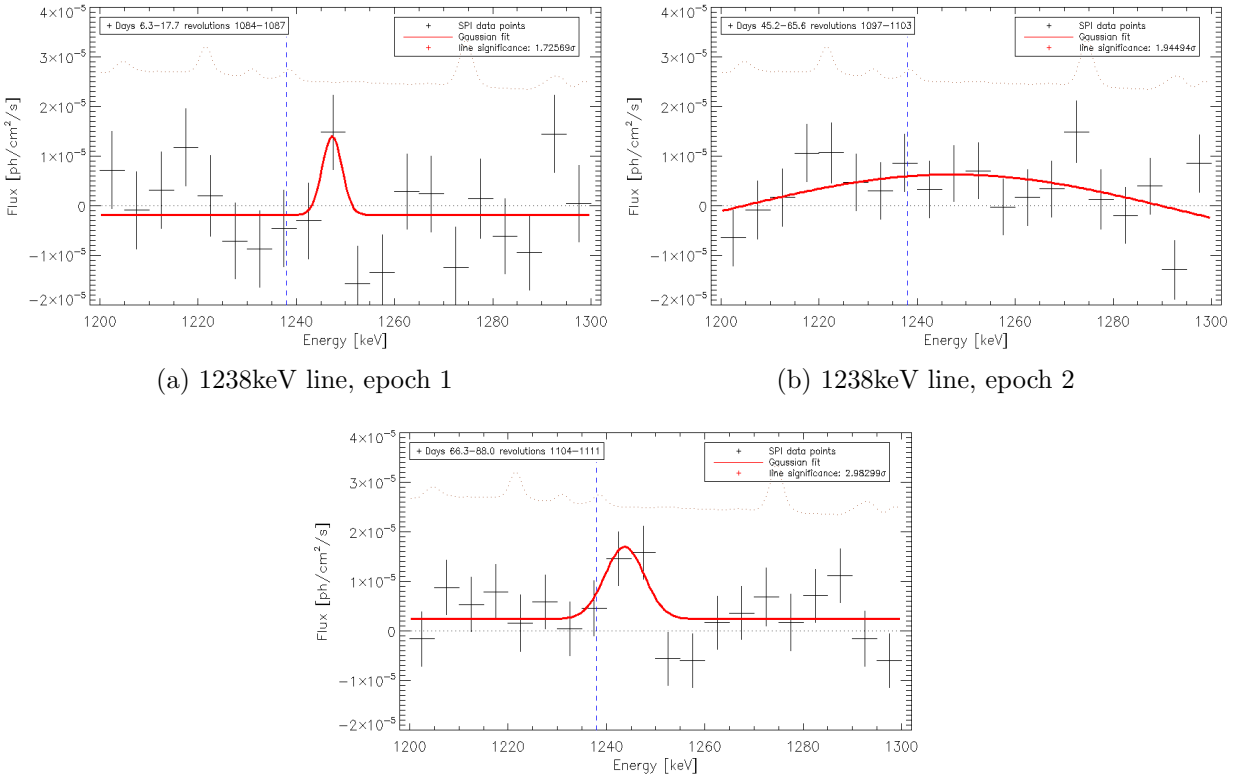

(a) 1238keV line, epoch 1

(b) 1238keV line, epoch 2

(c) 1238keV line, epoch 3

Figure 6.10.: Time series of the 1200-1300keV band for three epochs. Every data points corresponds to an energy bin of 10keV.

The emission the 1238keV line of ^{56}Co was analyzed in the 1200-1300keV γ-ray band. The obtained spectra are presented in Fig. 6.10. The lower branching ratio, as well as the increased line broadening, turn the detection of this line more challenging, than the one of 847keV line.

In epoch one, a narrow blue-shifted feature at $\approx$ 1250keV is present. The calculated blue-shift is only barely consistent with the one from the 847keV analysis. With a statistical significance of 1.7σ, no firm conclusions can be drawn. In epoch two the fitting algorithm completely fails to fit a physically meaningful Gaussian line to the data. A flux excess is apparent on both sides of the laboratory value, albeit physical conclusions cannot be made. In epoch three, a prominent feature with a statistical significance of $\sim 3\sigma$ at $\approx$ 1245keV is found. Assuming complete transparency and using Eq. (5.3), the flux can be converted to $\mathrm{M}(^{56}\mathrm{Ni}, \mathrm{t} = 0) = 0.87 \pm 0.54 \mathrm{M}_{\odot}$. This mass of synthesized ^{56}Ni would have left traces both in other wavelengths, as well as in the 800-900keV band. In addition, studying the line in narrow, 4keV-energy bins, does not reveal a regular Gaussian line form (see Appendix).

Epoch	Flux [10^{-4} ph/cm^2/s]	E_0 [keV]	Bulk velocity [km/s]	σ [keV]	Spread velocity [km/s]
Epoch 1	0.80 ± 0.78	1247.3 ± 1.3	2250 ± 300	2.0 ± 1.2	1000 ± 850
Epoch 2	–	–	–	–	–
Epoch 3	1.46 ± 0.84	1243.7 ± 1.8	1400 ± 400	4.0 ± 1.7	2200 ± 1000

Table 6.10.: Fitted 1238keV line parameters of SN2011fe

Upper limits

Following the same analysis procedure used for the 847keV line of SN2011fe, 2σ upper limits were derived for epochs one and two, where the spectra do not show any well-defined spectral feature. The line centroid was obtained from the free fit (see Tab. 6.10, column 2), while line width σ was varied this time between σ=1-22keV, to cover the same spread velocities as for the 847keV line.

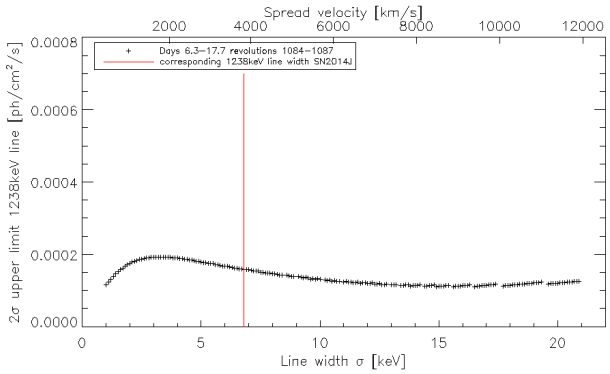

(a) 1238keV line, epoch 1

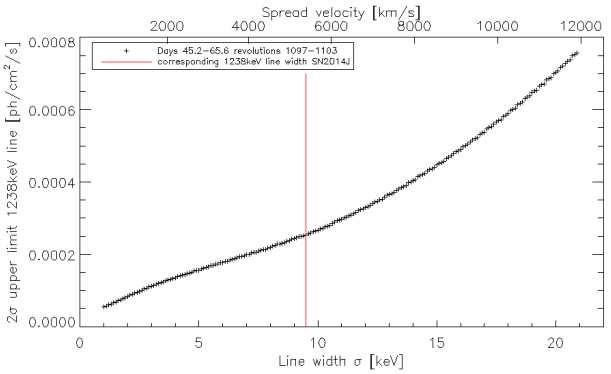

(b) 1238keV line, epoch 1

Figure 6.11.: 2σ upper limits for the 1238keV line of SN2011fe in epoch 1 and 2. The red vertical line marks the fitted line width of the same line and epoch in the SN2014J analysis. Note the difference in the axis scaling compared to Fig. 6.9.

The derived upper limits as a function of line width for the 1238keV line of SN2011fe are presented in Fig. 6.9. The slope of the upper limit determined in epoch one resembles closely the upper limits of the 847keV line. The upper limit of epoch two, however, increases for increasing line width. This is explained by the fact that most of the spectrum in epoch two shows positive fluxes. Thus, the larger the line width, the higher the flux measured and therefore the higher the upper limit. A few representative values for different spread velocities and both lines are given in Tab. 6.11

2σ upper limit [10^{-4} ph/cm^2/s]	Spread vel. v=2000km/s	Spread vel. v=5500km/s	Spread vel. v=8500km/s	Spread vel. v=12000km/s
847keV, epoch 2	2.629	2.690	2.403	2.333
847keV, epoch 3	2.118	2.249	2.081	2.079
1238keV, epoch 1	1.922	1.332	1.106	1.257
1238keV, epoch 2	1.265	2.592	4.399	7.564

Table 6.11.: Fitted 847keV line parameters of SN2011fe

The derived upper limits for both lines lie above the maximum luminosity of the brightest models of The and Burrows 2014 ($F_{847keV,max} \approx 1.2 \times 10^{-4}$ ph/cm^2/s and $F_{1238keV,max} \approx 0.9 \times 10^{-4}$

ph/cm^2/s). In consequence, no model can be excluded.

6.6.3. 1238keV line in 4-revolution time bins

The detection of the 1238keV line in epoch three (statistical significance: $\sim 3\sigma$) motivates its analysis in shorter observation windows, i.e. in four-revolutions averaged spectra. The two epochs are defined as follows:

- Revolutions 1104-1107, 66.3-77.5 days after the explosion
- Revolutions 1108-1111, 78.1-88.0 after the explosion

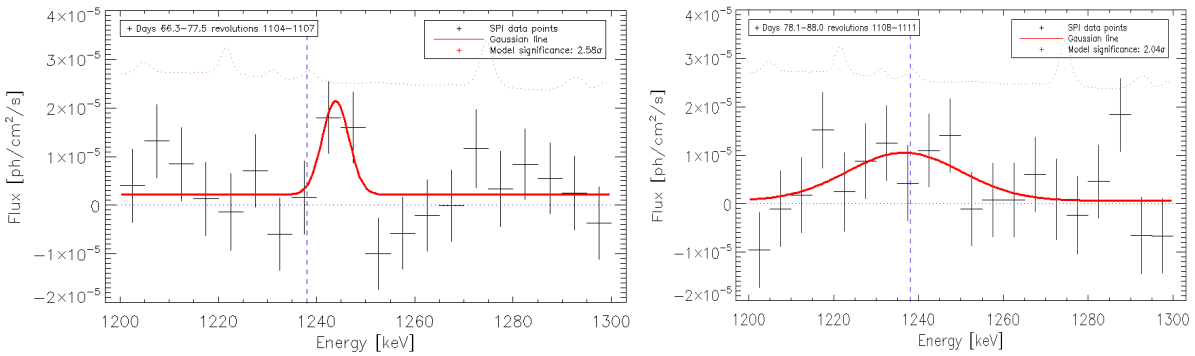

(a) 1238keV line, rev. 1104-1107

(b) 1238keV line, rev. 1108-1111

Figure 6.12.: Gamma-ray spectrum of the 1200-1300keV band in epoch 3 of the SN2011fe campaign, split into two smaller observation windows. The left panel corresponds to revolutions 1104-1107, the right panel to revolutions 1108-1111 Every data points corresponds to an energy bin of 10keV.

The emission displayed in the panels of Fig. 6.12 was fitted with free Gaussian lines models(for a smaller energy binning see Appendix). The fitted parameters, as well as the derived fluxes and velocities, are given in Tab. 6.12. In revolutions 1104-1107 a narrow blue-shifted line could be fitted to the data with a statistical significance of $\sim 2.6\sigma$, while in revolutions 1108-1111 a broader line almost at laboratory energy was found with a statistical significance of $\sim 2.0\sigma$.

Epoch	Flux [10^{-4} ph/cm^2/s]	E_0 [keV]	Bulk velocity [km/s]	σ [keV]	Spread velocity [km/s]
Rev. 1104-1107	1.31 ± 0.60	1243.9 ± 1.2	1400 ± 250	2.7 ± 1.0	1400 ± 650
Rev. 1108-1111	3.33 ± 2.74	1236.7 ± 6.9	300 ± 1700	13.4 ± 8.7	7650 ± 4950

Table 6.12.: Fitted 1238keV line parameters of SN2011fe, 4 revolution analysis

The fitted width of the line in the left panel corresponds to a spread velocity of 1400 ± 650 km/s. Considering the fact that this spectrum is obtained more than two months after first light, the calculated expansion velocity is small. Taking into account the form of the corresponding spectra of SN2014J (see Fig. 5.25), broad lines with smaller amplitudes were expected. On the other hand, the spread velocity calculated from the line in revolutions 1108-1111 reflects a more plausible ejecta configuration. Converting the measured line flux to an initial ^{56}Ni mass, yields: $M(^{56}\mathrm{Ni}, t = 0) = 2.10 \pm 1.77 M_\odot$. This amount is not supported by the results of the other lines

and reports from other energy bands. The line parameters of both lines are not coherent to each other and indicate a high degree of asymmetry if they picture the true distribution of radioactive ^{56}Co in the ejecta.

6.7. Positron annihilation in SN2011fe

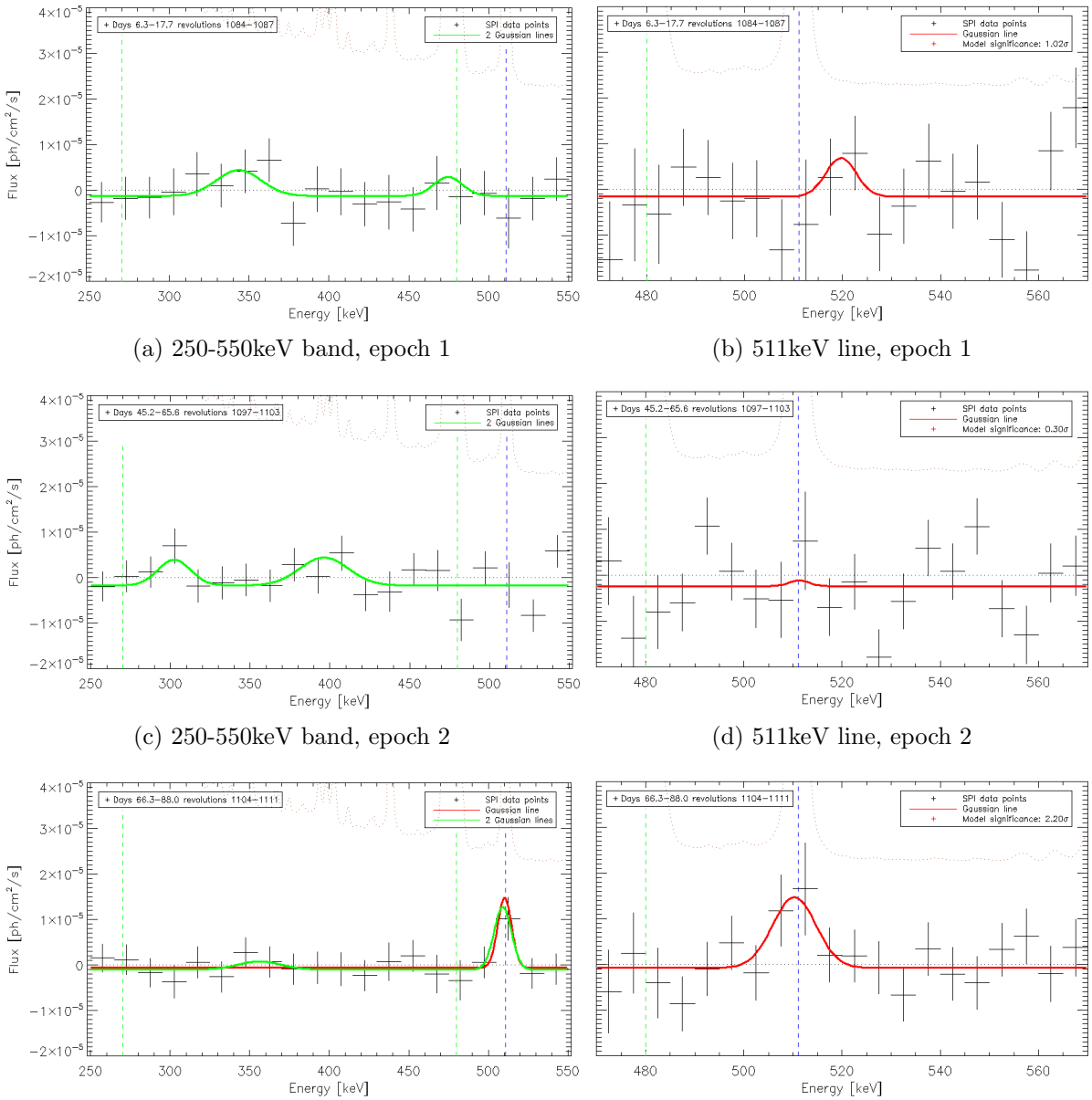

(a) 250-550keV band, epoch 1

(b) 511keV line, epoch 1

(c) 250-550keV band, epoch 2

(d) 511keV line, epoch 2

(e) 250-550keV band, epoch 3

(f) 511keV line, epoch 3

Figure 6.13.: Left column: Gamma-ray spectrum of the 250-550keV band with 24keV energy bin width. Right column: The same spectrum presented in 10keV energy bins and zoomed in the energy band 470-570keV, for a more detailed inspection of the positron annihilation line. The dashed blue vertical line marks the laboratory energy of the 511keV line, while dashed green vertical lines mark important transitions of ^{56}Ni.

The spectra focusing on the positron annihilation in SN2011fe are displayed in Fig. 6.13. The panels of the left column depict the whole energy range relevant for positron annihilation in broad 24keV energy bins, while the spectra on the right show the 470-570keV energy range, from 470 to 570keV, for a 511keV line analysis with 10keV energy binning.

Epoch	270-470keV flux green	270-470keV flux black [10^{-4} ph/cm^2/s]	270-470keV 2σ upper limit
Epoch 1	1.06 ± 7.03	-0.27 ± 3.80	4.85
Epoch 2	3.80 ± 2.70	0.71 ± 2.84	4.01
Epoch 3	2.49 ± 0.53	-0.88 ± 2.70	2.63

Table 6.13.: Fluxes and 2σ upper limits of the 511keV line and the 270-470keV band for the three observation epochs of SN2011fe.

Epoch	Flux [10^{-4} ph/cm^2/s]	E_0 [keV]	Bulk velocity [km/s]	σ [keV]	Spread velocity [km/s]
Epoch 1	0.66 ± 1.32 [1.26]	519.7 ± 4.7	5100 ± 2800	3.1 ± 5.1	4150 ± 7300
Epoch 2	0.06 ± 0.23 [0.99]	511.2 ± 6.4	150 ± 3750	2.0 ± 4.9	1500 ± 7500
Epoch 3	1.70 ± 1.33	510.3 ± 2.1	-400 ± 1250	4.4 ± 2.3	5950 ± 3250

Table 6.14.: 511keV line parameters of SN2011fe derived from a more detailed analysis of the 470-570keV energy band.

Epoch one shows covers days ∼6-18 after the explosion and contains the earliest spectra ever recorded for a thermonuclear supernova. Studying the 250-550keV band in panel (a), one should not expect a signal from positron annihilation, but rather continuum emission from the comptonized high-energy photons or the ^{56}Ni and ^{56}Co lines. This fact is also apparent in panels (a) and (b) (first row of Fig. 5.30), where emission in the 300-370keV energy range is observed. A positron annihilation signal at the 511keV line is insignificant at this time, producing only a 2σ upper limit reported in Tab. 6.14.

In epoch two, the fluxes of both the fitted and the integrated continuum reach their maximum. An enhanced emission can be found at $\approx$ 300keV and $\approx$ 400keV. The shape of the continuum shares several similarities with the corresponding spectrum of SN2014J, i.e. the emission is not uniformly distributed across the whole energy range, but rather concentrated in narrower energy bands. A 511keV line is still absent, similar to epoch two of SN2014J.

In epoch three, the weak continuum emission detected in earlier epochs becomes insignificant. On the other hand, considerable excess flux in the vicinity of the 511keV line emerges. Fitting the spectrum with a Gaussian line at 511keV yields a barely red-shifted line with a line flux of $1.70 \pm 1.33 \times 10^{-4}$ ph/cm^2/s and a statistical significance of $\approx 2.2\sigma$. The observed emission is situated exactly in the energy range of the instrumental 511keV line and it should be inspected, whether the observed flux is an artifact of inadequate background modeling.

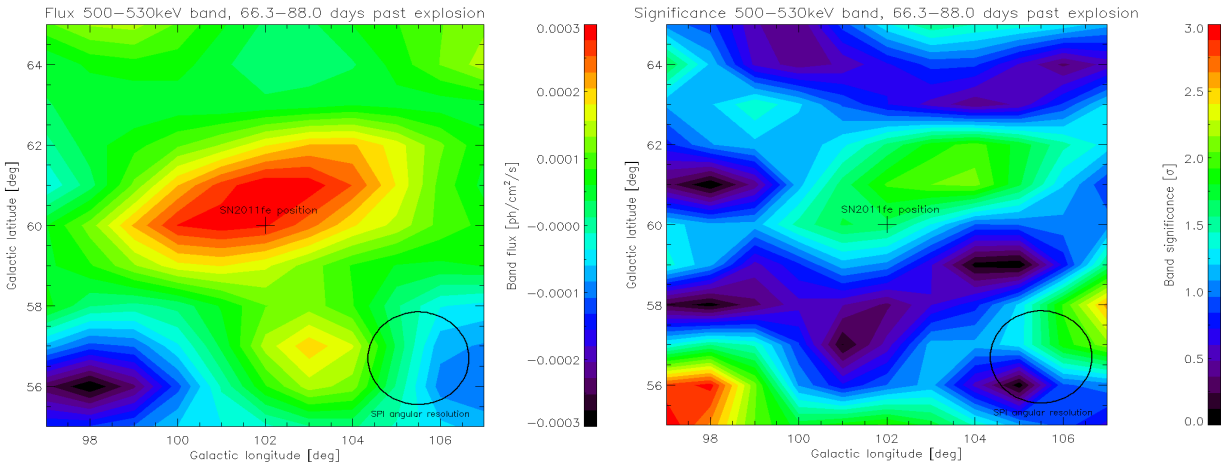

(a) Flux map, epoch 3

(b) Significance map, epoch 3

Figure 6.14.: Flux and significance maps in a $10° \times 10°$ grid around SN2011fe. Left: The flux in the 500-530keV band is integrated and color-coded for each grid of the map. Right: The significance of the emission for every grid is calculated by comparing the χ^2-values of spimofit-runs with and without SN2011fe.

The source grids depicted in Fig. 6.14 show that the enhanced flux in the proximity of the 511keV line coincides with the coordinates of SN2011fe. The compatibility of the background model was investigated by checking the residuals in the 500-530keV band. No significant deviations from zero were found (see Appendix). Consequently, the observed emission can be assigned to the celestial source to the 2-photon positron annihilation in SN2011fe.

Following the positron analysis done for SN2014J, the same procedure was followed to calculate the number of annihilating positrons and consequently the escape fractions for all three epochs for SN2011fe.

Epoch	$N_{e^+,f=0}^{511keV}$ $[10^{46}e/s]$	$N_{e^+,f=1}^{511keV}$ $[10^{46}e/s]$
Epoch 1	16.22±33.85	64.89±130.13
Epoch 2	1.53±5.61	6.14±22.42
Epoch 3	41.76±33.66	167.04±134.67

Table 6.15.: Annihilating e^+ of SN2011fe calculated from the flux of the 511keV line in each epoch

No firm estimate of the produced positrons in SN2011fe can be made, due to the weak detection of both the 847keV and the 1238keV lines. In addition, the 511keV line was detected only in epoch three. Hence, a positron escape fraction was calculated only for the last epoch. The corresponding positron production rate was calculated from the upper limit, as well as the fitted flux of the ^{56}Co 847keV line. Due to the detection of the 1238keV line in this epoch, a positron production rate was calculated using the flux of the 1238keV line.

Epoch	$N^{up.lim}_{e^+,847}$ [10^{46} e^+/s]	$N^{fit}_{e^+,847}$ [$10^{46}e^+$/s]	$N^{fit}_{e^+,1238}$ [$10^{46}e^+$/s]
Epoch 3	19.5	8.9 ± 5.2	194.3 ± 121.2

Table 6.16.: Lower limits of produced e^+ from three different flux approaches in SN2011fe

The calculated production rates with the three flux values mentioned above are given in Tab. 6.16. Comparing the derived values from the 847keV line to the ones reported in the same epoch (row 3 of Tab. 5.18) for SN2014J shows that the number of produced positrons for both explosions are compatible with each other. The value calculated from the flux of the 1238keV line is one order of magnitude higher than the ones from SN2014J. This was expected, due to the high flux measured in the 1200-1300keV band of SN2011fe in epoch three. Inserting the values of Tabs. 6.15 and 6.16 in Eq. (5.6) yields the following escape fractions for SN2011fe:

Epoch	$\eta^{up.lim}_{f=0}$	$\eta^{847keVfit}_{f=0}$	$\eta^{1238keVfit}_{f=0}$	$\eta^{up.lim}_{f=1}$	$\eta^{847keVfit}_{f=1}$	$\eta^{1238keVfit}_{f=0}$
Epoch 3	-1.14	-3.69 ± 4.67	0.79 ± 0.22	-7.57	-17.77 ± 18.68	0.14 ± 0.87

Table 6.17.: Calculated e^+ escape fractions of SN2011fe for epoch 3

The escape fractions reported in Tab. 6.17 do not allow a firm estimate of positron escape in SN2011fe 66.3-88.0 days after the explosion. Depending on the flux used to derive the positron production rate, different escape fractions are deduced. Using the fluxes derived from the 847keV line analysis would underestimate the number of positrons produced. On the other hand, the relatively high flux of the 1238keV line measured in epoch three, yield a high production rate. In other words, while the 511keV and the 1238keV lines suggest high positron production and annihilation rates in SN2011fe, the low flux of the 847keV line does not allow firm conclusions.

6.7.1. Positron annihilation in 4-revolution time bins

Following the analysis of the 1238keV line in 4-revolution time bins, the positron annihilation line was also analyzed in the same observation windows, to determine the time, when the 511keV line flux peaks, more precisely.

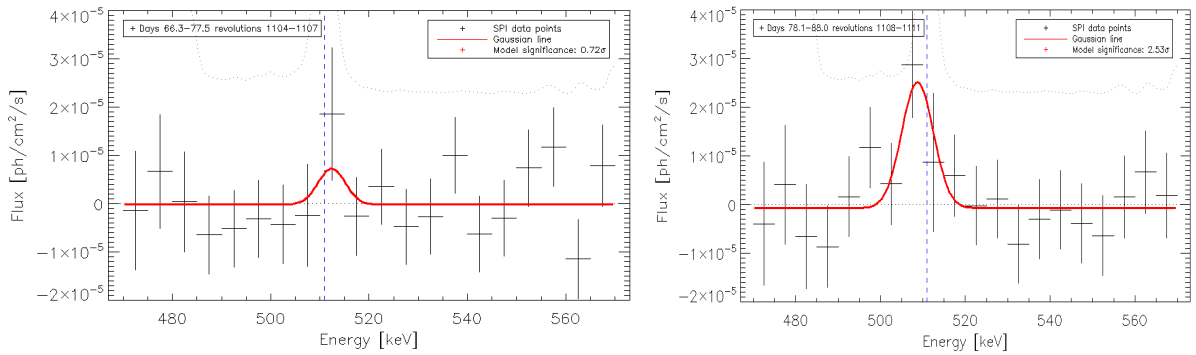

(a) 1238keV line, rev. 1104-1107

(b) 1238keV line, rev. 1108-1111

Figure 6.15.: Gamma-ray spectrum of the 470-570keV band in epoch 3 of the SN2011fe campaign, split into two smaller observation windows. The left panel corresponds to revolutions 1104-1107, the right panel to revolutions 1108-1111 Every data points corresponds to an energy bin of 10keV

The emission mear the 511keV line was fitted with free Gaussian lines models (for a smaller energy binning see Appendix). The spectra show that the largest fraction of the flux seen in panel (f) of Fig. 6.13 originates from revolutions 1104-1107. In particular, the spectra of revolutions 1104-1107 show do not show a particular flux excess near the 511keV and the Gaussian line fitted to the data has a statistical fit of $\sim 0.72\sigma$. In contrast, the right panel of Fig. 6.15 displays strong emission near the 511keV energy band. The statistical significance of the fitted Gaussian line is 2.5σ. The fitted parameters, as well as the derived fluxes and velocities, are given in Tab. 6.18.

Epoch	Flux [10^{-4} ph/cm^2/s]	E_0 [keV]	Bulk velocity [km/s]	σ [keV]	Spread velocity [km/s]
Rev. 1104-1107	0.52 ± 1.47	512.4 ± 5.6	800 ± 3300	2.8 ± 5.8	3650 ± 8450
Rev. 1108-1111	2.42 ± 1.64	508.7 ± 1.9	-1350 ± 1100	3.7 ± 1.8	5000 ± 2500

Table 6.18.: Fitted 1238keV line parameters of SN2011fe, 4 revolution analysis

The flux of the line in panel (b) of Fig. 6.15 suggests an annihilation rate of $N^{511keV}_{e^+,f=0} = (81.8 \pm 68.3) \times 10^{46} e^+/s$, which becomes four times larger, If a Ps-fraction of f=1.0 is assumed. The line is red-shifted by $\sim$ -1350$\pm$1100 km/s and indicates that positrons annihilate in areas with expansion velocities up to $\sim$ 5000$\pm$2500 km/s. Taking into account that the line was only found in the position of SN2011fe and the residuals (see Appendix) did not show any outliers, it is unfortunate that no later observations are available, to follow the evolution of this signal.

7. Summary and Conclusion

The purpose of this work was to provide a γ-ray picture of two recent nearby supernovae explosions. Both are classified as type Ia supernovae, SN2014J exploded in starburst galaxy M82, located $\sim$ 3.5Mpc away and SN2011fe in spiral galaxy M101, $\sim$ 6.5Mpc away. The distances of both supernovae should be within the maximum distance radius for observations with the currently available γ-ray instruments. In this sense, I analyzed data from spectrometer SPI, mounted on the International Gamma Ray Astronomy Laboratory (INTEGRAL) and exploited the whole observation window of both explosions for the highest possible signal-to-noise ratio.

The γ-ray emission of a type Ia supernova during its first months of evolution is believed to originate from the decay chain of ^{56}Ni, a radioactive element synthesized in large numbers during the explosion. With a mean lifetime of $\sim$ 8.8 days, a high γ-ray luminosity is generated inside the expanding supernova envelope, which according to theories, is reprocessed in the dense ejecta and gives rise to the optical light curve of the explosion (Arnett 1982). Whether γ-ray photons from the ^{56}Ni decay are able to escape without interactions, depends primarily on the spatial distribution of the radioactive material. The presence of radioactive material at low optical depths should allow the escape of these photons and result in an early γ-emission. ^{56}Co, the decay product of ^{56}Ni, is also unstable and decays with a mean lifetime of $\sim$ 111.3 days to stable ^{56}Fe, emitting a multitude of γ-ray photons with different intensity ratios. The longer mean lifetime of this isotope allows the supernova to expand and become optically thin for γ-rays, before the bulk of the radioactive ^{56}Co has decayed. As a consequence, late γ-ray photons from the ^{56}Co decay should encounter more dilute ejecta, transparent to γ-rays, and escape. A second channel for this decay is through the β^+-decay, which results in the emission of positrons. They are created at relativistic velocities and their fate in the supernova ejecta is still not conclusively explained. The most plausible theories expect them to thermalize quickly and annihilate into two or three photons, depending on the possible formation of Positronium, a meta-stable bound state involving a positron and an electron.

Despite the relatively short distance to their host galaxies, type Ia supernovae at extragalactic distances are faint γ-sources with respect to current γ-ray telescopes. Detecting their γ-radiation with a γ-ray telescope like INTEGRAL is not trivial, due to the high intrinsic background that dominates the spectra. To derive the celestial fluxes from the highly background-dominated raw data, I used the empirical background modeling approach developed and successfully implemented by our group (Diehl et al. 2018b). This approach relies on the longevity of the instrument and exploits the spectral information in broad energy-regions combined with prior knowledge about long-term detector response variations. A major part of this work was to tackle the large instrumental background and analyze its behavior over time. In this respect, I checked the response of the background model both in periods of quiet and extreme space weather conditions by adjusting several parameters, like the effect of nearby sources to the celestial supernova spectra or the influence of instrumental tracers on the background modeling. I aimed at maximizing the available exposure time, by including pointings near the Van Allen radiation belts. Hence, celestial spectra in the 100-1350keV energy band for all revolutions were generated and analyzed.

Analyzing the early spectra of both supernovae showed traces of early ^{56}Ni emission. In particular, the 812keV and the 158keV lines of the ^{56}Ni decay were detected with statistical significances of $\sim 2.8\sigma$ and $\sim 1.6\sigma$ in SN2014J and $\sim 2.7\sigma$ and 1.9σ in SN2011fe, respectively. The corresponding

fluxes can be translated into $M_{^{56}Ni}^{SN2014J}$=0.13±0.07$M_\odot$ and $M_{^{56}Ni}^{SN2011fe}$=0.19±0.12$M_\odot$ near the surface for each supernova. However, a consistency issue posed the non-detection of the neighboring 750keV line in both supernovae. I could not identify the origin of the non-detection, albeit I propose a destruction mechanism of the 750keV photons that could be associated with the photon-photon pair-production interaction, whose cross section peaks near this energy.

γ-ray emission from the prominent lines of ^{56}Co, the 847keV and the 1238keV lines was detected in the all-mission spectrum of SN2014J, as well as in shorter epochs, with detection significances that exceed 3σ. Several models, including parallel fitting, were fitted on the data and three independent procedures were followed to infer a synthesized ^{56}Ni mass. Assuming complete transparency in the latest epoch, $M_{^{56}Ni}^{SN2014J}$=0.57±0.48$M_\odot$ were calculated from the flux of a free fitted Gaussian line at $\sim$ 847keV and $M_{^{56}Ni}^{SN2014J}$=0.43±0.27$M_\odot$ by integrating the flux in the 834-872keV energy band. By scaling the light curves of different explosion models constructed by The and Burrows 2014 to the derived line fluxes, I derived a synthesized ^{56}Ni mass of $M_{^{56}Ni}^{SN2014J}$=0.53±0.07$M_\odot$ for the free Gaussian fit, $M_{^{56}Ni}^{SN2014J}$=0.81±0.06$M_\odot$ for a model involving a Gaussian line and a logistic function and $M_{^{56}Ni}^{SN2014J}$=0.59±0.03$M_\odot$ from integrating the fluxes in the 834-872keV band. Fitting the two main ^{56}Co lines simultaneously, yielded $M_{^{56}Ni}^{SN2014J}$=0.31±0.21$M_\odot$. From the 847keV line fluxes, also estimates on the positron production rate of SN2014J were made. In particular, the mission-averaged positron production rate, derived from the all mission 847keV line, is: $\overline{N}_{e^+}^{prod.}$=(5.8±3.0)×$10^{46}$ e^+/s. The two strongest ^{56}Co lines at 847keV and 1238keV were not unambiguously detected in SN2011fe, allowing only 2σ upper limits at $\sim 2.5\times10^{-4}$ ph/cm^2/s and 1.5×10^{-4} ph/cm^2/s, respectively, which were too high to constrain explosion models.

Finally, by analyzing the 250-550keV energy range, where positron annihilation with electrons should be measurable, the spectral signature of positron annihilation in both supernovae was inspected. An estimate for the Ps-fraction f and the positron escape fraction η for both supernovae was made. Unfortunately, the low signal-to-noise ratio and the large errors of the fitted parameters did not allow firm conclusions on the annihilation conditions of positrons in the young supernova envelope. In SN2014J, the 511keV positron annihilation line was detected with a statistical significance of $\sim 2.45\sigma$ in the all mission spectrum and with 1.7σ in days 133-163 after the explosion. The flux measured in the all-mission spectrum can be converted to a mean positron annihilation rate of $\overline{N}_{e^+}^{ann.}$=(6.7±5.2)×$10^{46}$ e^+/s. In addition, the continuum in the energy band, where the emission of the annihilation of ortho-Ps is expected showed higher fluxes than predicted by most explosion models. Whether the detected emission originates from Compton down-scattered photons of high-energy lines or the annihilation of ortho-Ps could not be disentangled. The comparison between the positron production rate inferred from the analysis of the 847keV line and the positron annihilation rate calculated from the flux of the 511keV line suggests a Ps-fraction of f=0 and an escape fraction of η=0 in the first five months after explosion, albeit due to the large errors I could only derive weak constraints.

In days 78-88 after the explosion of SN2011fe, the 511keV positron annihilation line wasw detected with a statistical significance of $\sim 2.6\sigma$. Its detection was supported by analyzing source grids around the source. The strength of the signal could not be explained by the fluxes of the ^{56}Co lines and may indicate an additional positron source in the supernova envelope. Associating this with the non-detection of 750keV photons could hint toward the creation of additional positrons from the photon-photon pair-production effect. Consequently, it would be interesting to include this effect in γ-radiation transfer codes. A firm estimate of the positron escape fraction of a thermonuclear supernova is crucial for the galactic positron puzzle. Unfortunately, the two explosions I analyzed in this work were too far away for this observational target.

Nonetheless, there is a lot of potential in the future to change that and achieve a complete γ-ray picture of a type Ia supernova. First of all, an explosion in one of the very nearby galaxies or satellite galaxies of the Milky Way would provide high-quality data and allow detailed studies of a larger number of γ-ray lines at various energies from the ^{56}Ni decay chain and even from other radioactive isotopes with lower abundances. The flux and line shape of every individual line could be modeled to draw conclusions about the distribution of the radioactive elements in the supernova ejecta, the composition of the supernova ejecta, the explosion mechanism, as well as the progenitor scenarios. This information is crucial to understand the nature type Ia supernovae and establish their use as precise distance indicators. The empirical background modeling approach of our high-energy group at the Max Planck Institute for extraterrestrial physics guarantees that the expected fluxes would be successfully extracted from the instrumental background.

In addition, a new γ-ray instrument with high imaging and increased spectroscopic capabilities, positioned at an optimized orbit for a minimum passage through the Van Allen radiation belts would increase the sensitivity in γ-observations and allow a more precise picture of the high-energy universe, including stellar explosions. Taking advantage of the experience gained from the INTEGRAL mission, a careful selection of the background-reducing mechanisms, as well as the materials used to build the spacecraft and the telescope could lead to an instrument with lower background rates and consequently higher sensitivity, able to decipher the messages sent from energetic phenomena at longer distances than today. This could be achieved with missions like GRIPS (Greiner et al. 2012) or H-ASTROGRAM (De Angelis 2018). Unfortunately, the costs of such missions have slowed them down and today, it is not known when a new state-of-the-art γ-ray telescope will be launched.

In general, scientific evolution is not a constant process. It can remain stagnant for several years or make colossal progress within a few months. Hence, there is no other option than exploit the current available methods for detecting γ-rays and at the same time hope for a more nearby incident or the launch of an new γ-ray mission with higher sensitivity, to gain an improved picture of one of the most exciting phenomena in the Universe.

A. Appendix

Additional figures and tables

Flux differences with different numbers of fitted sources

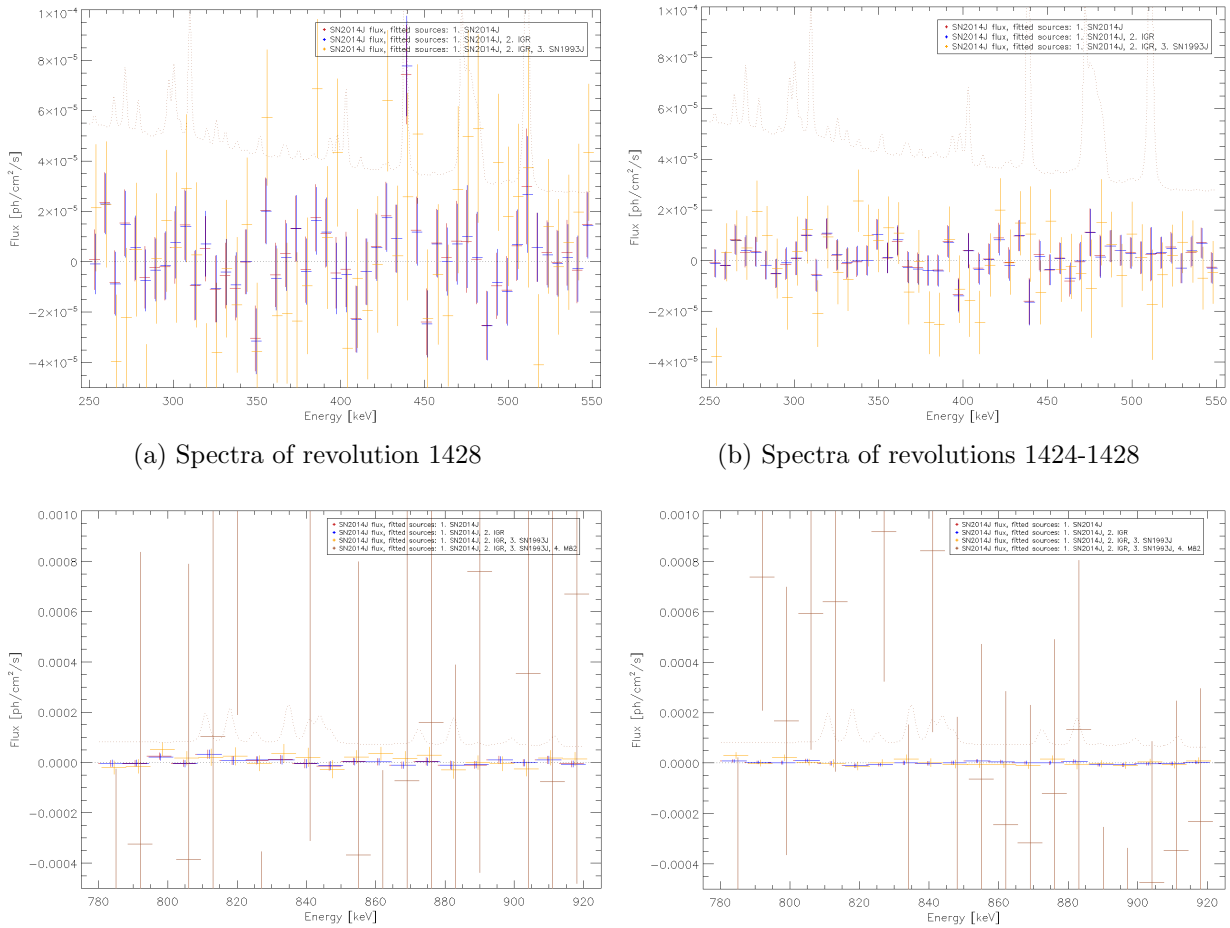

(a) Spectra of revolution 1428

(b) Spectra of revolutions 1424-1428

(c) Spectra of revolution 1428

(d) Spectra of revolutions 1424-1428

Figure A.1.: Top panels: Comparison of the SN2014J flux in the 250-550keV energy band for one (only SN2014J), two (SN2014J and IGR J09253+6929 and three (SN2014J, IGR J09253+6929, SN1993J) and three fitted celestial sources. Bottom panels: Comparison of the SN2014J flux in the 780-920keV energy band for one (only SN2014J), two (SN2014J and IGR J09253+6929), three (SN2014J, IGR J09253+6929, SN1993J) and four (SN2014J, IGR J09253+6929, SN1993J, M82) fitted celestial sources. Note that for illustration purposes, blue data points are shifted by 0.5keV, orange points by 1.0keV and brown by 1.5keV.

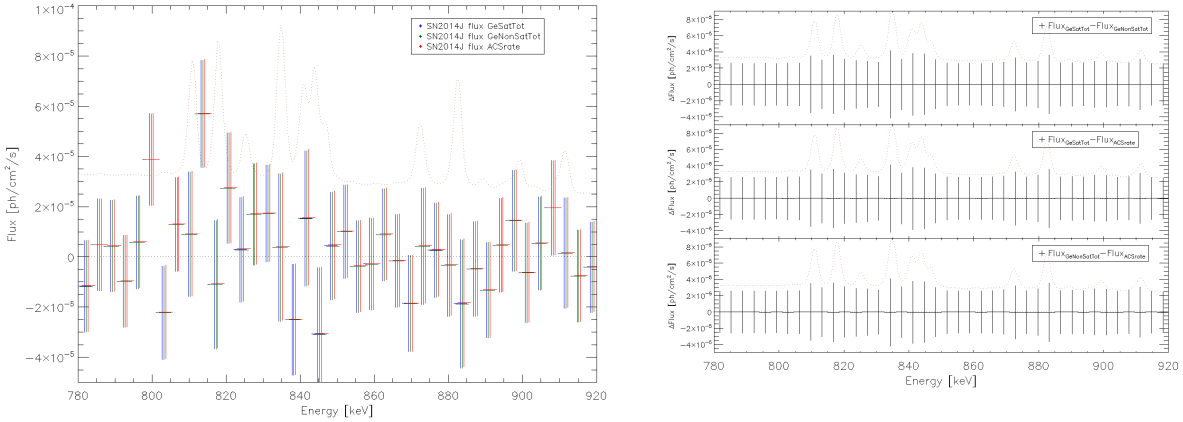

(a) Spectra of revolution 1380

(b) Flux differences

Figure A.2.: Comparison of a SN2014J spectrum in the 780-920keV energy band obtained with three different tracers. The blue data points correspond to a background description scaled with GeSatTot, dark green data points with GeNonSatTot and red data points with the ACS rate. Note that for illustration purposes, dark green points are shifted by 0.5keV and the red data points by 1keV.

Models of The and Burrows 2014

Overview of the supernova models constructed by The and Burrows 2014. For a detailed description of every model, see The and Burrows 2014. Here, only the γ-properties relevant to derive results are presented.

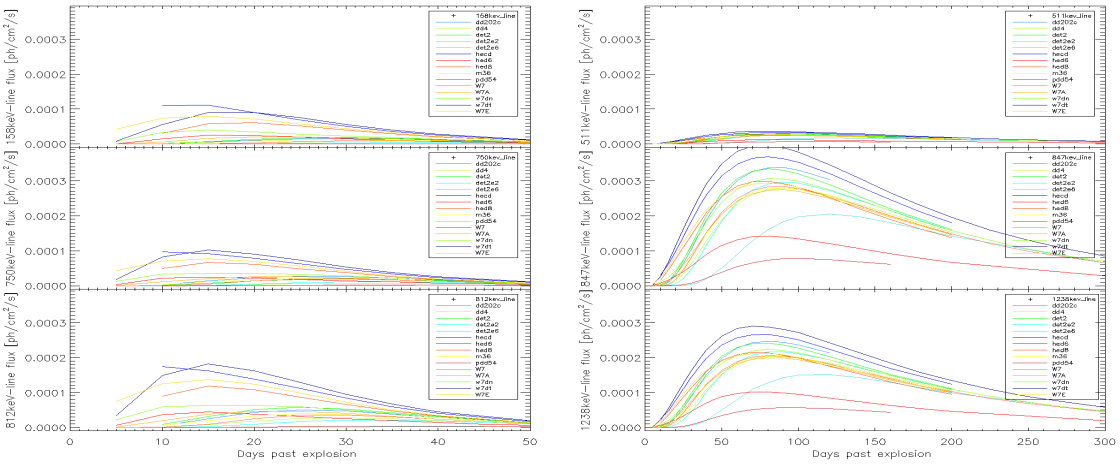

Figure A.3.: Light curves of the strongest γ-ray lines of ^{56}Ni and ^{56}Co, by The and Burrows 2014.

847keV line in 4-revolution time bins

Epoch	Flux [10^{-4} ph/cm^2/s]	E_0 [keV]	Bulk velocity [km/s]	σ [keV]	Spread velocity [km/s]
Epoch 1	0.62 ± 0.91 [1.32]	865.6 ± 1.7	6600 ± 600	2.0 ± 1.7	1450 ± 1600
Epoch 2	1.32 ± 1.43 [1.58]	865.2 ± 2.6	6450 ± 900	4.0 ± 2.7	3250 ± 2350
Epoch 3	0.69 ± 2.41 [0.64]	859.5 ± 20.4	4400 ± 7200	7.8 ± 24.1	6500 ± 20200
Epoch 4	3.54 ± 2.10 [3.02]	843.4 ± 2.4	-1300 ± 8500	5.7 ± 2.6	4700 ± 2250
Epoch 5	2.12 ± 1.28 [3.04]	867.7 ± 1.7	7350 ± 600	3.6 ± 1.7	2900 ± 1500
Epoch 6	2.51 ± 3.69 [1.44]	845.0 ± 10.5	-700 ± 3700	11.9 ± 15.3	9850 ± 12850
Epoch 7	2.60 ± 2.28 [2.12]	857.1 ± 5.0	3600 ± 1800	8.1 ± 5.8	6700 ± 4900
Epoch 8	3.42 ± 2.06 [2.72]	842.0 ± 3.3	-1750 ± 1150	8.2 ± 3.6	6800 ± 3050
Epoch 9	0.96 ± 4.00 [1.76]	858.9 ± 13.0	4200 ± 4600	4.7 ± 19.3	3850 ± 16450

Table A.1.: 847keV line, fitted parameters for four epochs, red fit (Gaussian line on constant offset). The values in square brackets present the statistical significance of the Gaussian lines.

Derivations

Calculating the line fluxes of The and Burrows 2014

The and Burrows 2014 provide light curves of the strongest γ-ray lines. However, the fluxes are given at specific times (e.g. at days 10, 20, 30 after the explosion). To adjust the light curves to the observation windows of both supernovae, the required fluxes were calculated, using a linear extrapolation between the two nearest model fluxes.

Assuming the following modeled light curve for an arbitrary line:

Days	M_{Day10}	M_{Day20}	M_{Day30}
Line Flux	5 ph/s/cm^2	30 ph/s/cm^2	20 ph/s/cm^2

Table A.2.: Example line fluxes to illustrate the extrapolation

If two available datasets D_1 and D_2 were obtained at days t_{D1}=12 and t_{D2}=28 after the explosion, their modeled fluxes are calculated by:

$$M_{Day12} = \frac{M_{Day20} - M_{Day10}}{t_{20} - t_{10}} \cdot (t_{D1} - t_{10}) + M_{Day10} \tag{A.1}$$

$$M_{Day28} = \frac{M_{Day30} - M_{Day20}}{t_{30} - t_{20}} \cdot (t_{D2} - t_{20}) + M_{Day20} \tag{A.2}$$

Calculating the additional ^{56}Ni masses to fit the lightcurves

Given the calculated line fluxes F_1, F_2, F_3 at times t_1, t_2, t_3 and the modeled fluxes from The and Burrows 2014 M_1, M_2, M_3, an additional flux F_{812keV} can be added to the modeled fluxes that depends on $M(^{56}Ni, t = 0)$.

$$F_{812keV,i} = \frac{M(^{56}Ni, t = 0) \cdot p_{812keV}}{4 \cdot \pi \cdot d_{M82}^2 \cdot m_{Ni} \cdot \exp\left(\frac{t}{\tau_{Ni}}\right)} \tag{A.3}$$

The new lightcurves have thus the form $M_{add.,i} = M_1 + F_{812keV,i}$. The additional mass $M(^{56}Ni, t = 0)$ is a free parameter and can be fitted to the data with the χ^2-technique, to obtain additional ^{56}Ni masses for every model.

Calculating the flux of the 270-470keV from the spectra of The and Burrows 2014

Continuum fluxes are not provided in The and Burrows 2014. Therefore, they must be calculated by fitting the spectra in the selected energy range with slopes.

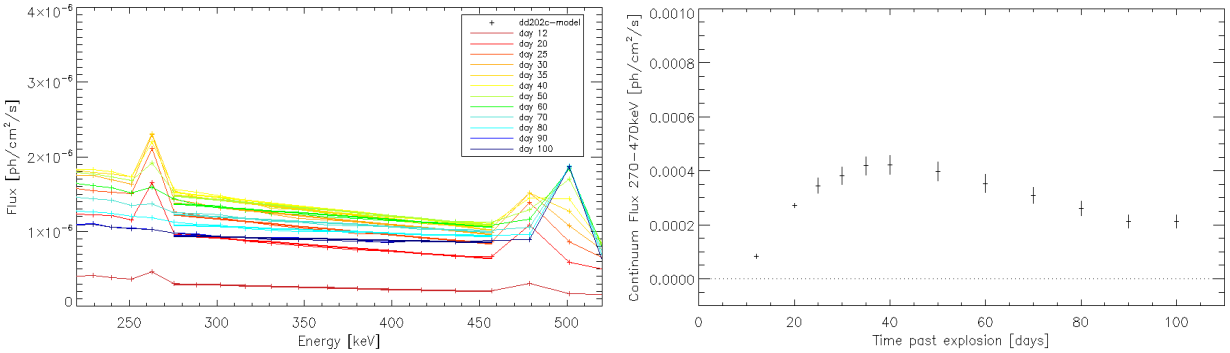

(a) Spectra of The and Burrows 2014

(b) Fitted continuum fluxes

Figure A.4.: Time series of the 800-840keV band for revolutions 1084-1088. Every data points corresponds to an energy bin of 4keV.

The derived fluxes are obtained with integration of the energy area of interest.

Adjusting the light curves of the 847keV line to the fitted lightcurves

Assuming three fitted fluxes for the 847keV line, $F_1 \pm \delta F_1$, $F_2 \pm \delta F_2$, $F_3 \pm \delta F_3$ and three modeled fluxes M_{t1}, M_2, M_3, the latter can be scaled to the fitted fluxes by multiplying them by a fitted parameter α. This parameters can be optimized using the χ^2-technique

$$\chi^2 = \sum_{i=1}^{3} \frac{(F_i - \alpha \cdot M_i)^2}{\delta F_i}, \tag{A.4}$$

Multiplying the mass of each supernova model with α delivers the adjusted ^{56}Ni masses at the time of explosion.

Bibliography

Aharonian, F., A. Akhperjanian, M. Beilicke, K. Bernlöhr, and H. G. e. a. Börst
2004. The Crab Nebula and Pulsar between 500 GeV and 80 TeV: Observations with the HEGRA Stereoscopic Air Cerenkov Telescopes. *ApJ*, 614(2):897–913.

Akasofu, S.-I. and S. Chapman
1961. The Ring Current, Geomagnetic Disturbance, and the Van Allen Radiation Belts. *Jgr*, 66:1321–1350.

Albernhe, F., J. F. Le Borgne, G. Vedrenne, D. Boclet, P. Durouchoux, and J. M. da Costa
1981. Detection of the positron annihilation gamma ray line from the Galactic Center region. *A&A*, 94:214–218.

Amanullah, R., A. Goobar, J. Johansson, M. M. Banerjee, and P. E. e. a. Nugent
2014. The Peculiar Extinction Law of SN 2014J Measured with the Hubble Space Telescope. *ApJL*, 788:L21.

Ambwani, K. and P. Sutherland
1988. Gamma-ray spectra and energy deposition for type IA supernovae. *ApJ*, 325:820–827.

Anderson, C. D.
1933. The Positive Electron. *Physical Review*, 43:491–494.

Antiochos, S. K., C. R. DeVore, and J. A. Klimchuk
1999. A Model for Solar Coronal Mass Ejections. *ApJ*, 510:485–493.

Arnett, W. D.
1969. A Possible Model of Supernovae: Detonation of ^{12}C. *ApSS*, 5:180–212.

Arnett, W. D.
1982. Type I supernovae. I - Analytic solutions for the early part of the light curve. *ApJ*, 253:785–797.

Axelrod, T. S.
1980. *Late time optical spectra from the Ni-56 model for Type 1 supernovae*. PhD thesis, California Univ., Santa Cruz.

Badenes, C., J. P. Hughes, E. Bravo, and N. Langer
2007. Are the Models for Type Ia Supernova Progenitors Consistent with the Properties of Supernova Remnants? *ApJ*, 662:472–486.

Barker, S., R. de Grijs, and M. Cerviño
2008. Star cluster versus field star formation in the nucleus of the prototype starburst galaxy M 82. *A&A*, 484:711–720.

Baur, G., G. Boero, A. Brauksiepe, A. Buzzo, W. Eyrich, R. Geyer, D. Grzonka, J. Hauffe, and K. K. et al.
1996. Production of antihydrogen. *Physics Letters B*, 368(3):251 – 258.

Berger, M. J. and S. M. Seltzer
1964. Tables of Energy Losses and Ranges of Electrons and Positrons. In *Studies in Penetration of Charged Particles in Matter*, P. 205.

Bethe, H. and W. Heitler
1934. On the Stopping of Fast Particles and on the Creation of Positive Electrons. *Proceedings of the Royal Society of London Series A*, 146:83–112.

Bethe, H. A.
1990. Supernova mechanisms. *Reviews of Modern Physics*, 62:801–866.

Bloom, J. S., D. Kasen, K. J. Shen, P. E. Nugent, N. R. Butler, M. L. Graham, D. A. Howell, U. Kolb, S. Holmes, C. A. Haswell, V. Burwitz, J. Rodriguez, and M. Sullivan
2012. A Compact Degenerate Primary-star Progenitor of SN 2011fe. *ApJL*, 744:L17.

Blumenthal, G. R. and R. J. Gould
1970. Bremsstrahlung, Synchrotron Radiation, and Compton Scattering of High-Energy Electrons Traversing Dilute Gases. *Reviews of Modern Physics*, 42:237–271.

Brown, B. L. and M. Leventhal
1987. Galactic center positronium fraction - Observations and simulations. *ApJ*, 319:637–642.

Bussard, R. W., R. Ramaty, and R. J. Drachman
1979. The annihilation of galactic positrons. *ApJ*, 228:928–934.

Cao, Y., M. M. Kasliwal, A. McKay, and A. Bradley
2014. Classification of Supernova in M82 as a young, reddened Type Ia Supernova. *The Astronomer's Telegram*, 5786.

Cappellaro, E., M. Turatto, D. Y. Tsvetkov, O. S. Bartunov, C. Pollas, R. Evans, and M. Hamuy
1997. The rate of supernovae from the combined sample of five searches. *A&A*, 322:431–441.

Caroli, E., J. B. Stephen, G. Di Cocco, L. Natalucci, and A. Spizzichino
1987. Coded aperture imaging in x- and gamma-ray astronomy. *Space Science Reviews*, 45(3):349–403.

Chan, K.-W. and R. E. Lingenfelter
1993. Positrons from supernovae. *ApJ*, 405:614–636.

Chandrasekhar, S.
1938. An Integral Theorem on the Equilibrium of a Star. *ApJ*, 87:535.

Chomiuk, L., A. M. Soderberg, M. Moe, R. A. Chevalier, M. P. Rupen, C. Badenes, R. Margutti, C. Fransson, W.-f. Fong, and J. A. Dittmann
2012. EVLA Observations Constrain the Environment and Progenitor System of Type Ia Supernova 2011fe. *ApJ*, 750:164.

Christodoulou, A. S.
2016. Positron Annihilation Spectroscopy of SN2014J. Bachelor thesis, MPE.

Churazov, E., R. Sunyaev, J. Isern, I. Bikmaev, E. Bravo, N. Chugai, S. Grebenev, P. Jean, J. Knödlseder, F. Lebrun, and E. Kuulkers
2015. Gamma-rays from Type Ia Supernova SN2014J. *ApJ*, 812:62.

Colgate, S. A.
1970. Positrons and Low Energy Cosmic Rays from Supernovae. *ApSS*, 8:457–462.

Colgate, S. A.
1991. Supernova Calculations and the Hot Bubble. In *Supernovae*, S. E. Woosley, ed., P. 352.

Colgate, S. A. and C. McKee
1969. Early Supernova Luminosity. *ApJ*, 157:623.

Colgate, S. A., A. G. Petschek, and J. T. Kriese
1980. The luminosity of type I supernovae. *ApJL*, 237:L81–L85.

Colgate, S. A. and R. H. White
1966. The Hydrodynamic Behavior of Supernovae Explosions. *ApJ*, 143:626.

Crannell, C. J., G. Joyce, R. Ramaty, and C. Werntz
1976. Formation of the 0.511 MeV line in solar flares. *ApJ*, 210:582–592.

Dalcanton, J. J., B. F. Williams, A. C. Seth, A. Dolphin, J. Holtzman, K. Rosema, and E. D. e. a. Skillman
2009. The ACS Nearby Galaxy Survey Treasury. *ApJS*, 183:67–108.

Daugherty, J. K. and A. K. Harding
1983. Pair production in superstrong magnetic fields. *ApJ*, 273:761–773.

De Angelis, A.
2018. Science with e-astrogam: A space mission for mev–gev gamma-ray astrophysics. *Journal of High Energy Astrophysics*, 19:1 – 106.

Deutsch, M.
1951. Evidence for the Formation of Positronium in Gases. *Physical Review*, 82:455–456.

Diamond, T. R., P. Hoeflich, E. Y. Hsiao, D. J. Sand, and G. e. a. Sonneborn
2018. Near-infrared Spectral Evolution of the Type Ia Supernova 2014J in the Nebular Phase: Implications for the Progenitor System. *ApJ*, 861:119.

Diehl, R.
2013. Cosmic Gamma-Ray Spectroscopy. *The Astronomical Review*, 8(3):19–65.

Diehl, R., D. H. Hartmann, and N. Prantzos
2018a. *Astrophysics with Radioactive Isotopes*. Springer Verlag.

Diehl, R., T. Siegert, J. Greiner, M. Krause, K. Kretschmer, M. Lang, M. Pleintinger, A. W. Strong, C. Weinberger, and X. Zhang
2018b. INTEGRAL/SPI γ-ray line spectroscopy. Response and background characteristics. *A&A*, 611:A12.

Diehl, R., T. Siegert, W. Hillebrandt, S. A. Grebenev, J. Greiner, M. Krause, M. Kromer, K. Maeda, F. Röpke, and S. Taubenberger
2014. Early ^{56}Ni decay gamma rays from SN2014J suggest an unusual explosion. *Science*, 345:1162–1165.

Diehl, R., T. Siegert, W. Hillebrandt, M. Krause, J. Greiner, K. Maeda, F. K. Röpke, S. A. Sim, W. Wang, and X. Zhang
2015. SN2014J gamma rays from the ^{56}Ni decay chain. *A&A*, 574:A72.

Dirac, P. A. M.
1928. The Quantum Theory of the Electron. *Proceedings of the Royal Society of London Series A*, 117:610–624.

Dirac, P. A. M.
1930. On the Annihilation of Electrons and Protons. *Proceedings of the Cambridge Philosophical Society*, 26:361.

D.Sc., E. R. M.
1903. Xv. the magnetic and electric deviation of the easily absorbed rays from radium. *The London, Edinburgh, and Dublin Philosophical Magazine and Journal of Science*, 5(26):177–187.

Einstein, A.
1905. Über einen die Erzeugung und Verwandlung des Lichtes betreffenden heuristischen Gesichtspunkt. *Annalen der Physik*, 322:132–148.

Ferrière, K. M.
2001. The interstellar environment of our galaxy. *Reviews of Modern Physics*, 73:1031–1066.

Filippenko, A. V.
1997. Optical Spectra of Supernovae. *Araa*, 35:309–355.

Fink, M., W. Hillebrandt, and F. K. Röpke
2007. Double-detonation supernovae of sub-Chandrasekhar mass white dwarfs. *A&A*, 476:1133–1143.

Fink, M., F. K. Röpke, W. Hillebrandt, I. R. Seitenzahl, S. A. Sim, and M. Kromer
2010. Double-detonation sub-Chandrasekhar supernovae: can minimum helium shell masses detonate the core? *A&A*, 514:A53.

Fossey, S. J., B. Cooke, G. Pollack, M. Wilde, and T. Wright
2014. Supernova 2014J in M82 = Psn J09554214+6940260. *Central Bureau Electronic Telegrams*, 3792.

Fowler, W. A. and F. Hoyle
1964. Neutrino Processes and Pair Formation in Massive Stars and Supernovae. *ApJS*, 9:201.

Gaisser, T. K.
2012. Spectrum of cosmic-ray nucleons, kaon production, and the atmospheric muon charge ratio. *Astroparticle Physics*, 35:801–806.

Galbany, L., M. E. Moreno-Raya, P. Ruiz-Lapuente, and J. I. e. a. González Hernández
2016. SN 2014J at M82 - I. A middle-class Type Ia supernova by all spectroscopic metrics. *MNRAS*, 457:525–537.

Gehrels, N.
1985. Instrumental background in balloon-borne gamma-ray spectrometers and techniques for its reduction. *Nuclear Instruments and Methods in Physics Research A*, 239:324–349.

Ginzburg, V. L.
1979. *Theoretical physics and astrophysics.*

Gómez-Gomar, J., J. Isern, and P. Jean
1998. Prospects for Type IA supernova explosion mechanism identification with gamma rays. *MNRAS*, 295:1–9.

Goobar, A., J. Johansson, R. Amanullah, Y. Cao, D. A. Perley, M. M. Kasliwal, R. Ferretti, and P. E. e. a. Nugent
2014. The Rise of SN 2014J in the Nearby Galaxy M82. *ApJL*, 784:L12.

Goobar, A., M. Kromer, R. Siverd, K. G. Stassun, J. Pepper, R. Amanullah, M. Kasliwal, J. Sollerman, and F. Taddia
2015. Constraints on the Origin of the First Light from SN 2014J. *ApJ*, 799:106.

Gould, R. J. and G. P. Schréder
1967. Pair production in photon-photon collisions. *Phys. Rev.*, 155:1404–1407.

Green, D. A. and S. F. Gull
1984. Two new young galactic supernova remnants. *Nat*, 312:527–529.

Greiner, J., K. Mannheim, F. Aharonian, and M. Ajello
2012. GRIPS - Gamma-Ray Imaging, Polarimetry and Spectroscopy. *Experimental Astronomy*, 34:551–582.

Guessoum, N., P. Jean, and W. Gillard
2005. The lives and deaths of positrons in the interstellar medium. *A&A*, 436:171–185.

Guessoum, N., R. Ramaty, and R. E. Lingenfelter
1991. Positron annihilation in the interstellar medium. *ApJ*, 378:170–180.

Heger, A., C. L. Fryer, S. E. Woosley, N. Langer, and D. H. Hartmann
2003. How Massive Single Stars End Their Life. *ApJ*, 591:288–300.

Heitler, W.
1954. *Quantum theory of radiation*.

Hillebrandt, W., M. Kromer, F. K. Röpke, and A. J. Ruiter
2013. Towards an understanding of Type Ia supernovae from a synthesis of theory and observations. *Frontiers of Physics*, 8:116–143.

Hoeflich, P. and A. Khokhlov
1996. Explosion Models for Type IA Supernovae: A Comparison with Observed Light Curves, Distances, H 0, and Q 0. *ApJ*, 457:500.

Hofstadter, R.
1948. Alkali Halide Scintillation Counters. *Physical Review*, 74:100–101.

Hoyle, F. and W. A. Fowler
1960. Nucleosynthesis in Supernovae. *ApJ*, 132:565.

Hubbell, J. H.
2006. Electron positron pair production by photons: A historical overview. *Radiation Physics and Chemistry*, 75:614–623.

Iben, Jr., I., K. Nomoto, A. Tornambe, and A. V. Tutukov
1987. On interacting helium star-white dwarf pairs as supernova precursors. *ApJ*, 317:717–723.

Iben, Jr., I. and A. V. Tutukov
1984. Supernovae of type I as end products of the evolution of binaries with components of moderate initial mass (M not greater than about 9 solar masses). *ApJS*, 54:335–372.

Isern, J., E. Bravo, and P. Jean
2017. Gamma-rays from SNIa. *arXiv e-prints*.

Isern, J., P. Jean, E. Bravo, R. Diehl, J. Knödlseder, A. Domingo, A. Hirschmann, P. Hoeflich, X. Zhang, C. Badenes, I. Domínguez, C. Jordi, G. Lichti, G. Vedrenne, and P. e. a. Von Ballmoos
2013a. Observation of SN2011fe with INTEGRAL. I. Pre-maximum phase. *A&A*, 552:A97.

Isern, J., P. Jean, E. Bravo, R. Diehl, J. Knödlseder, A. Domingo, A. Hirschmann, and P. e. a. Hoeflich
2013b. Observations of SN2011fe with INTEGRAL. *arXiv e-prints*.

Isern, J., P. Jean, E. Bravo, J. Knödlseder, F. Lebrun, E. Churazov, and R. e. a. Sunyaev
2016. Gamma-ray emission from SN2014J near maximum optical light. *A&A*, 588:A67.

Iwata, K., R. G. Greaves, and C. M. Surko
1997. γ-ray spectra from positron annihilation on atoms and molecules. *Pra*, 55:3586–3604.

Janka, H.-T.
2011. *Supernovae und kosmische Gammablitze*. MPA institut, Garching: Springer Spektrum.

Janka, H.-T.
2016-2017. Lecture notes in Exploding Stars.

Jauch, J. and F. Rohrlich
1976. *The Theory of Photons and Electrons*. Springer Verlag Berlin Heidelberg.

Jean, P., J. Knödlseder, W. Gillard, N. Guessoum, K. Ferrière, A. Marcowith, V. Lonjou, and J. P. Roques
2006. Spectral analysis of the Galactic e^+e^- annihilation emission. *A&A*, 445:579–589.

Jean, P., J. E. Naya, and P. von Ballmoos
1997. Performance of an INTEGRAL Spectrometer Model. In *The Transparent Universe*, volume 382 of *ESA Special Publication*, P. 635.

Jean, P., G. Vedrenne, J. P. Roques, V. Schönfelder, B. J. Teegarden, A. von Kienlin, and J. e. a. Knödlseder
2003. SPI instrumental background characteristics. *A&A*, 411:L107–L112.

Jean, P., P. von Ballmoos, G. Vedrenne, and J. E. Naya
1996. Performance of advanced Ge-spectrometer for nuclear astrophysics. In *Gamma-Ray and Cosmic-Ray Detectors, Techniques, and Missions*, volume 2806 of *ProcSpie*, Pp. 457–471.

Jensen, P. L., K. Clausen, C. Cassi, F. Ravera, G. Janin, C. Winkler, and R. Much
2003. The INTEGRAL spacecraft - in-orbit performance. *A&A*, 411:L7–L17.

Johnson, W. N., J. D. Kurfess, R. L. Kinzer, W. R. Purcell, and M. S. Strickman
1989. The Oriented Scintillation Spectrometer Experiment (OSSE) instrument description. *NASA STI/Recon Technical Report N*, 91.

Johnson, III, W. N., F. R. Harnden, Jr., and R. C. Haymes
1972. The Spectrum of Low-Energy Gamma Radiation from the Galactic-Center Region. *ApJL*, 172:L1.

Karachentsev, I. D. and O. G. Kashibadze
2006. Masses of the local group and of the M81 group estimated from distortions in the local velocity field. *Astrophysics*, 49:3–18.

Karshenboim, S. G.
2004. Precision Study of Positronium:. *International Journal of Modern Physics A*, 19:3879–3896.

Kelly, P. L., O. D. Fox, A. V. Filippenko, K. J. Shen, and W. e. a. Zheng
2014. Constraints on the Progenitor System of the Type Ia Supernova 2014J from Pre-explosion Hubble Space Telescope Imaging. *ApJ*, 790:3.

Khokhlov, A. M.
1991. Delayed detonation model for type IA supernovae. *A&A*, 245:114–128.

Khokhlov, A. M.
1995. Propagation of Turbulent Flames in Supernovae. *ApJ*, 449:695.

Kinzer, R. L., W. R. Purcell, W. N. Johnson, J. D. Kurfess, G. Jung, and J. Skibo
1996. OSSE observations of positron annihilation in the Galactic plane. *Aaps*, 120:317–320.

Klein, O. and T. Nishina
1929. Über die Streuung von Strahlung durch freie Elektronen nach der neuen relativistischen Quantendynamik von Dirac. *Zeitschrift fur Physik*, 52:853–868.

Klemperer, O. and J. Chadwick
1934. On the annihilation radiation of the positron. *Proceedings of the Cambridge Philosophical Society*, 30:347.

Knödlseder, J., P. Jean, V. Lonjou, G. Weidenspointner, N. Guessoum, W. Gillard, B. Teegarden, V. Schönfelder, and C. e. a. Winkler
2005. The all-sky distribution of 511 keV electron-positron annihilation emission. *A&A*, 441:513–532.

Knoll, G. F.
2000. *Radiation detection and measurement*.

Kretschmer, K.
2013. *Dissertation*. PhD thesis, Technische Universität München.

Kromer, M., S. A. Sim, M. Fink, F. K. Röpke, I. R. Seitenzahl, and W. Hillebrandt
2010. Double-detonation Sub-Chandrasekhar Supernovae: Synthetic Observables for Minimum Helium Shell Mass Models. *ApJ*, 719:1067–1082.

Kundu, E., P. Lundqvist, M. A. Pérez-Torres, R. Herrero-Illana, and A. Alberdi
2017. Constraining Magnetic Field Amplification in SN Shocks Using Radio Observations of SNe 2011fe and 2014J. *ApJ*, 842:17.

Law, W. Y. and H. Ritter
1983. The formation of massive white dwarfs in cataclysmic binaries. *A&A*, 123:33–38.

Leibundgut, B.
1995. Observations of Supernovae. In *NATO Advanced Science Institutes (ASI) Series C*, volume 450 of *NATO Advanced Science Institutes (ASI) Series C*, P. 3.

Leibundgut, B.
2001. Cosmological Implications from Observations of Type Ia Supernovae. *Araa*, 39:67–98.

Leone, M. and N. Robotti
2010. Frédéric Joliot, Irène Curie and the early history of the positron (1932-33). *European Journal of Physics*, 31:975–987.

Leventhal, M., C. J. MacCallum, A. F. Huters, and P. D. Stang
1980. Gamma-ray lines and continuum radiation from the galactic center direction. *ApJ*, 240:338–343.

Leventhal, M., C. J. MacCallum, and P. D. Stang
1978. Detection of 511 keV positron annihilation radiation from the galactic center direction. *ApJL*, 225:L11–L14.

Li, W., J. S. Bloom, P. Podsiadlowski, A. A. Miller, and S. B. e. a. Cenko
2011a. Exclusion of a luminous red giant as a companion star to the progenitor of supernova SN 2011fe. *Nat*, 480:348–350.

Li, W., J. Leaman, R. Chornock, A. V. Filippenko, and S. e. a. Jha
2011b. Nearby supernova rates from the Lick Observatory Supernova Search - II. The observed luminosity functions and fractions of supernovae in a complete sample. *MNRAS*, 412:1441–1472.

Lichti, G. G. and R. e. a. Georgii
2001. Exploring the gamma-ray universe. In *Exploring the Gamma-Ray Universe*, A. Gimenez, V. Reglero, and C. Winkler, eds., volume 459 of *ESA Special Publication*, Pp. 83–86.

Lightman, A. P. and A. A. Zdziarski
1987. Pair production and Compton scattering in compact sources and comparison to observations of active galactic nuclei. *ApJ*, 319:643–661.

Lund, N., C. Budtz-Jørgensen, N. J. Westergaard, S. Brandt, and I. L. e. a. Rasmussen
2003. JEM-X: The X-ray monitor aboard INTEGRAL. *A&A*, 411:L231–L238.

Lundqvist, P., M. Kromer, B. J. Shappee, and A. e. a. Goobar
2015. No trace of a single-degenerate companion in late spectra of supernovae 2011fe and 2014J. *A&A*, 577:A39.

Maeda, K. and Y. Terada
2016. Progenitors of type Ia supernovae. *International Journal of Modern Physics D*, 25:1630024.

Margutti, R., J. Parrent, A. M. Soderberg, M. R. Drout, and R. e. a. Kirshner
2014. No X-Rays from the Very Nearby Type Ia SN 2014J: Constraints on Its Environment. *ApJ*, 790:52.

Margutti, R., A. M. Soderberg, L. Chomiuk, and R. e. a. Chevalier
2012. Inverse Compton X-Ray Emission from Supernovae with Compact Progenitors: Application to SN2011fe. *ApJ*, 751:134.

Marion, G. H., D. J. Sand, E. Y. Hsiao, D. P. K. Banerjee, S. Valenti, and M. D. e. a. Stritzinger
2015. Early Observations and Analysis of the Type Ia SN 2014J in M82. *ApJ*, 798:39.

Masetti, N., P. Parisi, E. Palazzi, E. Jiménez-Bailón, and V. e. a. Chavushyan
2010. Unveiling the nature of INTEGRAL objects through optical spectroscopy. VIII. Identification of 44 newly detected hard X-ray sources. *A&A*, 519:A96.

Milne, P. A., A. L. Hungerford, P. A. Pinto, and L.-S. e. a. The
2004. Unified One-Dimensional Simulations of Gamma-Ray Line Emission from Type Ia Supernovae. *ApJ*, 613:1101–1119.

Milne, P. A., J. D. Kurfess, R. L. Kinzer, and M. D. Leising
2002. Supernovae and positron annihilation radiation. *Nar*, 46:553–558.

Milne, P. A., L.-S. The, and M. D. Leising
1999. Positron Escape from Type IA Supernovae. *ApJS*, 124:503–526.

Mohorovičić, S.
1934. Möglichkeit neuer Elemente und ihre Bedeutung für die Astrophysik. *Astronomische Nachrichten*, 253:93.

Mohr, P. J., D. B. Newell, and B. N. Taylor
2016. Codata recommended values of the fundamental physical constants: 2014. *Rev. Mod. Phys.*, 88:035009.

Mould, R. F.
1995. *A century of X-rays and radioactivity in medicine: with emphasis on photographic records of the early years.*

Nadyozhin, D. K.
1994. The properties of NI to CO to Fe decay. *ApJS*, 92:527–531.

Niemeyer, J. C. and W. Hillebrandt
1995. Turbulent Nuclear Flames in Type IA Supernovae. *ApJ*, 452:769.

Nomoto, K.
1984. Evolution of 8-10 solar mass stars toward electron capture supernovae. I - Formation of electron-degenerate O + Ne + Mg cores. *ApJ*, 277:791–805.

Nomoto, K., F.-K. Thielemann, and K. Yokoi
1984. Accreting white dwarf models of Type I supernovae. III - Carbon deflagration supernovae. *ApJ*, 286:644–658.

Nugent, P. E., D. A. Howell, D. Bishop, E. Waagen, and A. e. a. Grenier
2011. Supernova 2011fe in M101 = Psn J14030581+5416254. *Central Bureau Electronic Telegrams*, 2792.

Ore, A. and J. L. Powell
1949. Three-Photon Annihilation of an Electron-Positron Pair. *Physical Review*, 75:1696–1699.

Ozel, F. and P. Freire
2016. Masses, Radii, and Equation of State of Neutron Stars. *ArXiv e-prints.*

Pakmor, R., M. Kromer, S. Taubenberger, S. A. Sim, F. K. Röpke, and W. Hillebrandt
2012. Normal Type Ia Supernovae from Violent Mergers of White Dwarf Binaries. *ApJL*, 747:L10.

Parrent, J. T., D. A. Howell, B. Friesen, R. C. Thomas, R. A. Fesen, D. Milisavljevic, and F. B. e. a. Bianco
2012. Analysis of the Early-time Optical Spectra of SN 2011fe in M101. *ApJL*, 752:L26.

Penney, R. and P. Hoeflich
2014. Thermonuclear supernovae: Probing magnetic fields by positrons and late-time ir line profiles. *The Astrophysical Journal*, 795:84.

Pereira, R., R. C. Thomas, G. Aldering, P. Antilogus, C. Baltay, and S. e. a. Benitez-Herrera
2013. Spectrophotometric time series of SN 2011fe from the Nearby Supernova Factory. *A&A*, 554:A27.

Pérez-Torres, M. A., P. Lundqvist, R. J. Beswick, I. Martí-Vidal, and J. C. e. a. Guirado
2014. Constraints on the Progenitor System and the Environs of SN 2014J from Deep Radio Observations. *ApJ*, 792:38.

Perlmutter, S., G. Aldering, G. Goldhaber, R. A. Knop, P. Nugent, P. G. Castro, S. Deustua, S. Fabbro, and A. e. a. Goobar
1999. Measurements of Ω and Λ from 42 High-Redshift Supernovae. *ApJ*, 517:565–586.

Peters, P. C.
1964. Gravitational radiation and the motion of two point masses. *Phys. Rev.*, 136:B1224–B1232.

Phillips, M. M., P. Lira, N. B. Suntzeff, R. A. Schommer, M. Hamuy, and J. Maza
1999. The Reddening-Free Decline Rate Versus Luminosity Relationship for Type IA Supernovae. *AJ*, 118:1766–1776.

Piro, A. L. and E. Nakar
2014. Constraints on Shallow ^{56}Ni from the Early Light Curves of Type Ia Supernovae. *ApJ*, 784:85.

Prantzos, N., C. Boehm, A. M. Bykov, and R. e. a. Diehl
2011. The 511 keV emission from positron annihilation in the Galaxy. *Reviews of Modern Physics*, 83:1001–1056.

Purcell, W. R., D. A. Grabelsky, M. P. Ulmer, W. N. Johnson, and R. L. e. a. Kinzer
1994. The distribution of galactic 511 keV positron annihilation radiation. In *American Institute of Physics Conference Series*, American Institute of Physics Conference Series.

Ramaty, R., B. Kozlovsky, and R. E. Lingenfelter
1979. Nuclear gamma-rays from energetic particle interactions. *ApJS*, 40:487–526.

Reames, D. V.
1999. Particle acceleration at the Sun and in the heliosphere. *Ssr*, 90:413–491.

Riess, A. G., A. V. Filippenko, P. Challis, A. Clocchiatti, and A. e. a. Diercks
1998. Observational Evidence from Supernovae for an Accelerating Universe and a Cosmological Constant. *AJ*, 116:1009–1038.

Röpke, F. K. and W. Hillebrandt
2005. Full-star type Ia supernova explosion models. *A&A*, 431:635–645.

Röpke, F. K., M. Kromer, I. R. Seitenzahl, R. Pakmor, S. A. Sim, and S. e. a. Taubenberger
2012. Constraining Type Ia Supernova Models: SN 2011fe as a Test Case. *ApJL*, 750:L19.

Roques, J. P., S. Schanne, A. von Kienlin, J. Knödlseder, and R. e. a. Briet
2003. SPI/INTEGRAL in-flight performance. *A&A*, 411:L91–L100.

Ruiter, A. J., K. Belczynski, S. A. Sim, I. R. Seitenzahl, and D. Kwiatkowski
2014. The effect of helium accretion efficiency on rates of Type Ia supernovae: double detonations in accreting binaries. *MNRAS*, 440:L101–L105.

Ruiter, A. J., S. A. Sim, R. Pakmor, M. Kromer, and I. R. e. a. Seitenzahl
2013. On the brightness distribution of Type Ia supernovae from violent white dwarf mergers. *MNRAS*, 429:1425–1436.

Ruiz-Lapuente, P. and H. C. Spruit
1998. Bolometric Light Curves of Supernovae and Postexplosion Magnetic Fields. *ApJ*, 500:360–373.

Schwabe, M.
1843. Die Sonne. Von Herrn Hofrath Schwabe. *Astronomische Nachrichten*, 20:283.

Segre, E., J. R. Grover, and H. P. Noyes
1977. *Annual Review of Nuclear Science. Volume 27.*

Seitenzahl, I. R., C. A. Meakin, D. Q. Lamb, and J. W. Truran
2009. Initiation of the Detonation in the Gravitationally Confined Detonation Model of Type Ia Supernovae. *ApJ*, 700:642–653.

Seitenzahl, I. R., F. K. Röpke, M. Fink, and W. e. a. Hillebrandt
2013. Three-dimensional delayed-detonation models with nucleosynthesis for Type Ia supernovae. *MNRAS*, 429:1156–1172.

Shappee, B. J. and K. Z. Stanek
2011. A New Cepheid Distance to the Giant Spiral M101 Based on Image Subtraction of Hubble Space Telescope/Advanced Camera for Surveys Observations. *ApJ*, 733:124.

Shen, K. J., D. Kasen, N. N. Weinberg, L. Bildsten, and E. Scannapieco
2010. Thermonuclear .Ia Supernovae from Helium Shell Detonations: Explosion Models and Observables. *ApJ*, 715:767–774.

Siegert, T.
2013. High-precision cosmic gamma-ray line spectroscopy. Master thesis, MPE.

Siegert, T.
2017. *Positron-annihilation spectroscopy throughout the Milky Way.* PhD thesis, MPE.

Sim, S. A. and P. A. Mazzali
2008. On the γ-ray emission of Type Ia supernovae. *MNRAS*, 385:1681–1690.

Skinner, G. K.
2004. Coded mask imagers when to use them - and when not. *Nar*, 48:205–208.

Skinner, G. K.
2008. Sensitivity of coded mask telescopes. *Ao*, 47:2739–2749.

Smartt, S. J.
2015. Observational Constraints on the Progenitors of Core-Collapse Supernovae: The Case for Missing High-Mass Stars. *Pasa*, 32:e016.

Soddy, F.
1913. The Radio-Elements and the Periodic Law. *Nat*, 91:57–58.

Sokolov, A. A., I. M. Ternov, V. G. Bagrov, D. V. Gal'tsov, and V. C. Zhukovskii
1968. Radiation-induced self-polarization of the electron spin for helical motion in a magnetic field. *Soviet Physics Journal*, 11(5):4–7.

Srivastav, S., J. P. Ninan, B. Kumar, G. C. Anupama, D. K. Sahu, D. K. Ojha, and T. P. Prabhu
2016. Optical and NIR observations of the nearby type Ia supernova SN 2014J. *MNRAS*, 457:1000–1014.

Stritzinger, M., P. A. Mazzali, J. Sollerman, and S. Benetti
2006. Consistent estimates of ^{56}Ni yields for type Ia supernovae. *A&A*, 460:793–798.

Sukhbold, T., T. Ertl, S. E. Woosley, J. M. Brown, and H.-T. Janka
2016. Core-collapse Supernovae from 9 to 120 Solar Masses Based on Neutrino-powered Explosions. *ApJ*, 821:38.

Summa, A., F. K. Röpke, S. A. Sim, I. R. Seitenzahl, and R. e. a. Diehl
2013. Gamma-ray diagnostics of Type Ia supernovae. Predictions of observables from three-dimensional modeling. *A&A*, 554:A67.

Tammann, G., W. Loeffler, and A. Schroeder
1994. The galactic supernova rate. *The Astrophysical Journal Supplement Series*, 92:487–493.

Taubenberger, S., S. Hachinger, G. Pignata, P. A. C. e. a. Contreras
2008. The underluminous Type Ia supernova 2005bl and the class of objects similar to SN 1991bg. *MNRAS*, 385:75–96.

Telesco, C. M., P. Höflich, D. Li, C. Álvarez, C. M. Wright, P. J. Barnes, S. Fernández, J. H. Hough, N. A. Levenson, N. Mariñas, C. Packham, E. Pantin, R. Rebolo, P. Roche, and H. Zhang
2015. Mid-IR Spectra of Type Ia SN 2014J in M82 Spanning the First 4 Months. *ApJ*, 798:93.

The, L.-S. and A. Burrows
2014. Expectations for the hard x-ray continuum and gamma-ray line fluxes from the type ia supernova sn 2014j in m82. *The Astrophysical Journal*, 786(2):141.

Ubertini, P., F. Lebrun, G. Di Cocco, A. Bazzano, A. J. Bird, and K. e. a. Broenstad
2003. IBIS: The Imager on-board INTEGRAL. *A&A*, 411:L131–L139.

van den Heuvel, E. P. J., D. Bhattacharya, K. Nomoto, and S. A. Rappaport
1992. Accreting white dwarf models for CAL 83, CAL 87 and other ultrasoft X-ray sources in the LMC. *A&A*, 262:97–105.

Vedrenne, G., J.-P. Roques, and V. e. a. Schönfelder
2003. SPI: The spectrometer aboard INTEGRAL. *A&A*, 411:L63–L70.

Veigele, W. J.
1973. Photon Cross Sections from 0.1 KeV to 1 MeV for Elements Z = 1 to Z = 94. *Atomic Data*, 5:51.

Villard, P.
1900. Sur la réflexion et la réfraction des rayons cathodiques et des rayons déviables du radium. *Comptes rendus*, 130:1010–1012.

von Kienlin, A., V. Beckmann, G. Skinner, A. Strong, and R. e. a. Williams
2003. INTEGRAL Spectrometer SPI's GRB detection capabilities. GRBs detected inside SPI's FoV and with the anticoincidence system ACS. *A&A*, 411:L299–L305.

Waller, W. H., R. C. Bohlin, R. H. Cornett, M. N. Fanelli, and W. L. e. a. Freedman
1997. Ultraviolet Signatures of Tidal Interaction in the Giant Spiral Galaxy M101. *ApJ*, 481:169–173.

Wang, W., M. G. Lang, R. Diehl, H. Halloin, P. Jean, J. Knödlseder, K. Kretschmer, P. Martin, J. P. Roques, A. W. Strong, C. Winkler, and X. L. Zhang
2009. Spectral and intensity variations of Galactic ^{26}Al emission. *A&A*, 496:713–724.

Webbink, R. F.
1984. Double white dwarfs as progenitors of R Coronae Borealis stars and Type I supernovae. *ApJ*, 277:355–360.

Weidenspointner, G., P. Jean, N. Guessoum, R. Diehl, and C. e. a. Winkler
2006. The sky distribution of positronium annihilation continuum emission measured with SPI/INTEGRAL. *A&A*, 450:1013–1021.

Weidenspointner, G., J. Kiener, M. Gros, P. Jean, R. Diehl, J. Knödlseder, P. Leleux, V. Lonjou, J.-P. Roques, V. Schönfelder, and G. e. a. Vedrenne
2003. First identification and modelling of SPI background lines. *A&A*, 411:L113–L116.

Weidenspointner, G., G. Skinner, P. Jean, J. Knödlseder, and C. e. a. Winkler
2008. An asymmetric distribution of positrons in the Galactic disk revealed by γ-rays. *Nat*, 451:159–162.

Whelan, J. and I. Iben, Jr.
1973. Binaries and Supernovae of Type I. *ApJ*, 186:1007–1014.

Wiktorowicz, G., K. Belczynski, and T. Maccarone
2014. Black hole X-ray transients: The formation puzzle. In *Binary Systems, their Evolution and Environments*, P. 37.

Winkler, C., N. Lund, G. G. C. Palumbo, J. Paul, J.-P. Roques, V. Schönfelder, R. Sunyaev, B. Teegarden, P. Ubertini, and G. e. a. Vedrenne
2003. The INTEGRAL mission. *A&A*, 411:L1–L6.

Woosley, S. E., A. Heger, and T. A. Weaver
2002. The evolution and explosion of massive stars. *Reviews of Modern Physics*, 74:1015–1071.

Woosley, S. E. and T. A. Weaver
1994. Sub-Chandrasekhar mass models for Type IA supernovae. *ApJ*, 423:371–379.

Yang, Y., L. Wang, D. Baade, P. J. Brown, and P. A. e. a. Höflich
2017. Interstellar-medium Mapping in M82 through Light Echoes around Supernova 2014J. *ApJ*, 834:60.

Zheng, W., I. Shivvers, A. V. Filippenko, K. Itagaki, K. I. Clubb, O. D. Fox, M. L. Graham, P. L. Kelly, and J. C. Mauerhan
2014. Estimating the First-light Time of the Type Ia Supernova 2014J in M82. *ApJL*, 783:L24.